JAERI-M
84-190

BIENNIAL REPORT OF THE DEPARTMENT OF HIGH TEMPERATURE ENGINEERING

(April 1, 1982 - March 31, 1984)

October 1984

Department of High Temperature Engineering

日本原子力研究所
Japan Atomic Energy Research Institute

JAERI-Mレポートは，日本原子力研究所が不定期に公刊している研究報告書です。
入手の問合わせは，日本原子力研究所技術情報部情報資料課（〒319-11茨城県那珂郡東海村）あて，お申しこしください。なお，このほかに財団法人原子力弘済会資料センター（〒319-11 茨城県那珂郡東海村日本原子力研究所内）で複写による実費頒布をおこなっております。

JAERI-M reports are issued irregularly.
Inquiries about availability of the reports should be addressed to Information Section, Division of Technical Information, Japan Atomic Energy Research Institute, Tokai-mura, Naka-gun, Ibaraki-ken 319-11, Japan.

編集兼発行　日本原子力研究所
印　　刷　いばらき印刷㈱

JAERI-M 84-190

Biennial Report of the Department of High Temperature Engineering

(April 1, 1982 - March 31, 1984)

Department of High Temperature Engineering

(Received September 22, 1984)

Research activities conducted in the Department of High Temperature Engineering during fiscal 1982 and 1983 are described. Research and development works of the department are mainly related to a multi-purpose very high-temperature gas-cooled reactor (VHTR) and a fusion reactor.

This report deals with the main results obtained on material test, heat transfer, fluid-dynamics, structural mechanics, development of computer codes and operation of an M + A (Mother and Adapter) section and a T_1 test section of the HENDEL (Helium Engineering Demonstration Loop).

Keywords : High-Temperature , Gas-cooled Reactor, Fusion Reactor, Material Test, Heat Transfer, Fluid-Dynamics, Structural Mechanics, Code Development, Helium Gas Loop

---

JAERI－M 84 － 190

高温工学部隔年報

（昭和57年4月1日－昭和59年3月31日）

日本原子力研究所東海研究所高温工学部

（1984年9月22日受理）

本報告は，昭和57年度と58年度における高温工学部の研究開発活動を述べたものである。

当部の研究開発は主として多目的高温ガス実験炉，核融合炉に関するものであり，伝熱工学，流体力学，構造工学，材料試験，計算コードの開発，ヘンデルの運転，ヘンデルの燃料体スタック実証試験部（T_1）による試験で得た主要な研究成果を記載した。

CONTENTS

目　　次

FOREWORD

The research and development works carried out in the Department of High Temperature Engineering are mainly focused on the multi-purpose very high-temperature gas-cooled reactor (VHTR), and several foundamental experiments concerning fusion reactor technology, such as tests of fusion reactor materials and of the divertor composite plate under thermal cycling have been conducted as well.

The department has six divisions:

HENDEL Operation Division
HENDEL Development Laboratory
Heat Transfer Laboratory
Materials Strength Laboratory, and
Engineering Service Division.

The number of people working in the department was 72, as of March, 1984.

The items of activities in fiscal 1982 - 1983 are summarized as follows:

(1) Helium engineering demonstration loop (HENDEL)

A fuel stack test section, the first test section of HENDEL, was installed in M_1 loop and was operated for 1550 hours. The operation hours of M_2 loop (M_2 + A section) totaled 860 hours.

The principal specification of an in-core test section of HENDEL was decided, and the preliminary design work was started.

(2) Engineering studies on high-temperature structural components

The cross flow studies have been carried out both experimentally and analitically. Tests on leakage flow between the core blocks, as well as in bottom-core structures, seal elementt leakage flow test, foundamental experiments on thermal mixing in the plenum, and also the preliminary dynamical tests of coaxial double-pipe structure have been conducted.

(3) Heat transfer studies related to the VHTR

Thermo-hydraulic experiments on VHTR fuel and control rods, reversed coolant flow established in VHTR core in case of accident, as well as foundamental studies on transition flow in a concentric annulus, natural

circulation built in parallel vertical channels with different heat generations bave been analyzed.

(4) High-temperature strength properties of graphite and 2¼Cr-1Mo steel

Screening test of thermal barrier materials for the VHTR was completed. Six carbon materials were extensively examined.

Tests on the fracture, toughness, ring compressive fatigue of graphites have been carried out, and also the effects of oxidation on compressive deformation behavior of nuclear-grade isotropic graphite have been studied.

The Charpy impact tests and irradiation embrittlement and fracture toughness tests on 2¼Cr-1Mo steel, a candidate metal for VHTR reactor vessel, have been performed.

(5) Experiments related to fusion reactor technology

More than 1000 times thermal cycling tests of tungsten-copper duplex structure for a divertor plate have been conducted, and low-cycle fatigue tests of TiC-coated Molybdenum was completed.

This report describes the main results obtained on the above-mentioned research and development works in fiscal 1982 - 1983.

Department of High Temperature Engineering
Yoshizo Okamoto, Director
Konomo Sanokawa, Deputy Director

1. HELIUM ENGINEERING DEMONSTRATION LOOP (HENDEL)

H. Shimomura, M. Hishida, S. Tomobe, N. Izawa, S. Nekoya, Y. Hoshi
Y. Ohuchi, H. Hayashi, T. Kunitama, S. Kawaji, T. Kobayashi, M. Kato
Y. Ohta, R. Hino, Y. Kondo, S. Watanabe, H. Aita, S. Ohsone,
H. Yonekawa, H. Seki and K. Sekiyama
(HENDEL Operation Division)

T. Tanaka, K. Takase, K. Kunitomi, Y. Inagaki, S. Maruyama, K. Ioka
M. Okamoto, K. Umenishi, Y. Mizokami and N. Zaima
(HENDEL Development Laboratory)

1.1 General Description of VHTR and HENDEL

1.1.1 VHTR and its high-temperature components

A helium engineering demonstration loop (HENDEL) at JAERI for a very high-temperature reactor (VHTR) is designed as a large-scale model testing facility for a verification of the integrity of high-temperature components, such as an intermediate heat exchanger (IHX), a high temperature piping, an emergency isolation valve and a core support structure of the VHTR, which are supposed to be exposed to extremely severe conditions.

Its operation was started in April, 1982, specifically to demonstrate performances and integrities of these components of the VHTR from a standpoint of licensing.

During the last several years, the design studies of the VHTR have been conducted at JAERI. The conceptual design was completed in 1976, and the more detailed design works and the safety analyses of the VHTR are being continued. The VHTR is a helium-cooled, graphite-moderated reactor with a thermal output of 50 MW, and the coolant temperature at the outlet of the reactor is 950°C. The tests which are to be conducted using the VHTR as follows:

(1) Demonstration test for nuclear process heat applications,
(2) Irradiation test for development of fuel and material for high-temperature use, and
(3) Verification of the VHTR plant safety.

The design parameters of the VHTR are determined, taking into consideration these objectives. The reactor is provided with two primary cooling circuits. Each of the circuits is connected to a secondary cooling circuit through an intermediate heat exchanger. The components for process heat applications, such as a steam reformer, will be installed in one of the two secondary circuits.

Emphasis is placed on maintaining the outlet coolant temperature as high as possible. The type of fuel block chosen is a prismatic graphite block with a hexagonal cross section, accommodating a hollow fuel pin sheathed with a graphite sleeve. The core is composed of a regular array of these graphite blocks, which are piled up vertically.

As the reactor and the components for process heat applications are somewhat different from the conventional ones, analyses must be carried out especially from a safety standpoint. In this context, verification tests for the reactor and the high-temperature components using HENDEL are planned.

1.1.2 HENDEL and its objectives

Figure 1.1 shows HENDEL test sections with reference to the VHTR. High-temperature key components are:

(1) fuel stack and control rods,
(2) support structure exposed to direct impingement of core outlet flow,
(3) reactor internal components and structure neccessary to establish structural, thermal and fluid flow parameters, and
(4) high-temperature components of heat removal system.

HENDEL test sections are expected to be parts of the VHTR research and development program, which include the design and analysis of the reactor core and plant components, as well as tests using component test facilities, such as a large-scale high-temperature helium gas loop (HTGL) for flow and heat transfer studies.

Test conditions of HENDEL test sections should be determined so as to enable the evaluation in actual VHTR conditions. A finally determined conditions are shown in Tables 1.1 and 1.2.

HENDEL consists of Mother section, Adapter section and Test sections. A flowsheet of HENDEL is shown in Fig. 1.2. Mother section circulates helium gas of a specified flow rate (0.4 and 4.0 kg/s), pressure (4MPa),

and purity (less than 10 ppm). It consists of helium circulators, heaters, coolers, mixing tanks and filters, a helium gas storage, a purification system and a cooling system. Adapter section heats helium gas up to 1000°C, and consists of high-temperature heaters and coolers. Test sections are to be provided with four test sections, the test items of which are:

(1) Fuel stack test section (T_1)
   1. Heat transfer and fluid-dynamic characteristics at power transient condition
   2. Heat transfer and fluid-dynamic characteristics at partial load
   3. Effects of lateral power distribution
   4. Integrity of graphite fuel block
   5. Fluid-dynamic test of control rod

(2) In-core structure test section (T_2)
   1. Seal performance at high-temperature region of core
   2. Performance at high integrity of the thermal insulation structure
   3. Mixing behavior at high-temperature gas plenum
   4. Integrity of core support structure (graphite post, diagrid, etc.)
   5. Integrity of high-temperature outlet piping

(3) In-core flow test section (T_3)
   1. Core flow distribution
   2. Integrity of core restraint structure
   3. Building of in-core structural assemblies
   4. In-service inspection technology of reactor vessel
   5. Functional test of stop valve

(4) Heat removal test section (T_4)
   1. Intermediate heat exchanger
   2. Steam generator
   3. Integrity of emergency isolation valve
   4. Hot gas duct
   5. Performance of heat transfer system at partial load and power transient condition
   6. In-service inspection technology

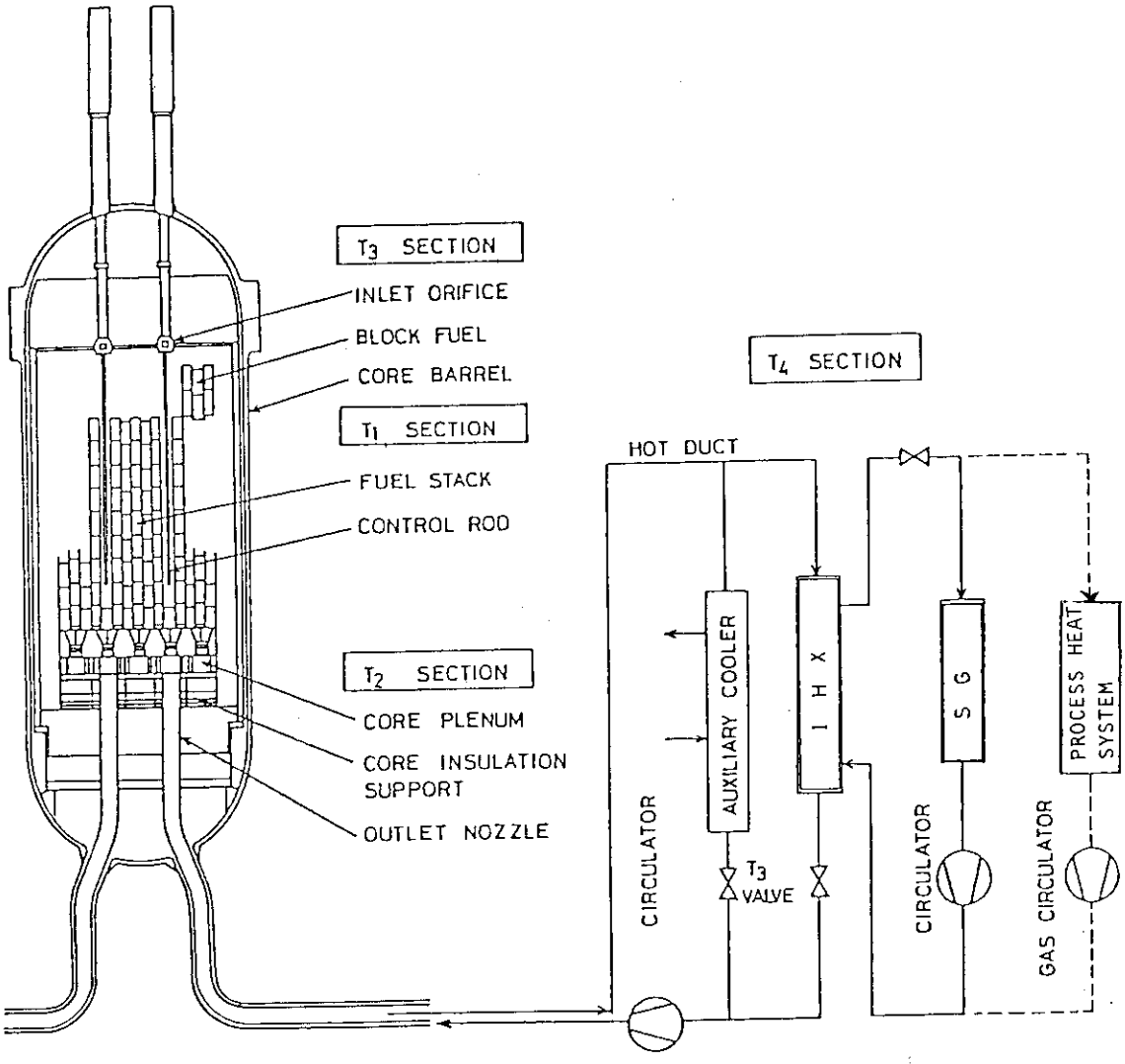

Fig. 1.1 HENDEL test sections with reference to VHTR

Table 1.1 Test conditions of HENDEL test sections

ITEMS	FUEL STACK TEST SECTION (T_1)	IN-CORE STRUCTURE TEST SECTION (T_2)	CORE FLOW TEST SECTION (T_3)	HEAT REMOVAL TEST SECTION (T_4)
TEMPERATURE (°C)	400 ∿ 1000 (MAX.1200)	1000 (MAX.1200)	∿400	∿1000
FLOW RATE (kg/sec)	0.4	2.8(4.0)	4.0	2.8(4.0)
PRESSURE (MPa)	4.0	4.0	4.0	4.0
TEST COMPONENTS	FUEL STACK CONTROL ROD	BOTTOM-CORE PLENUM INSULATION SUPPORT OUTLET NOZZLE	INLET ORIFICE FUEL BLOCK CORE BARREL MAIN VALVE	HOT GAS DUCT H.T. SHUT-OFF VALVE IHX SG

Table 1.2 Specifications of HENDEL in comparison with VHTR

ITEMS	VHTR	HENDEL
TEMPERATURE	400°C/ 950°C	400°C/1000°C
PRESSURE	4.0 MPa	4.0 MPa
FLOW RATE	TOTAL FLOW RATE : 16 kg/sec LOOP FLOW RATE : 8 kg/sec COLUMN FLOW RATE:210 g/sec (AVG.) CHANNEL FLOW RATE : 18 g/sec (AVG.)	M_2 : 4 + 4 kg/sec M_1 : 400 g/sec
THERMAL OUTPUT POWER, ELECTRICAL INPUT POWER	TOTAL POWER : 50 MW (TWO LOOPS)	M_2 + A : ∿11 MW
PURIFICATION SYSTEM	FLOW RATE : ∿160 g/sec	FLOW RATE : 100 g/sec
HOT GAS DUCT	LINER TUBE DIAM.: ∿36 cm	LINER TUBE DIAM.: 36 cm

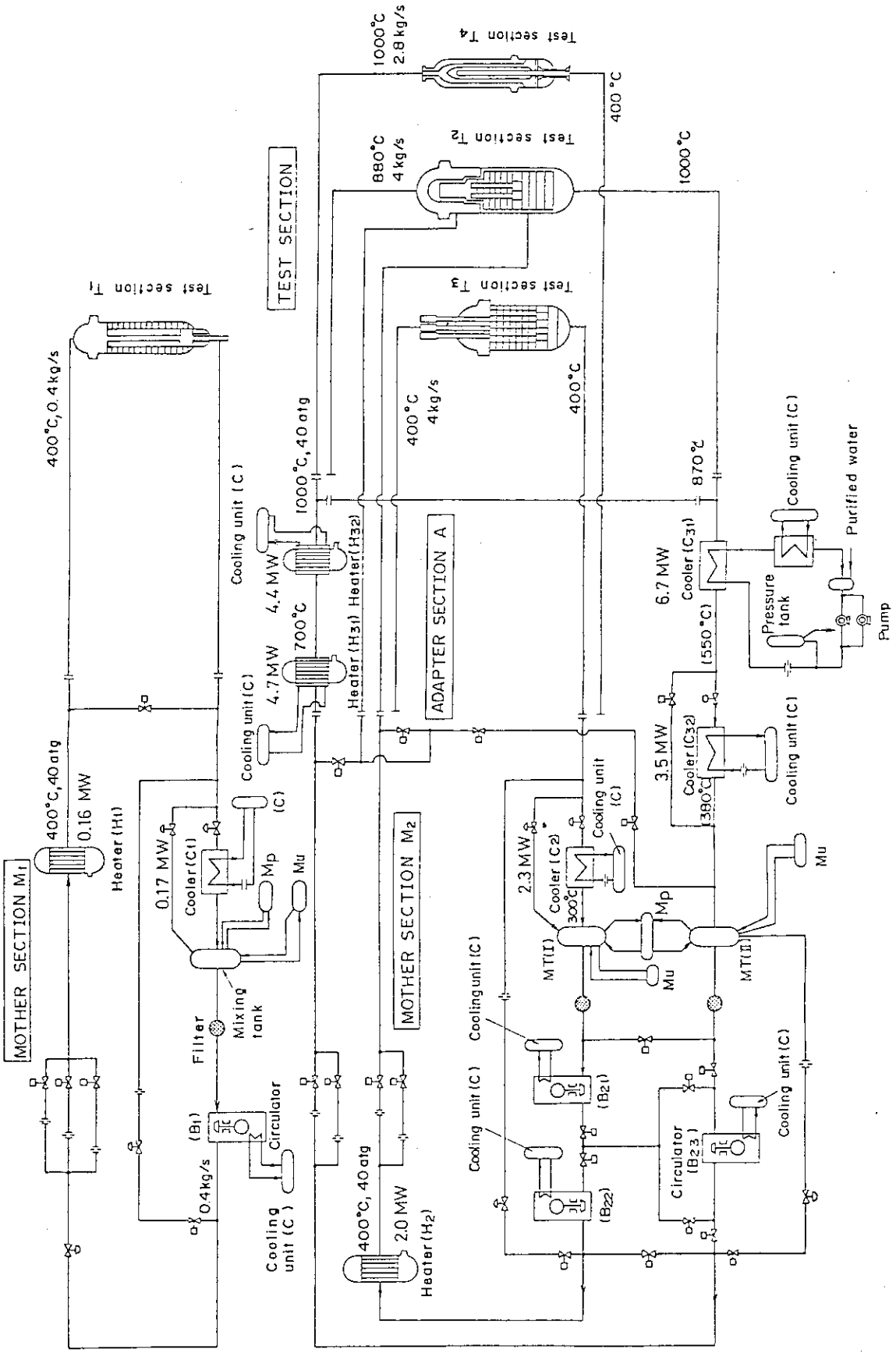

Fig. 1.2 Flowsheet of HENDEL

1.2 Mother-Adapter Section (M+A)

N. Izawa, H. Hayashi, T. Kunitama, Y. Hoshi, S. Nekoya, S. Tomobe, M. Hishida and H. Shimomura

M+A section is provided with gas circulators, electric heaters, water coolers, piping and valves, to supply helium gas of a specified temperature, pressure and flow rate to each test section.

Since the completion of installment of M+A section, the operations have been performed seven times, and each operating history is shown in Figs. 1.3-1.9. The preliminary test operation was performed to test major components of M+A section. The first and second test operations were to study the characteristics of the components. The third test operation was for a preliminary test of the fuel stack test section (T_1), and the other four operations were for the study on heat transfer and fluid-dynamic characteristics of T_1 test section as well as hot gas ducts.

After these seven operations, inspections on the heaters of M+A section were made. Some of these results and test data on an auxiliary gas circulator (B_{24}) will be described.

1.2.1 Inspection of the helium gas heater (H_{31})

H_{31} is one of the two heaters installed in M+A section to heat helium gas up to a temperature of 720°C by electically heated Incoloy-800H tube elements, as shown in Fig. 1.10.

An inspection was made to check electrical insulation resistance and also to confirm soundness of the inner structures, such as heater elements, boron-nitride insulators, etc., after about 3000 hours' operation in October, 1983.

The inspection included overhaul of the pressure vessel, sampling and analysis of dust in the vessel, non-destructive inspection on heater elements, insulation test of the power supply and instrumentation circuits.

(1) Sampling and analysis of dust in the vessel

The inner surface of the vessel and components of the heater were uniformly covered with dark gray dust. The dust was easily scraped off by a knife from the surface of structures, and the color was nearly dark

green.

The analysis of dust revealed the following:

(a) Fe-Mn-C oxide, Fe-Cr-C oxide and Fe-Mn-Cr oxide were detected. These chemical complex may be due to oxidation of the materials of vessel and piping such as Incoloy-800H, mild steel (SB), 2¼Cr-1Mo (SCMV), etc. (Photo 1.1)

(b) Al-Si-Ca oxide was also detected. This material seems to come from glass fibre (Contents: SiO_2 98.1%, Al_2O_3 25%, CaO 15%, etc.) used as an insulation cover of thermocouples fixed on the heater elements and thermal insulation used in the pressure vessel. (Photo 1.2)

(2) Inspections of the heater element

Visual inspection, dimensional check, immersion test, micro structure analysis by means of replica and Vickers hardness test were performed with respect to a heater element which was extracted from the heater.

(a) The color of the element surface turned into dark gray, but the defects such as surface corrosion, disfigurement or blister of the heater element, thickness reduction of pipe and crack on welded part, were not detected.

(b) Granular substance was found more at the helium gas outlet of the element than near the helium gas inlet.
It may be due to the temperature as high as 720°C at the helium gas outlet, but no defect was observed on the micro structure of the material, as shown in Photo 1.3.

(c) Vickers hardness of the inlet tube, the welded part near the inlet, the outlet tube, the welded part near the outlet are respectively 157 - 176 Hv, 173 Hv, 143 - 162 Hv and 155 Hv. Namely the age-hardening effect at the inlet tube is larger than that at the outlet tube.

These results show that the surface condition of the tube and welded part of the heater element are sound, and the micro structures of materials are unchanged.

(3) Insulation resistance

Total insulation resistance of the heater element bundle against the

pressure vessel which was measured before inspection was 50 kilo-ohm, while the value measured after inspection was 150 kilo-ohm.

The average insulation resistance of each pair of the elements against the vessel was about 0.1 mega-ohm, and the values measured before inspection were 0.3 and 1.0 mega-ohm, but after inspection they were all 4.0 mega-ohm.

The insulation resistance measured at the outside of the vessel without an upper tube plate against the earth was 23.0 mega-ohm, but the value with a tube plate was 15.0 mega-ohm.

This shows that the boron-nitride insulator was polluted by conductive dust, but the value of insulation resistance is considered to be large enough.

1.2.2 Inspection of the helium gas heater (H_{32})

H_{32} is a second-stage helium gas heater of Adapter section and the temperature is the highest among the components in M+A section, and has been operated over 1100 hours including about 640 hours at a temperature from 750°C to 950°C and about 340 hours at a temperature over 950°C. To verify the soundness of major components of the heater, inspection was performed. A graphite heater element was extracted from the heater for a detailed check and some insulation washers made of boron-nitride, were replaced because defects were found.

Visual inspection, electrical measurements, X-ray micro analysis, chemical analysis of graphite, sampling and analysis of dust were carried out.

(1) Visual inspection on the heater element

Oxidized part on the surface of the heater element, separating binder used in sintering of boron-nitride insulator, surface of insulator covered with graphite particles were observed. Figure 1.11 shows a heater element of H_{32}.

(2) Electrical measurement

(a) Insulation resistance of the heater element was 0.1 - 0.15 mega-ohm, and even after cleaning the value was not changed.

(b) The resistance of the used heater element was the same as that of a new element, as shown in Figs. 1.12 and 1.13.

(3) Secondary electron image and X-ray micro analysis

(a) The surface of the outlet tube was covered with a Ca oxide film, and other part of the surface was partially oxidized. Photo 1.4 shows a secondary electron image of the used heater element.

(b) Through the surface where the heater element was in contact with the upper tube plate insulator, Ca oxide was diffused into graphite to a depth of 30 micron, as shown in Photos 1.5 and 1.6.

(4) Chemical analysis of the graphite

Based on the results of a chemical components analysis, the bulk density and bending strength were compared with initial values, but they changed little.

(5) Impurity analysis

Impurities in a sample taken from the heater element were measured. The impurities detected were mainly Fe and Ca oxides, which are considered to give no significant influence on the performance of heaters.

(6) Boron-nitride insulator

(a) Insulator of the upper tube plate

The insulation resistance of the insulator was reduced by graphite particles deposited on the surface, and when graphite particles were scraped off the surface the resistance recovered its normal value.

(b) Washer plate of the side plate of upper plenum

A secondary electron image and an X-ray micro analysis revealed that some Ca particles, which are used as a binder and a conglutination with graphite, came out of boron-nitride insulator, as shown in Photo 1.7.

(c) Dust on the insulator

A survey of dust by means of secondary electron image, an elemental analysis by an X-ray micro analyser and an X-ray spectroscopic analyser showed that dust was only oxidized particles of heater structure materials. But there were no problem found with respect

to the electrical insulation.

1.2.3 Installement of an additional helium gas circulator (B_{24})

An additional helium gas circulator (B_{24}) is for the coming test sections (T_2, T_3, T_4), to increase the total flowrate, and it was installed for a test in M+A section in 1983.

Figure 1.14 shows a schematic flow diagram with the circulator. Major specification of B_{24} is shown in Table 1.3, and this was confirmed in the sixth cycle operation of HENDEL.

Figure 1.15 shows a Q-H curve of the circulator.

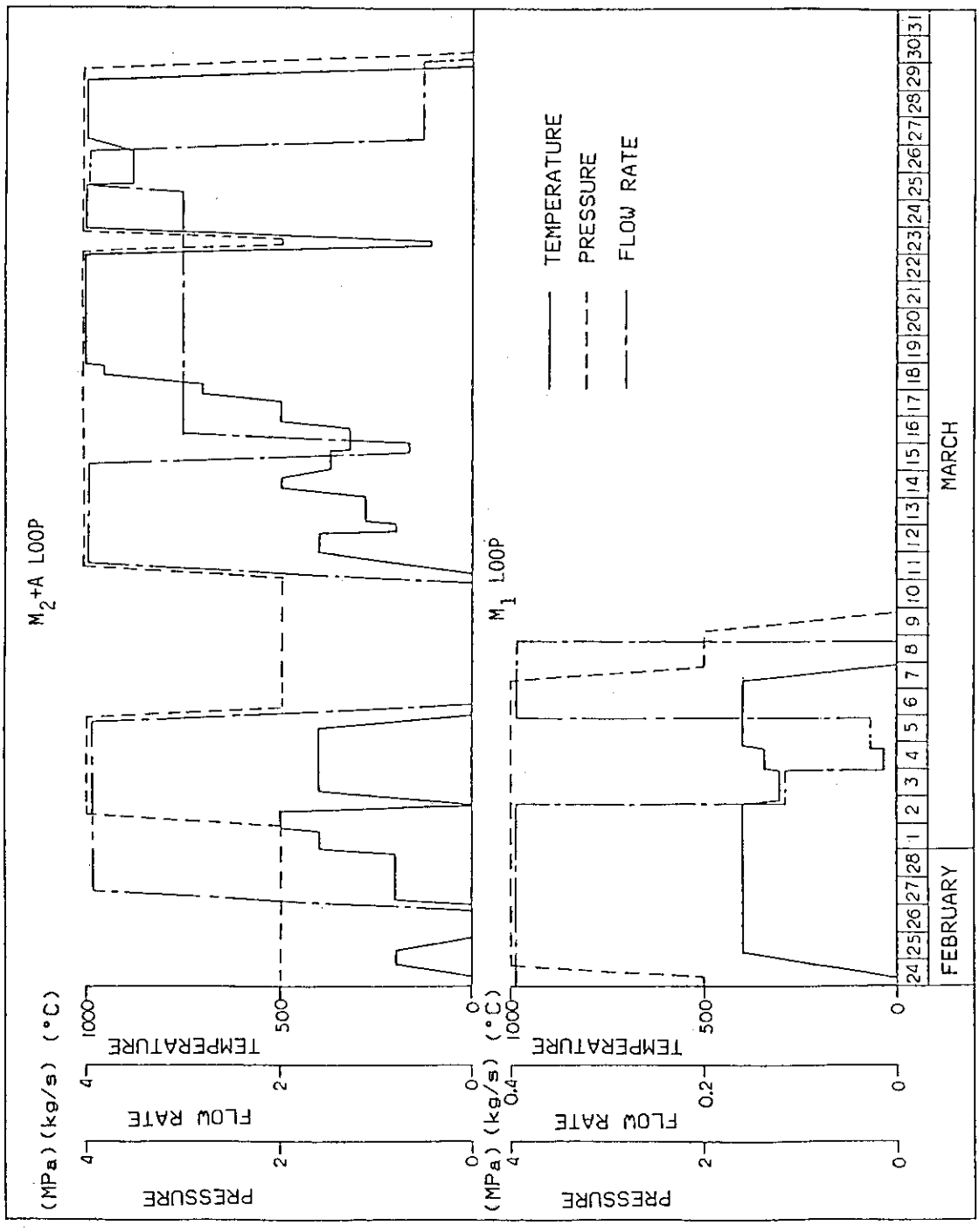

Fig. 1.3 Operating history of preliminary test (Feb. 24, 1982 - Mar. 30, 1982)

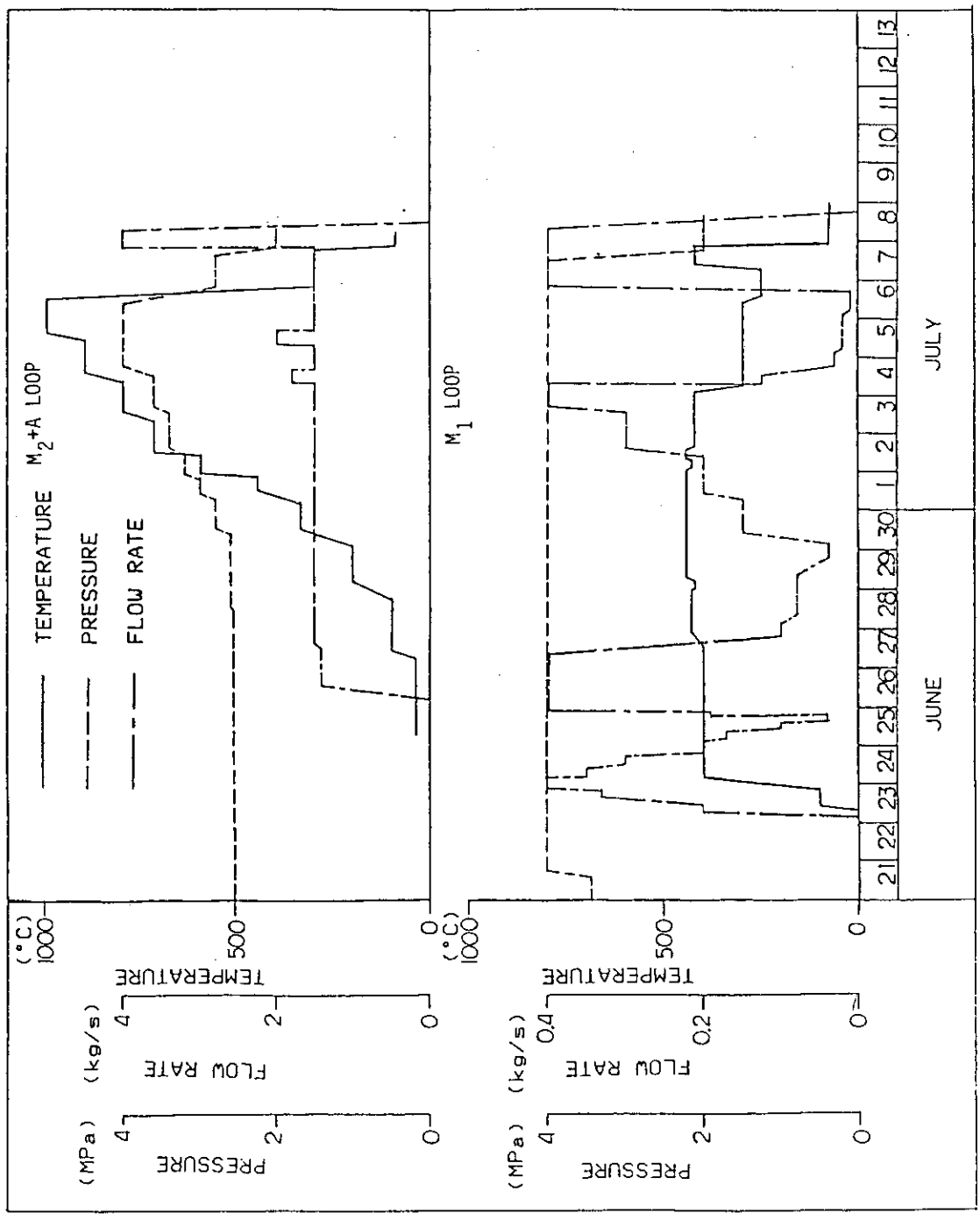

Fig. 1.4 Operating history of the first cycle (June 21, 1982 - July 9, 1982)

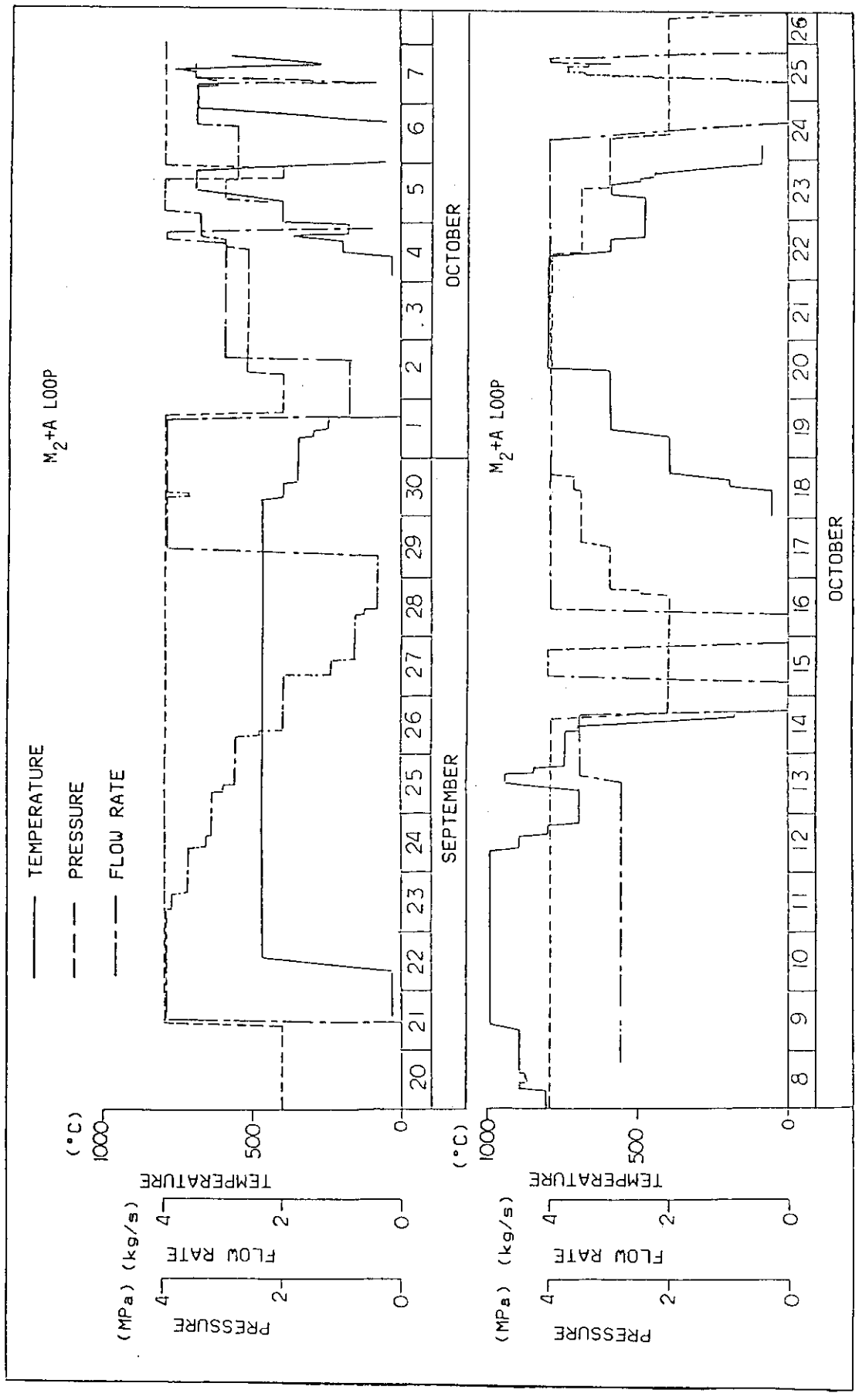

Fig. 1.5 Operating history of the second cycle (Sept. 20, 1982 - Oct. 26, 1982)

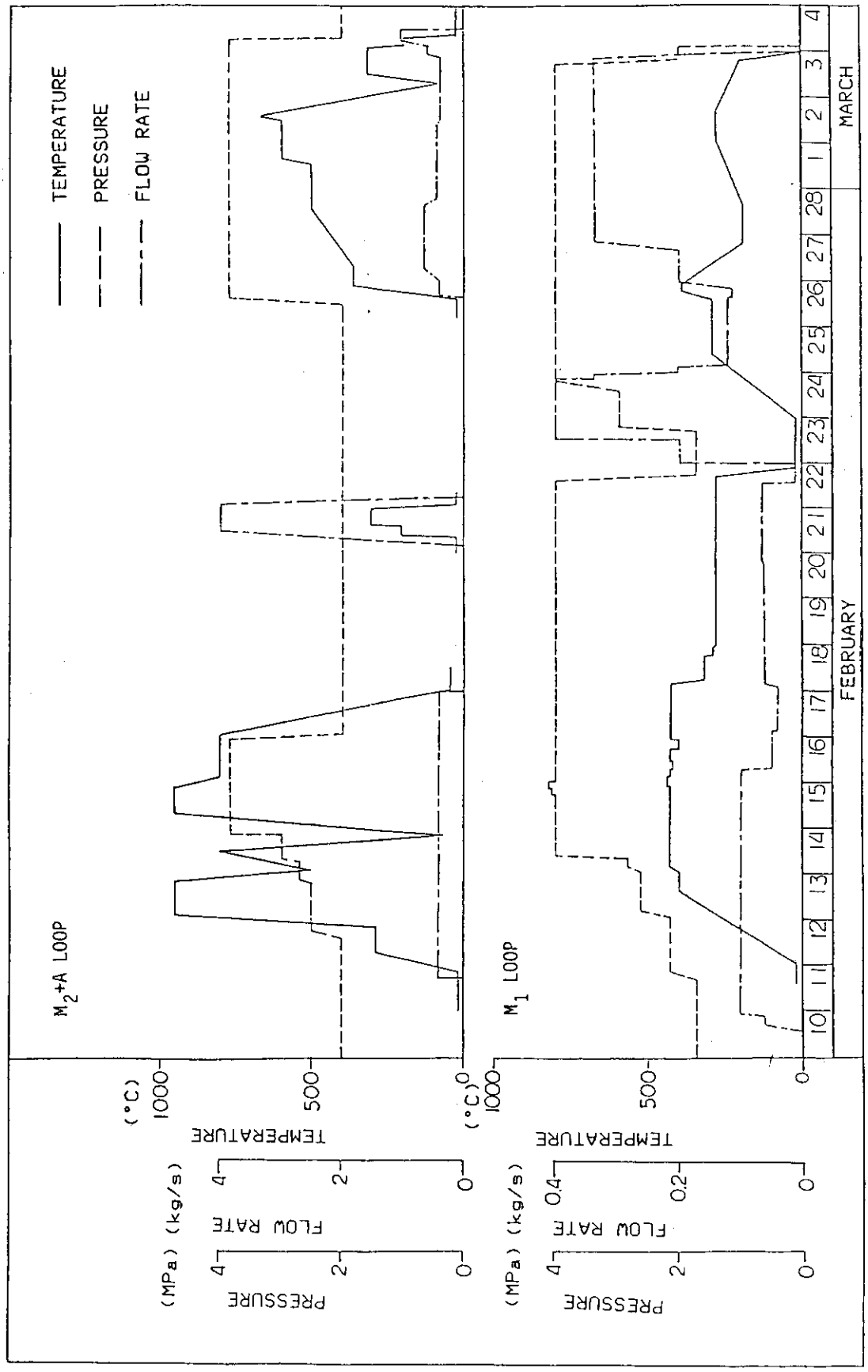

Fig. 1.6 Operating history of the third cycle (Feb. 10, 1983 - Mar. 4, 1983)

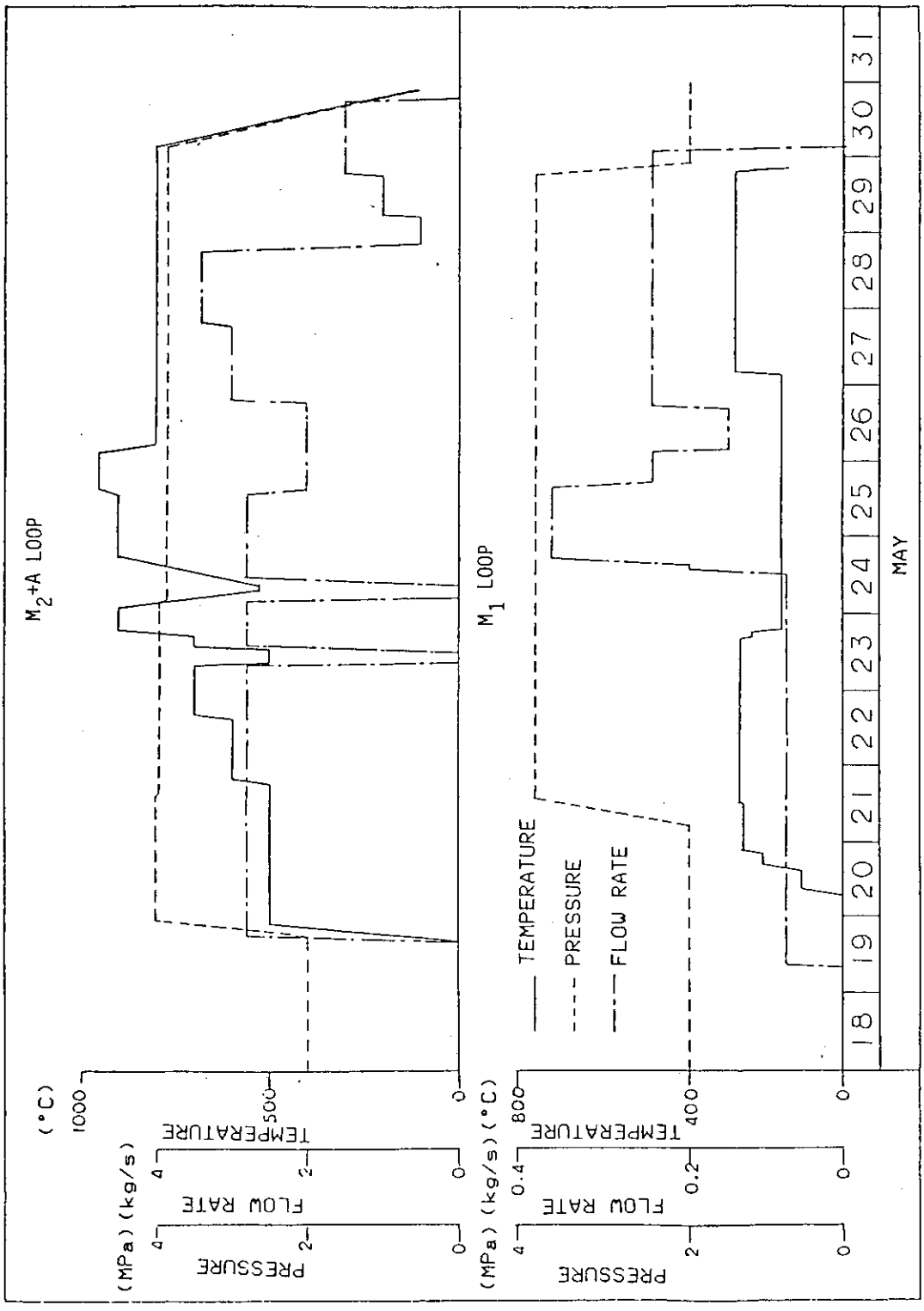

Fig. 1.7 Operating history of the fourth cycle (May 18, 1983 - May 30, 1983)

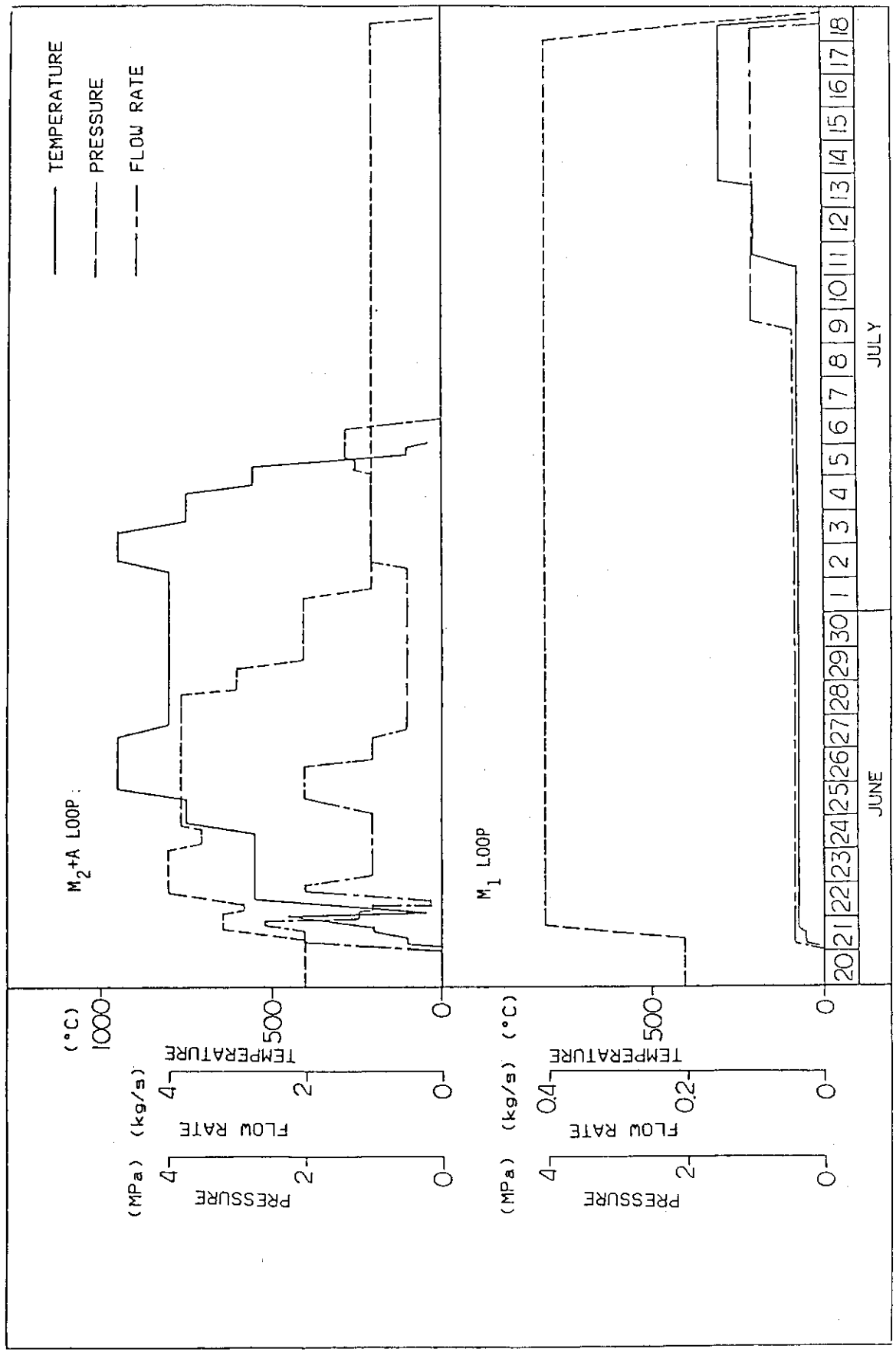

Fig. 1.8 Operating history of the fifth cycle (June 20, 1983 - July 18, 1983)

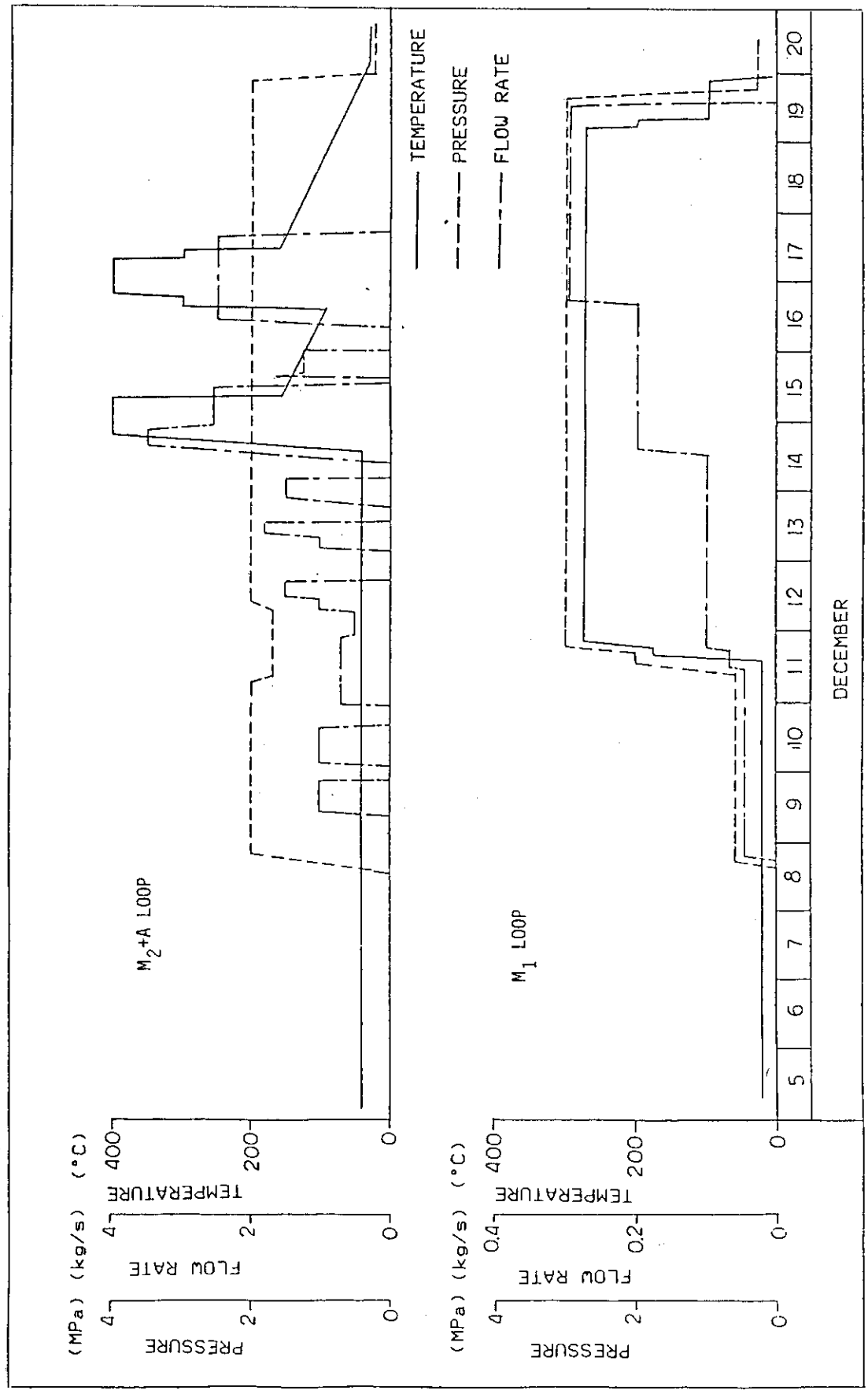

Fig. 1.9 Operating history of the sixth cycle (Dec. 5, 1983 - Dec. 20, 1983)

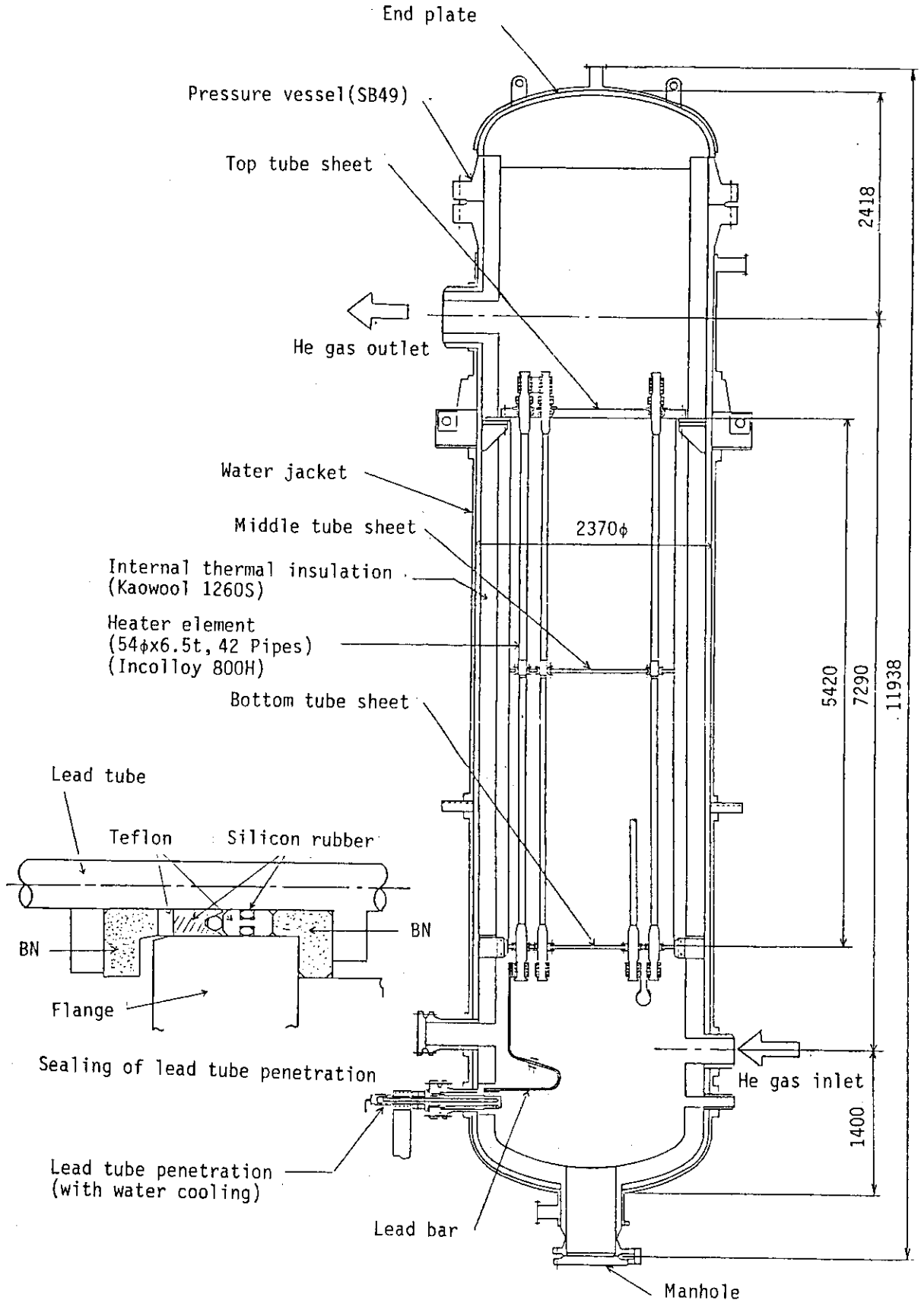

Fig. 1.10 He gas heater H_{31}

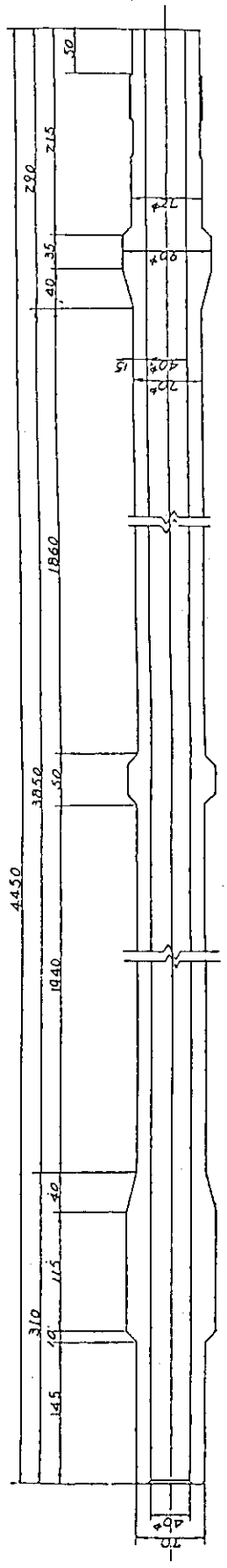

Fig. 1.11 Heater element of H_{32}

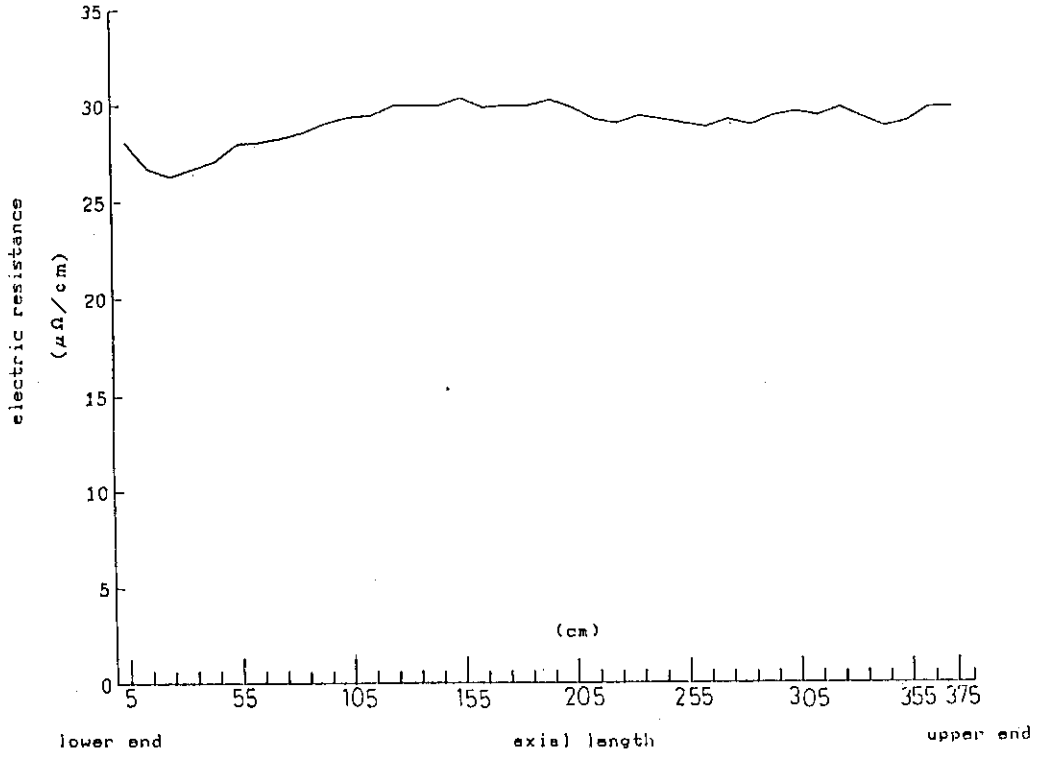

Fig. 1.12 Electric resistance distribution of used heater tube

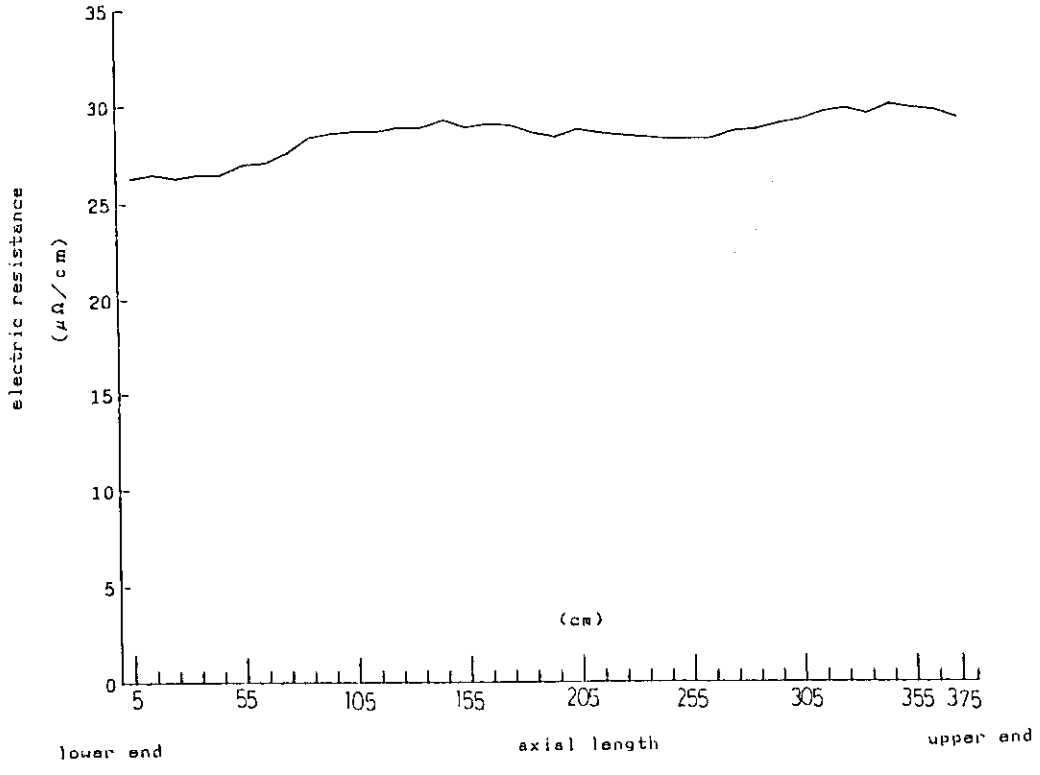

Fig. 1.13 Electric resistance distribution of unused heater tube

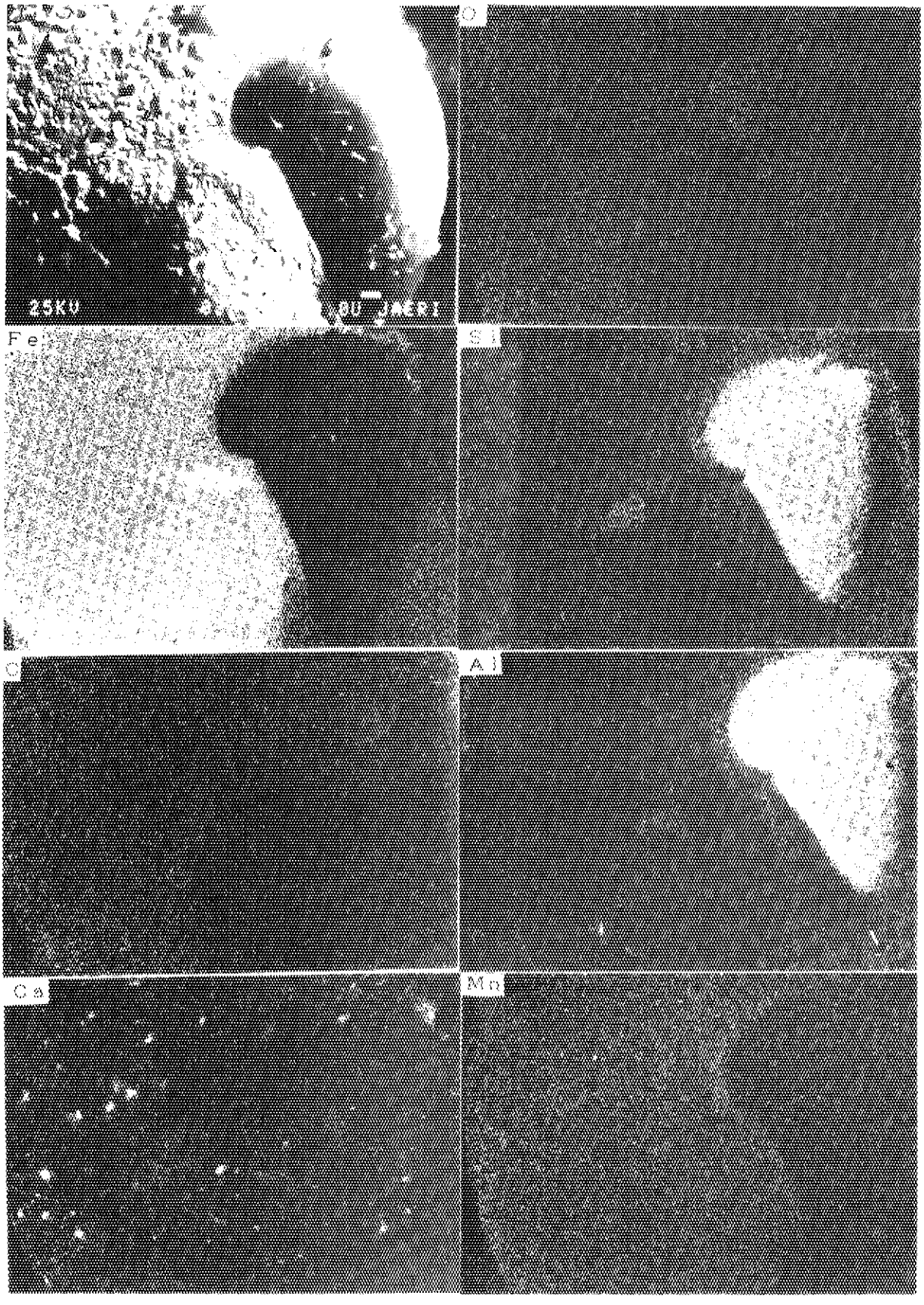

Photo.1.1 Secondary electron image and X-ray micro analysis of dust from H_{31}

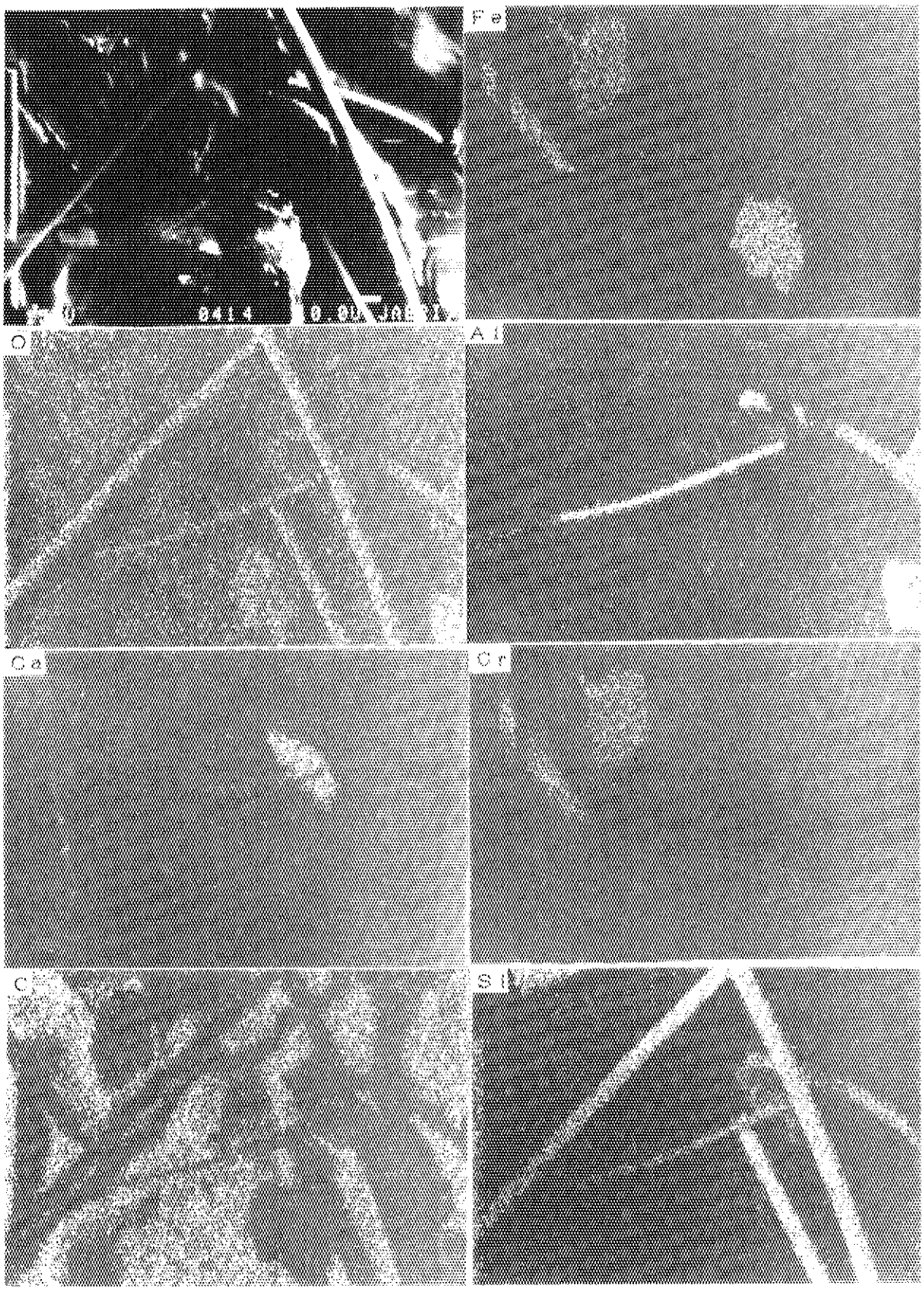

Photo.1.2 Secondary electron image and X-ray micro analysis of dust from H_{31}

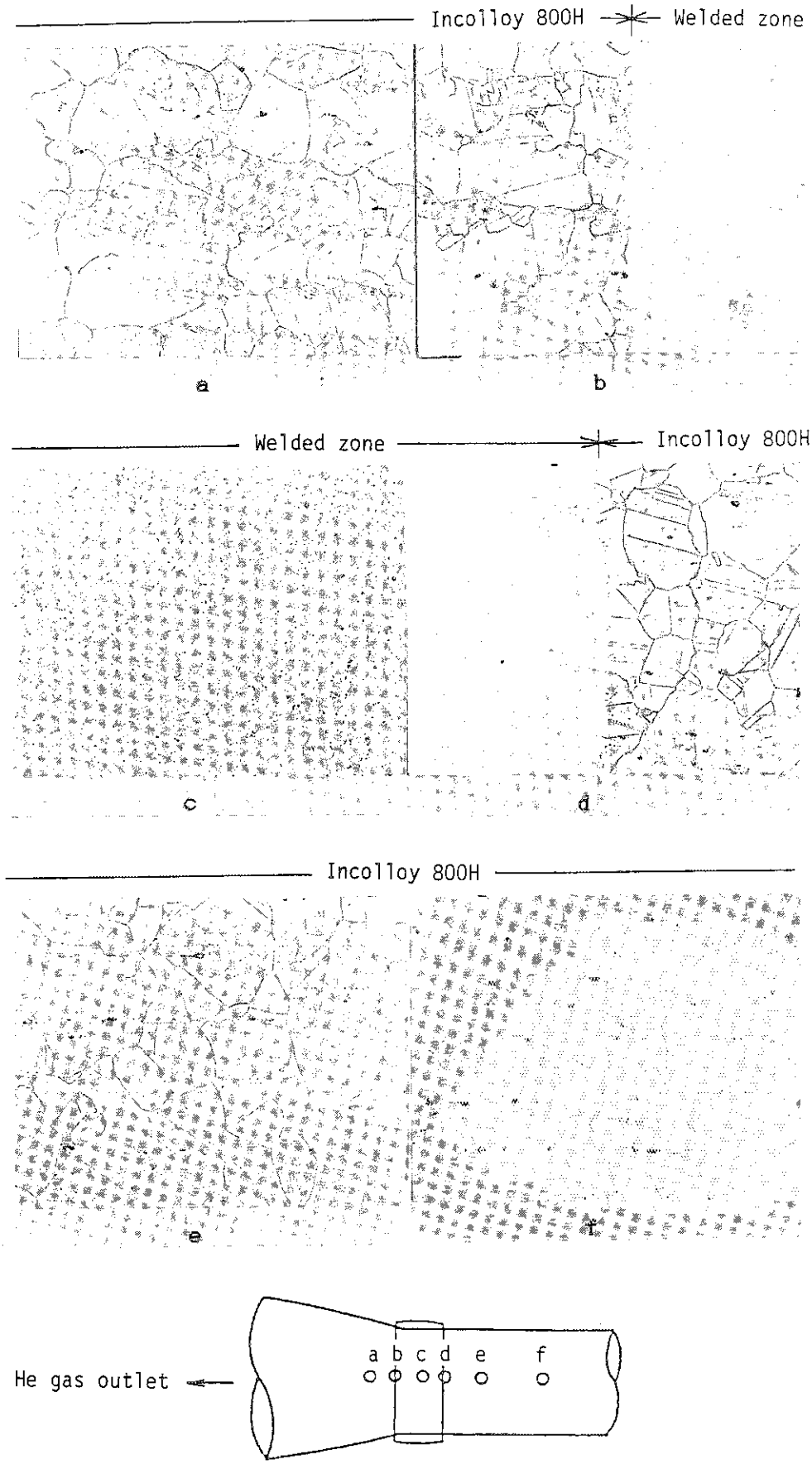

Photo.1.3 Microstructure of welded zone in the outlet of a heater element

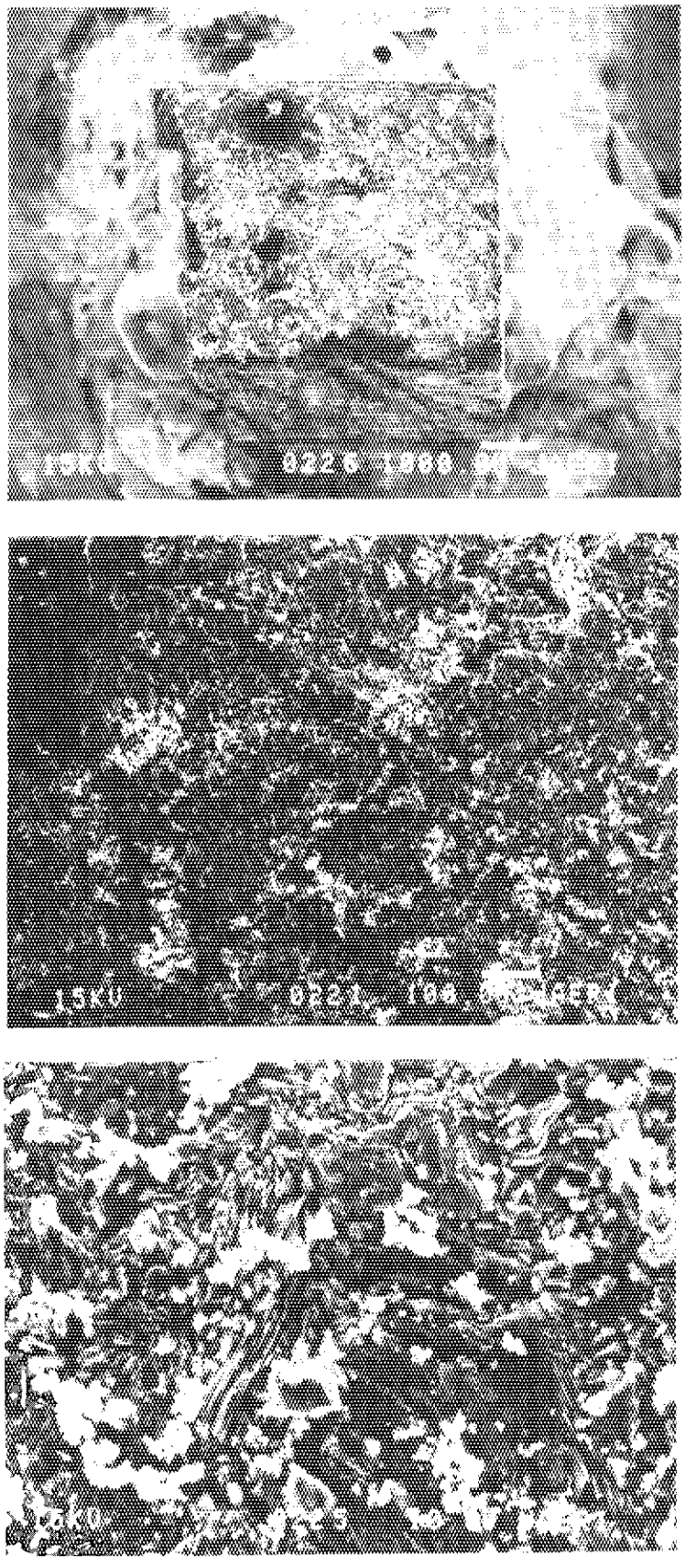

Photo.1.4 Secondary electron image of inner surface of heater element in contact with insulator

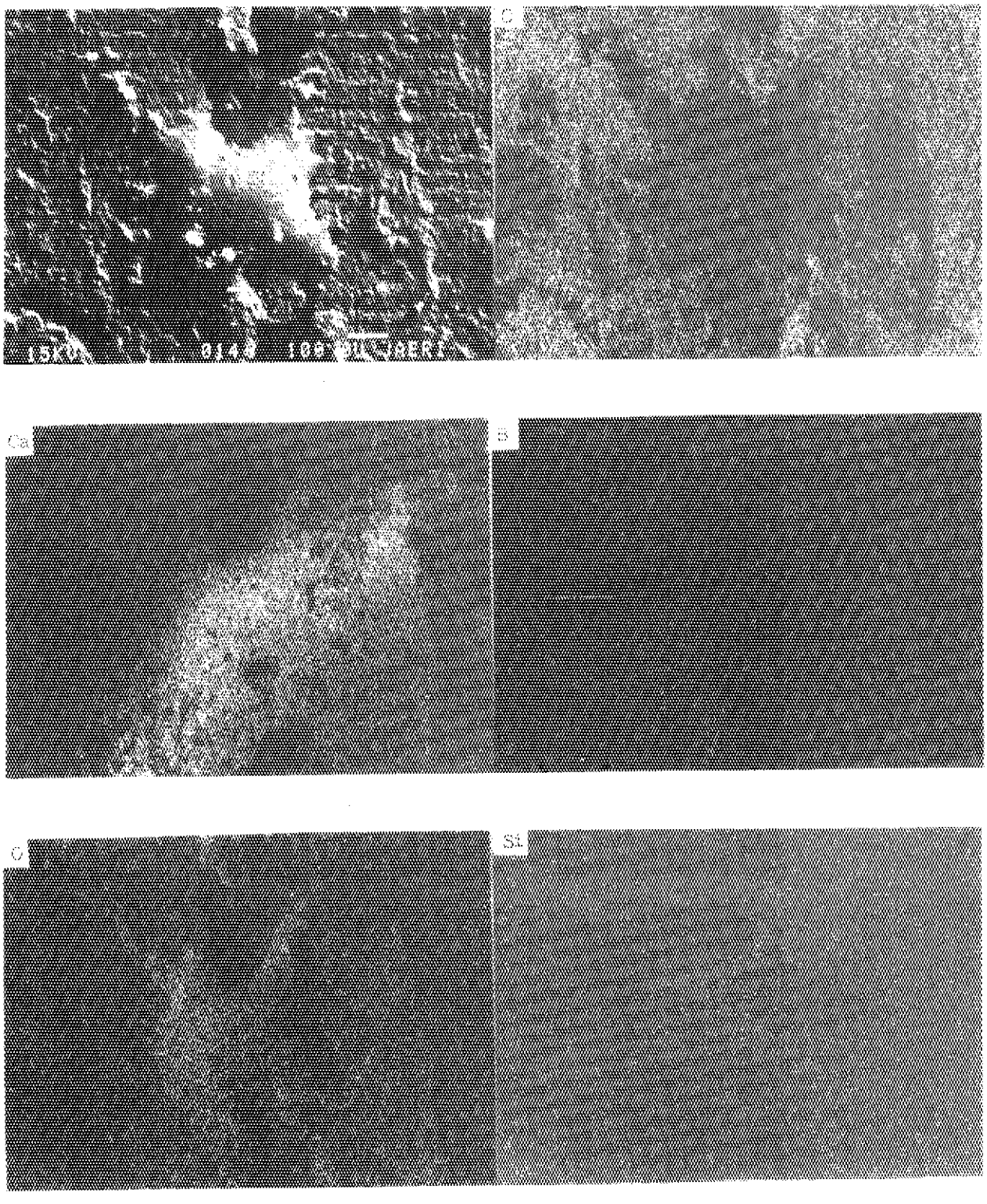

Photo.1.5 Secondary electron image and x-ray micro analysis of outer surface in contact with insulator

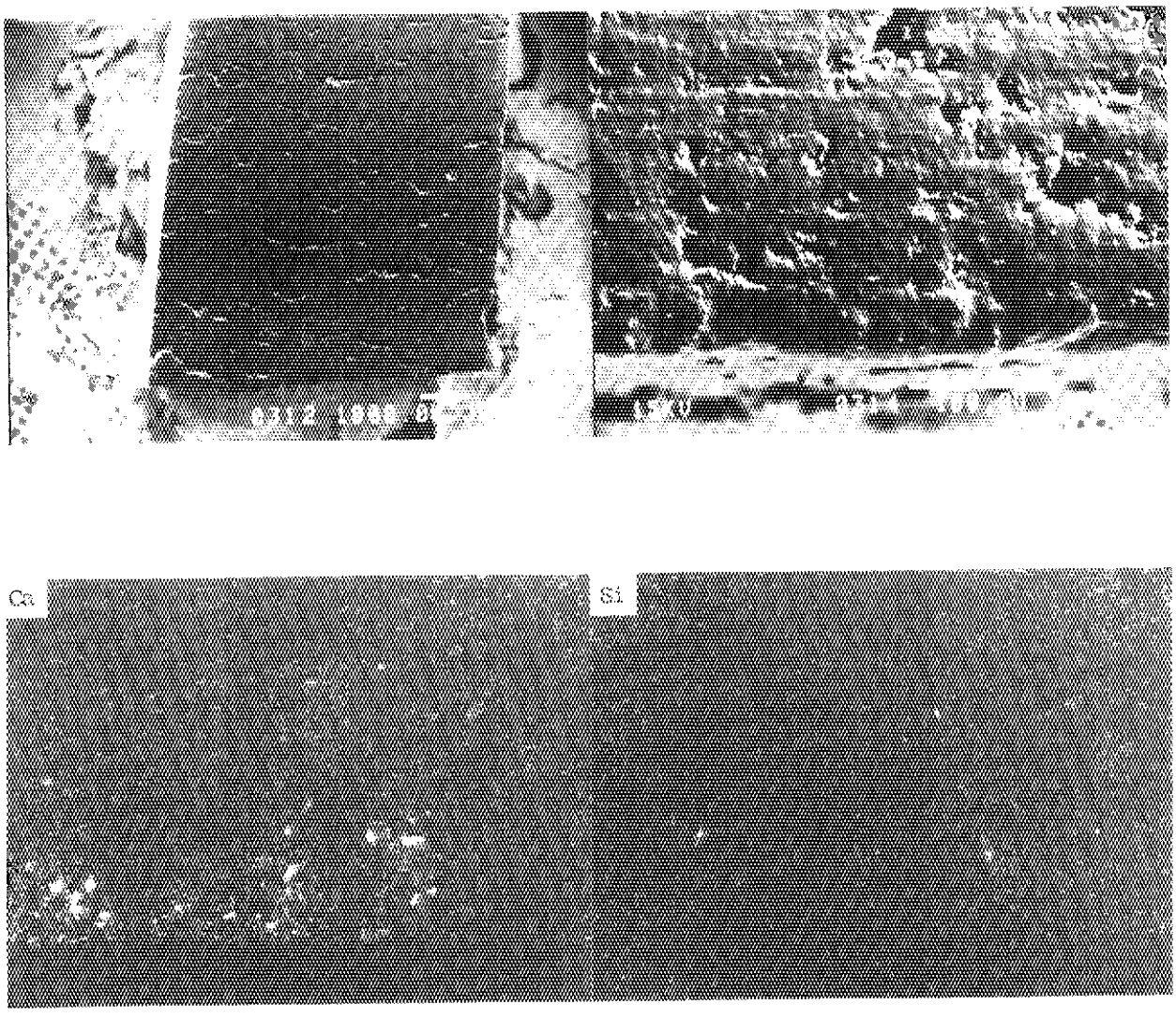

Photo. 1.6 Secondary electron image and x-ray micro analysis of cross-cut section of heater element in contact with insulator

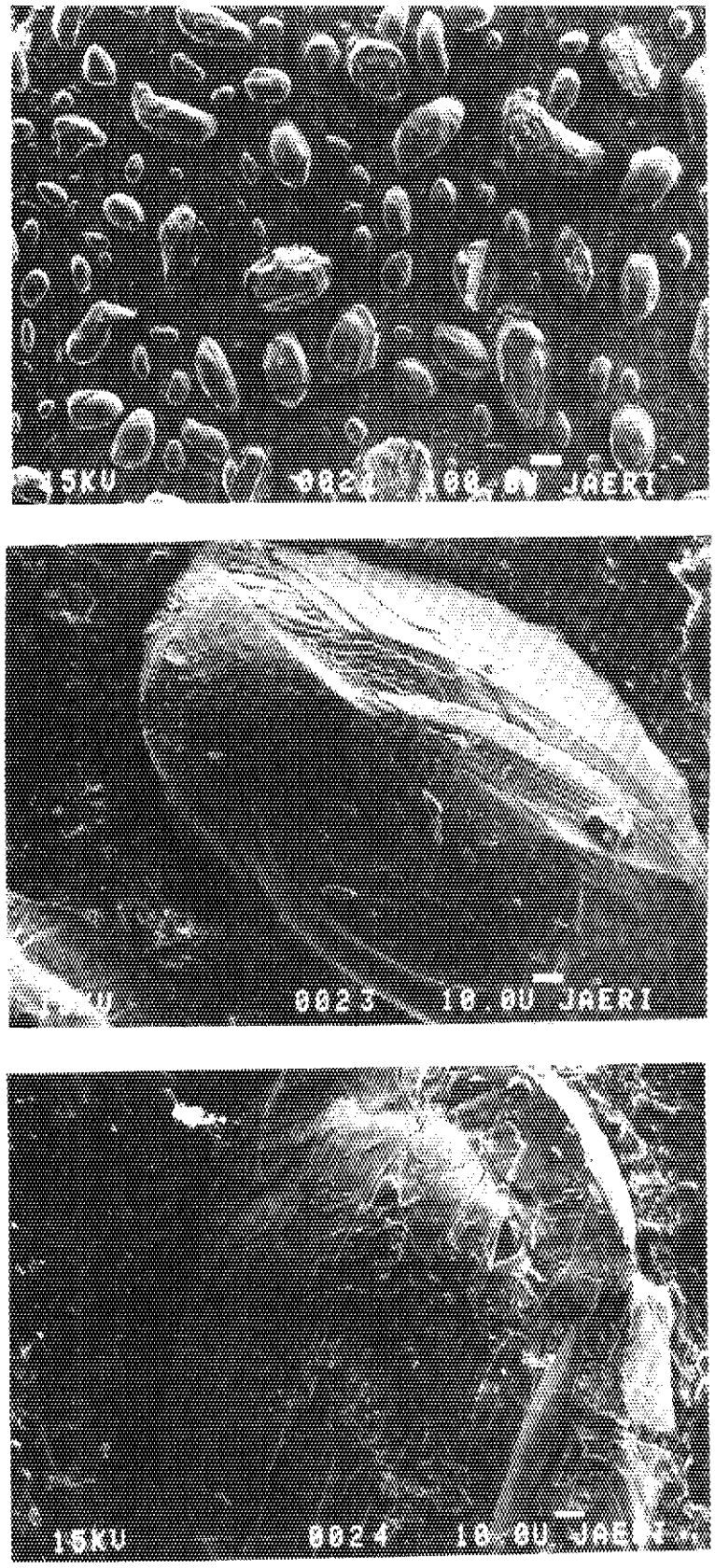

Photo.1.7 Secondary electron image of outer surface of heater element in contact with insulator

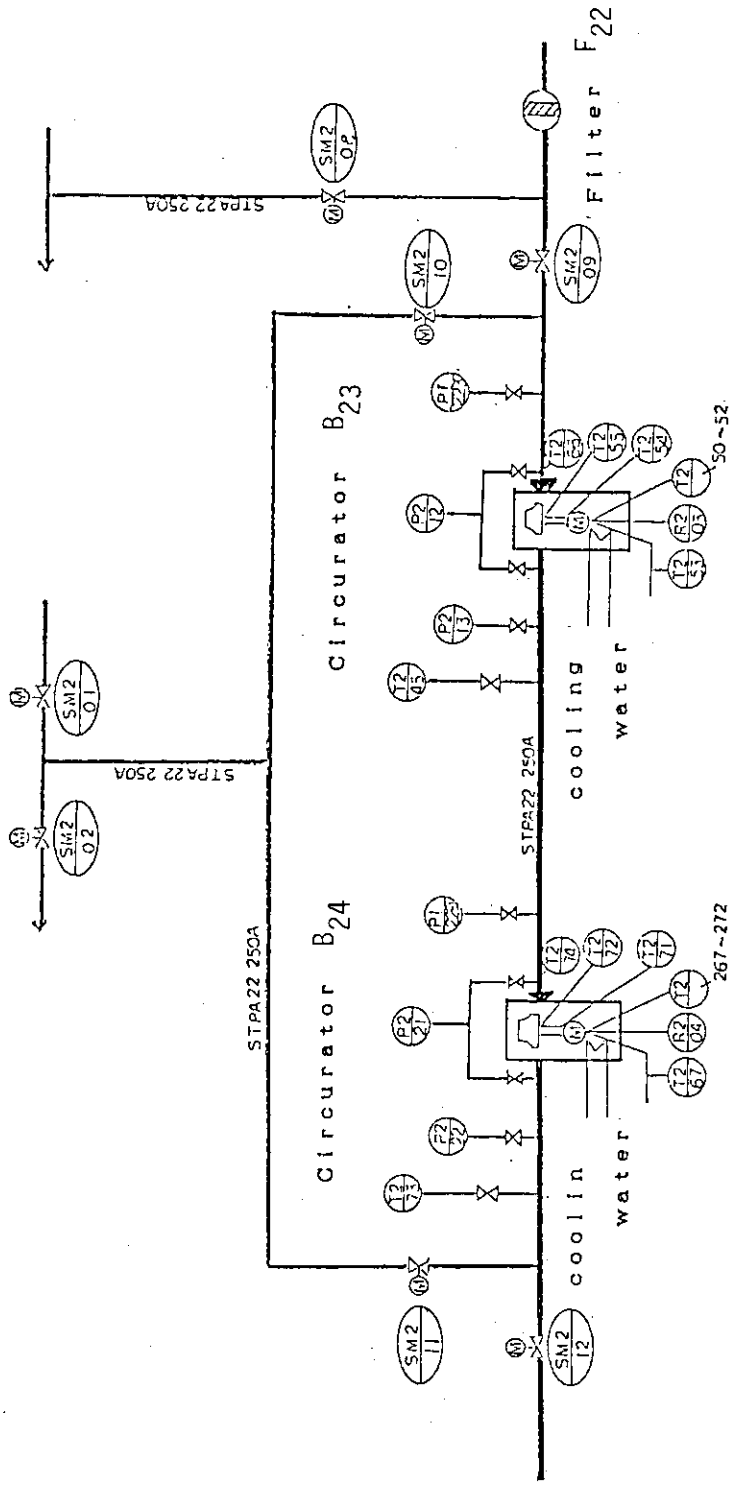

Fig. 1.14 Schematic flow diagram with a circulator B_{24}

Table 1.3 Specification of B_{24}

Compressor		Motor	
Type	Variable Speed, Hydro-dynamic Gas Bearing	Speed Control Range	3000~12000 rpm
Fluid	Helium Gas	Type	Three Phases, Two Poles, Squirell, 440 V
Flow Rate	4 kg/s		
Inlet Pressure	4 MPa	Nominal Power	250 kW
Outlet Pressure	4.1 MPa		
Inlet Temperature	380°C		
Outlet Temperature	400°C		
Designed Pressure	4.5 MPa		
Designed Temperature	450°C		

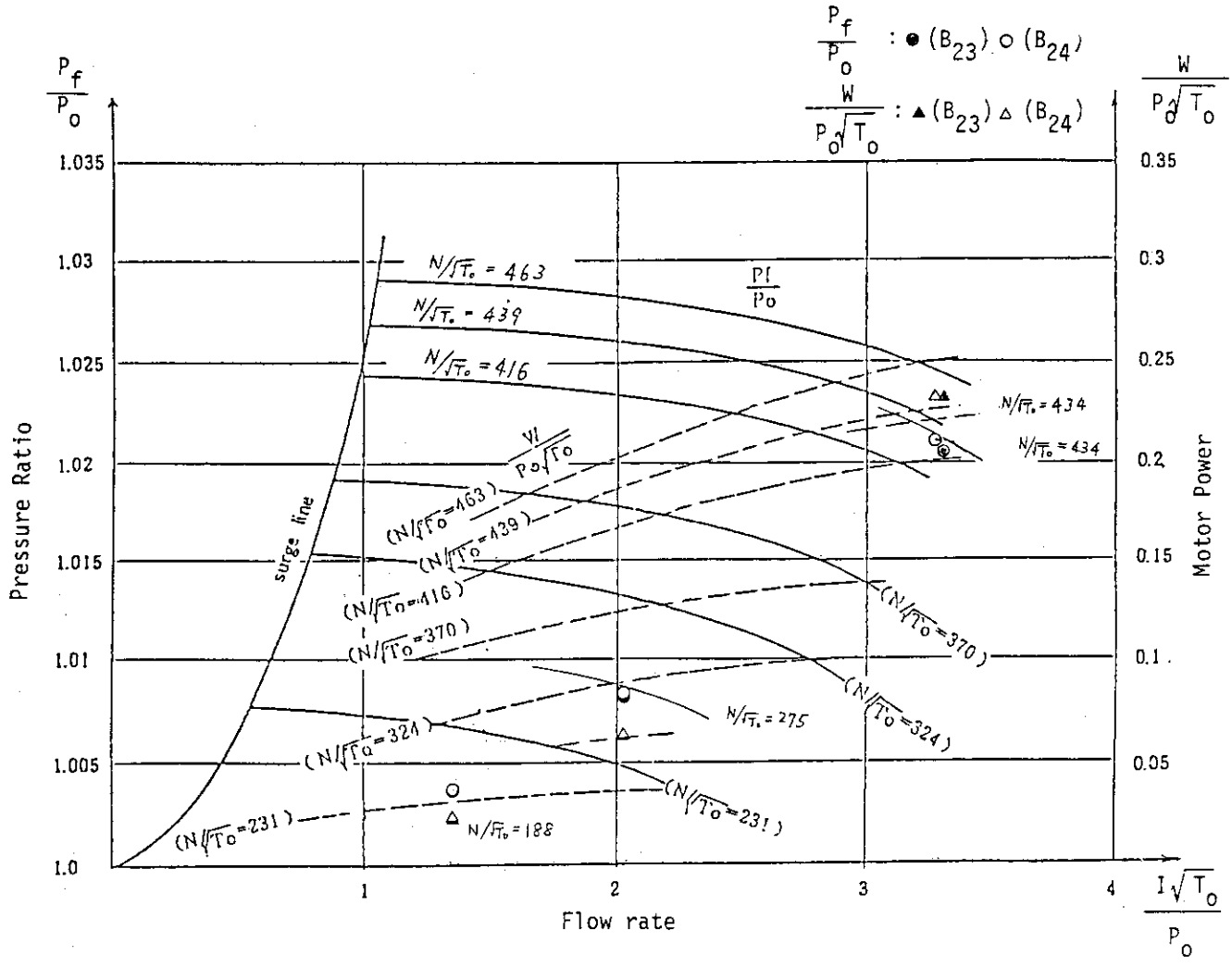

Outlet pressure	: P_f kg/cm^{2}a	Flow rate	: I kg/s
Inlet pressure	: P_o kg/cm^{2}a	Revolution	: N rpm
Inlet temperature	: T_o K	Power	: W kW

Fig. 1.15 Q-H curve of B_{24}

1.3 Fuel Stack Test Section (T_1)

N. Izawa, K. Takase, S. Maruyama, M. Hishida, T. Tanaka
and H. Shimomura

1.3.1 General description

In order to evaluate heat transfer fluid-dynamic characteristics of a fuel assembly under the same condition of the VHTR, the fuel stack test section (T_1) is constructed as the first test section of HENDEL. The T_1 test section consists of two test rigs, one is called a single-channel test rig (T_{1-S}) for only one cooling channel of the fuel assembly, the other a multi-channel test rig (T_{1-M}) for one hexagonal graphite column with eleven graphite blocks and twelve cooling channels.

The construction of the test section was completed and the performance of the components were confirmed in the third cycle operation of HENDEL in March, 1983. Since the completion, four operations were carried out.

Table 1.4 shows test items of the fuel stack test section. The heat transfer and fluid-dynamic characteristics test are planned under two different conditions, one is a high-temperature test and the other is a moderate-temperature test.

The moderate-temperature test is planned to be performed under the same heat flux, and the same Reynolds number at the inlet as those of the VHTR. The high-temperature test is planned at the same temperature of the VHTR, and the flow rate was in a range from 3 to 50 g/s per channel, while an average flow rate of the VHTR is 17.2 g/s per channel.

As to the single-channel test rig, three operations for moderate-temperature test and two operations for high-temperature test were performed. While, as to the multi-channel test rig, five operations for moderate-temperature test were carried out.

For an effective operation of HENDEL, JAERI developed a full automatic data management system, which consists of on-line calculators and data communication interfaces in connection with a general-purpose interface bus (GPIB). The functions of the system are: firstly to collect automatically data of M+A section, and also data of the T_1 control system and test section, secondly to calcurate Reynolds number, Nusselt number, friction factor, heat flux, etc., and thirdly to display the

operating conditions on the test components and test rigs.

Once a steady state condition is established, the data are stored on magnetic data files, which are supported by a data control system so as to access easily.

1.3.2 Single-channel test rig (T_{1-S})

(1) Test components of the T_{1-S} test rig

T_{1-S} test rig simulates one fuel stack of the VHTR. Figure 1.16 shows a single-channel test rig, which consists of a pressure vessel, a pre-heater, an outer tube, compensation heaters, a cooler, a mock-up heater pin and various measuring devices. Helium gas supplied from M_1 loop, enters the top nozzle and flows downward through an annular channel which is formed by the heater pin and the outer tube.

A pre-heater is installed in the upper plenum in order to compensate heat loss through the piping between the heater (H_1) and the single-channel test rig, and the heater consists of a main sheath heater (4.5 kW), a micro heater (3 kW) and a pre-heater (1.5 kW).

The outer tube is placed vertically at a temperature of 1000°C in the pressure vessel which is made of temperature-resistant stainless steel Hastelloy-X. The dimensions of the tube are 6370 mm in length, 53 mm in diameter and 4.5 mm in thickness. Ten pressure taps are installed on the tube corresponding to each stage of the heater pin, and nine thermocouples on the outer surface of outer tube. Three thermo-couples are embedded in the outlet of heating section to detect temperature of outlet helium gas. The tube is surrounded by thermal insulation of 90 mm in thickness.

The heating element, thermal insulation and casing are respectively Kantal A-1, ceramic blocks and stainless steel. These heaters are to keep the temperature of ceramic blocks the same as that of the outer tube so as to reduce the heat loss in the radial direction.

The configuration and dimension of mock-up heater pin are the same as those of the fuel pin of the VHTR. Two types of the heater pins are prepared for the tests, one is for moderate-temperature test and the other for high-temperature test. Their dimensions are the same: 46 mm in diameter and 570 mm in length; the differences are material, structure, electrical power and design temperature. The material of

the heating element for moderate-temperature test is nickel-chromium, while that for high-temperature test a spiral shape graphite. Electric powers of heater pins are 70 kW for moderate-temperature test and 100 kW for high-temperature test, and coolant temperatures are heated up to 1000°C and 750°C respectively.

Each type has three kinds of heater pins whose heat flux distributions are flat, cosine and exponential distributions. Figures 1.17 and 1.18 show heater pins for high-temperature and moderate-temperature tests. To measure the temperature of the graphite sleeve in the case of moderate-temperature tests, fourteen thermocouples are installed on the surface, and in the case of high-temperature tests six thermocouples are embedded in the grooves of the graphite sheath, and at the top of thermocouples are cemented by ceramic. The effective heating length of each heater pin is 460 mm or 529 mm.

Figure 1.19 shows measuring locations for temperatures, pressures and pressure drops.

(2) Experimental conditions

The experimental research on heat transfer and fluid-dynamic characteristics using high- and moderate-temperature heater pins with flat heat flux distribution were performed from April, 1983 to March, 1984.

The experimental conditions were as follows:

Inlet helium gas temperature	30 - 400°C
Power of the heater pin (moderate-temperature test)	max. 70 kW
(high-temperature test)	max.100 kW
Helium gas flow rate	0 - 45 g/s
Reynolds number at the inlet	0 - 21000
Helium gas pressure	0.3 - 4 MPa.

(3) Results of the tests

A friction factor of isothermal flow is defined by the following equation.

$$f = dp \cdot De/2 \cdot Z \cdot \gamma \cdot V, \qquad (1.1)$$

where dP is a measured pressure drop for each stage of fuel pin, De is an equivalent hydraulic diameter (Do - Di = 53mm - 46mm = 7 mm),

Z is an axial distance from the top of heating section, γ is a specific density and V is a velocity of helium gas. The factor f includes various resistance factors, like a wall share stress, a shape resistance caused by spacer ribs and so on.

Figure 1.20 shows a relation between friction factor f and Reynolds number Re. The solid line in the figure represents friction factor correlations for a smooth concentric annulus, which are expressed by

$$f = 24/Re \quad (Re < 2000) \tag{1.2}$$

$$f = 0.079 \times Re^{\frac{1}{4}} \quad (Re \geq 2000). \tag{1.3}$$

The results of the tests are about 17% higher than these correlations and are expressed by the following equations:

$$f = 27.6/Re \quad (Re < 2000) \tag{1.4}$$

$$f = 0.094 \times Re^{\frac{1}{4}} \quad (Re \geq 2000). \tag{1.5}$$

Local Nusselt number Nu, based on the measured pin surface temperature T_w, is obtained as follows:

$$Nu = \frac{q \cdot De}{(T_w - T_g) \times Lamda}, \tag{1.6}$$

where q is a heat flux, T_g is a helium gas temperature and Lamda is a thermal conductivity, which is calculated from the inlet helium gas temperature T_{in}, helium gas flow rate G and power of each stage Q as follows:

$$T_g = T_{in} + Q/(G \cdot C_p). \tag{1.7}$$

Figure 1.21 shows a relation between Nusselt number Nu and Reynolds number Re. The experimental values are compensated for the effect of heat transfer caused by radiation. A solid line in the figure represents correlations for a smooth concentric annulus, which are expressed by

$$Nu = 0.018 \times (Di/Do)^{-0.16} \times Re^{0.8} \times Pr^{0.4} \quad (Re > 7500) \quad (1.8)$$

$$Nu = 0.084 \times (Re^{2/3} - 110) \times Pr^{0.4} \quad (3000 < Re < 7000) \quad (1.9)$$

$$Nu = 5.6 \quad (\text{at } Re < 3000), \quad (1.10)$$

where Di/Do is 0.868 and Pr is a Prandtl number.

The results of the tests are higher than the values calculated by Eqs. (1.8) - (1.10) in a region of Re 2000. The increase in heat transfer is likely due to spacer ribs which promote turbulence.

1.3.3 Multi-channel test rig (T_{1-M})

(1) Test components of the T_{1-M} test rig

T_{1-M} test rig consists of twelve heater pins, eleven hexagonal graphite blocks, eighteen compensation heaters, four internal coolers, as shown in Fig. 1.22. The fuel stack model consists of twelve heater pins and eleven graphite blocks, which simmulates one column of the VHTR core.

The configuration of the heater pin is the same as that of the fuel rod of the VHTR, except the length: the fuel rod of the VHTR consists of seven separated fuel elements, the lengths of which are all 570 mm, while the heater pin of T_{1-M} test rig is 3990 mm (570x7) in length. The heater pin have two types, one is for moderate-temperature test whose objective is to study heat transfer characteristics in a temperature range from room temperature to 750°C. The heating element is nickel-chromium alloy and the maximum electric power is 70 kW. For measurement of the surface temperature of graphite seven thermocouples are used.

The other type is for high-temperature test, which is to be carried out at extremely high-temperature of 1000°C, high pressure of 4 MPa, and large mass flow rate of 400 g/s. The heater element is made of graphite spiral coil. The maximum electric power is 100 kW. Only six thermocouples are embedded on the surface of grqphite sheath.

Each heater pin has respective axial power distributions: they are flat, cosine and exponential axial power distributions. The effective heating length of these heater pins is 460 mm or 529 mm, while

the actual heating length of the fuel rod of the VHTR is 529 mm. In order to avoid measurement error caused by flow disturbance, thermocouples are led through the grooves on the inner surface of graphite sleeve in the case of the moderate-temperature heater pin; while in the case of high-temperature heater pin, thermocouples are led through the grooves on the surface of graphite sleeve and thermocouples in the groove near the top is filled with ceramic cement.

The graphite blocks simulate the hexagonal fuel elements, and also the top and bottom removable reflectors of the VHTR. Dimensions of the graphite blocks are 570 mm in height and 299 mm in diameter. The bottom reflectors are cylindrical blocks of 390 mm in diameter and 570 mm in height. The fuel stack model is surrounded with side-blocks which are made of SUS 304, Incoloy 800H and compensation heaters. Functions of the side-blocks are to support and reinforce the fuel stack and to fill the gap between the fuel stack and compensation heaters. The compensation heaters are made of Kantal A-1, ceramic thermal insulation blocks and stainless steel casing. They are controlled to make the temperature of compensation heaters equal to that of the surface of graphite blocks, as well as to reduce the heat loss in the radial direction. Therefore the side surface of the fuel stack is kept adiabatic.

Figure 1.23 shows measuring locations for heat transfer and fluid-dynamic tests. Thermocouples for measuring the surface temperature of the heater pin are located at the position of 410 mm from the top of each stage. Internal temperature in the graphite blocks of heated sections are measured at the locations corresponding to those of the heater pin. For the measurement of temperature distribution of the fuel pin, seven thermocouples are embedded in the graphite sleeve at the same location of each heater element.

Each heater pin is controlled independently so as to reproduce the horizontal power distribution of the VHTR core.

Helium gas velocities at the channel inlet and outlet are measured by total head tubes and Pitot tubes. Helium gas temperature at each channel inlet are measured by thermocouples embedded on the heater electrodes. Helium gas temperature at each channel outlet are measured by thermocouples inserted into channels of the eleventh-stage graphite block.

(2) Test conditions and results

From April, 1983 to March, 1984, heat transfer and flow distribution tests were carried out using moderate-temperature heater pins of flat heat flux distribution in the axial direction.

The heat transfer test conditions were as follows :

Helium gas temperature at each channel inlet	: 270°C
Electric power of each heater pin	: 11 - 58 kW
Helium gas flow rate	: 50 - 270 g/s
Reynolds number of helium gas at each channel inlet	: 1800 - 10000
Helium gas pressure	: 3 MPa
Power distribution in the horizontal plane	: flat.

The test condition for flow distribution was the same as that for heat transfer, except the horizontal power distribution. The electrical power of No. 12 heater pin is varied from 0 kW to 58 kW to control flow distribution over twelve channels.

The results of the heat transfer tests are shown in Fig. 1.24. Symbol of "o" indicates experimental datum excludingly the case of the third channel. The solid line shows a correlation between Nusselt number for a smooth annulus in laminar, transitional and turbulent flows, and Reynolds number, which is expressed by Eqs. (1.8), (1.9) and (1.10).

Nusselts numbers obtained in the tests are 1.1 or 1.2 times as large as those for a smooth annulus at the same Reynolds number, this may be due to turbulence produced by spacer ribs. The flow distribution of helium gas at the outlet is shown in Fig. 1.25.

From the result of flow distribution test, it is concluded that the flow rates of No.12, No.1 and No.6 channels increase as the electric power of No.12 heater pin decreases. This phenomenon is due to the difference of friction and acceleration loss between No.12 channel and the other channels.

Table 1.4 Test items of T_1

Test item	test component	test rig
Heat transfer and fluid-dynamic characteristic tests on single-channel	mock-up fuel pin	$T_{1\text{-}S}$
Vibration test of fuel pin	mock-up fuel pin	$T_{1\text{-}S}$
Fluid-dynamic character-istic test of control rod	mock-up control rod	$T_{1\text{-}S}$
Heat transfer and fluid-dynamic characteristic tests on multi-channel (including partial load and channel choking)	mock-up fuel pin	$T_{1\text{-}M}$
Heat transfer and fluid-dynamic characteristic tests on multi-channel with stagnant coolant	mock-up fuel pin circulation piping	$T_{1\text{-}M}$

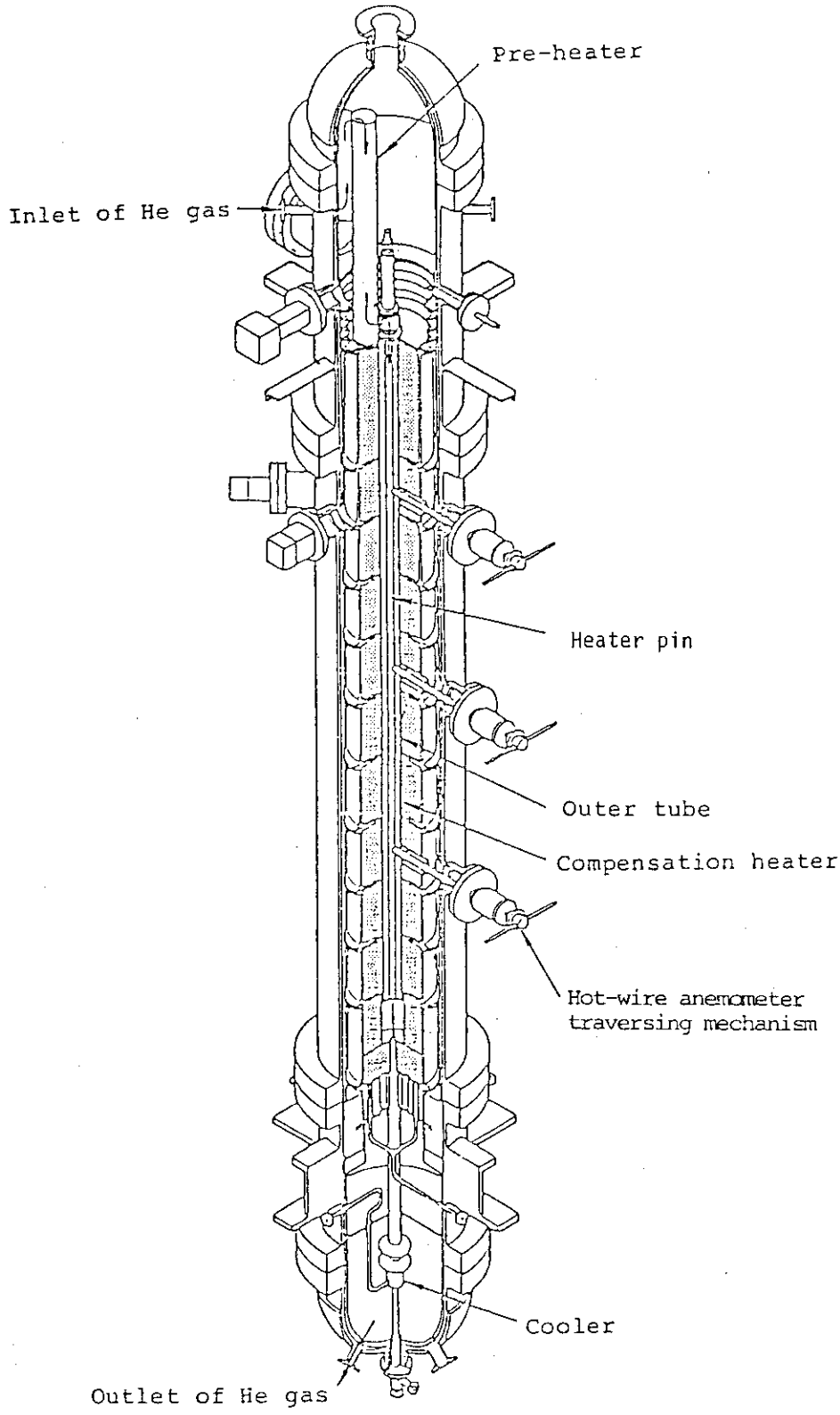

Fig. 1.16 Single-channel test rig(T_{1-s}) of T_1 test section

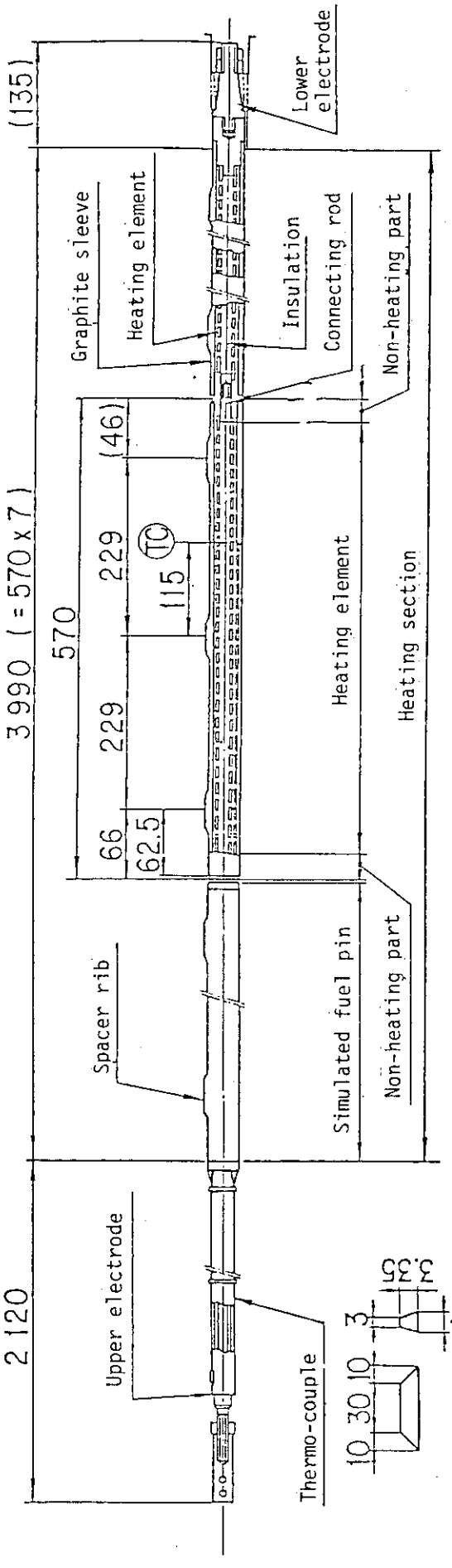

Fig. 1.17 A heater pin for high-temperature test

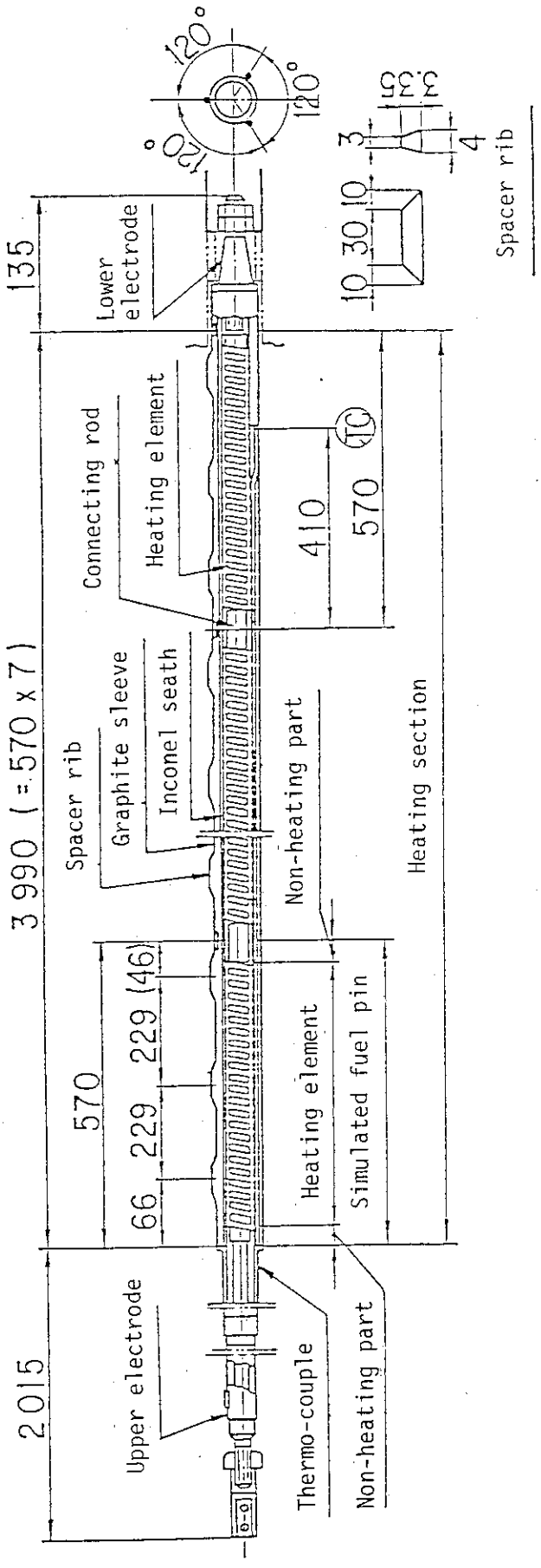

Fig. 1.18 A heater pin for moderate-temperature test

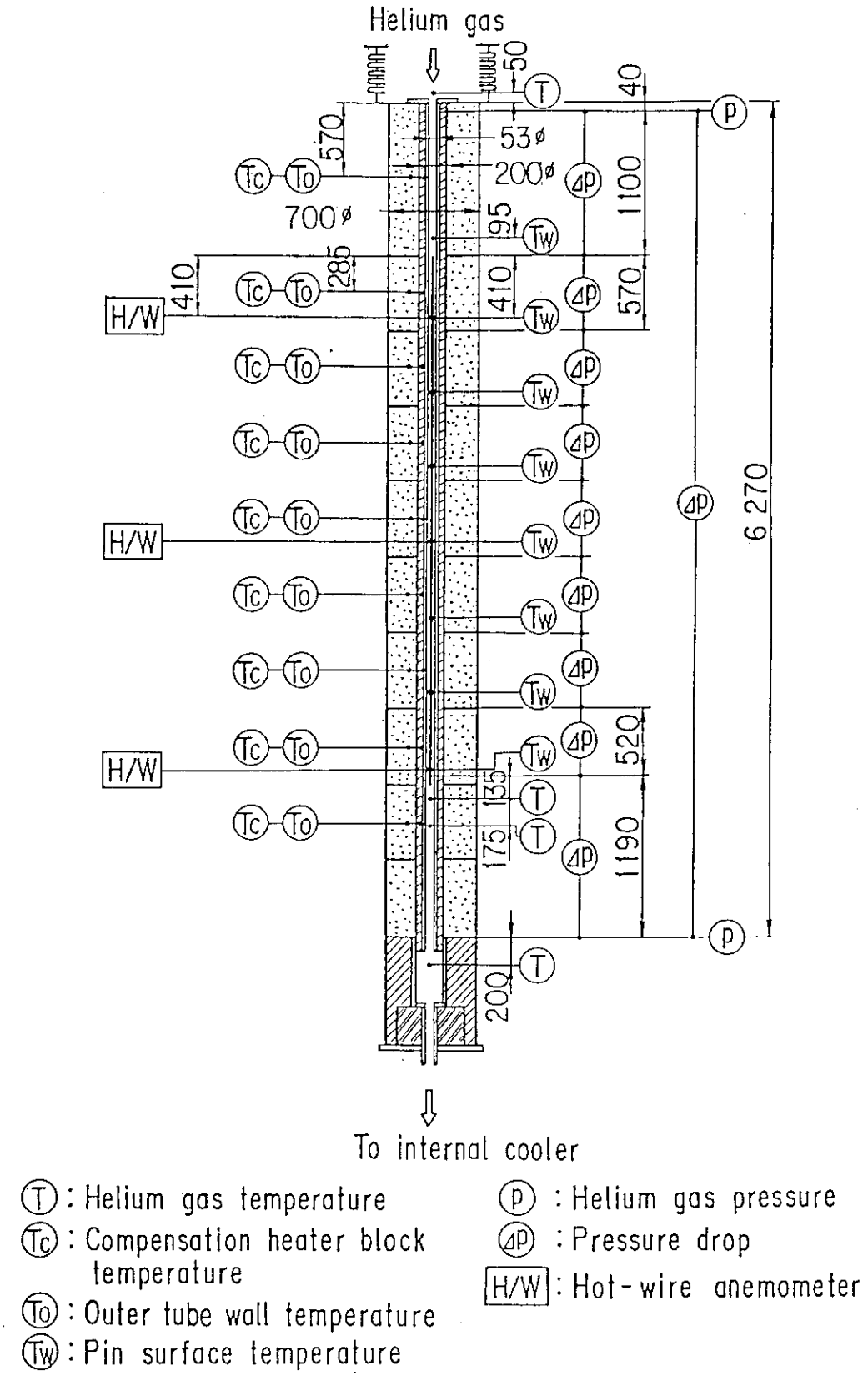

Fig. 1.19 Measuring locations for temperature, pressure and pressure drop in a single-channel test section

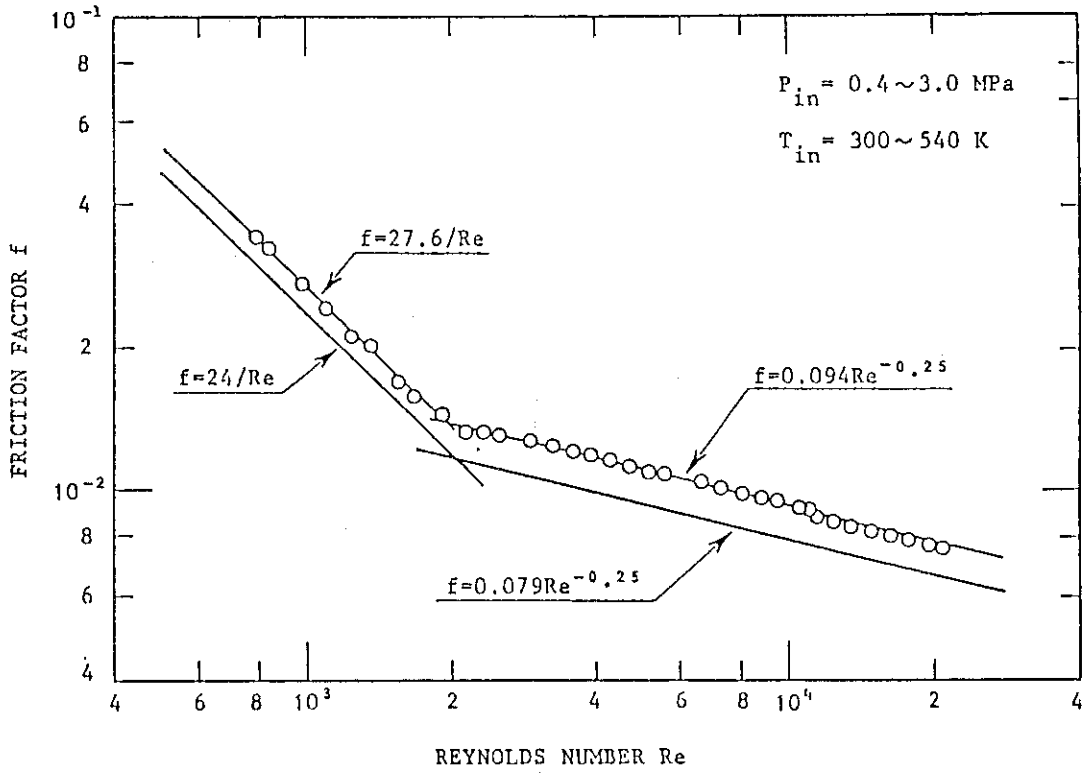

Fig. 1.20 Relation between friction factor f and Reynolds number Re for isothermal flow

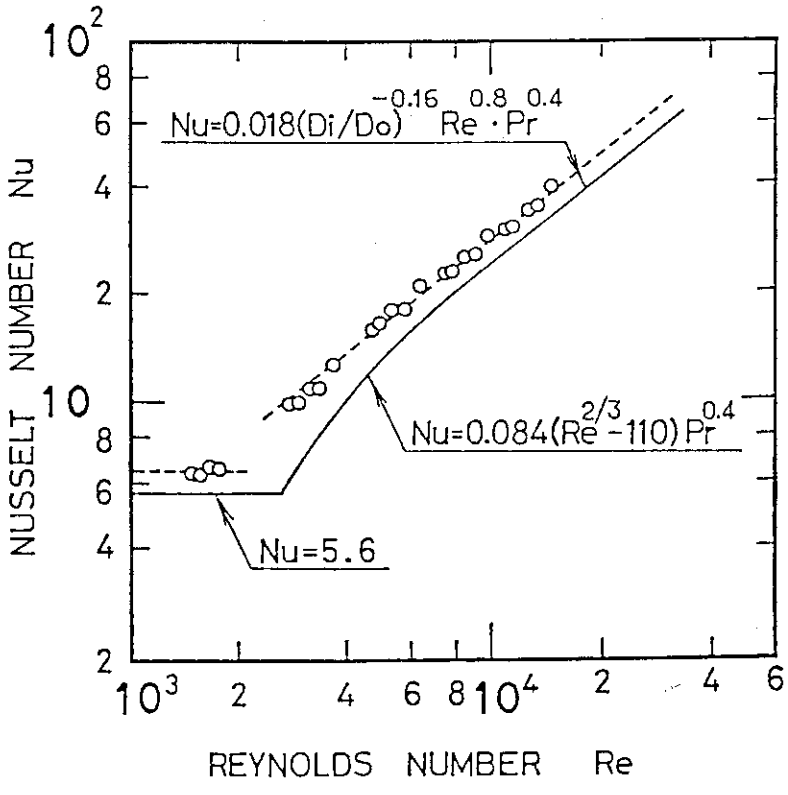

Fig. 1.21 Relation between Nusselt number Nu and Reynolds number Re

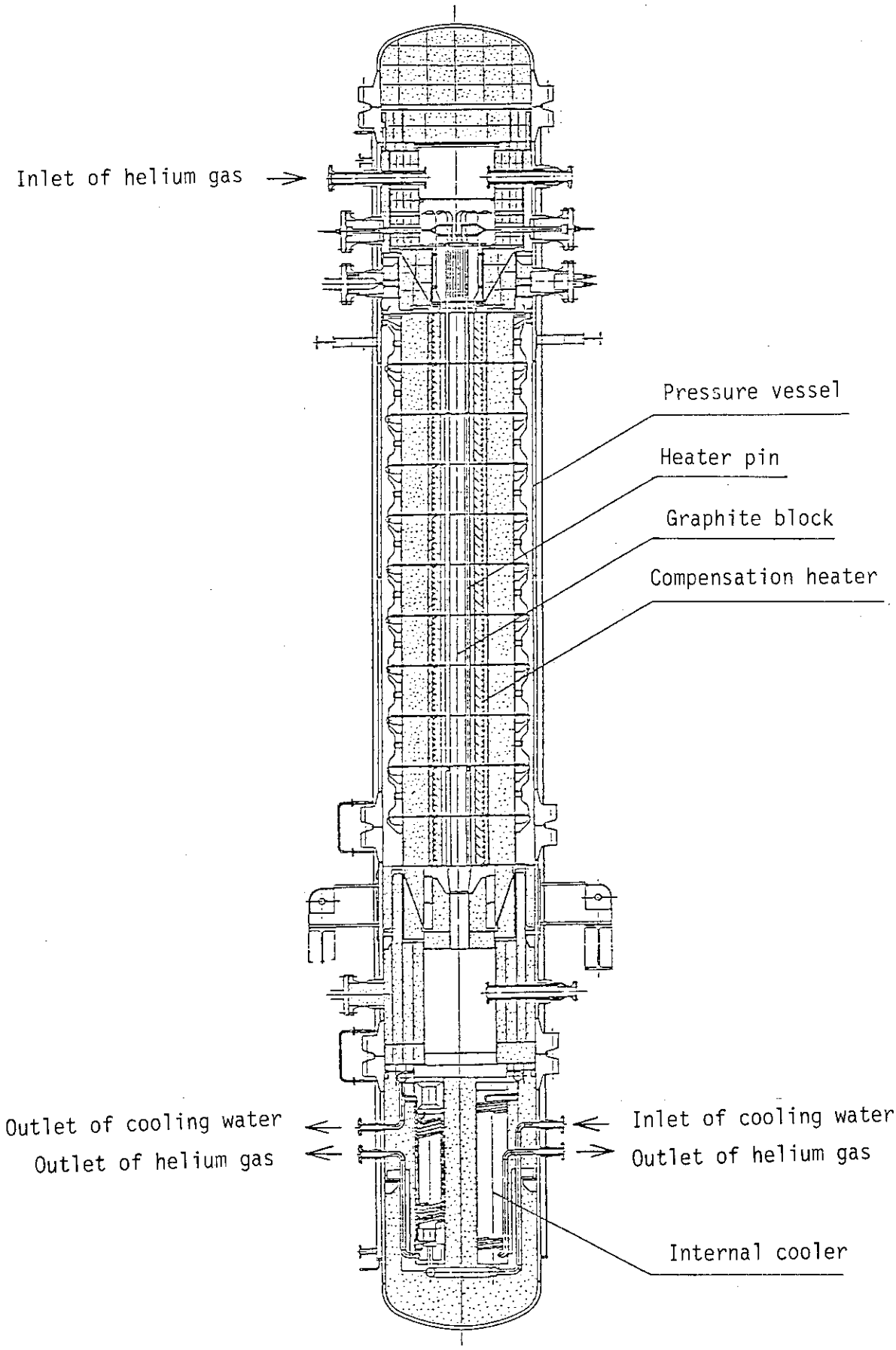

Fig. 1.22 $T_{1\text{-}M}$ test rig

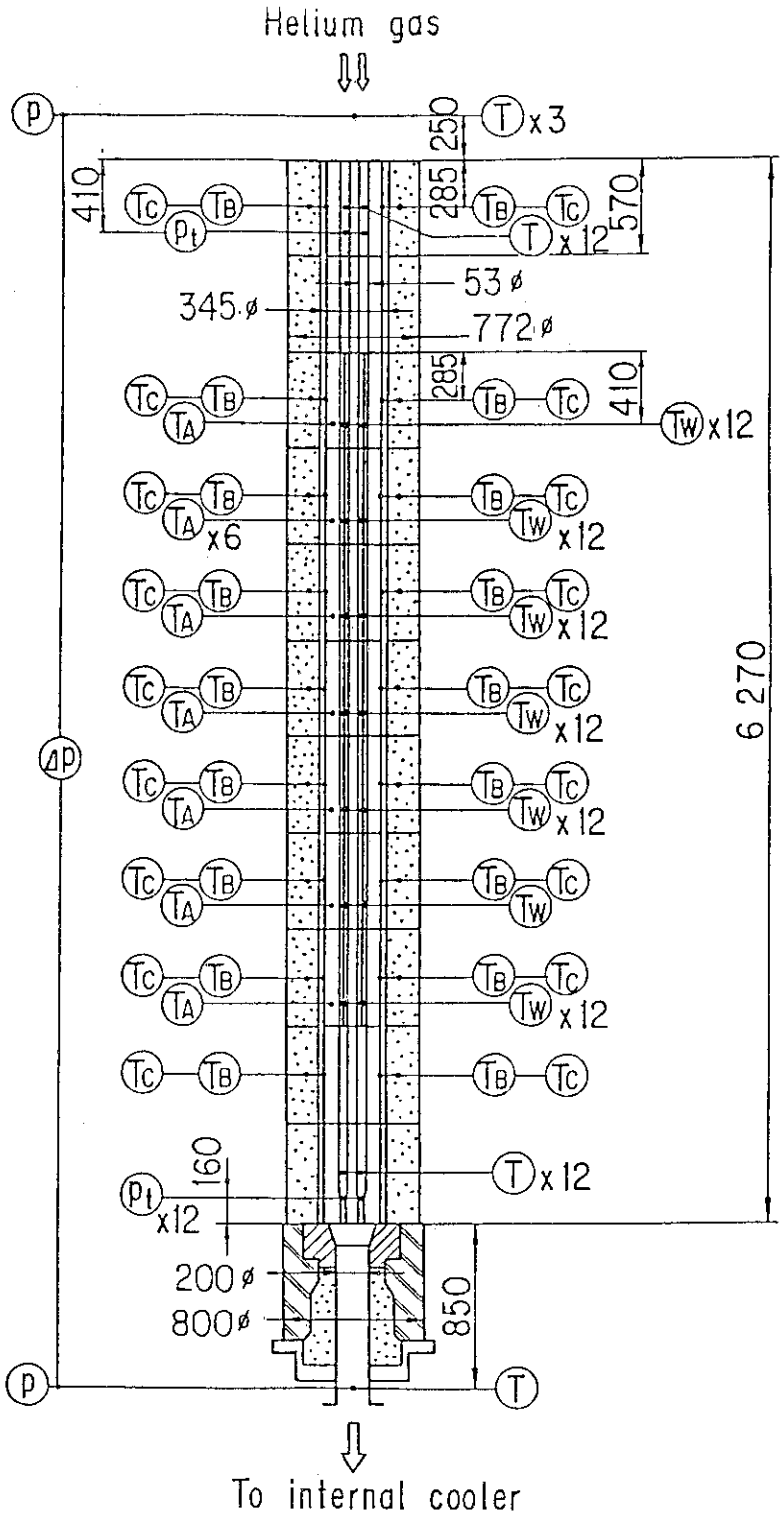

Ⓣ : Helium gas temperature
Ⓣ$_A$: Fuel block inner temperature
Ⓣ$_B$: Fuel block surface temperature
Ⓣ$_C$: Compensation heater block temperature
Ⓣ$_W$: Pin surface temperature
Ⓟ : Helium gas pressure
Ⓓ$_P$: Pressure drop
Ⓟ$_t$: Pitot tube

Fig. 1.23 Measuring locations for temperature, pressure and pressure drop in a multi-channel test section

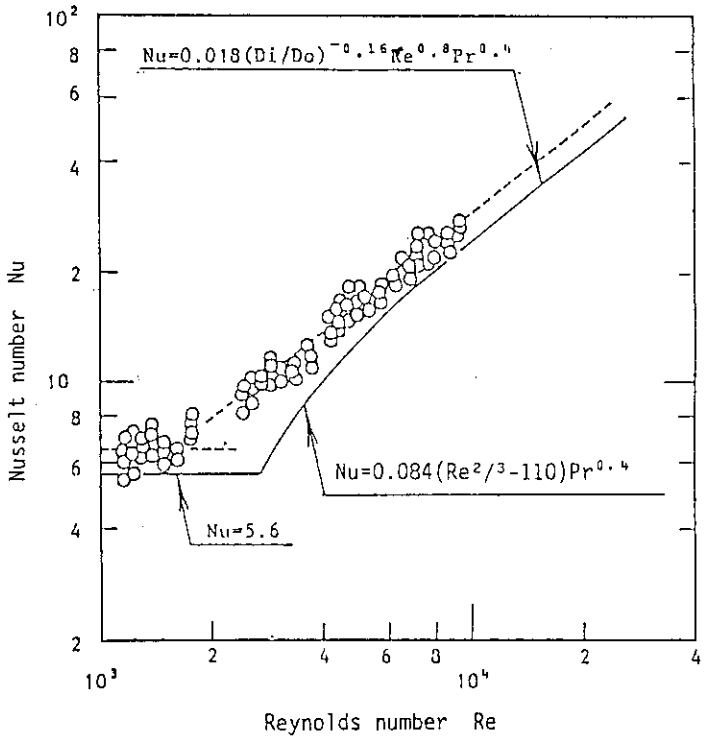

Fig. 1.24 Relation between Nusselt number Nu and Reynolds number Re obtained in a multi-channel test section

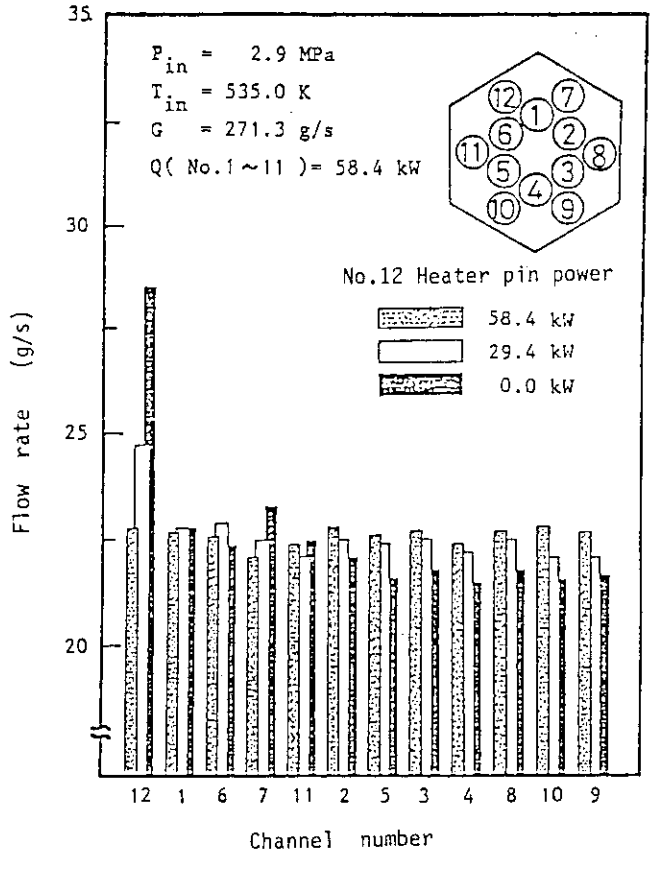

Fig. 1.25 Flow distribution at channel outlets in the case when electric power of No.12 heater pin decreased

1.4 In-core Structure Test Section (T_2) and In-core Flow Test Section (T_3)

K. Kunitomi, Y. Inagaki, K. Ioka, K. Umenishi, Y. Hoshi, H. Hayashi, T. Kunitama, N. Izawa, M. Hishida, T. Tanaka and H. Shimomura

1.4.1 In-core structure test section (T_2)

The aim of the experiments using T_2 test section is to examine the performance and soundness of sealing and insulation as well as the flow characteristics in the core. T_2 test section simulates a part of the lower plenum structure, consisting of plenum blocks, core support posts, insulation layers, core support plate, high-temperature outlet ducts and so on. Figs.1.26 and 1.27 show a flow sheet and a general view of T_2 test section respectively. T_2 test section has two main flow lines, one is to cool steel structures and the other is to supply high-temperature helium gas from M+A section to T_2 test section. The difference of pressures of the two lines are controlled less than 0.03 MPa.

In the test section, 400°C helium gas, supplied from M+A section, flows through the outer tube of the hot gas duct to cool diagrid, core support plates, core barrels and core-restraint mechanism, then finally helium gas flows through the outer tube of the upper duct to M+A section. On the other hand, helium gas, which is heated up to 930°C by heaters of Adapter section, flows through the inner tube of the upper duct to a flow rate regulator, a heater and the lower plenum structure which composes seven core regions, and returns to Adapter section through the lower duct. Table 1.5 shows test items of T_2 test section, and Table 1.6 shows test conditions of T_2 test section. These conditions are the same as those of the VHTR, and the total flow rate of T_2 test section is about 1/4 as much as that of the VHTR.

JAERI already made a contract of T_2 test section with Fuji Electric Co., and the design works of the test rigs and components are now in progress.

1.4.2 In-core flow test section (T_3)

T_3 test section simulates complicated coolant flow such as bypass flow or cross flow established between graphite blocks in the VHTR. The test items of T_3 are as follows :

(1) Flow distribution in the core,
(2) Characteristics of the flow regulation orifice,
(3) Soundness of the core-restraint mechanism, and
(4) Assembling and disassembling of the in-core structures.

1.4.3 Simulation of the VHTR conditions

An in-core cooling condition, which has a close relation to sealing efficiency, is a little different from that of the VHTR. Namely the outer diameter of the test section is almost 70 %, the total flow rate is 25 % and sealing length is 50 % as large as those of the VHTR. And if the sealing characteristics of the test section and the VHTR are the same, the estimated leakage rate is nearly 17 % as large as that of the VHTR. Therefore, when the pressure difference in the test section is 0.01 MPa, which is half as much as that of the VHTR, the leakage rate of T_2 test section is the same as that of the VHTR.

In order to control the pressure difference in the test section, pressure fluctuation in M+A section must be maintained small.

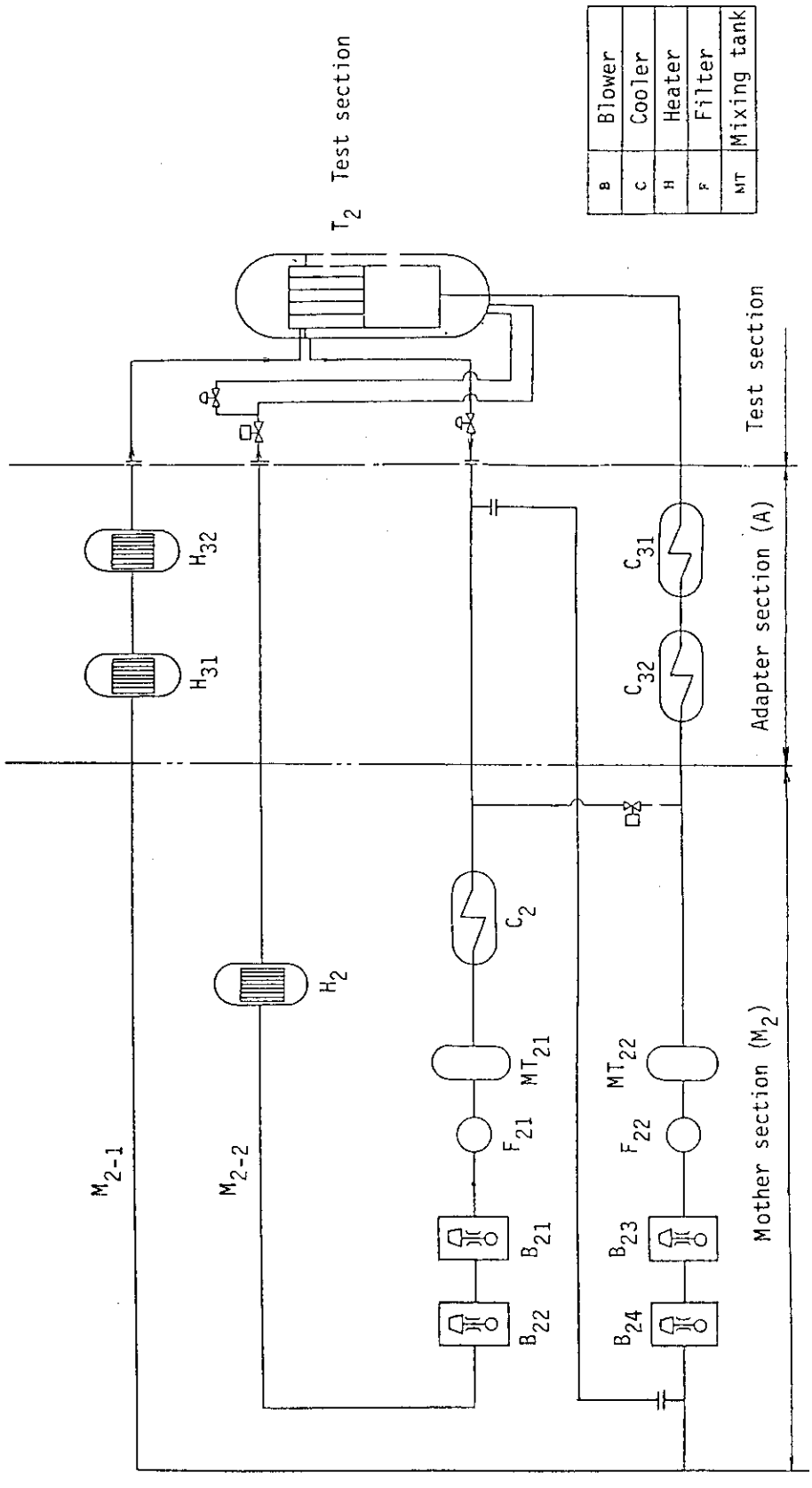

Fig. 1.26 Flowsheet of T_2 test section

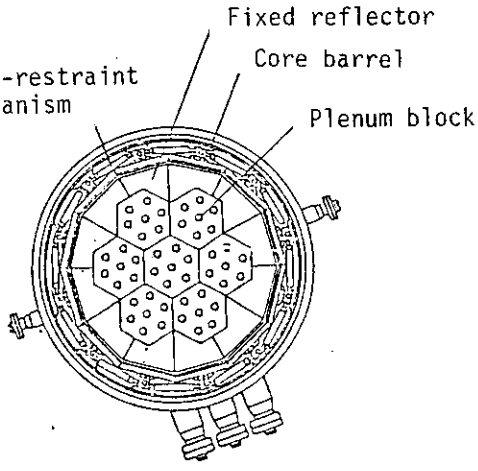

A-A CROSS SECTION

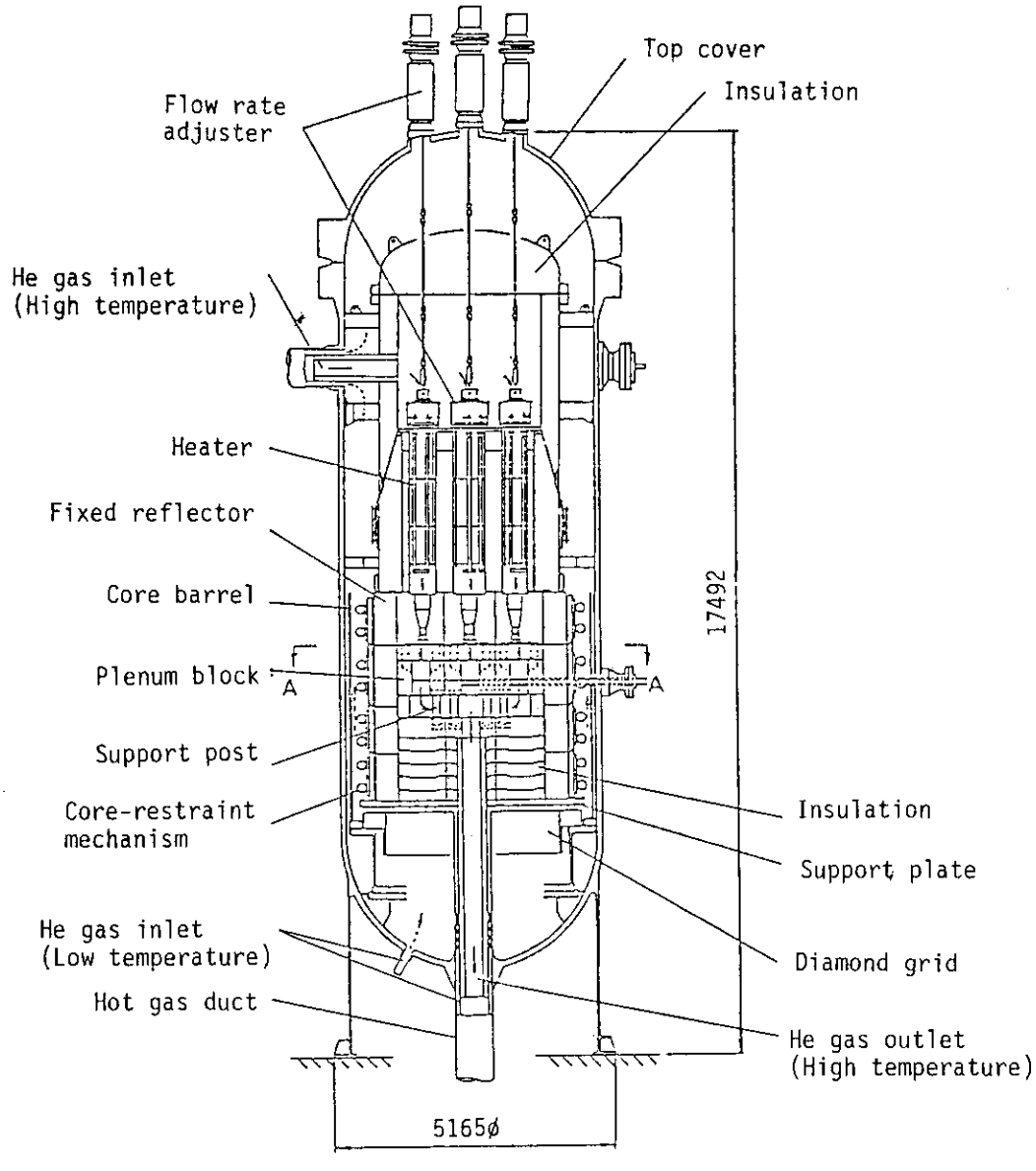

Fig. 1.27 T_2 test section

Table 1.5 Test items of T_2 test section

1. Mixing characteristics of helium gas in the hot plenum.
2. Performance of sealings around the hot plenum.
3. Characteristics of cooling under the support plate and cooling core-restraint mechanism.
4. Characteristics of thermal displacement
5. Aging effect by thermal cycle
6. Structural integrity of the core-restraint mechanism, thermocouples, side refrector blocks against the thermal shock.

Table 1.6 Test conditions of T_2 test section

Items	Pressure	High temperature part		Low temperature part		Leakage flow rate	Mixing
		Inlet flow rate	Region heater outlet temperature	Inlet flow rate	Inlet temperature		
1.Room temperature test mode	1.8 MPa	4.0 kg/s	Room temperature	4.0 kg/s	Room temperature	1.0 kg/s	Room temperature
2.Heating test mode							
(1) Average heating test mode	4.0 MPa	0.74 ∿ 4.0 kg/s	< 1050°C	1.0 ∿ 4.0 kg/s	400°C	0 kg/s	950°C
(2) Leakage test mode	"	3.5 kg/s	< 1050°C	1.6 ∿ 4.0 kg/s	400°C	0 ∿ 0.6 kg/s	950°C
(3) Mixing test mode	"	4.0 kg/s	enter region 1050°C non-center region —	4.0 kg/s	400°C	0 kg/s	950°C

1.5 Heat Removal Test Section (T_4)

Y. Inagaki, M. Okamoto, Y. Mizokami, N. Zaima and T. Tanaka

T_4 test section consists of an intermediate heat exchanger (IHX), a steam generator (SG), hot gas ducts, a high-temperature shut-off valve, etc. The objective of T_4 test section is to demonstrate heat transfer performance and structural integrity of high-temperature components.

T_4 test section is an about 1/3-scale model of the VHTR. Figures 1.28 and 1.29 show a flowsheet and a plot plan of the test section. Specification of the test section and the major test items are shwon in Tables 1.7 and 1.8 respectively.

The test program has been revised according to the revised specifications of the VHTR, such as reactor outlet helium gas temperature, flowsheet and components.

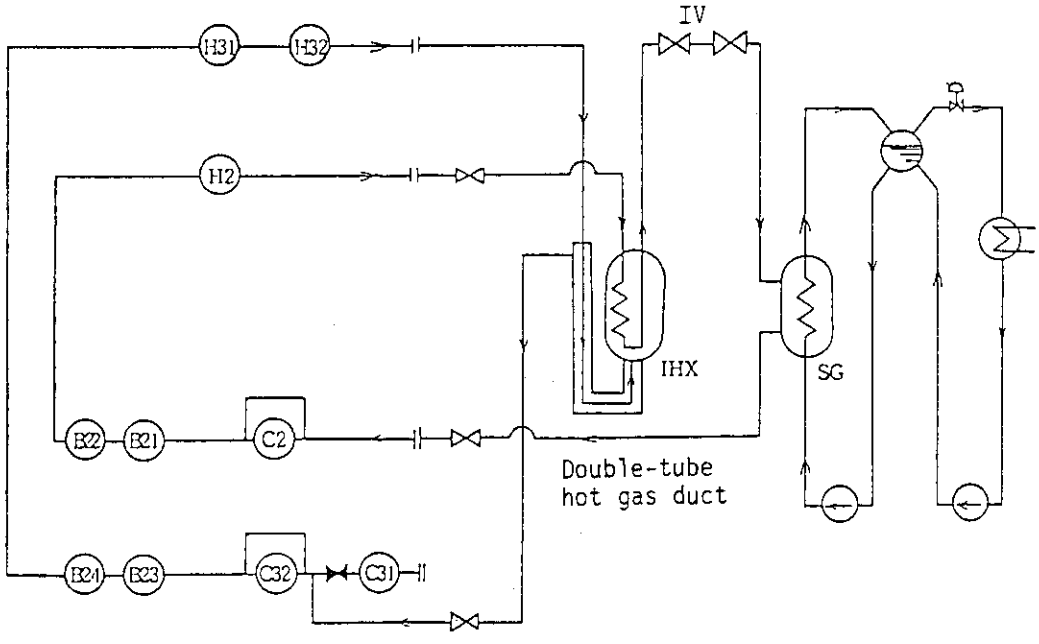

Fig. 1.28 Flowsheet of T_4 test section

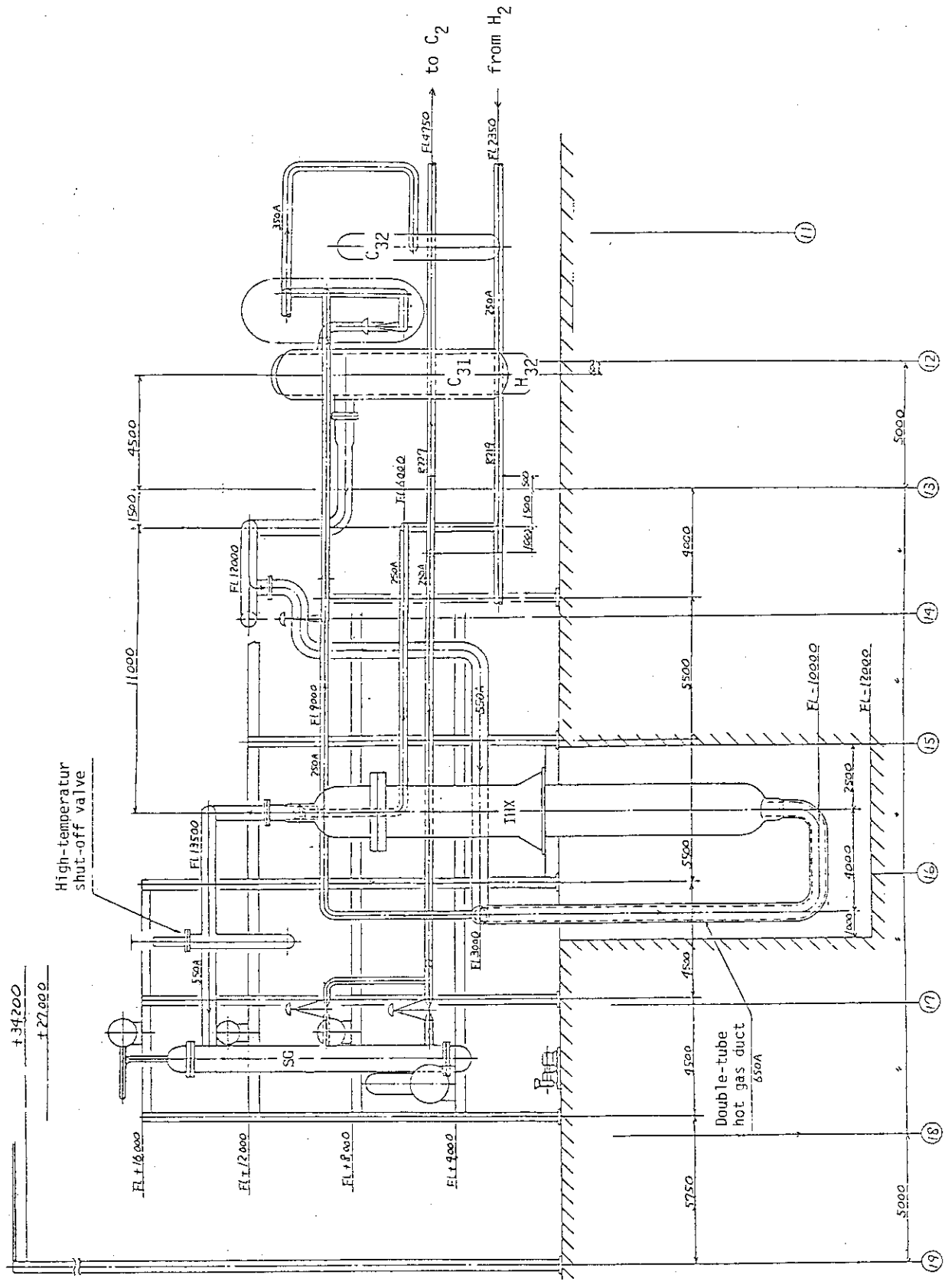

Fig. 1.29 Plot plan of T_4 test section

Table 1.7 Specification of T_4 test section

Items	Unit	
1. Primary Helium Circuit		
1) Flow Rate	kg/s	3.0
2) Operating Temperature		
M+A Heater Outlet	°C	966.0
IHX Inlet	°C	940.0
IHX Outlet	°C	378.0
3) Operating Pressure	MPa	4.0
2. Secondary Helium Circuit		
1) Flow Rate	kg/s	2.7
2) Operating Temperature		
IHX Outlet	°C	905.0
SG Inlet	°C	891.0
SG Outlet	°C	270.0
IHX Inlet	°C	283.0
3) Operating Pressure	MPa	4.3
3. Steam/Water Circuit		
1) Flow Rate of SG	kg/s	39.6
2) Temperature of Steam	°C	233.0
3) Pressure of Steam	MPa	3.0

Table 1.8 Test items of T_4 test section

Component	Test Items
IHX	1. Thermal and hydraulic performance test •steady state performance •dynamic performance 2. Structural integrity test •hot header •tube •insulation •vibrating performance of tube bundle •wearing performance of tube support 3. Verification of safety and reliability of operation system 4. Maintenance test 5. Fabrication test
SG	1. Thermal and hydraulic performance test .steady state performance .dynamic performance .controllability of He gas outlet temperature 2. Thermal insulation test 3. Structural integrity test 4. Aseismatic test 5. Maintenance test 6. Fabrication test
High-temperature shut-off valve	1. Leakage rate measuring test .high temperature operation .pressure and thermal cycle 2. Shut-off test . shut-off test .responce of plant system 3. Structural integrity test 4. Sealing test of valve 5. Wearing test of seat and disk 6. Normal operating test 7. ISI test
Hot Gas Duct	1. Thermal and hydraulic performance test 2. Structural integrity test 3. Fabrication test 4. Maintenance test 5. Aseismatic test

1.6 Performance Test of Hot Gas Ducts

K. Kunitomi, K. Umenishi, I. Ioka, M. Hishida, T. Tanaka
and H. Shimomura

Hot gas ducts provided with internal thermal insulations are installed in M+A section. Helium gas of high-temperature (max. 1000°C) and high-pressure (max. 4 MPa) flows in the hot gas ducts. The hot gas duct is designed so as to separate the pressure and temperature boundaries because there exists no material which is resistant for the two roles in such a severe environment.

This type of hot gas duct will be used for the VHTR, and the following items are to be verified :

(a) Effective thermal conductivity of hot gas ducts,
(b) Temperature distribution of the pressure tube, and
(c) Heat flux distribution of the pressure tube.

(1) Hot gas ducts of HENDEL

Figure 1.30 shows a configuration of the hot gas duct. A liner tube made of Hastelloy-X forms a helium gas passage. An internal thermal insulation of ceramic fibre is packed between the liner tube and the pressure tube in order to maintain the temperature of the pressure tube lower than the design temperature of 350°C.

The insulation is divided into three layers by stainless steel foils in the radial direction and separated by V-shape end plate at intervals of 0.7 - 1.4 m in the axial direction so that bypass or permeation flow might not occur. Radial thermal expansion difference between the liner tube and the pressure tube is absorbed by clearance at pin joints, and the axial thermal expansion difference at sliding joints.

(2) Test procedure

Heat loss from the hot gas duct was measured by heat flux meters whose sensors were fixed on the surface of horizontal, vertical and bent parts of the hot gas duct. A heat flux meter, an Er-2 type of Showa Denko Co., consists of a film of silicon rubber, C-A thermocouples and a cover of silicon rubber. Temperature of the pressure tube was measured with C-A thermocouples seathed with glass fibre clothes.

(3) Test results

As shown in Fig. 1.31, temperature distributions on the surface of horizontal, vertical and bent parts of the tube were almost uniform. There was no hot spot higher than 350°C.

Heat flux distribution of the pressure tube is shown in Fig. 1.32 and was uniform on the same surface where the temperature distribution was measured. Effective thermal conductivity of the internal thermal insulation was calculated by the temperatures of the pressure and liner tubes and the heat flux of the pressure tube. Figure 1.33 shows effective thermal conductivity at the horizontal and vertical sections of the duct. The value of vertical tube was slightly higher than that of horizontal tube.

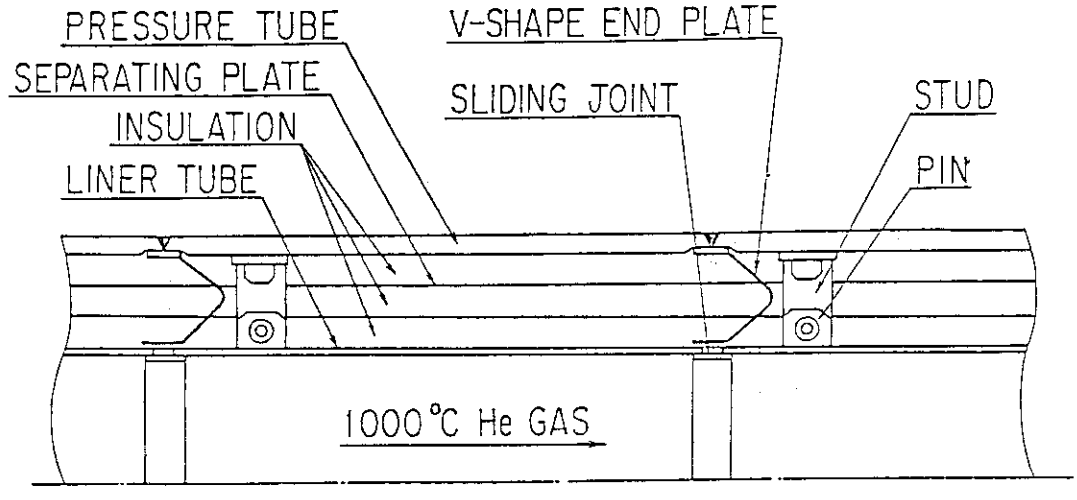

Fig. 1.30 Configuration of a hot gas duct

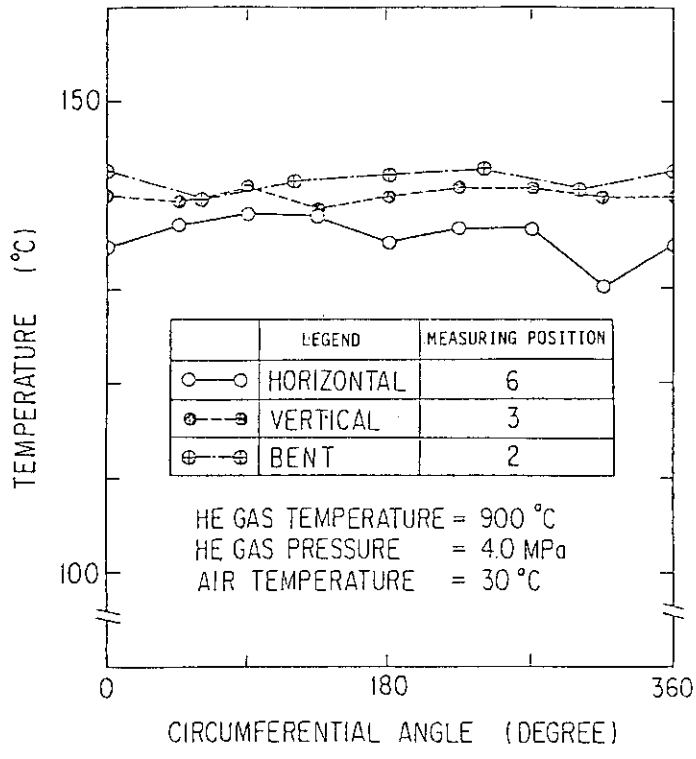

Fig. 1.31 Temperature distribution of a pressure tube

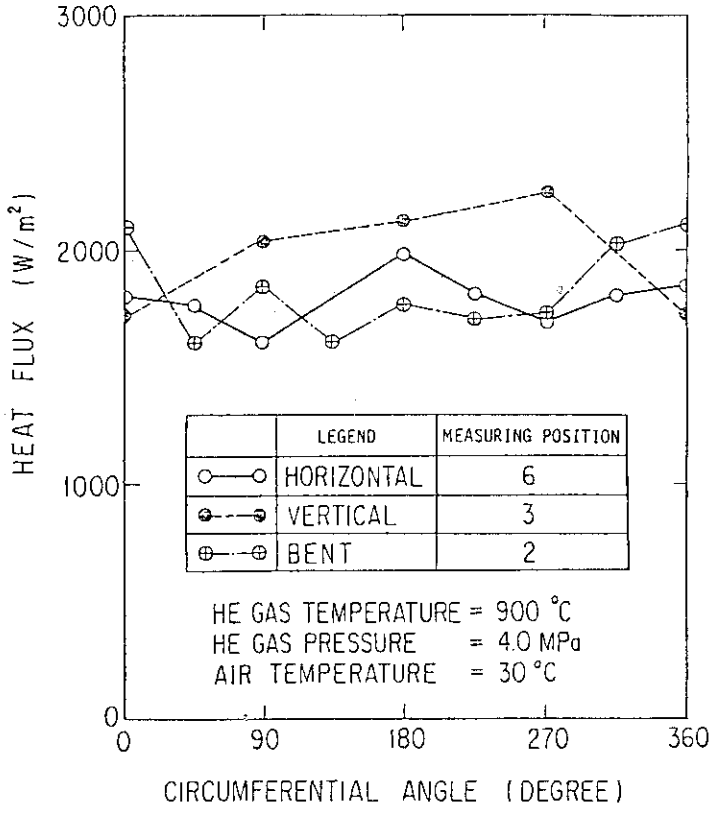

Fig. 1.32 Heat flux distribution of a pressure tube

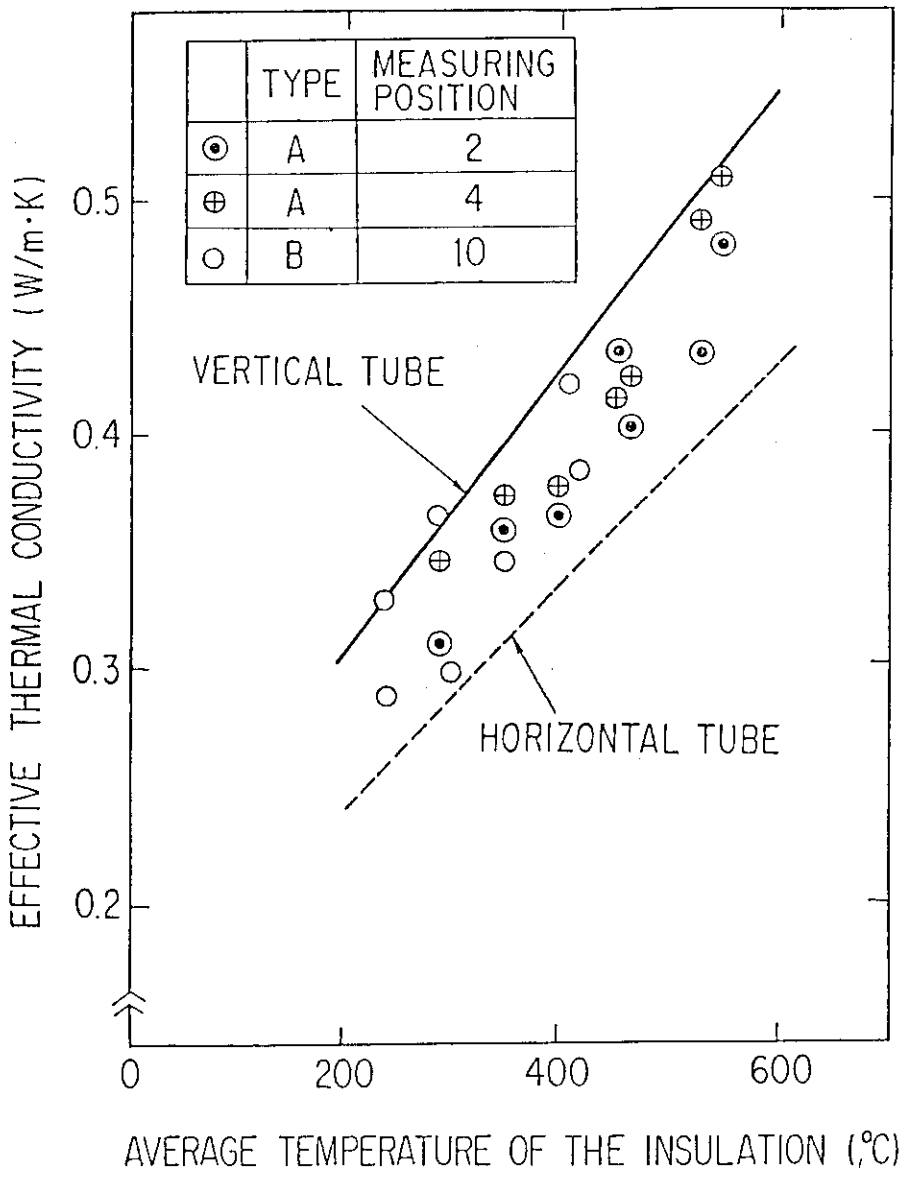

Fig. 1.33 Effective thermal conductivity of insulation

1.7 High-temperature Components (Heaters and Coolers)

Y. Inagaki, N. Zaima, M. Hishida, T. Tanaka and H. Shimomura

(1) High-temperature heaters

H_{31} and H_{32} are resistance-heating pipe heaters. The heater elements of H_{31} are made of Incoloy-800H and H_{32} has graphite elements. Helium gas flows inside the elements of both heaters which have thermal insulation inside the pressure vessel, and the outer surface of these vessels are cooled by water.

It is demonstrated that helium gas is heated up to 1000°C by the two heaters at a flow rate of 3.2 kg/s, while in the case of a flow rate of 4.0 kg/s, helium gas is heated up to 900°C.

Figure 1.34 shows heating efficiencies of the heaters H_{31} and H_{32}. The efficiency is 75 - 90 % as much as the electric input power.

Figure 1.35 shows heat transfer characteristics of heater elements of H_{32}. Nusselt numbers are 10 % larger than the values calculated by Dittus-Boelter's equation. However, there still remains doubt in the accuracy of measurement.

(2) Coolers

C_{31} is a step-up baffled type cooler with a water cooling straight tube bundle. Helium gas of 1000°C, heated by H_{31} and H_{32}, enters from the upper nozzle and flows circumferentially on the shell-side of the tube bundle. Flow direction of helium gas is changed by the baffle.

The maximum capacity of heat removal by C_{31} is 10.6 MW and 70 % greater than the design value, this may be attributed to the followings:

(a) Heat transfer area is 20 % greater than the designed value,
(b) There is no fouling inside the water cooling tubes, and
(c) Heat transfer coefficient of the outer tubes is larger than the design value.

Figure 1.36 shows heat transfer characteristics of the outer tubes of C_1, C_2, C_{31} and C_{32} which are installed in M+A section. The coolers except for C_{31} are of segmental baffled type. As to C_{31}, Nusselt number is twice larger. In conclusion, cooling performance of a step-up baffled type cooler is superior to a segmental baffled type.

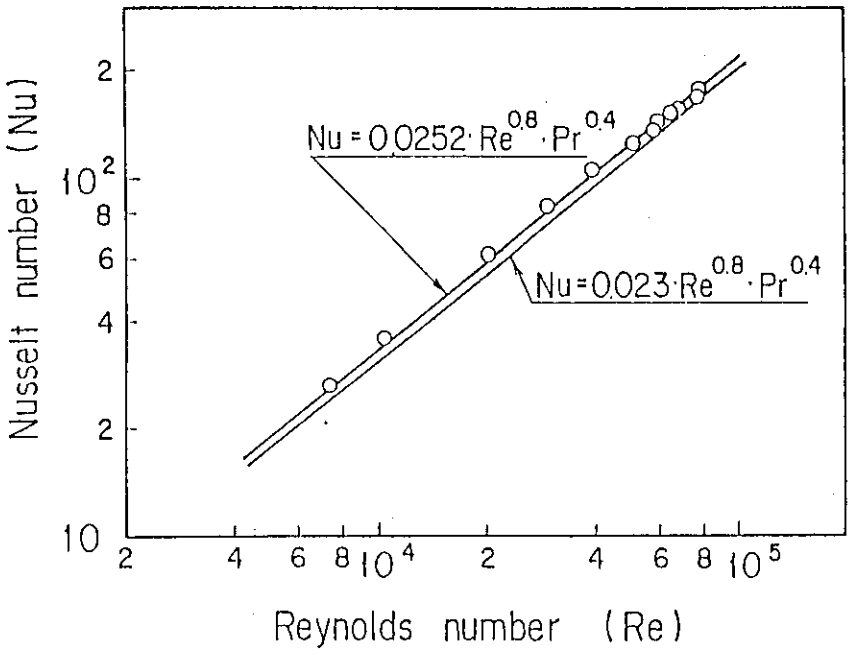

Fig. 1.34 Heat transfer characteristics of heater elements of heater H_{32}

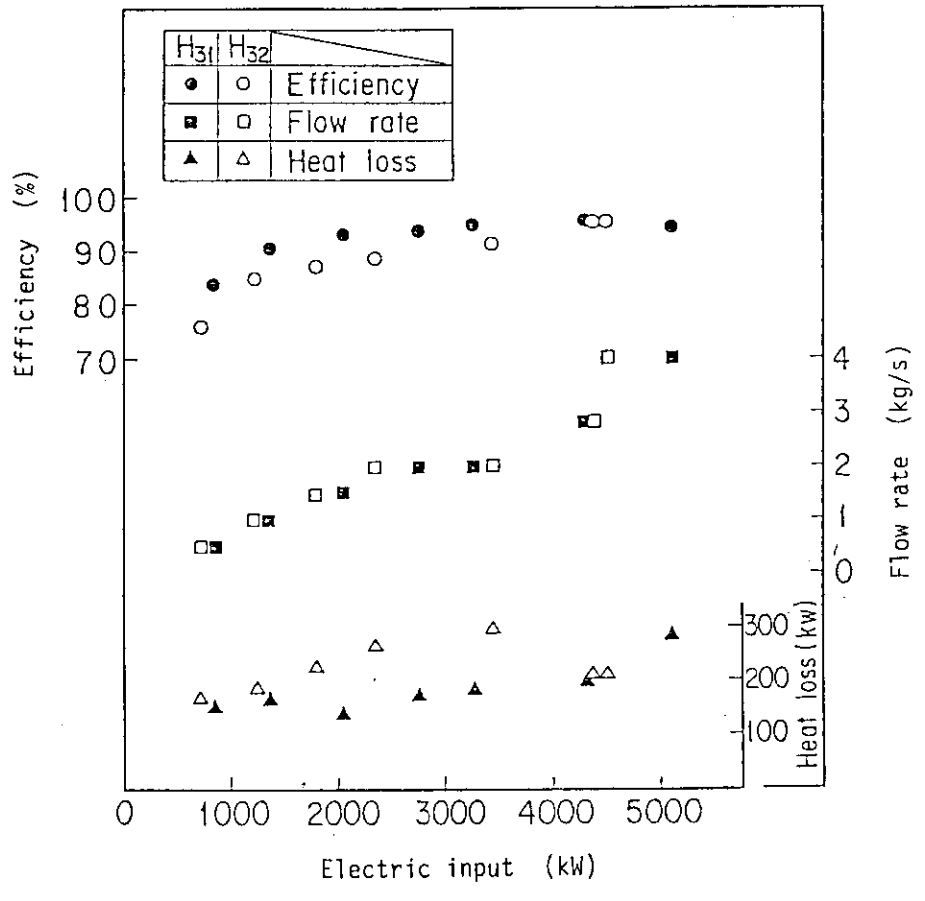

Fig. 1.35 Efficiencies of heaters H_{31} and H_{32}

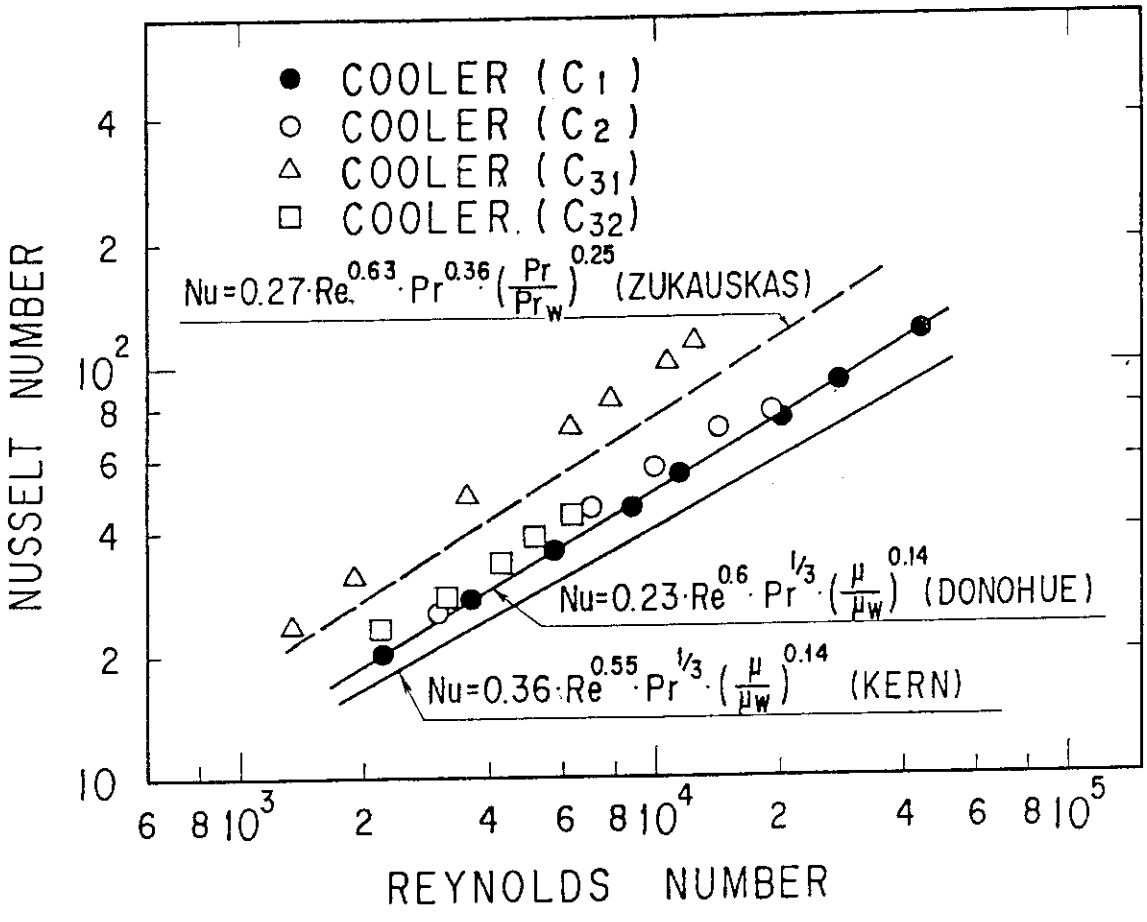

Fig. 1.36 Heat transfer characteristics of tube bundles with baffle plate of He gas coolers

1.8 Test of Core-restraint Mechanism

K. Kunitomi and T. Tanaka

In the VHTR, there are fixed side-reflector blocks around the core. These blocks are tightened by a core-restraint mechanism. This mechanism is designed so that the thermal expansion coefficient might be the same as that of the side-reflector blocks and also the force acting on the side-reflector blocks might be unchanged even in high-temperature operation.

However, since tension force of the core-restraint mechanism is the maximum 22 tons at 450∿500°C, it may decrease in a long-term operation owing to the relaxation.

It is necessary for the VHTR design, to test the relaxation of the core-restraint mechanism.

(1) Test pieces

Figure 1.37 shows a model of core-restraint mechanism and a test specimen. The core-restraint mechanism of the VHTR has four pipes combined with four dissimilar materials so that the thermal coefficient might be the same as that of graphite.

The model of core-restraint mechanism is a pipe combined with two dissimilar materials, but the length is half as much as that of the core-restraint mechanism of the VHTR. The test specimen is 100 mm in length.

(2) Test results

Figure 1.38 shows residual stresses of the test speciman. The vertical axis indicates the residual stress of the test specimen or of the outer spacer pipe of the model.

In the case of 450°C, there is no significant difference between the test specimen and the model. In the case of 500°C, residual stress of the model is 5 MPa higher than that of the test specimen. However, since the difference is not so large from the VHTR design point of view, the relaxation of the model is well understood by the results of the test specimen.

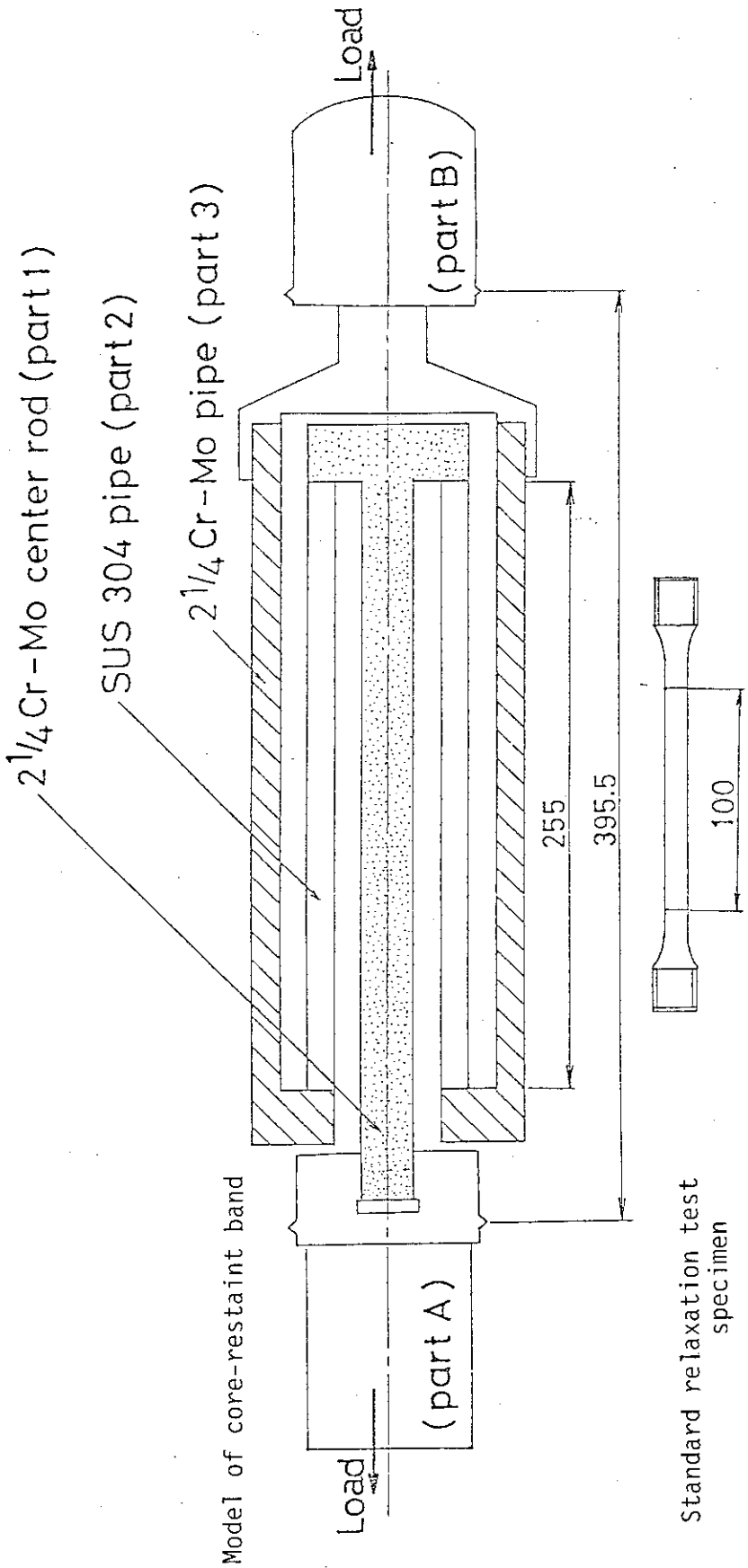

Fig. 1.37 Model of core-restraint band and standard relaxation test specimen

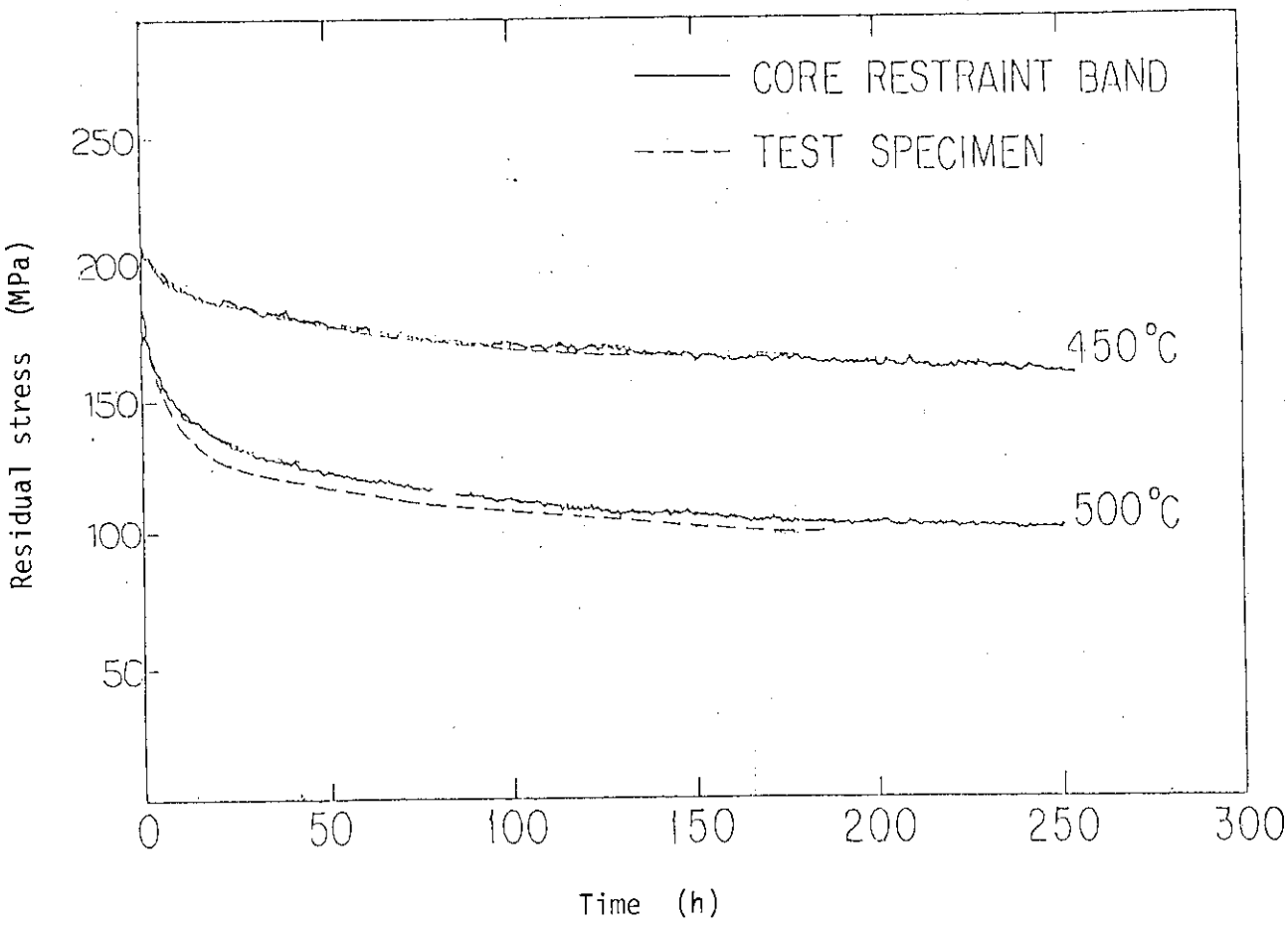

Fig. 1.38 Change of residual stress with lapse of time

1.9 Bottom-core Structure Test

Y. Inagaki, H. Hayashi, M. Kato and T. Tanaka

Figure 1.39 shows a flowsheet of a bottom-core structure test section. Helium gas is supplied from a mini-loop which consists of a cooler, blowers, heaters, valves and helium gas suppling bombes.

The insulation layer of the test section, which is half in scale and a one-region model of the VHTR, consists of carbon blocks, graphite blocks and stainless steel plates. The graphite heater heats a hot gas plenum placed on the insulation layer, and helium gas cools a support plate placed below the insulation layer.

The bottom-core structure test has been carried out for two test sections. The outside of the insulation layer of the one test section is surrounded by ceramic blocks and compensation heaters to study the one-dimensional insulation performance, while the outside of insulation layer of the other test section is surrounded by graphite reflectors to study three-dimensional insulation performance. Figure 1.40 shows the second test section.

The followings are test items for the bottom-core structure test

(1) One-dimensional performance of the insulation layer,
(2) Three-dimensional performance of the insulation layer,
(3) Sealing performance of the graphite reflectors, and
(4) Cooling characteristics of the support plate by helium gas.

The test conditions are as follows:

Helium gas temperature at the inlet	50°C
Helium gas temperature in the plenum	700°C
Helium gas flow rate	max. 0.2 kg/s
Helium gas pressure	1.0 MPa.

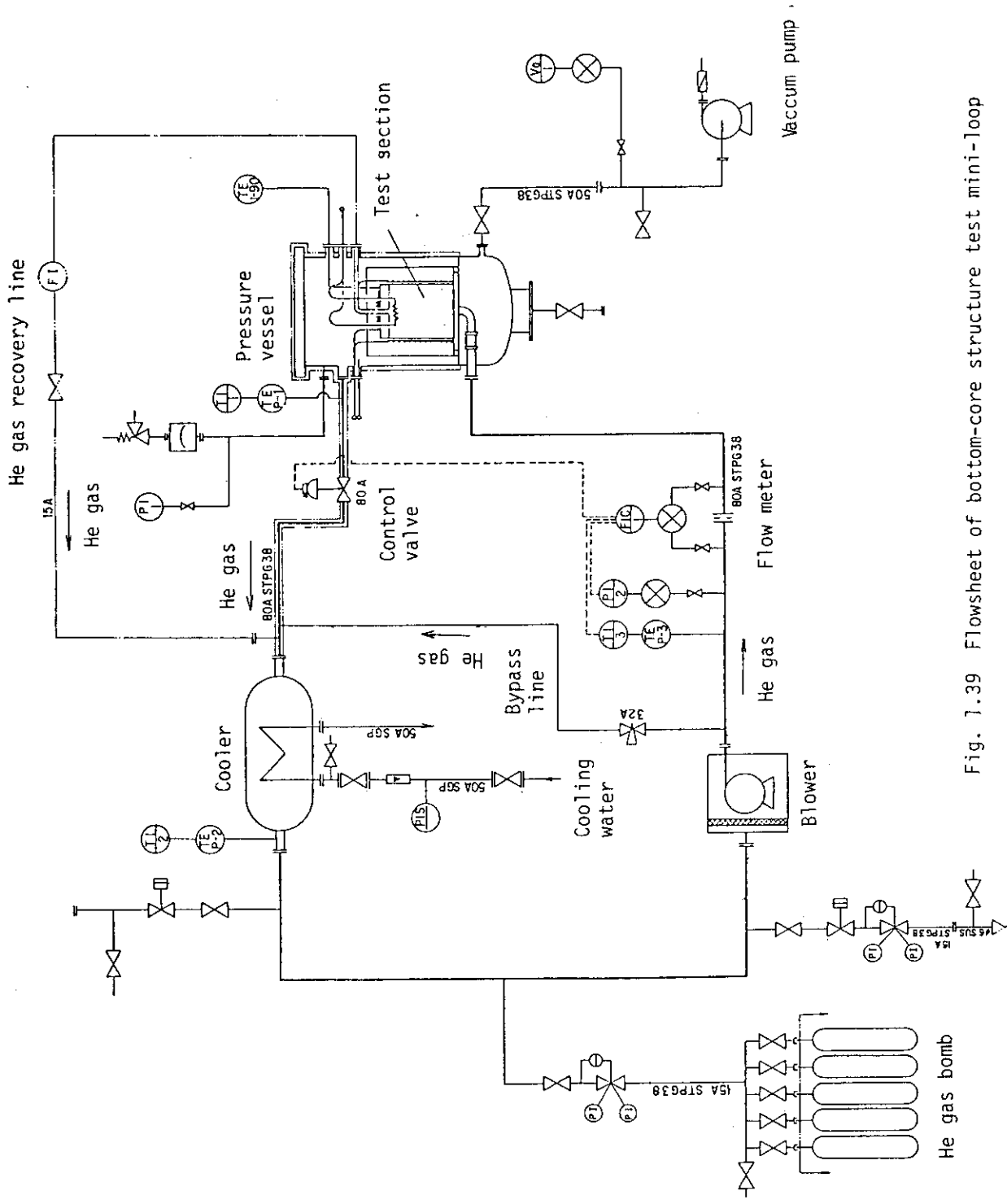

Fig. 1.39 Flowsheet of bottom-core structure test mini-loop

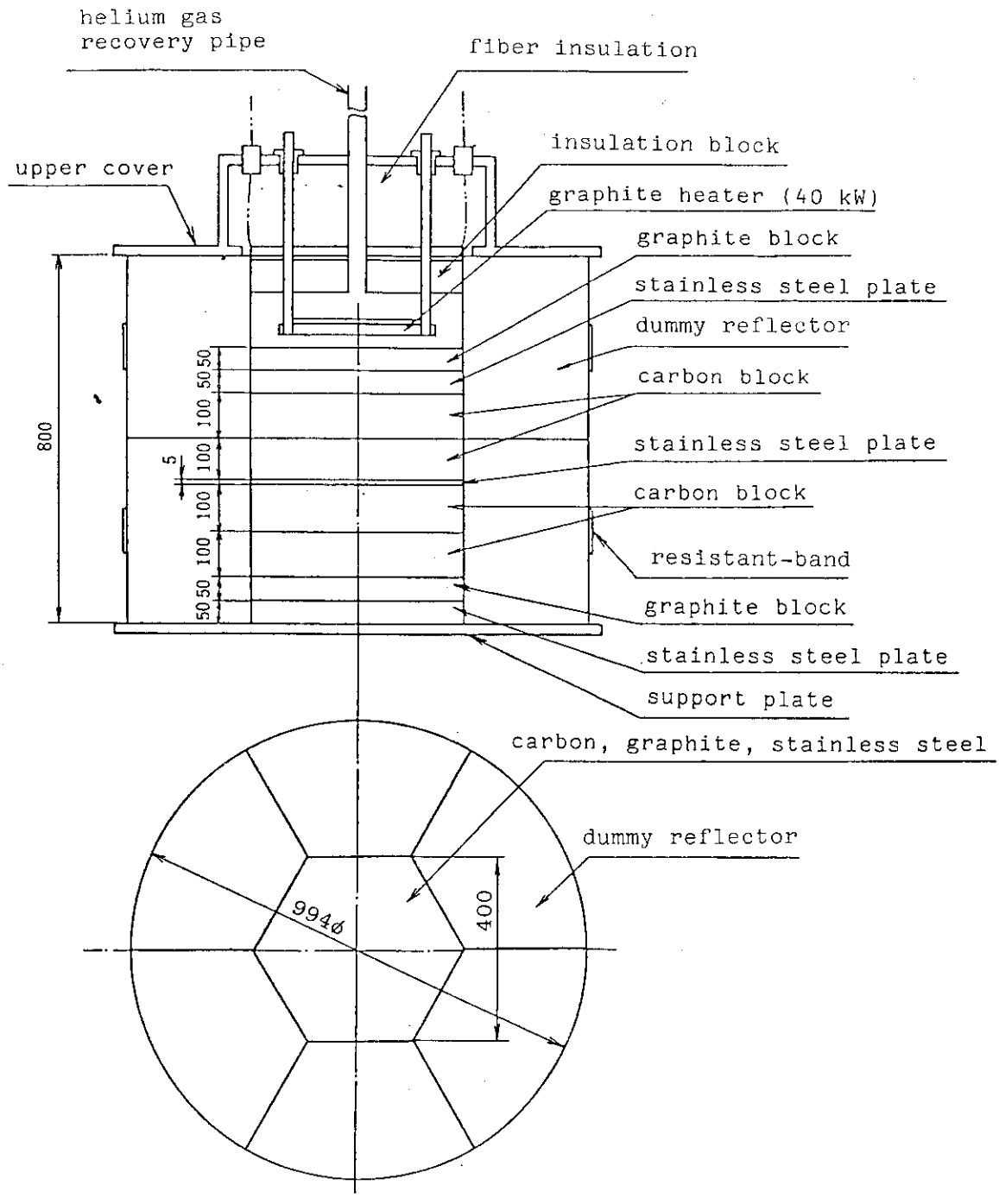

Fig. 1.40 The second test section of a bottom-core structure

1.10 Test of Hot Gas Valve for Pressure Control

Y. Mizokami, Y. Hoshi, Y. Inagaki, T. Tanaka and H. Shimomura

The objective of the test is to develop a hot gas valve for pressure control, which will be used in a bypass line of T_2 test section. A new type hot gas valve is now being manufactured and the test will be started in March, 1984.

(1) Test rig

A test rig consists of a valve disc, a valve sheet, a valve casing, internal thermal insulation, an electric heater and an actuator. Figure 1.41 shows the test rig.

The valve disc, the valve sheet and the stem guide are cooled by water. Helium gas is heated up to about 800°C by the heater in the valve casing. The axial load and shut-off time are controlled by the actuator.

(2) Test items

(a) Leakage performance test

This test is to study what factors affect the leakage ratio. The test conditions were as follows:

Pressure	max. 0.9 MPa
Temperature	max. 800°C
Axial load	max. 4 kg/mm^2 .

(b) Test in high-temperature environment

This test was carried out at a high-temperature of 800°C under a long-time operation.

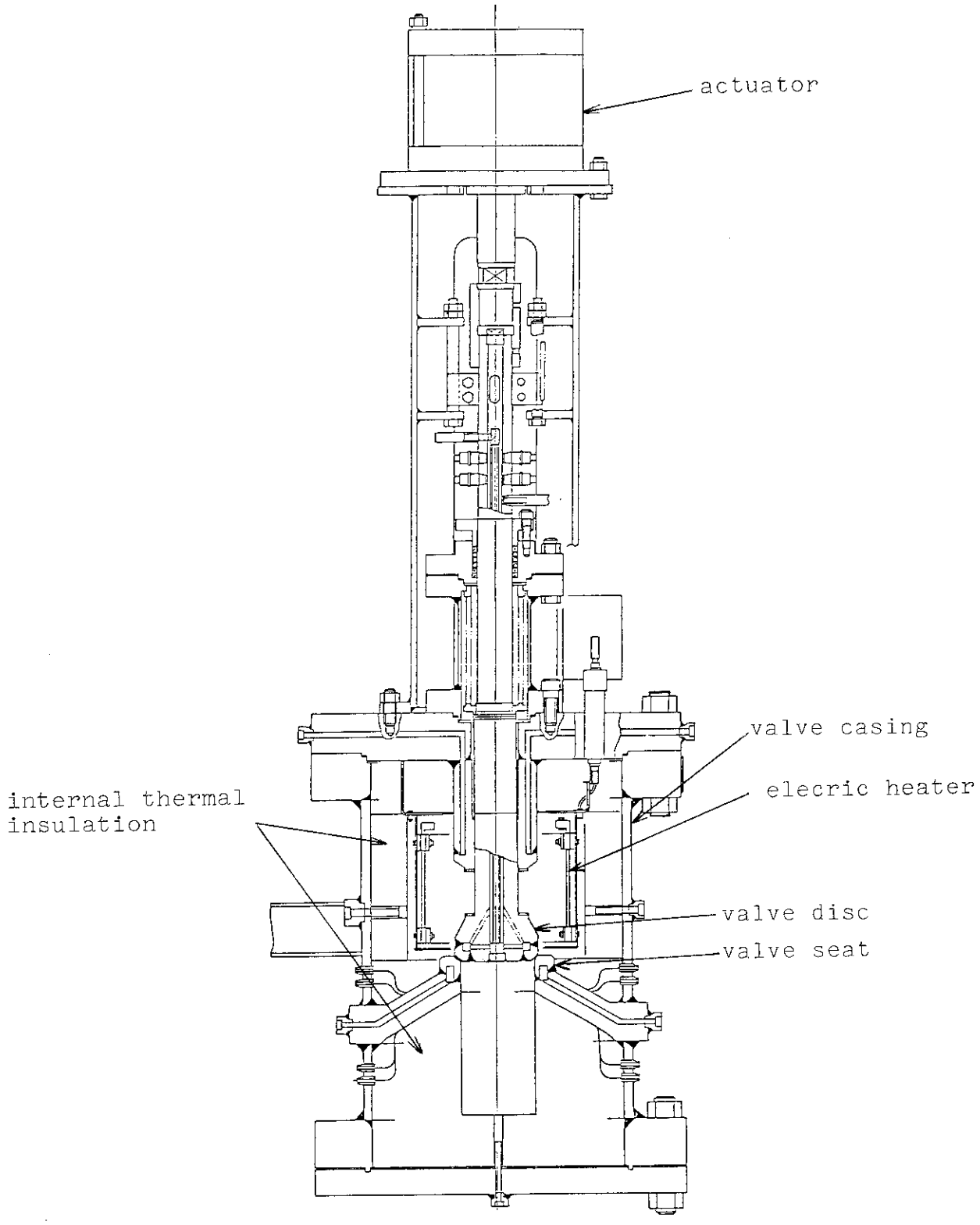

Fig. 1.41 Test rig of hot gas valve for pressure control

1.11 Thermal Insulation Test

I. Ioka, N. Zaima, M. Kato, M. Hishida and T. Tanaka

Hot gas ducts and heat exchangers in the VHTR are used in a high-temperature, high-pressure helium gas environment. In these components, thermal insulation is used in order to protect the pressure boundary from high-temperature and also to minimize the heat loss. Figure 1.42 shows a flowsheet of an apparatus for investigating characteristics of thermal insulation.

(1) Thermal insulation of ceramic fibre

Ceramic fibre is used as thermal insulation layer in the hot gas ducts of M+A section. The results in No.4 and No.5 cycle operations of HENDEL show that the performance of thermal insulation layer in the vertical tube of hot gas ducts is inferior to in the horizontal one. It may be due to a natural convection of helium gas in thermal insulation layer. The test items are as follows:

(a) Characteristics of effective thermal conductivity, and
(b) Integrity of thermal insulation.

(2) Castable thermal insulation

Castable thermal insulation is very attractive for hot gas ducts of the VHTR, because it is very easy to be manufactured and is possible to reduce the total cost of hot gas ducts.

In order to get various data about the castable thermal insulation, the following tests will be carried out.

(a) Sintering test : to obtain an amount of out-gas on sintering condition.
(b) Steady state test : to obtain a steady state characteristics and out-gas ratio.
(c) Material test.

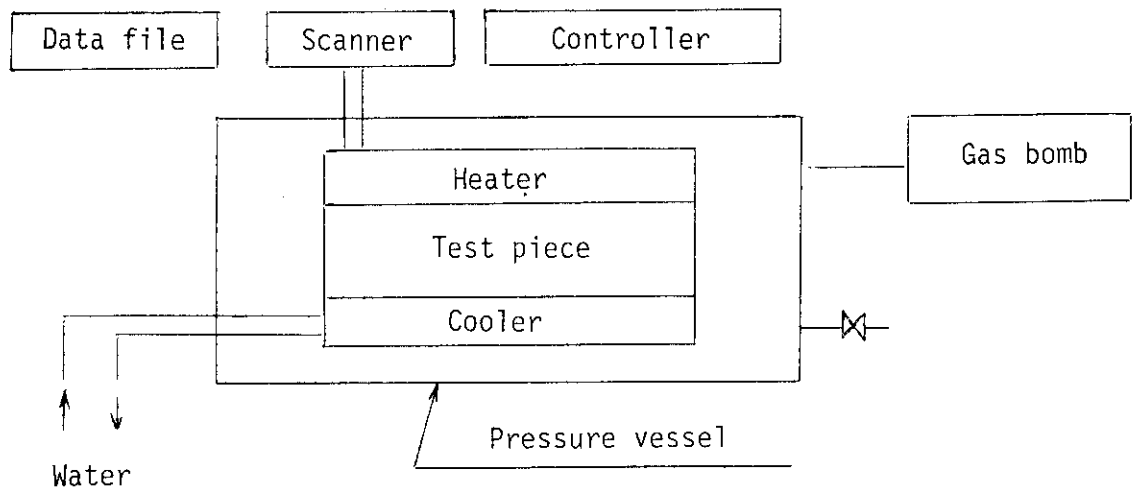

Fig. 1.42 Flow diagram of thermal insulation test

1.12 Test of Simulated Fuel Rod

S. Maruyama and M. Hishida

The main objective of this test is to investigate reliablity of temperature measurement of fuel rod surface.

Figure 1.43 shows a flowsheet of the test rig. The simulated fuel rod, which consisted of a metal-sheath heater and a graphite sleeve, was fabricated on the same principle as a moderate-temperature heater pin for T_1 test section. The graphite sleeve is the same shape of a fuel rod which is to be used in the VHTR.

(1) Test conditions and results

From April, 1982 to March, 1983, tests have been performed to study the influence of fitting conditions of thermocouples on the measurement of temperature. Test conditions and main specification of the simulated fuel rod are shown in Table 1.9, and a procedure of fitting thermocouples are as follows:

(a) Insert into a special groove whose shape is like an upside-down greek letter "ohm",
(b) Insert into a special groove same as that of (a), and filled the groove with ceramic cement at a part near the top of thermocouples,
(c) Insert into the same type groove and weld to metal pin,
(d) Set in a square groove and fill with ceramic cement, and
(e) Set in a square groove, fill with ceramic cement and weld to metal pin.

As no difference has been observed among these five cases, measurements made in the test of $T_{1\text{-}S}$ and $T_{1\text{-}M}$ test rigs are reliable.

(2) Further schedule

The influence of axial heat conduction is open to further investgation because the length of the rig was not long enough. Therefore we are planning to replace the pressure vessel by a new one to reduce this effect by the end of June, 1984.

The new test rig is different from the present one in the following respects:

(a) Measuring holes for hot wire anemometers are installed,

(b) Tests in the case when the simulated fuel rod is eccentrically located,

(c) Micro-heaters are installed on the outer wall of the vessel to study heat transfer characteristics on the wall of heated annular tube, and

(d) Heating length of the simulated fuel rod and flow channel are longer than the present ones.

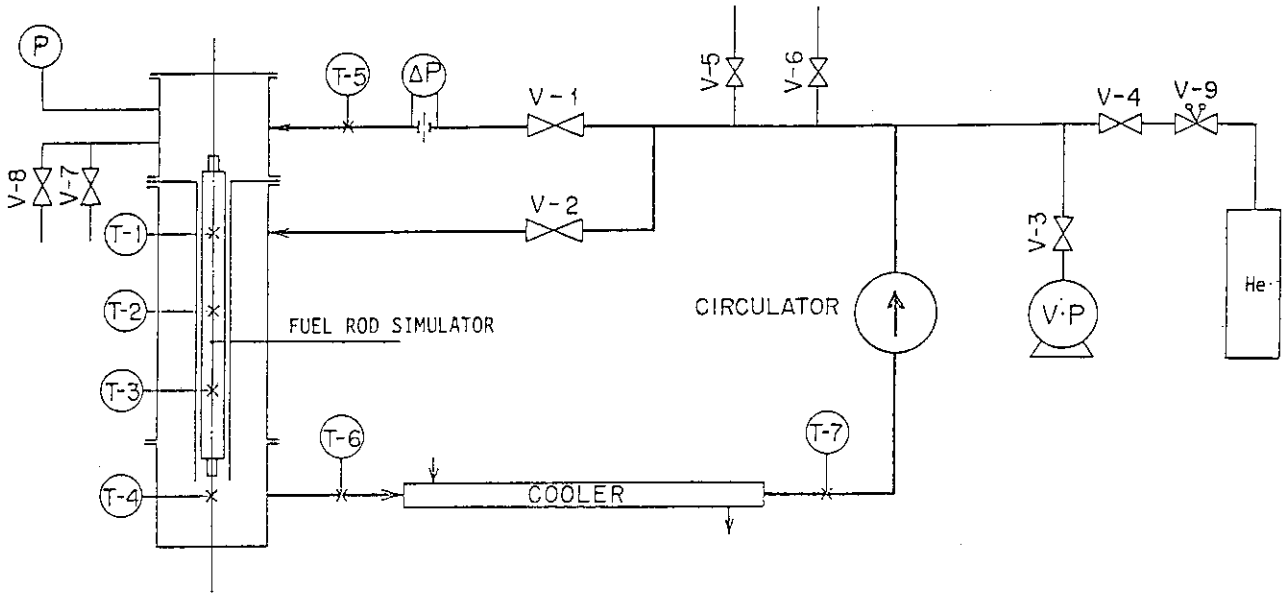

Fig. 1.43 Flowsheet of simulated fuel rod test

Table 1.9 Test conditions

Item	Condition
Annular channel	
Inner diameter	46 mm
Outer diameter	53 mm
Length	580 mm
Coolant	Helium gas
Inlet temperature	Room temperature
Pressure	0.1 MPa
Flow rate	0 ∿ 5.36 g/s
Heating conditions	
Maximum input	10 kW
Surface temperature	max. 1000°C
Heat flux distribution	Uniform

2. RESEARCH ON THERMAL STRUCTURE

2.1 Crossflow Test

T. Takizuka, H. Kaburaki, T. Kunugi, K. Hashimoto* and Y. Muto

The core of the VHTR is constructed with a large number of fuel blocks. Although most primary coolant flows downward through annular coolant channels of fuel blocks, some coolant bypasses through the gaps between blocks. At block interfaces, clearances are produced by non-uniform dimensional changes of graphite owing to thermal expansion and irradiation. The leakage flow through the interface is called crossflow. Crossflow decreases the effective flow rate necessary for sufficient cooling of the VHTR core.

In order to investigate crossflow characteristics, two crossflow tests were conducted. One was a two-block test to determine total crossflow rate and crossflow distribution among coolant channels, the other was a one-column test to study flow distribution in a fuel column and bypass gap. This report describes the two-block crossflow test.

Apparatus

Figure 2.1 shows a schema of two-block crossflow test model. Two full-scale graphite test blocks are vertically stacked in a test rig and are surrounded by a shroud which serves to control bypass pressure. Air at room temperature and at atmospheric pressure is used as fluid. The maximum pressure difference between coolant channel and bypass gap, which is produced by a blower, is 0.2 kg/cm^2. Total crossflow rate through the interface gap was measured by laminar flow meters in a bypass duct connected to the shroud. Crossflow rate in each channel is calculated by the difference of the flow meters at the inlet and outlet ducts. A graphite block deformation was simulated by inserting a shim between two test blocks. Parallel gap and wedge-shaped gap models were tested with gap width varied from 0.03 mm to 2.0 mm. Figure 2.2 shows a type I fuel block used in the test.

---

* Kawasaki Heavy Industries, Ltd.

Result

The results were correlated by a crossflow loss coefficient factor K/A^2 [m^{-4}] and Reynolds number Re. The crossflow loss coefficient factor for one block interface is defined by the following equation.

$$\frac{K}{A^2} = \frac{2\rho\Delta p}{M^2} , \qquad (2.1)$$

where Δp : pressure difference, M : crossflow mass flow rate, ρ : fluid density.

Reynolds number at the outer edge of block interface is defined as

$$Re = \frac{4M}{\mu L} , \qquad (2.2)$$

where L : wetted perimeter, μ : fluid viscosity.

Figure 2.3 shows crossflow loss coefficient factors as a function of Reynolds number in the case of parallel gap. In this figure, parameter δ indicates a gap width. It can be seen that crossflow loss coefficient factors decrease with increase in gap width. In a range where Reynolds number is small, crossflow loss coefficient factors are nearly in inverse proportional to Reynolds number. On the other hand, in a range of high Reynolds number, crossflow loss coefficient factors take almost constant values independently of Reynolds number.

A typical result of crossflow distributions among coolant channels is shown in Fig. 2.4. In this case, crossflow mostly goes into the outer coolant channels (Channel No. 1 - 6).

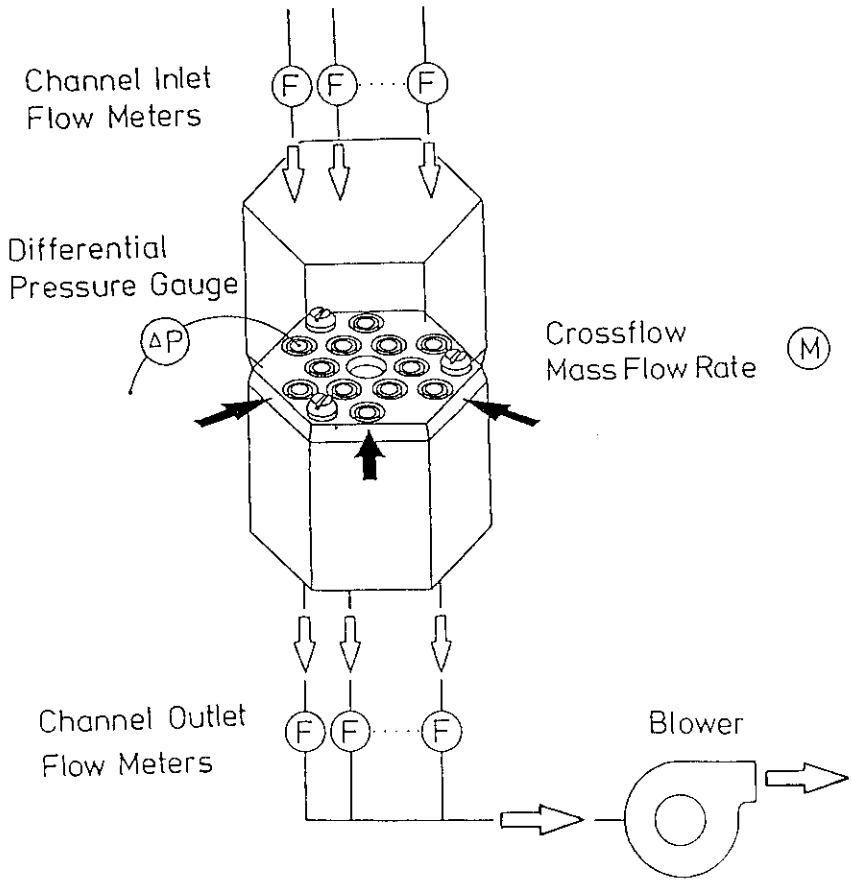

Fig. 2.1 Schema of two-block crossflow test model

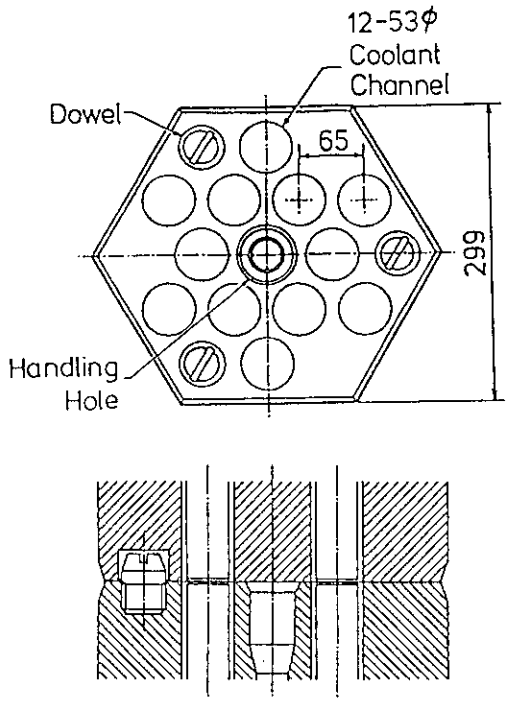

Fig. 2.2 Type I fuel block

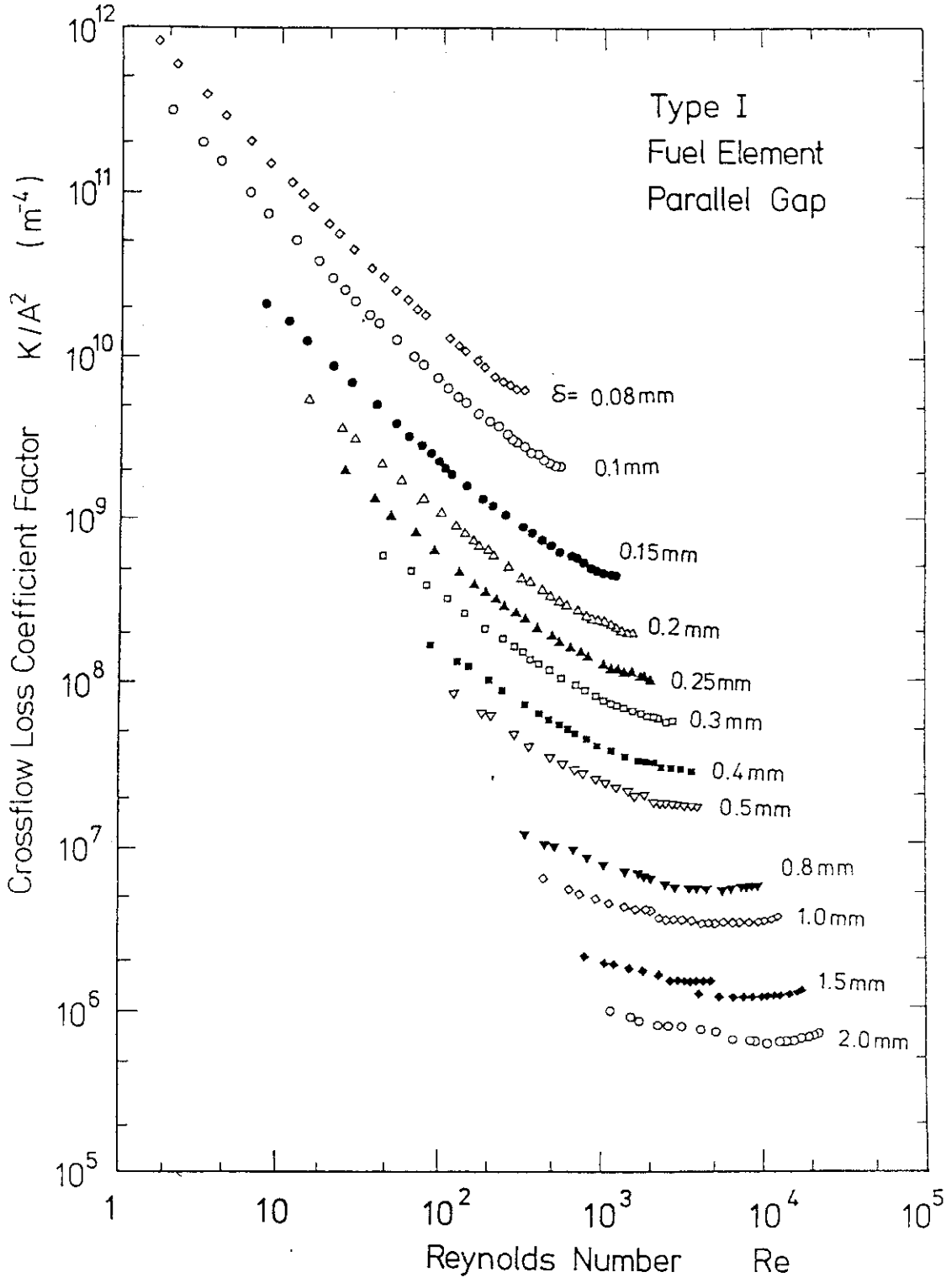

Fig. 2.3 Crossflow loss coefficient factors as a function of Reynolds number in parallel gap case

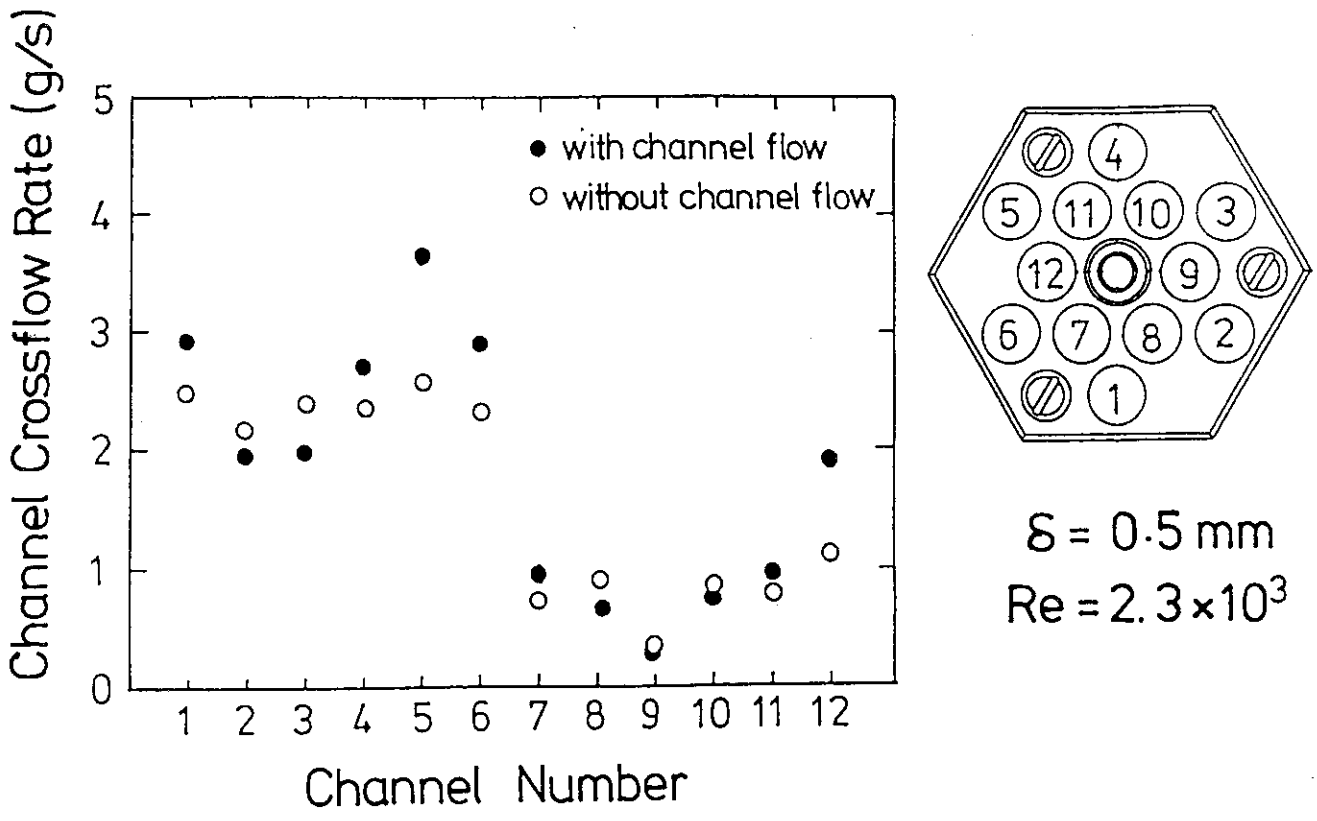

Fig. 2.4 Crossflow distribution between coolant channels

2.2 Numerical Analysis on Crossflow

H. Kaburaki, H. Hashimoto*, T. Takizuka and T. Kunugi

Two-block crossflow tests on type I fuel block have been carried out under various conditions of pressure difference and interface gap. Overall crossflow loss coefficient factors, which describe the average pressure loss for one fuel element interface, were evaluated from the experiments. A model is devised to predict quantitatively detailed crossflow characteristics. Crossflow loss coefficient between parallel gaps of type I fuel block was obtained and compared with the result of the experiment. The obtained correlation was found to predict well the data.

The crossflow is modeled as a two-dimensional flow between parallel planes with a gap width δ, as shown in Fig. 2.5. The two-dimensional pressure distribution between parallel planes, $p = p(x,z)$, is expressed by a quasi-harmonic equation.

$$\frac{\partial}{\partial x}\left(G\frac{\partial p}{\partial x}\right) + \frac{\partial}{\partial z}\left(G\frac{\partial p}{\partial z}\right) = 0 \quad , \tag{2.3}$$

where G denotes a viscosity correction factor. If we assume that the flow is turbulent and fully-developed, G is expressed by the following integral:

$$G = \int_0^1 d\eta \int_0^\eta \frac{(\frac{1}{2} - \eta')}{d(\eta')}\, d\eta' \quad , \tag{2.4}$$

where

$$f(\eta') = 1 + \kappa[h_c^+\eta - \delta_\ell^+ \tanh(\frac{h_c^+}{\delta_\ell^+}\eta)]$$

$$h_c^+ = \frac{\delta}{\nu}\sqrt{\frac{\tau_w}{\rho}} \quad , \quad \tau_w = \sqrt{(\frac{\partial p}{\partial x})^2 + (\frac{\partial p}{\partial z})^2} \quad ,$$

where ν is kinematic viscosity and ρ is density. The optimum values 0.4 and 10.7 are used for κ and δ_ℓ^+ respectively. To derive Eq. (2.4), we use

---

* Kawasaki Heavy Inductries, Ltd.

the Reichardt formula which describes the entire velocity profile in the wall region. When the flow is laminar, the value of G reduces to 1.

The pressure assumes the constant values at the two boundaries. Thus, let $p = p_0$ along the external boundary of the block interface, and $p = p_i$ along the internal boundary of fuel element holes (Fig. 2.6). The Neumann condition is applied around the dowel. The area is discretized into about 1000 triangular elements as shown in Fig. 2.7 and pressure distribution p is calculated from Eq. (2.3) by the finite element method. The results of the calculation are shown in Figs. 2.8 (a) and (b). In these figures, the pressure difference between the channels and the external boundary of the fuel element is normalized to be unity. The mass flow rates M_x and M_z in the x and z directions are calculated by the following formulas.

$$M_x = -G \frac{\delta^3}{\nu} \frac{\partial p}{\partial x}$$

$$M_z = -G \frac{\delta^3}{\nu} \frac{\partial p}{\partial z} \qquad (2.5)$$

Crossflow loss coefficient factors are thus evaluated as a function of Reynolds number and gap width. Numerical results are shown in Fig. 2.9 by solid lines and predict well the experimental data.

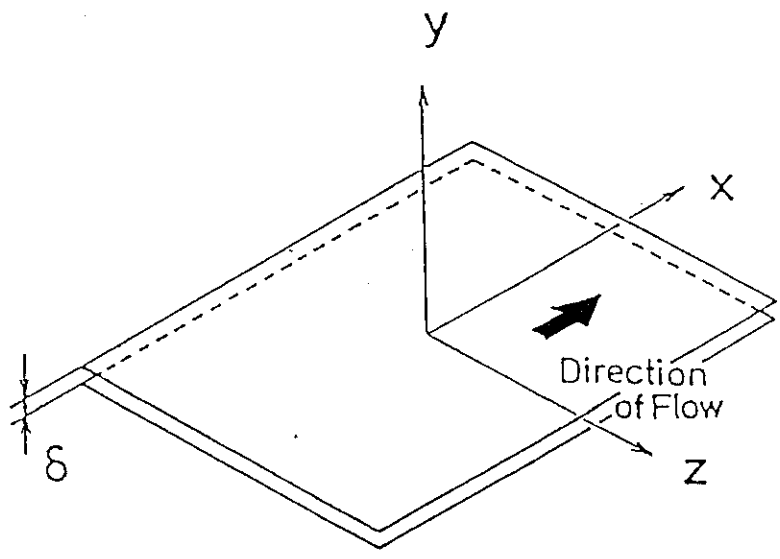

Fig. 2.5 Flow between parallel planes

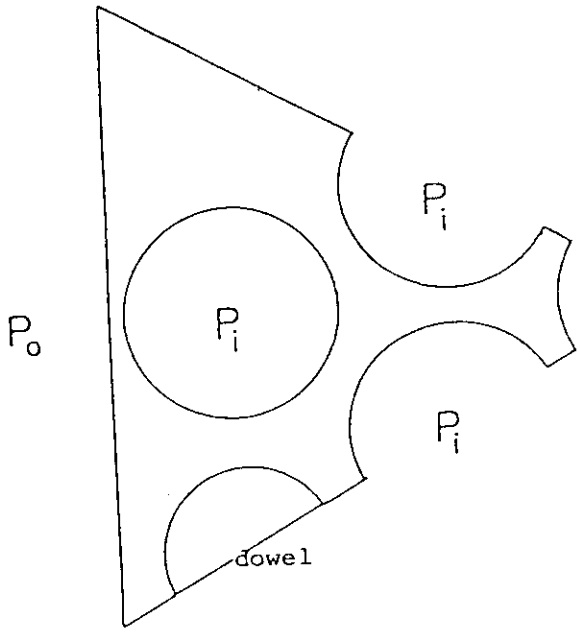

Fig. 2.6 Boundary condition

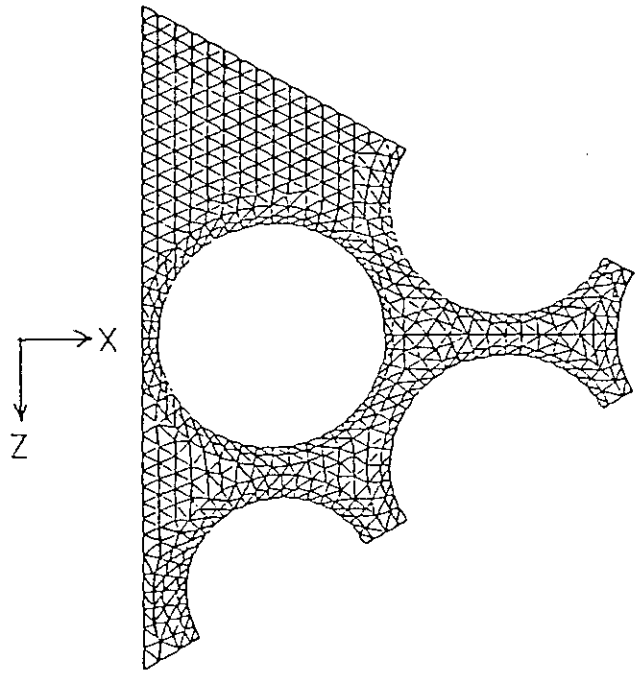

Fig. 2.7 Finite element discretization

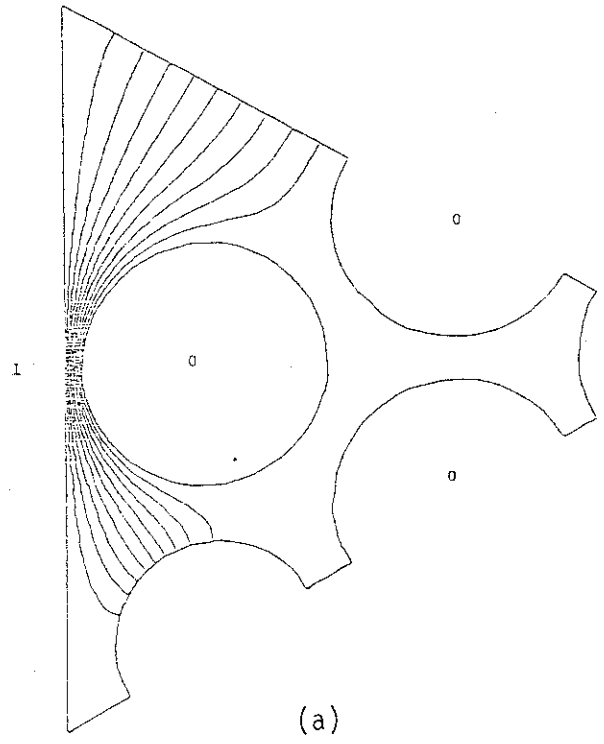

(a) Small Reynolds number region (Laminar flow)

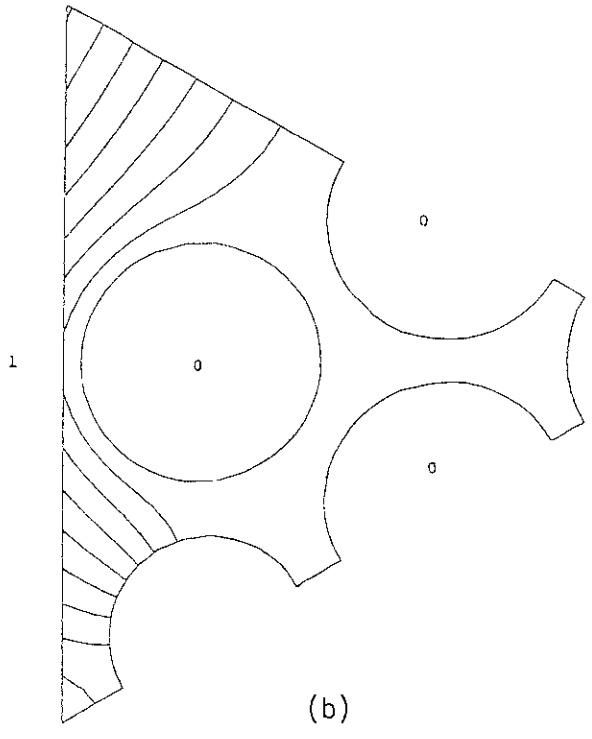

(b) Large Reynolds number region (Gap width=1.0mm, Re= 5600)

Fig. 2.8 Pressure distributions

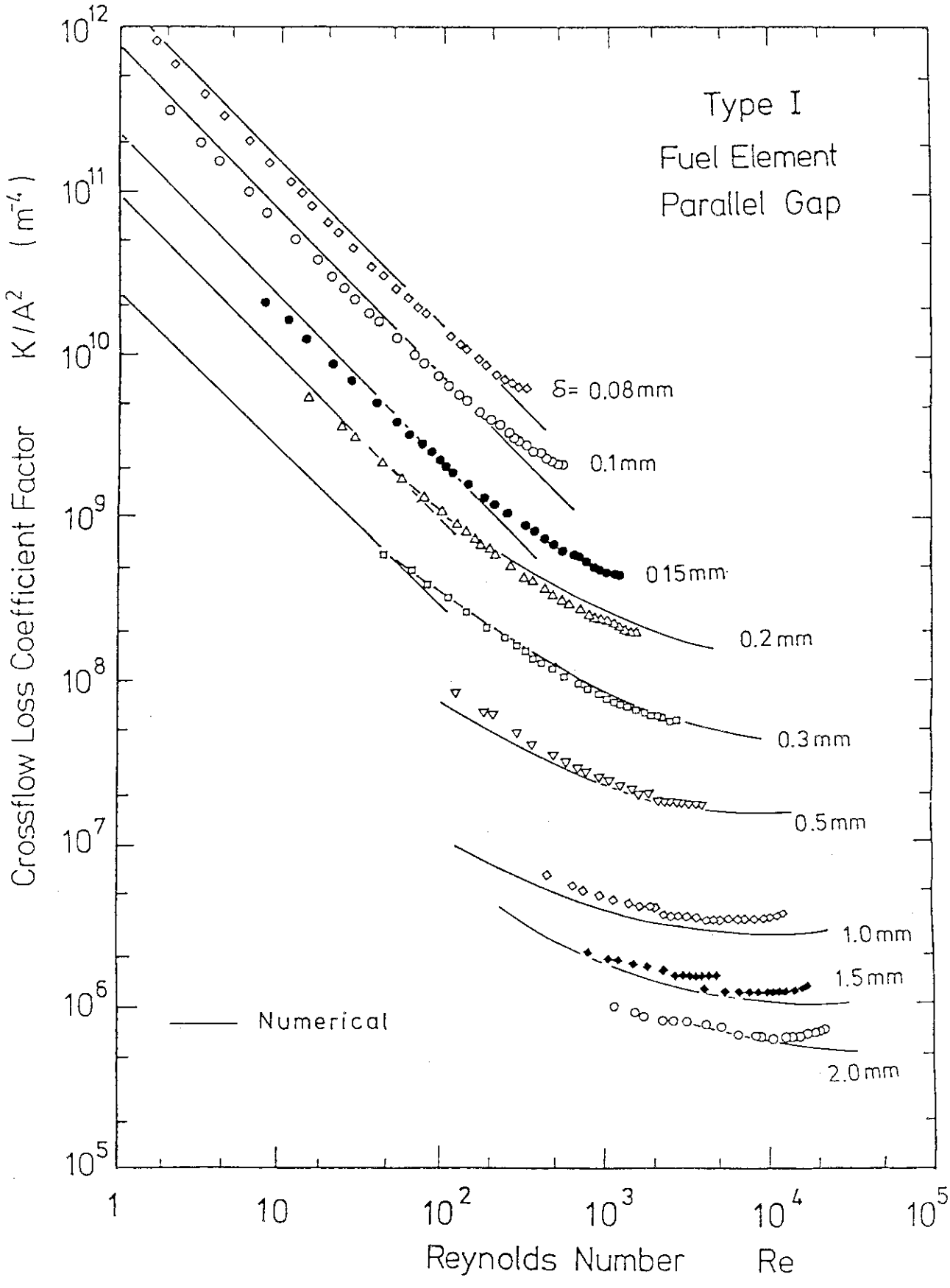

Fig. 2.9 Crossflow loss coefficient factor

2.3 Leakage Flow in Bottom-core Structure

K. Kikuchi, M. Futakawa and Y. Muto

The temperature of fuel elements and the thermal stress of hot plenum blocks are supposed to be unexpectedly so large that the reduction in in-core coolant flow rate owing to leakage flow into a hot plenum region becomes unfavorable to the core-cooling of the VHTR[1]. Hot plenum blocks and fixed reflectors are tightened to narrow the block gap distance between blocks by core-restraint mechanism surrounded outside of the fixed reflectors, and seal elements are placed in the gaps in order to reduce leakage flow rate. A relationship between core restraint force and block gap, which is derived from the experiments with a 1/2.75-scale model of the bottom-core structure, was obtained.

The effects of core restraint force on the block gap between the hot plenum blocks are represented in Fig. 2.10. Block gap distribution in a range of $0 \sim 0.05$ mm shows almost constant when the core restraint force becomes 3.2×10^3 N, and no increase is shown even when the core restraint force increases. The maximum block gap in a range where core restraint force is larger than 3.2×10^3 N is 0.15 mm. Whereas, in the case of block gap between hot plenum block and fixed reflector, a peak does not appear, and the values of the gap lie in a range of $0 \sim 0.5$ mm independently of the core restraint force, as shown in Fig. 2.11. The result shows that the core-restraint mechanism are effective in tightening of hot plenum blocks, but ineffective in tightening between hot plenum blocks and fixed reflectors.

The reason may be attributed to the difference of friction forces acting on both hot plenum blocks and fixed reflectors, and this allows them to move. Actually fixed reflectors do not slide easily because of large sliding friction force either against fixed reflector or against support plate. On the contrary, hot plenum blocks move easily because of very small friction force due to rolling contact with support post. Consequently, hot plenum blocks are easily constrained by some fixed reflectors which are in contact with them, but the other fixed reflectors are able to be protruded uneasily toward the center by core-restraint mechanism.

Reference

1) JAERI: The present status of experimental very high-temperature gas-cooled reactor research and development, (1983).

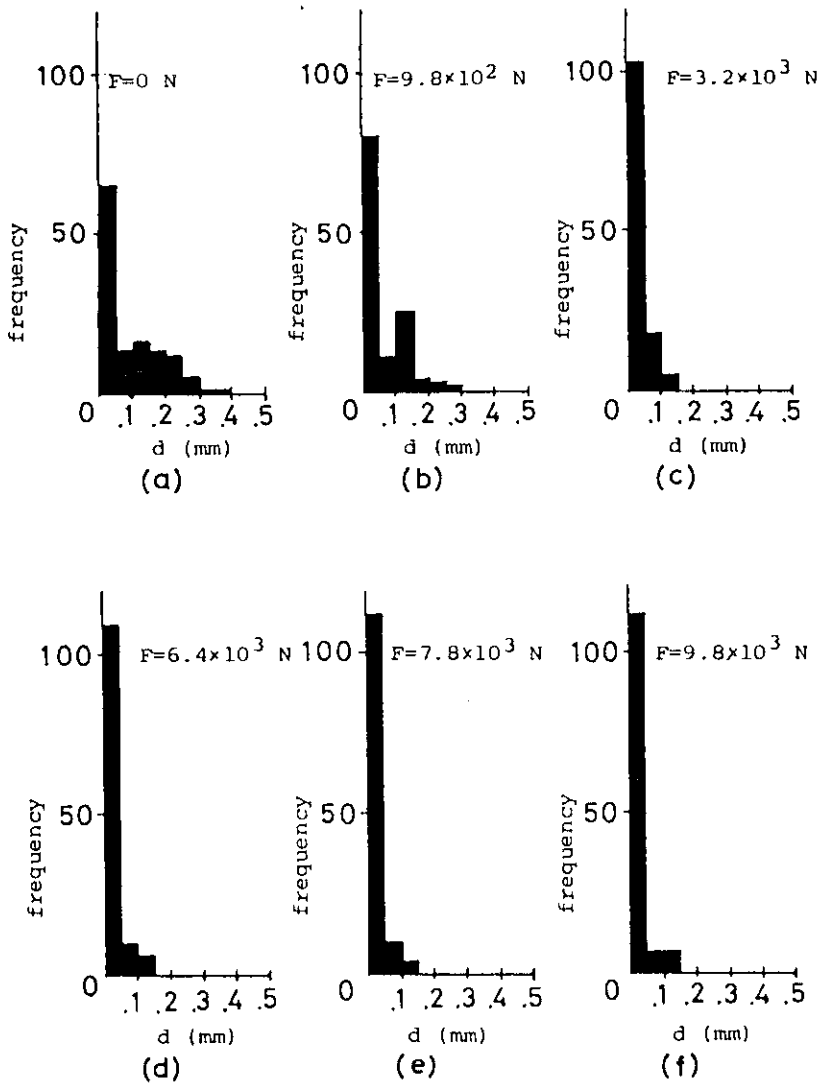

Fig. 2.10 Distributions of gaps between the side-surfaces of hot plenum blocks

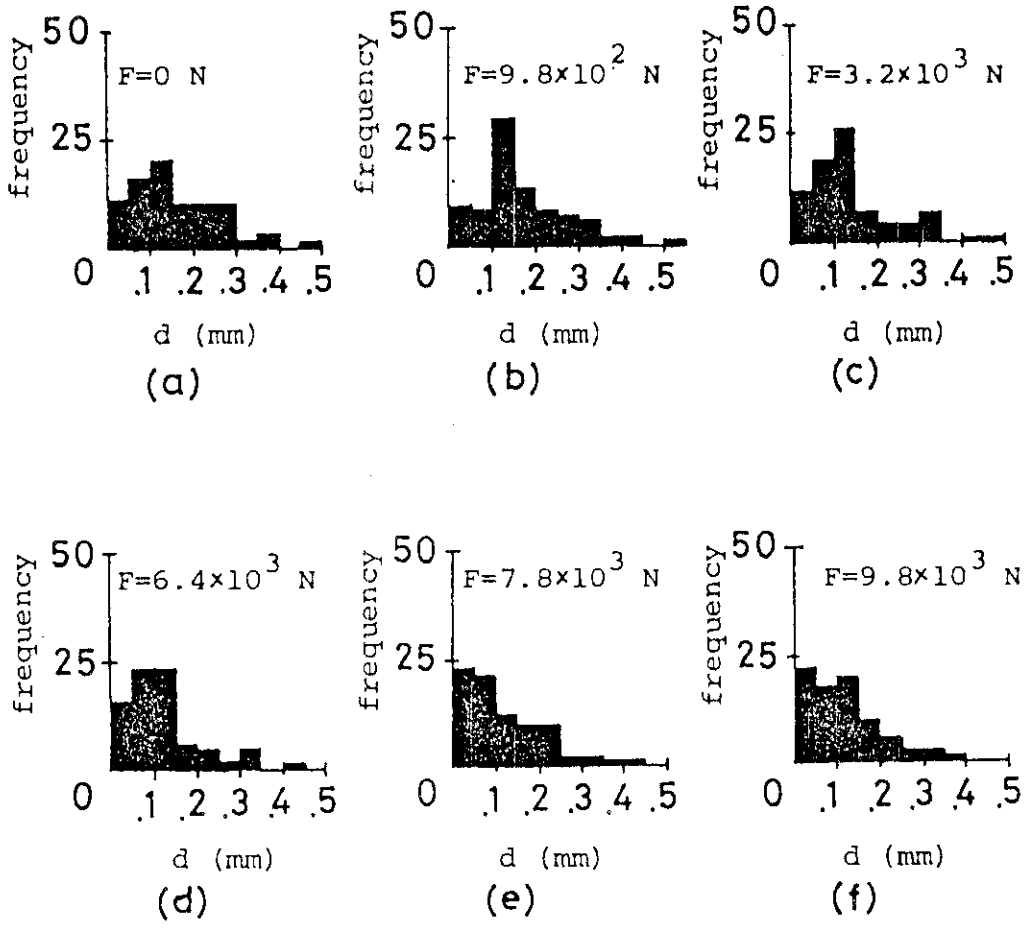

Fig. 2.11 Distributions of gaps between the side-surfaces of hot plenum block and fixed reflector

2.4 Seal Element Leakage Flow Tests

H. Kaburaki, T. Takizuka and Y. Muto

The analysis of flow distribution in the core suggests that crossflow, gap flow between columns and leakage flow through gaps between side-reflectors have a significant effect on the temperature and stresses of fuel element. In the VHTR design, a graphite plate is placed as a seal between hot plenum blocks to reduce the above-mentioned leakage flow. In order to verify the leakage flow characteristics of seal, full-scale seal element tests are to be conducted. A test section is shown in Fig. 2.12. An air and helium gas flow test loop, which supplies pressurized gas to the test section, is under construction. The specifications of the test loop are as follows:

Flow rate of helium gas	5 g/s
Pressure Drop	∿10 kPa
Pressure	0.1 - 0.9 MPa
Temperature	20 - 500 °C .

Leakage flow tests will be carried out at room temperature under atmospheric or pressurized conditions by using air or helium gas as working fluid. The heater is provided for heating hot plenum blocks to study the effects of the temperature difference between seal (∿500°C) and gas (∿20°C) on leakage flow characteristics. Moreover, the effects of thermal-cycling on leakage flow characteristics are to be studied.

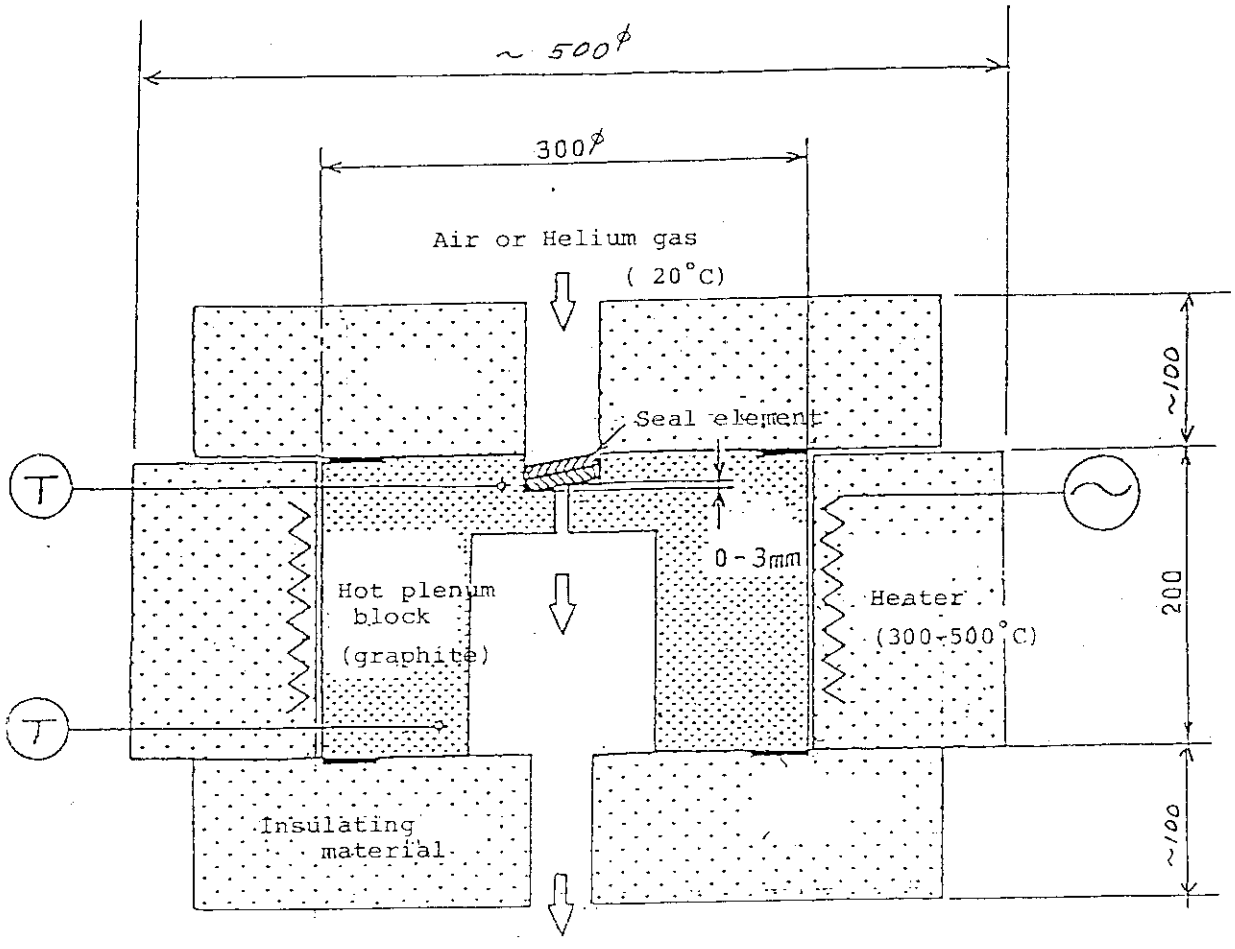

Fig. 2.12 Test section

2.5 Preliminary Thermal Mixing Test

T. Kunugi, H. Kaburaki, T. Takizuka and K. Tachibana

Core flow distribution in the VHTR is adjusted by 19 inlet orifice valves which are placed at the top of each core region. These valves are controlled by measuring coolant temperature at each core region outlet. The primary coolant through the cooling channels of each column flows downward and comes together into a mixing cavity of each plenum block. The coolant temperature is measured by a temperature sensor installed within the cavity. To prevent hot streaks, it is required to make the core region outlet temperature uniform. Therefore it is considered to be indispensable to obtain the fundamental characteristics of coolant mixing in the cavity.

The objective of this preliminary thermal mixing test is to clarify the characteristics of two-jet mixing in the cavity and to obtain a prefereable configuration for good thermal mixing.

Experimental results and discussions

A temperature influence coefficient defined by ambient temperature t_c (unheated jet temperature at a nozzle outlet) as a reference temperature is:

$$T = (t - t_c)/(t_h - t_c) \quad , \tag{2.6}$$

where t denotes measured local temperature, t_h is heated jet temperature at a nozzle outlet.

In order to evaluate the mixing in the cavity, a standard deviation using a mean temperature at each horizontal cross-section of the cavity is important and is defined by

$$\sigma = \left\{ \frac{\int_0^{2\pi} \int_0^R \left(\frac{T}{T_z} - 1\right)^2 r\,dr\,d\psi}{\pi R^2} \right\}^{\frac{1}{2}} \quad , \tag{2.7}$$

where T_z is a mean temperature at each horizontal cross-section:

$$T_z = \frac{\int_0^{2\pi} \int_0^R T\, r\,dr\,d\psi}{\pi R^2} \quad . \tag{2.8}$$

Note that R is a cavity radius, r and ψ are radial and circumferential coordinates with respect to the cavity respectively.

1) Characteristics of thermal mixing in the cavity

A standard deviation σ is varied with a ratio of two-jet volumetric flow rate Q_R for the nozzle angle ranging from 30°to 90°, as shown in Figs. 2.13 and 2.14. Large variations in the standard deviation found in a range of $Q_R < 1$, and this clearly shows that two-jet streams are interacted strongly in this range.

In view of the objectives of the test and the contributions to the VHTR design, the results in a range of $Q_R > 1$ are more important to be discussed.

The standard deviation decreases with increase in nozzle angle and also in length L from the center of heated jet nozzle outlet, and decreases with decrease in length L_0/D between nozzle outlets ranging from 1.45 to 0.08, as shown in Figs. 2.15 and 2.16. It seems that 60°and 90° nozzle angles are preferable for good thermal mixing.

In 60° nozzle angle, thermal mixing increases with increase in nozzle diameter ratio d_R ($d_R = d_h/d_c$; d_h and d_c are the diameters of heated and unheated jet nozzle outlets respectively), as shown in Fig. 2.16. It seems that $d_R = 1.84$ gives good thermal mixing.

2) Deflection angle of merged jet after impingement of two jets

Two turbulent circular jets impinge with a nozzle angle θ and a merged stream after impingement grows into a deflected jet, as shown in Fig. 2.17.

From the momentum balance on the deflected jet axis, a deflected jet angle β is expressed by

$$\beta = \arctan \{\sin\theta/(\cos\theta + J_R^{-1})\} , \qquad (2.9)$$

where J_R denotes a ratio of the momentum of heated jet to that of unheated jet.

Figures. 2.18 and 2.19 show the contour lines of temperature influence coefficients on the vertical cross-section of the cavity. Most of the experimental results are in good agreement with the calculared ones.

3) Experimental relationship of axial variation in mean temperature of the cavity

The mean temperature at each cross-section of a mixing cavity is varied linearly with length L, as shown in Fig. 2.20.
The mean temperature at any cross-section of the cavity can be expressed by

$$T_z = T_{zp} + n \log(L/L_p), \qquad (2.10)$$

where T_{zp} denotes a mean temperature at the point of two-jet impingement, n denotes a slope of each solid line in Fig. 2.21, and L_p denotes a length between the heated jet outlet and the impingement point.

Figure 2.21 shows a relationship between n and $T_m - T_{zp}$, where T_m is a mixed mean temperature, and the data were correlated by a linear equation:

$$n = k(T_m - T_{zp}). \qquad (2.11)$$

The coefficient k was derived by means of the least square method for each angle, and was correlated by an equation of 3rd degree, as shown in Fig. 2.22.

$$k = 11.51 - 0.5658\theta + 0.010278^2 - 0.000063\theta^3. \qquad (2.12)$$

By substituting Eqs. (2.11) and (2.12) into Eq. (2.10), an equation for predicting mean temperature variation of the mixing cavity can be obtained.

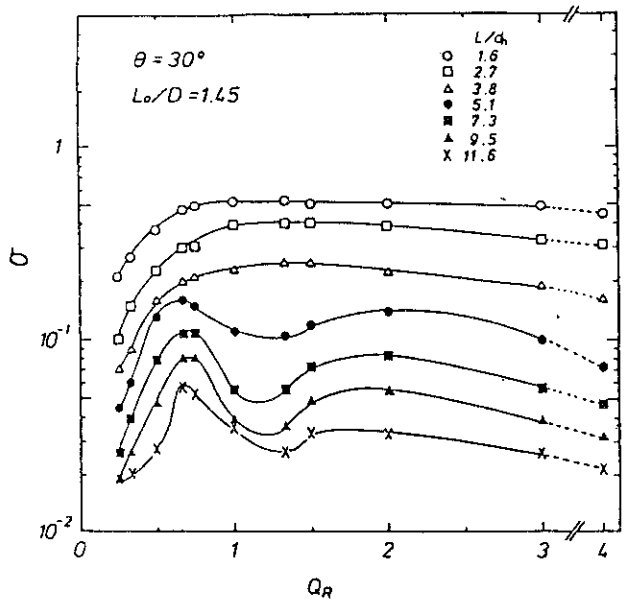

Fig. 2.13 Effect of L/d_h on standard deviation at nozzle angle 30°

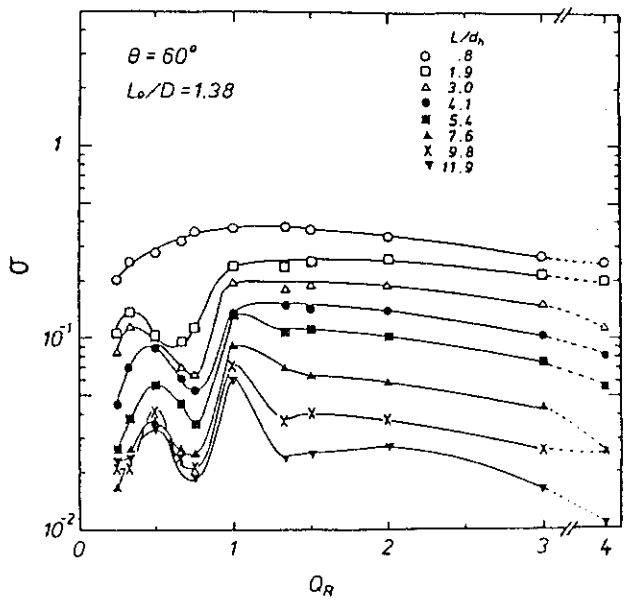

Fig. 2.14 Effect of L/d_h on standard deviation at nozzle angle 60°

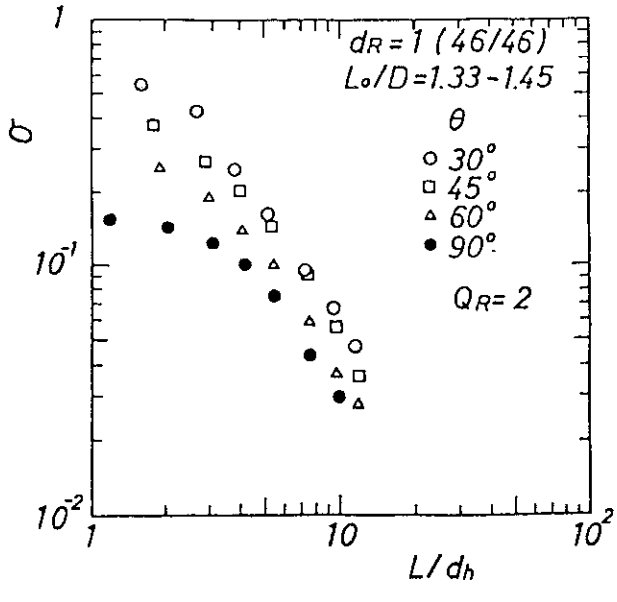

Fig. 2.15 Effect of nozzle angle on standard deviation

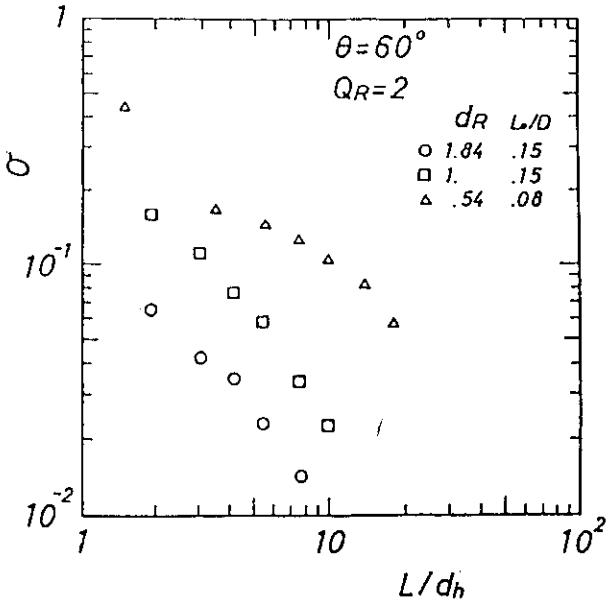

Fig. 2.16 Effect of d_R and L_0/D on standard deviation

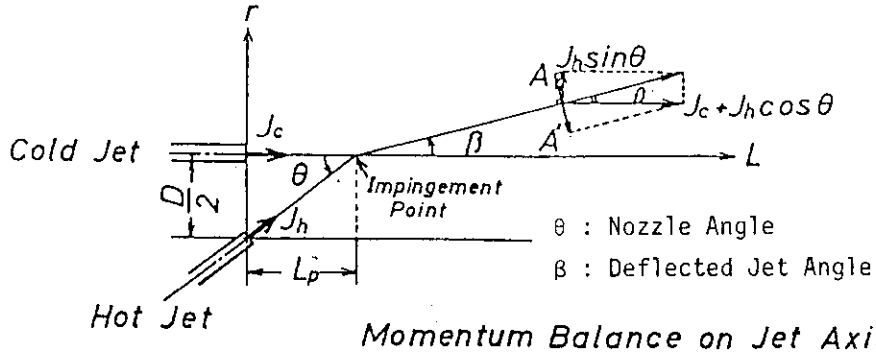

Momentum Balance on Jet Axis

$$A = A'$$

$$J_h\sin\theta\cos\beta = (J_c + J_h\cos\theta)\sin\beta$$

$$\therefore \quad \beta = \tan^{-1}(\sin\theta / (1/J_R + \cos\theta))$$

in which $J_R = J_h / J_c$

Fig. 2.17 Schematic representation of two-jet impingement

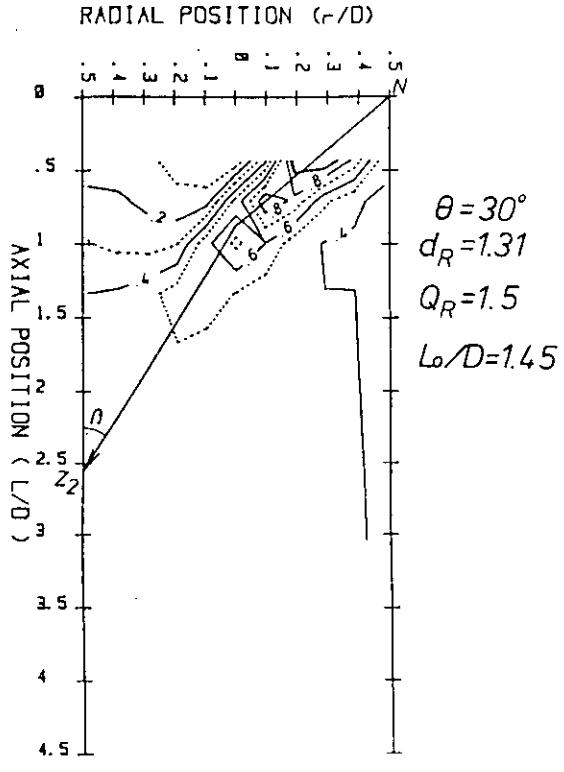

Fig. 2.18 Contour lines of temperature influence coefficients and a deflected jet angle β at nozzle angle 30°

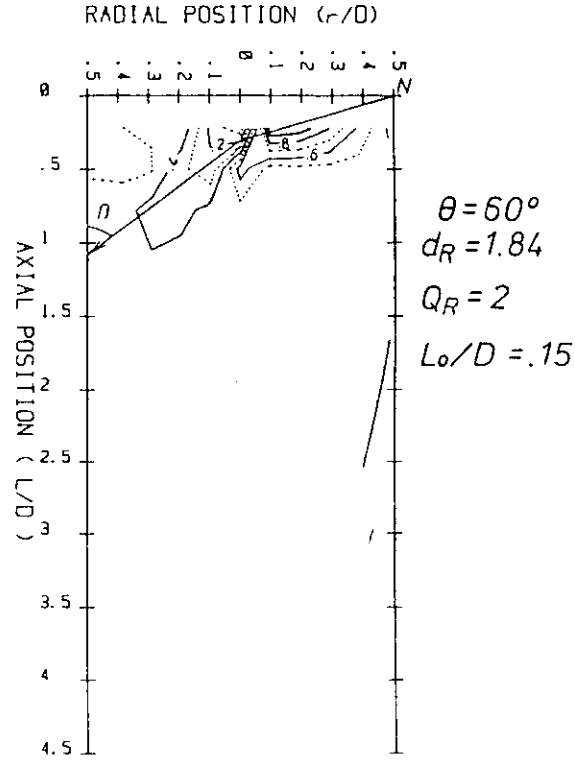

Fig. 2.19 Contour lines of temperature influence coefficients and a deflected jet angle β at nozzle angle 60°

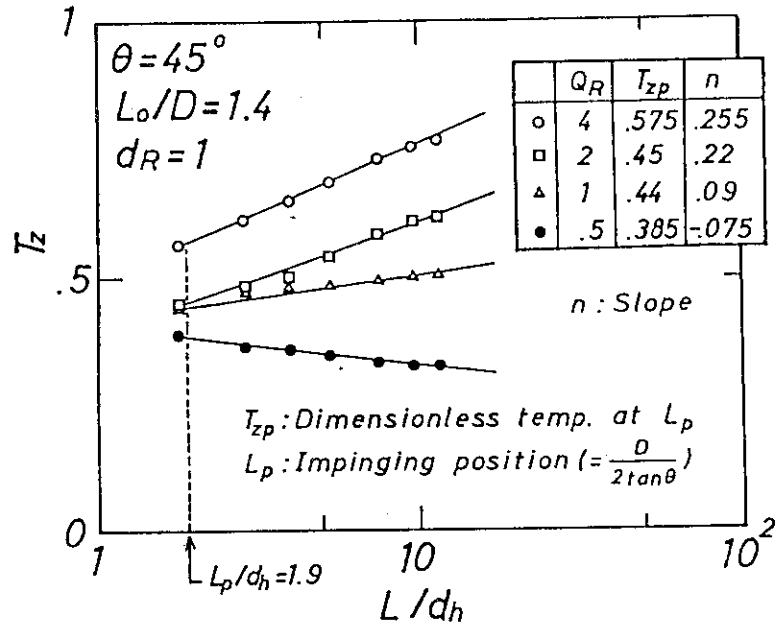

	Q_R	T_{zp}	n
○	4	.575	.255
□	2	.45	.22
△	1	.44	.09
●	.5	.385	-.075

Fig. 2.20 Mean temperature at horizontal cross-section of a cavity as a function of L/d_h

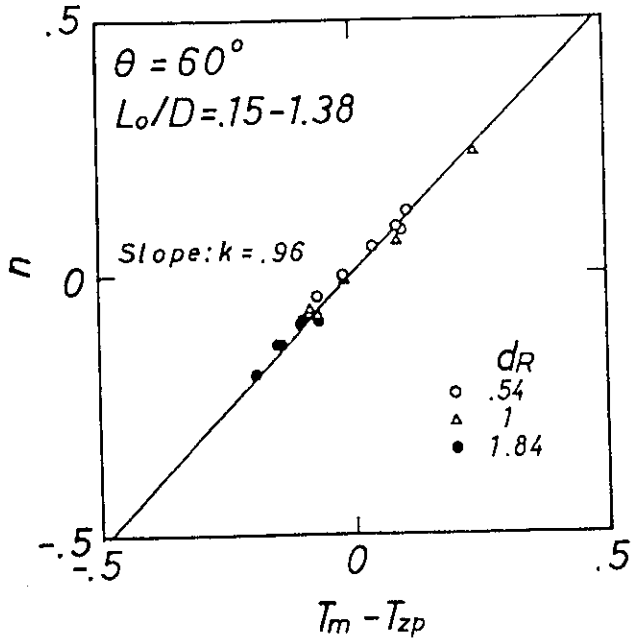

Fig. 2.21 Relationship between n and $T_m - T_{zp}$

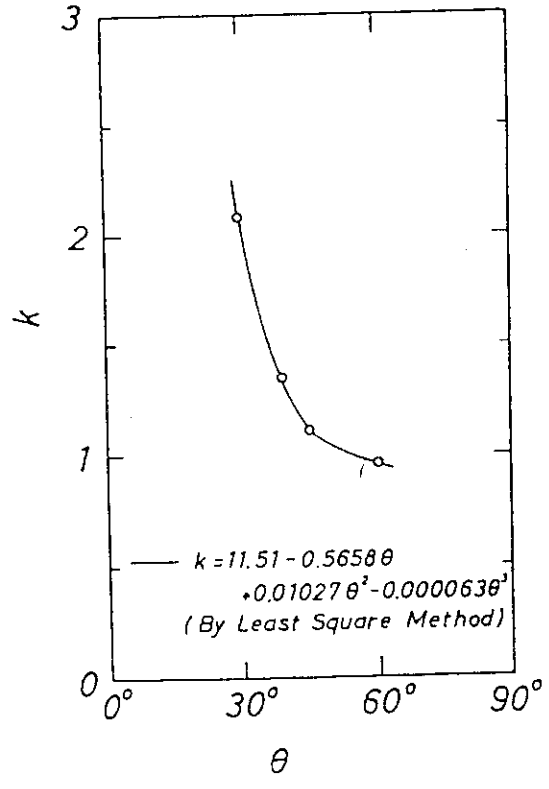

Fig. 2.22 Relationship between k and nozzle angle

2.6 Dynamical Characteristics of Coaxial Double-pipe Structure

M. Futakawa, K. Kikuchi and Y. Muto

A coaxial double-pipe structure is to be used in the main and auxiliary primary coolant systems of the VHTR, and consists of an inner pipe, an outer pipe and internal thermal barrier components such as insulation layers, liner pipes and so on. The inner pipe is supported by spacers which are placed circumferentially and axially aginst the outer pipe to form an annular channel.

The objective of this experiment is to study the effect of an axial pitch of spacers on the dynamical characteristics such as natural frequencies, vibrational modes and damping factors of coaxial double-pipe structure.

Two kinds of test models of coaxial double-pipe structure were fabricated: one is called a straight type model which is composed of only a straight pipe, 4.5 m in length, and the other an elbow type model which is composed of both two straight pipes, 1.5 m in length and an elbow pipe, 1 m in radius curvature, as illustrated in Fig. 2.23.

The inner pipe is supported against the outer pipe by so-called bolt-type spacers which are fixed to the outer pipe and in contact with the inner pipe at the ends. Two kinds of experiments: the test of a straight type model under a condition that the outer pipe is simply supported, and the test of an elbow type model under a condition that the outer pipe is fixed; were conducted. Furthermore, the fibrous insulation of 0.2 g/cm^3 in density was inserted in the inner pipe to study the effect of its weight.

The natural frequencies and vibrational modes of these models were obtained by hammering to measure acceleration against the impact force.

For the analysis of dynamical characteristics of coaxial double-pipe structure, as shown in Fig. 2.24, a parallel-beam type model, which simulates inner and outer pipes, is recommended. In computation, the weight of insulation was added to that of inner pipe beam. The SAP-V code was used to calculate the natural frequencies and vibrational modes.

Consequently, only the results in an elbow type model are shwon in this report, because no significant difference between the dynamical characteristics of an elbow type model and that of a straight type model

was found. Table 2.1 summarizes the natural frequencies at each mode of experimental and analytical results of an elbow type model. The analytical results are in good agreement with experimental ones and the insulation in the inner pipe shows the slightly lower natural frequencies. Natural frequencies in the case of 3-point supported parallel-beam model are smaller than those of the other cases, except for the 1st mode. Figure 2.25 shows a comparison of experimental and analytical results of vibrational modes in the case of 9-point supported elbow type model. The analytical results show almost the same as those of the experimental ones. The insulation in the inner pipe does not markably affect the vibrational modes of coaxial double-pipe structure.

Table 2.1 Comparison of experimental and analytical values of natural frequencies of a parallel-beam model

Mode number	Natural frequencies (Hz)									
	Parallel-beam model									
	3-point		4-point		5-point		7-point		9-point	
	Ex.	Nu.	Ex.	Nu.	Ex.	Nu.	Ex.	Nu.	Ex.	Nu.
1st	26.5	27.8	27.0	28.6	27.2	28.9	27.0	28.9	26.8	28.9
	25.6#	26.9#	26.4#	27.8#	26.6#	28.1#	26.4#	28.1#	26.1#	28.1#
2nd	53.6	46.1	68.0	82.8	68.4	83.6	68.1	83.7	68.0	83.7
	46.0#	40.8#	66.1#	80.0#	66.6#	81.2#	66.3#	81.3#	66.2#	81.4#
3rd	67.8	79.7	85.7	89.3	84.9	89.6	84.8	90.4	84.5	90.6
	61.2#	73.1#	81.4#	86.2#	82.5#	86.3#	82.4#	87.8#	82.3#	88.1#
4th	81.6	81.1	98.8	102.5	152.7	160.9	167.8	164.3	167.8	164.3
	76.0#	75.0#	92.8#	91.0#	151.7#	144.9#	162.4#	159.0#	162.2#	159.0#

Ex. : Experimental value
Nu. : Analytical value
: Inner pipe is insulated

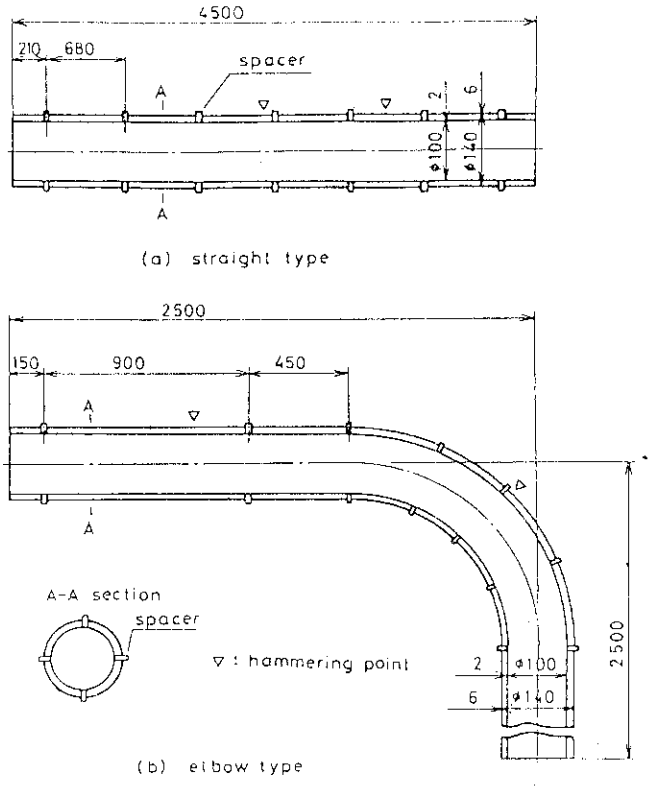

Fig. 2.23 Straight and elbow type models of coaxial double-pipe structure

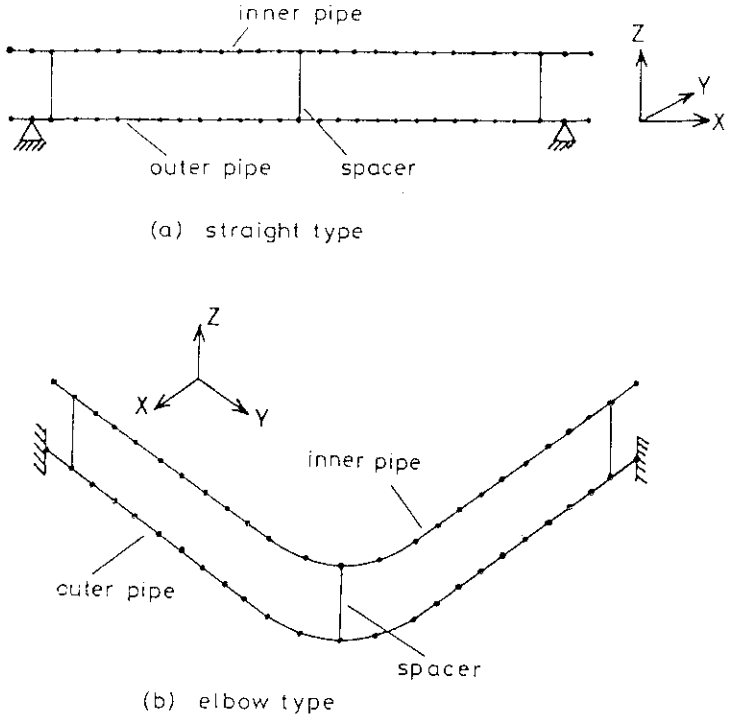

Fig. 2.24 Nodes of a 3-point supported parallel-beam type model

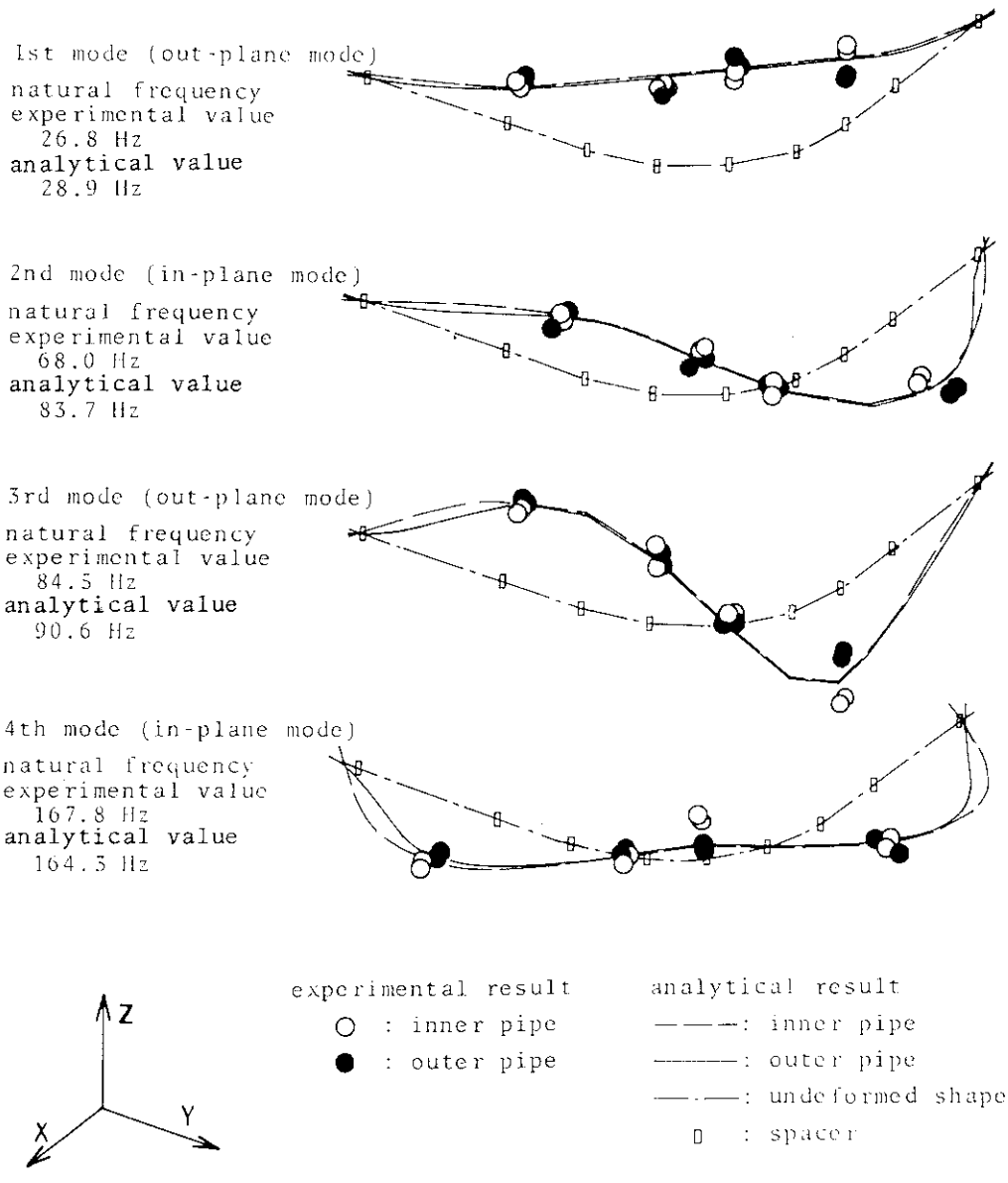

Fig. 2.25 Vibrational modes of a 9-point supported elbow type model

3. RESEARCH ON HEAT TRANSFER AND FLUID DYNAMICS

3.1 Thermo-hydraulic Test on VHTR Fuel Rod

N. Akino, S. Nakauchi*, K. Hashimoto** and K. Suzuki

The current thermal design of the VHTR core is based on a correlation for a smooth annular channel. An actual coolant channel, however, has spacer-ribs and gaps between fuel subrods. To determine their effects on heat transfer and pressure drop, an experiment on a simulated fuel rod has been carried out using He gas as coolant.

Experimental apparatus

The experiment was conducted with a gas loop, which circulates pure He gas with a flow rate of up to 30 g/s and a pressure of up to 0.4 MPa. He gas is compressed by a reciprocal compressor and enters a surge tank to reduce pressure fluctuations. After the measurement of flow rate, it passes through a liquid-nitrogen cooler to an inlet nozzle of a test section, in which it flows downward. Then He gas returns to the compressor through the another surge tank.

The test section is about 6 m in height, and made up of a channel with an inner diameter of 53 mm. Five simulated fuel subrods connected axially, as shown in Fig. 3.1. Heat transfer and pressure drop were measued at the middle part of the test section. Each subrod is 46 mm in outer diameter and 570 mm in length, and is heated by electric current passing through its wall. On the outer surface, 3 sets of spacer-ribs (3 pieces at each axial position) made of boron-nitride are attached to support the annular channel with a uniform gap and to insulate electrically the simulated fuel rod from the channel wall.

The channel is equipped with 44 pressure taps to measure detailed pressure distribution in the flow direction. Eighty nine thermocouples (type K) are fixed on the inner surface of 5 simulated fuel subrods to measure the distribution of heat transfer coefficient. They are taken

* Fuji Electric Co., Ltd.

** Kawasaki Heavy Industries, Ltd.

out through the hollow bore in the center of the rod so as not to disturb the coolant flowing. A preliminary test was done to measure the temperature distribution in a region affected by a spacer-rib.

Results and discussion

(1) Pressure drop

Pressure drop measurements were made under an adiabatic condition. Figure 3.2 shows a typical pressure distribution along the channel axis at a Reynolds number of 1×10^4 (turbulent flow condition). The dashed line is a calculated pressure distribution based on a smooth annular channel with the same geometry. The pressure drop along the channel is larger by about 15% than that of a smooth annular channel. This may be due to the spacer-ribs and gaps. Under laminar flow condition, the additional pressure drop was about 8%.

Figure 3.3 shows a pressure distribution around a spacer-rib. Except at the spacer-rib, the pressure decreases linerarly. So the local friction factor can be evaluated, and is shown in Fig. 3.4. A dimensionless local pressure loss (dP_{s-r} : observed at the position of spacer-rib) coefficient K_{s-r} is shown in Fig. 3.5.

At the positions of the gaps between fuel subrods, another local pressure loss was observed in turbulent flow condition, but not in laminar flow condition.

(2) Heat transfer

Figure 3.6 shows a typical result of measured temperature distributions in the test section, and a calculated temperature of fuel rod surface based on the smooth annular channel correlation. The zigzag temperature distribution is due to the configuration of the simulated fuel subrods. The open symbol denotes the temperature along the spacer-rib axis. At the position of each spacer-rib, the wall temperature decreases locally. The solid symbol denotes the wall temperature along the middle line between spacer-rib axis; and the effect of spacer-ribs was not clearly observed. On the other hand, in the downstream of each gap, both temperature distributions were almost the same. This probably means that the effect of spacer-ribs is circumferentially localized, while that of gaps is uniform.

Figure 3.7 shows a distribution of measured heat transfer coefficients

along the spacer-rib axis on 4 simulated fuel subrods at a Reynolds number of about 1×10^4 (turbulent flow condition). Heat transfer is augumented markably at the spacer-ribs.

Figure 3.8 shows a relation between Nusselt number and Reynolds number at two typical points. At N-A position, Nusselt number is larger than that of a smooth annular channel, namely heat transfer is enhanced. At N-B position, no augumentation is observed even in turbulent flow condition. But Nusselt number is larger than the one estimated by the smooth annular correlation for transitional region even near the laminar region.

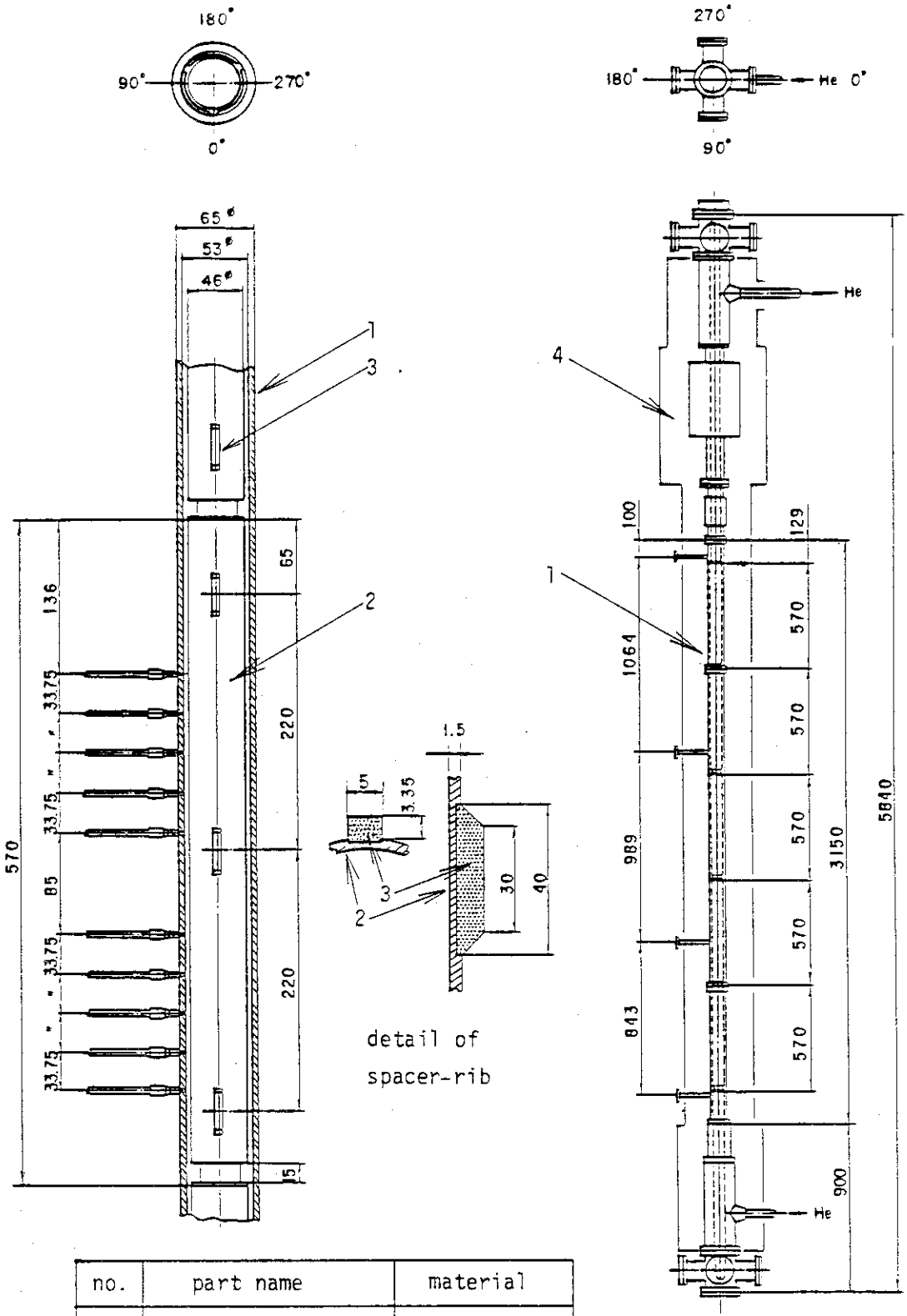

no.	part name	material
1	test channel	sus304
2	simulated fuel rod	sus304
3	spacer rib	boron nitride
4	thermal insulation	Kaowool

Fig. 3.1 Test section

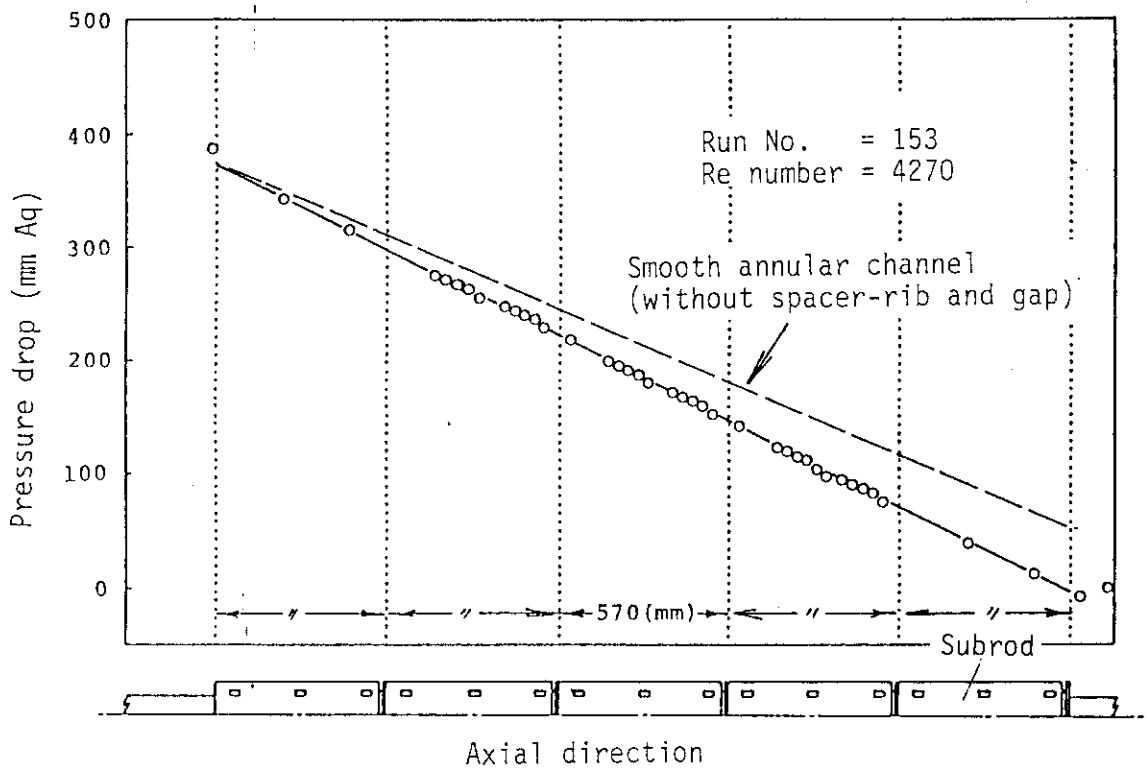

Fig. 3.2 Pressure distribution along the axis of the test section

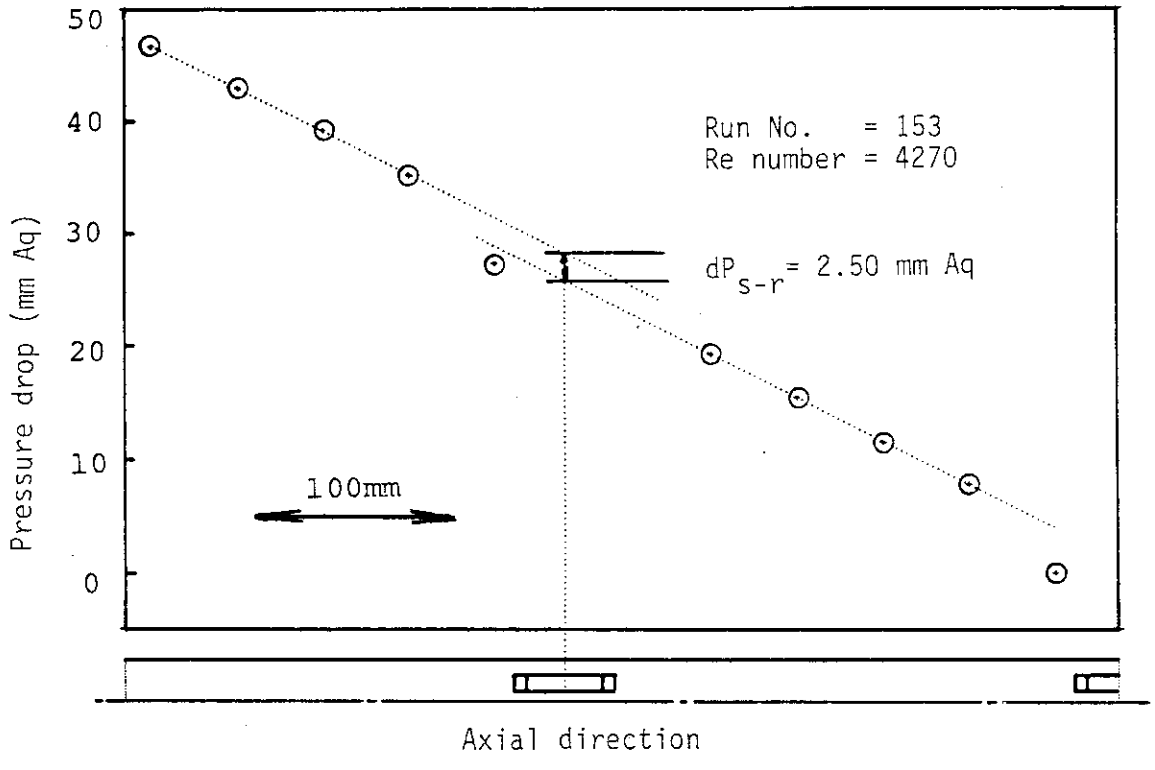

Fig. 3.3 Pressure distribution around a spacer-rib

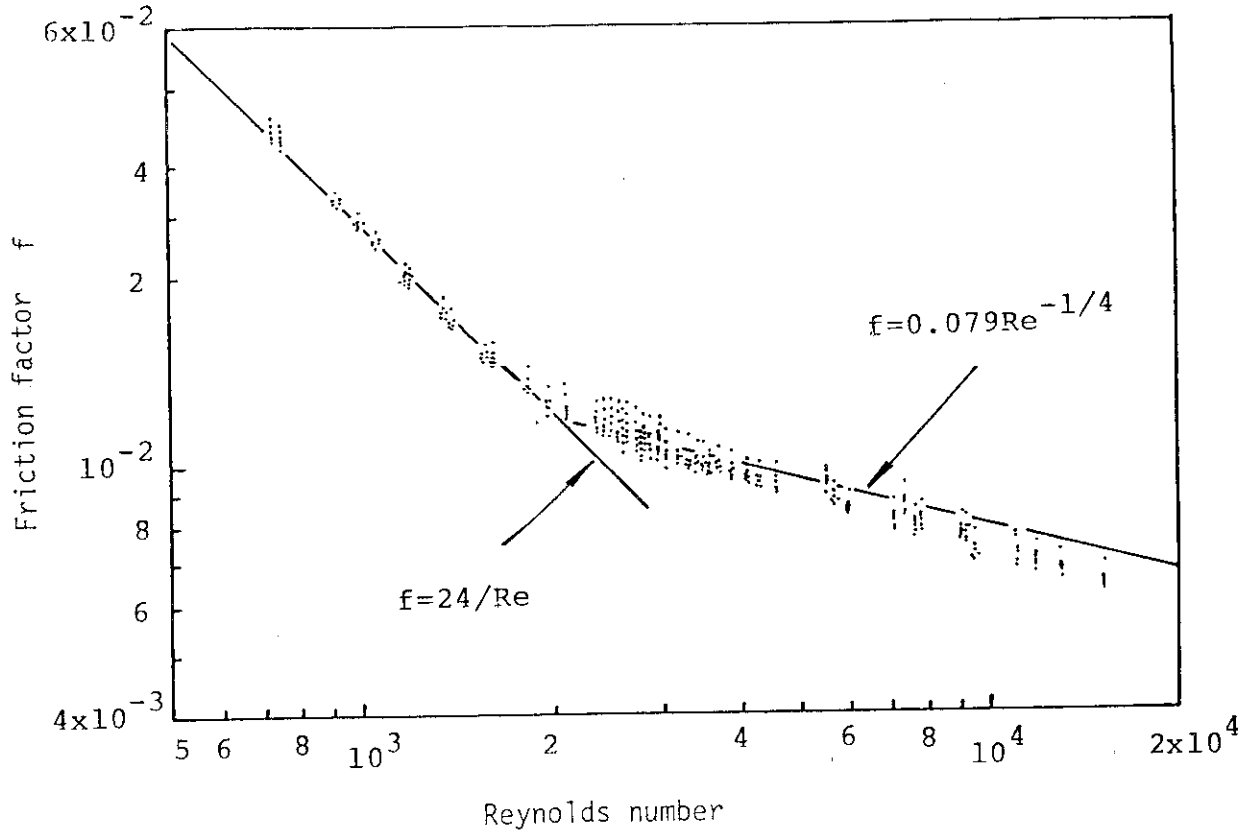

Fig. 3.4 Local friction factor of annular channel

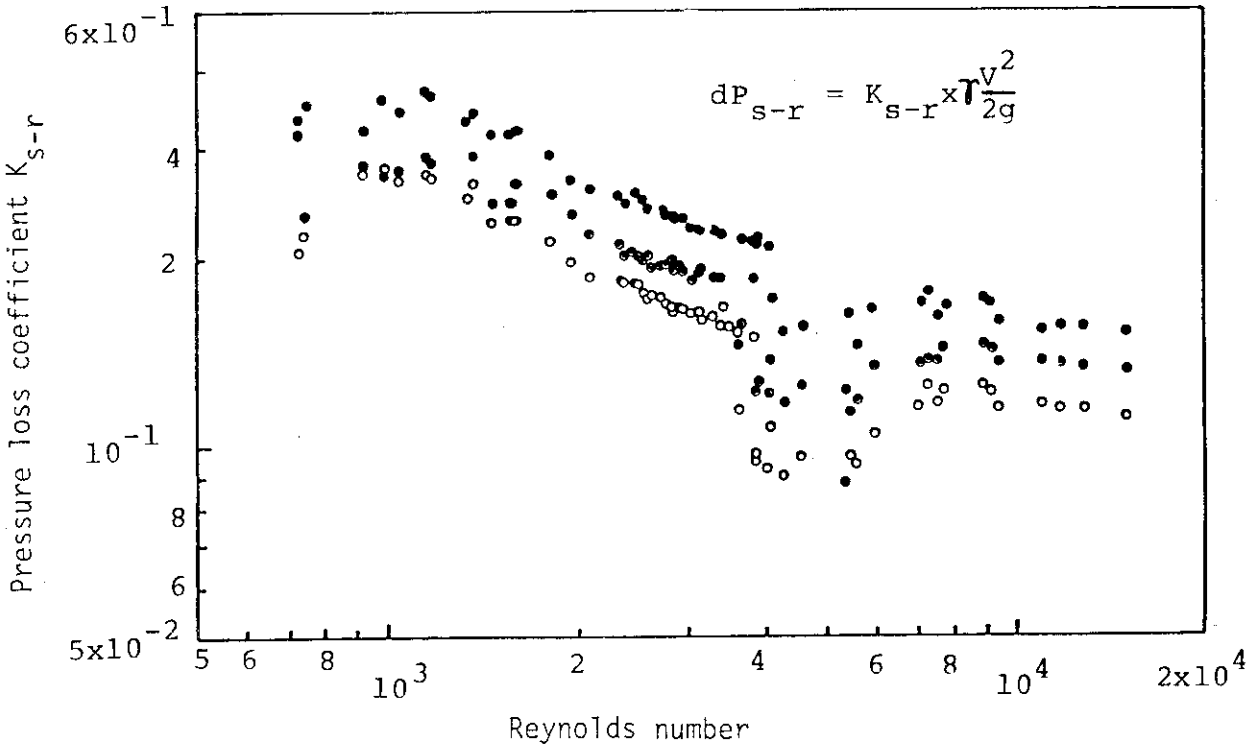

Fig. 3.5 Pressure loss coefficients at a spacer-rib

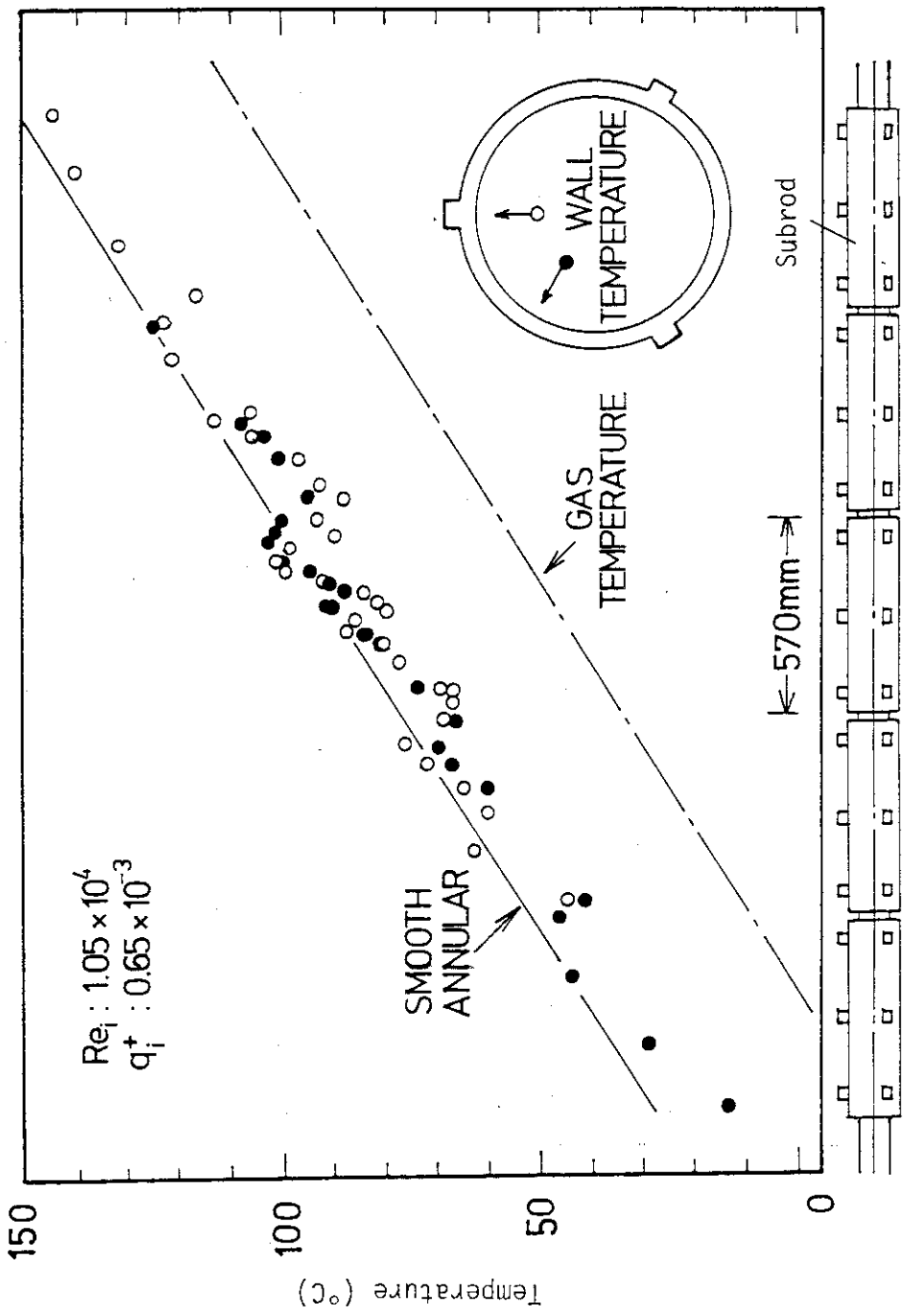

Fig. 3.6 Temperature distribution

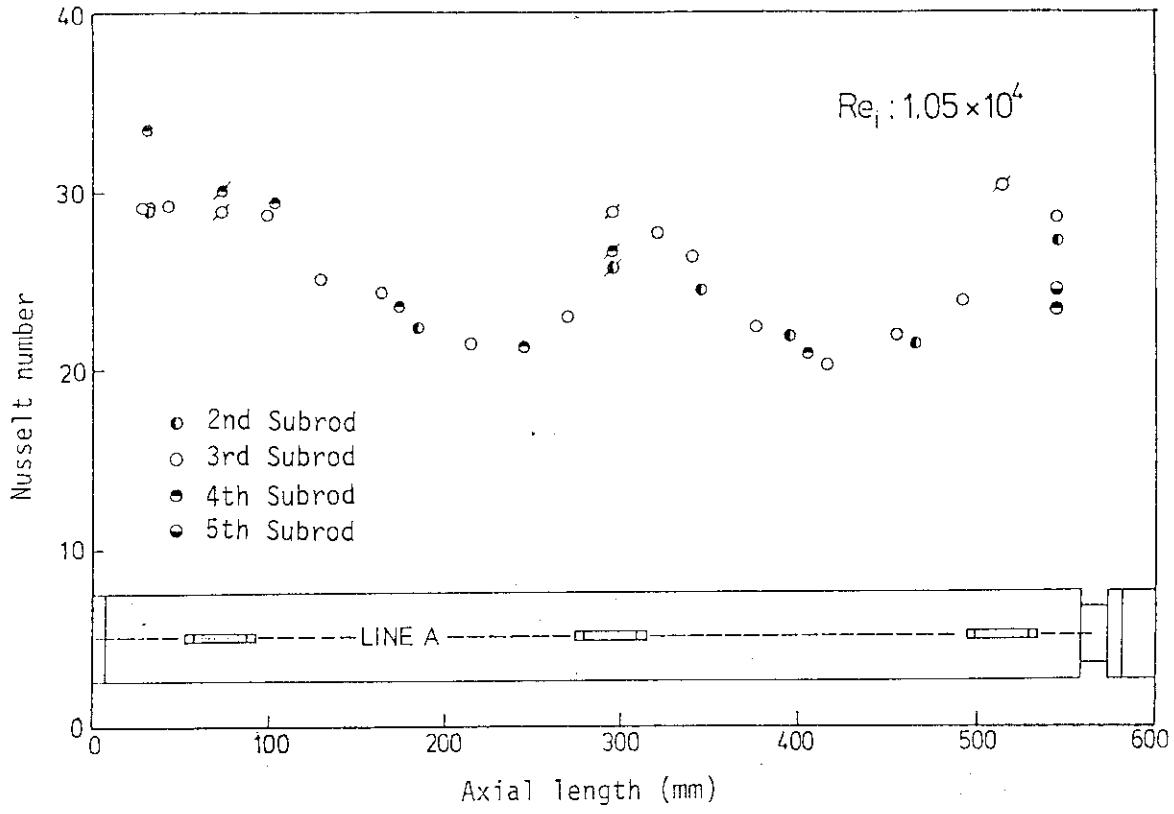

Fig. 3.7 Nusselt number distribution along the spacer-rib axis

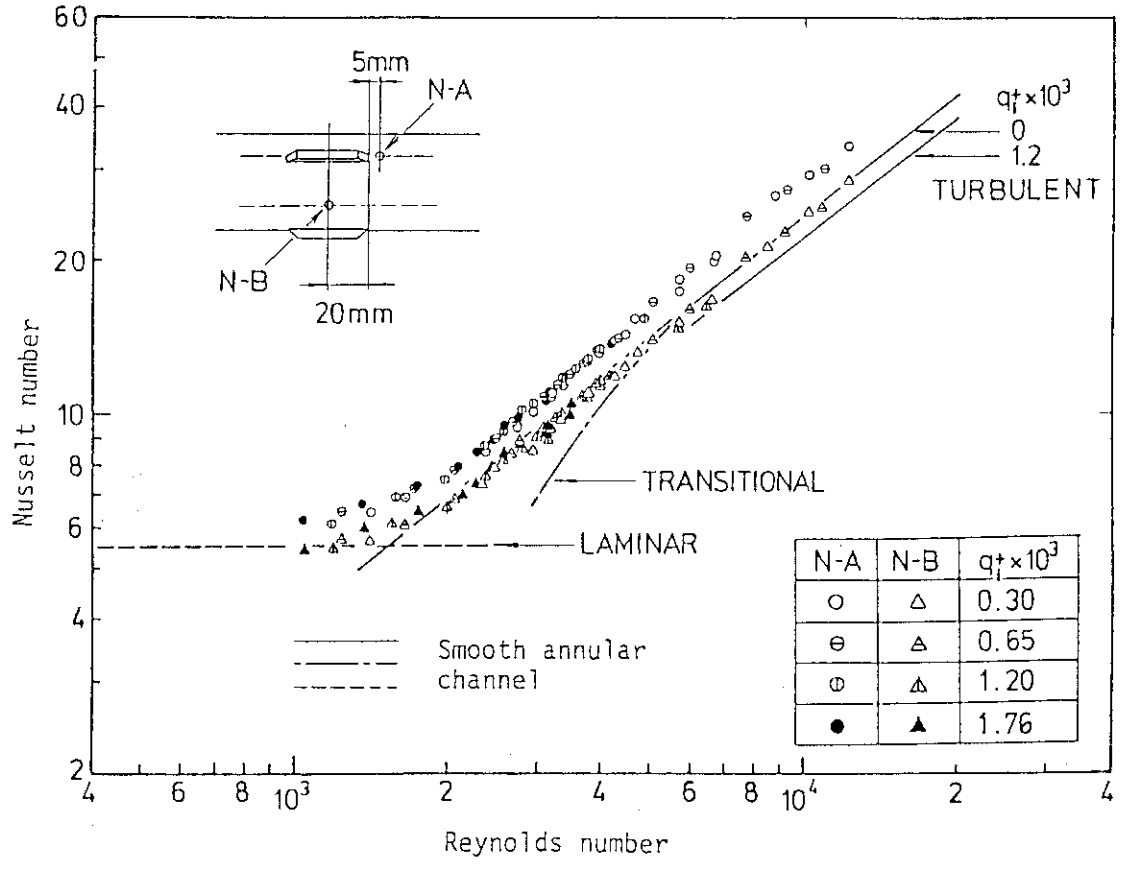

Fig. 3.8 Nusselt number at two typical points near a spacer-rib

3.2 Experiment on Heat Transfer and Fluid Dynamics of Control Rod

M. Ogawa, N. Akino, K. Fujimura, K. Hashimoto*, M. Ouchi, K. Emori, I. Myodo and H. Kawamura

A control rod of the VHTR consists of 13 hollow cylindrical elements. These elements are flexibly connected in the axial direction with gaps among them. He gas flows both outside and inside of the control rod. In the VHTR, a ratio of flow rates in the outer and inner channels is unity. The inner coolant flow is turbulent, and the Reynolds number is about 5000; while the outer coolant flow is laminar and the Reynolds number is about 1500. Hence, different flow modes simultaneously exist around the control rod. Since these flows interact through the gaps among subrods, the inner and outer flows might be unstable. Accordingly local temperature rise of the element occurs. Furthermore, since the configuration of the element is not so simple that heat transfer, pressure loss and flow rate distributions in the inner and outer channels must be determined experimentally. In order to study these characteristics, an experimental apparatus was constructed.

Apparatus

Figure 3.9 shows a flowsheet of a gas loop for the study on heat transfer and hydrodynamics of the simulated control rod. The main specifications are as follows:

Fluids	:	He gas, Air
Pressure	:	Max. 0.9 MPa
Flow rate	:	Max. 0.1 kg/s
Temperature	:	He gas Max. 300°C
		Wall Max. 600°C
Stability	:	± 1 %

He gas compressed by a reciprocal compressor flows into a snubber tank to reduce pressure fluctuations. He gas flow rate is regulated

---

* Kawasaki Heavy Industries, Ltd.

by a flow control valve provided in a bypass line. Before He gas enters a test section, the temperature is set to be a specified value by a temperature control unit which consists of an electric pre-heater and a water cooler.

The simulated control rod with 5 elements is placed in the test section, as shown in Fig. 3.10. The configuration is the same as that of the VHTR. Electric heaters were embedded in the elements to simulate the neutronic heat generation in the control rod. Among the five elements, the No.1 element is not heated, and each of the Nos. 2, 3 and 5 elements has a single heater as shown in Fig. 3.11. The No.4 element, as shown in Fig. 3.12, has two heaters at both inside and outside of the element. An electric heater is herically wound around the outer surface of the flow conduit pipe to simulate heat transferred to the flow from fuel assemblies. In order to reduce heat loss from the flow conduit pipe, inner and outer thermal insulations, and guard heaters were provided with the pipe.

Holes for inserting hot-wires and pressure taps are opened through the flow conduit pipe. The total flow rate was measured with a flow control unit. The flow rate of the outer channel was calculated from the velocity distribution measured by traversing a hot-wire. The flow rate of the inner channel was obtained by subtracting the flow rate of the outer channel from the total flow rate. Pressure losses of the outer channel were measured by differential pressure gages of a pressure loss measuring unit. Temperature was measured by means of type-K thermocouples.

Several runs of the experiments for fiscal 1984 are scheduled.

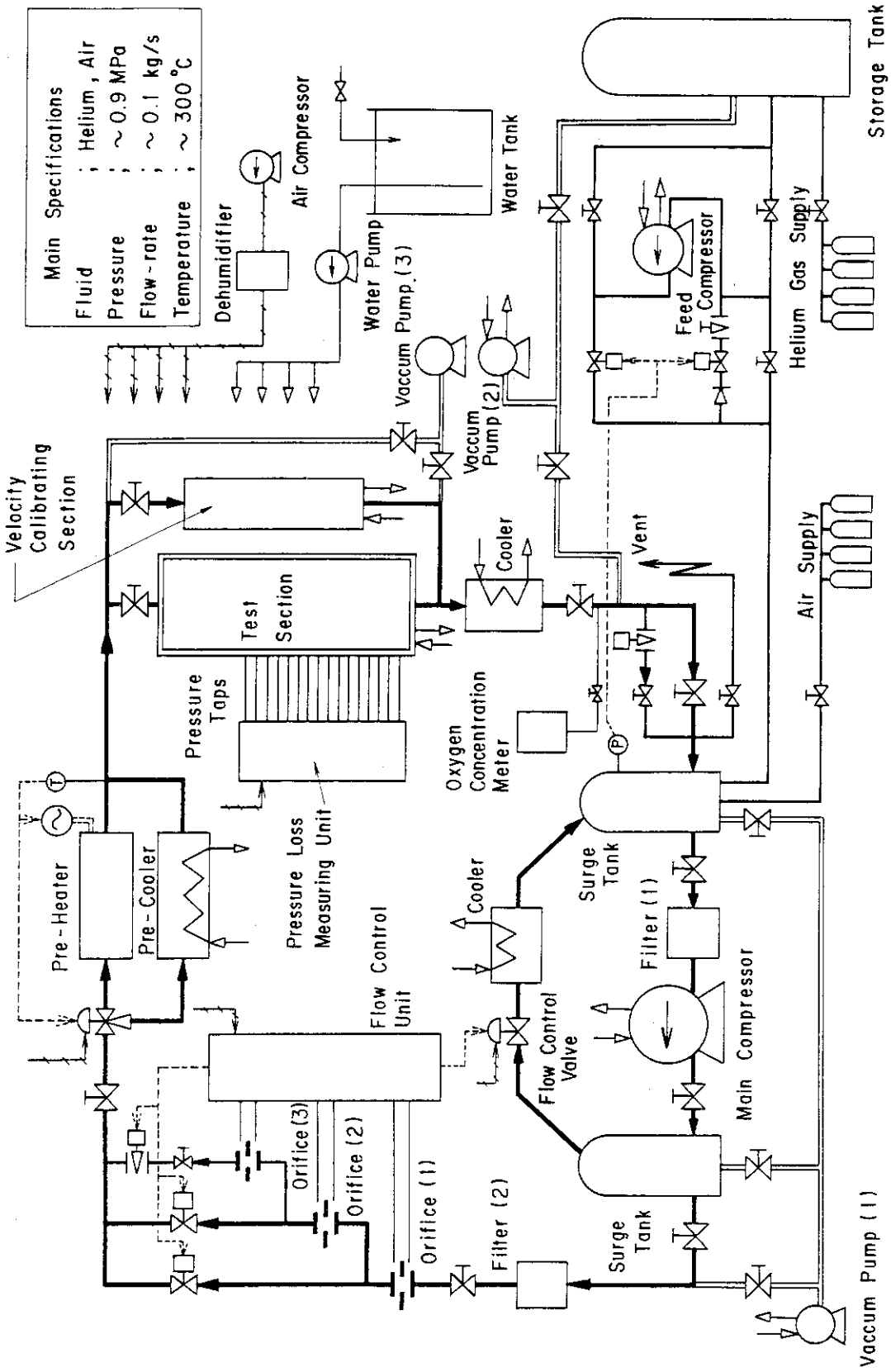

Fig. 3.9 Flowsheet of a gas loop

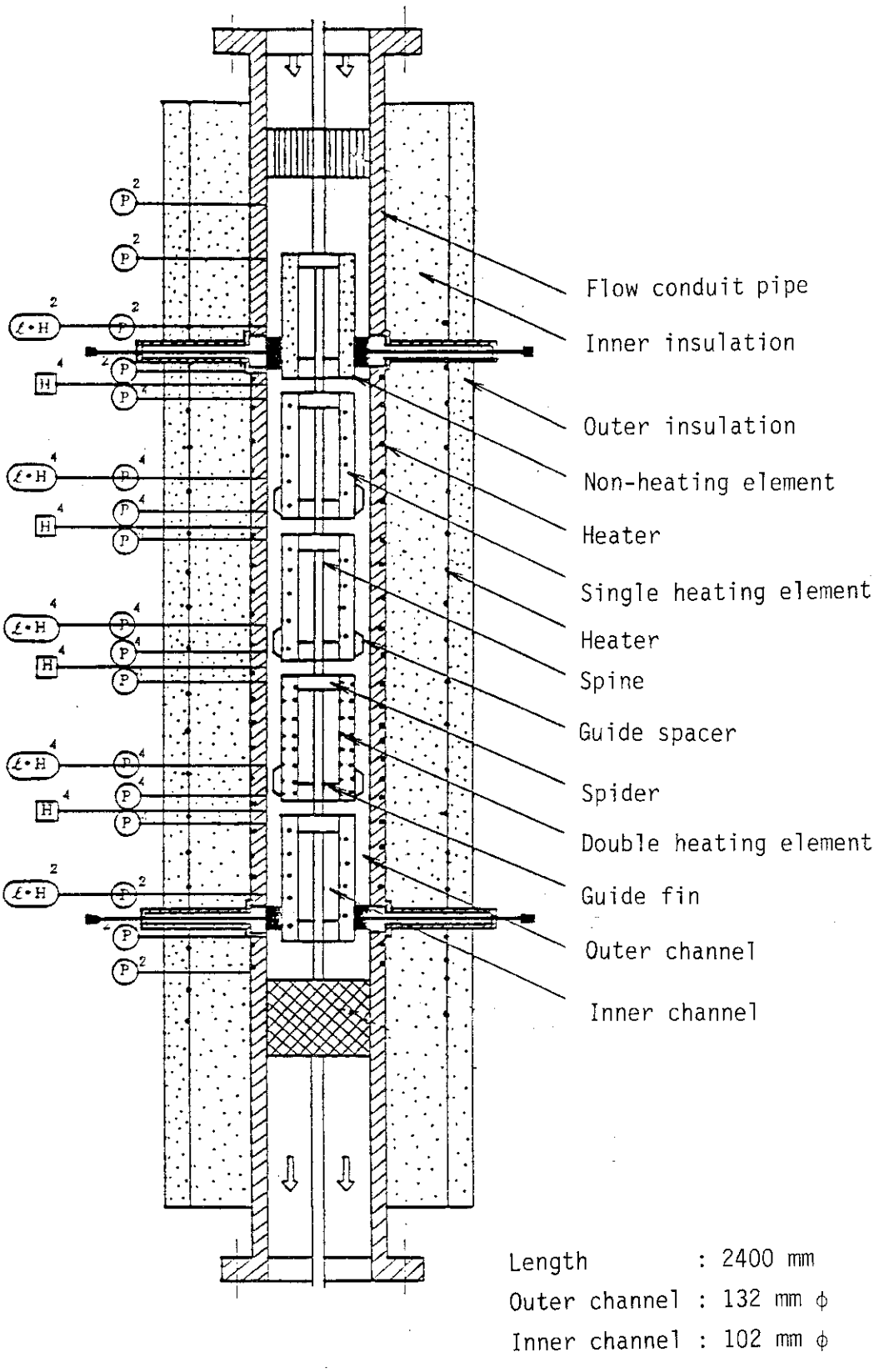

Fig. 3.10 Test section

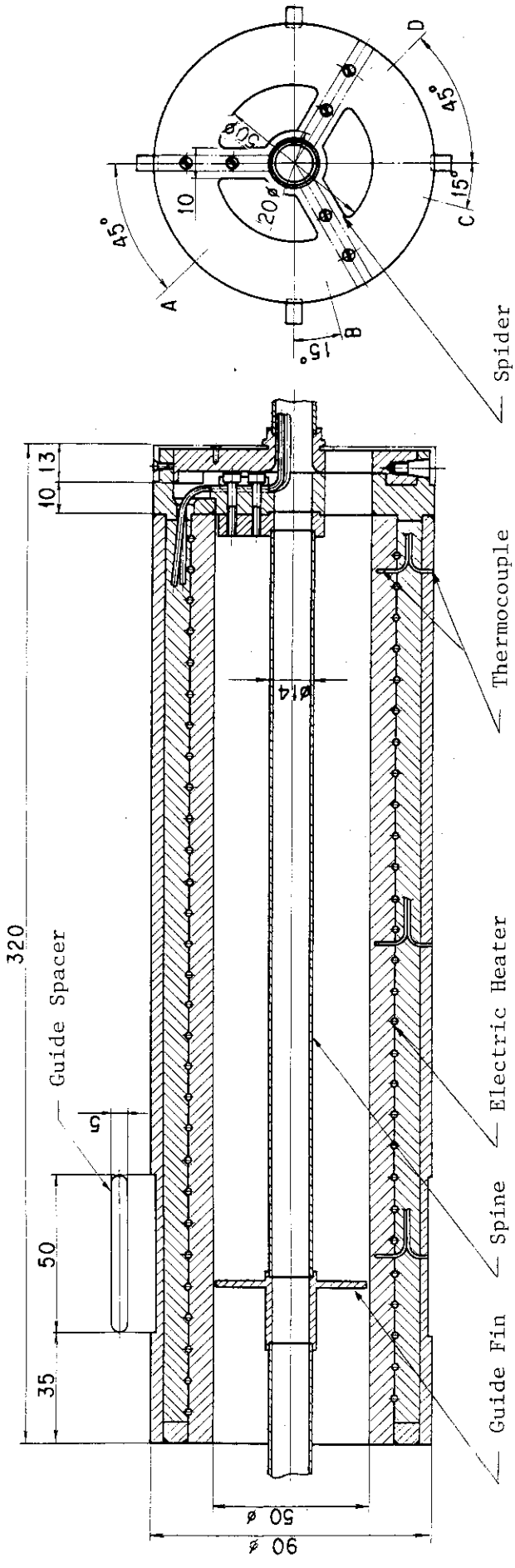

Fig. 3.11 Element of simulated control rod with a single heater

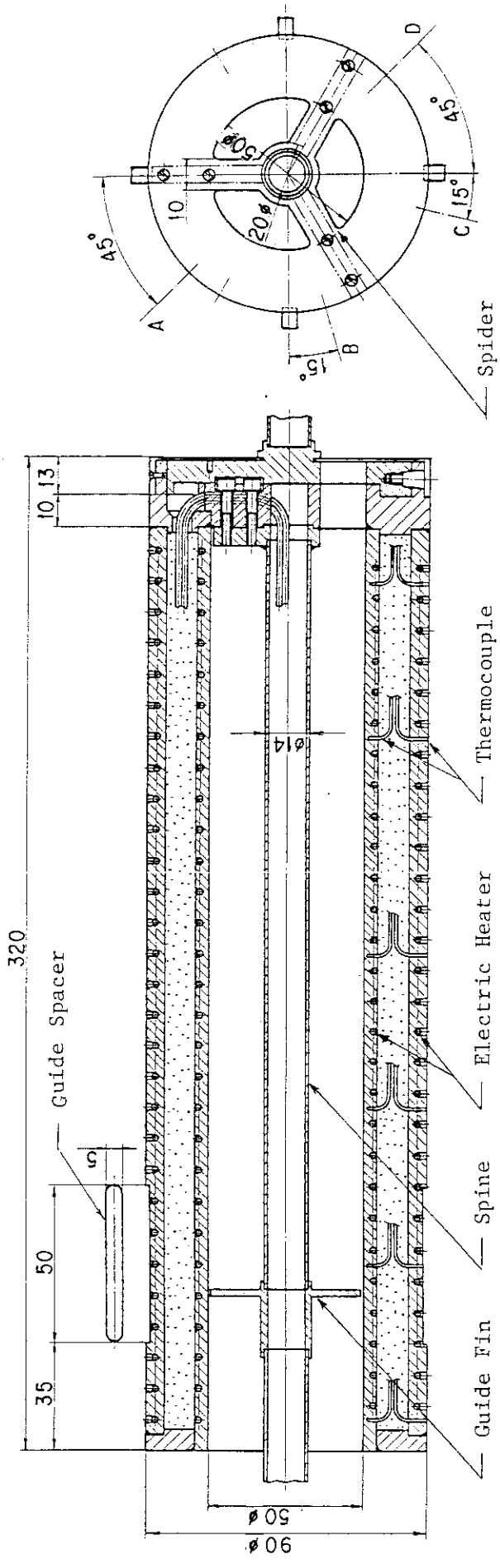

Fig. 3.12 Element with two heaters

3.3 Transition in a Concentric Annulus

K. Fujimura

In the case of an accident in a core cooling system of the VHTR, the coolant flow rate decreases and accordingly the flow regime changes from turbulent to laminar. The transition process in the reactor core is important from the safety viewpoint.

We have already investigated the laminar-to-turbulent transition in a circular tube. In this case, hot-wire traces showed that turbulent "slugs" intermittently appeared at a reference point. The turbulent slugs were equivalent to axisymmetrically developed turbulent spots. This transition characteristics was observed only when the disturbance at the inlet of the channel (hereafter we refer to an initial disturbance) was sufficiently suppressed. On the other hand, when the initial disturbance was retained at some finite level, the other transition regime, turbulent "puffs", appeared. Turbulent puffs were produced owing to relaminarization process. We will show that these two different characteristics in laminar-to-turbulent transition exist also in a concentric annulus.

A schematic diagram of the experimental apparatus is shown in Fig. 3.13. The outer tube is 46.5 mm in inner diameter, while the inner tube is 32 mm in outer diameter. The test section without a spacer is 2500 mm in length, and the cross-section of the channel contracts to 1/25 at the inlet. Air is led to honey combs and screens in order to suppress the initial turbulence.

At the inlet of the test section, there is an injection hole of disturbance (1 mm in diameter) for introducing weak pulse jet into the flow by using a loudspeaker. Hot-wires are inserted at x/D=3.3, 37.5, 106.5 and 140.8; where x denotes a distance from the injection hole of disturbance, and D a hydraulic diameter. Azimuthal angles of hot-wire locations are 0° and 120° with respect to the position of the injection hole.

Careful suppression of the initial disturbance enabled us to obtain a laminar flow even at a Reynolds number of nearly 9090. At this value, the flow field was disturbed by a weak pulse from the loudspeaker. Hot-wire traces are shown in Fig. 3.14. The left column (trace A) shows the traces at 0° angle; while the right column (trace B) shows the ones at 120° angle. At Reynolds number 9090, weak disturbance was introduced in

the flow by the loudspeaker. At x/D=3.3, an effect of introduction of the disturbance is not observed in the trace B, indicating that the disturbance does not spread over the whole corss-section of the flow field. At x/D=37.5, disturbance-like signals appear in the trace B, but the magnitude of the signals is smaller in the trace B than in the trace A. This implies that the flow field is not symmetrical at x/D=37.5, but the symmetry is established at x/D=72.2. The hot-wire trace in an annular tube is quite similar to the one in a circular tube.

A normalized passing time $\gamma\nu/fD^2$ of turbulent slugs at three reference points is plotted in Fig. 3.15 against the intermittency; where f is a frequency of turbulent slugs, $\gamma=\lim_{T\to\infty}\frac{1}{T}\int_t^{t+T} I(t)dt$, I(t) an intermittent function defined as I(t)=1 for turbulent regime and otherwise I(t)=0. Although these data scatter, the tendency is almost similar to the one in a circular tube. The result of a circular tube is also shown in Fig. 3.15. The passing time in an annular tube is three times as large as the one in a circular tube. It is concluded that if the initial disturbance is suppressed to a very low level, the transition process in an annular tube is similar to the one in a circular tube.

An experiment was performed also on a high initial disturbance level. The initial disturbance level was maintained as high as possible at low Reynolds numbers. Figure 3.16 shows five hot-wire traces at different Reynolds numbers at x/D=140.8. At a Reynolds number of 2222, the flow field is probably laminar even though some low-frequency fluctuations still remain. At a Reynolds number of 2525, intermittent high-frequency fluctuation signals appear in low-frequency fluctuation signals. As Reynolds number increased, high-frequency fluctuations became more frequent, and thereafter the flow field was covered by turbulence. In a circular tube, no low frequency fluctuation in laminar regime was observed. The difference is due to different stability characteristics of these two flow fields; that is, the flow in a circular tube is stable, while the flow in an annular tube has a critical Reynolds number. A laminar and turbulent boundary was observed more clearly in a circular tube than in an annular tube. But it is important that the laminar-to-turbulent transition of the flow with high initial disturbance occurs intermittently.

We found that the laminar-to-turbulent transition in a concentric annulus is quite similar to the one in a circular cylinder.

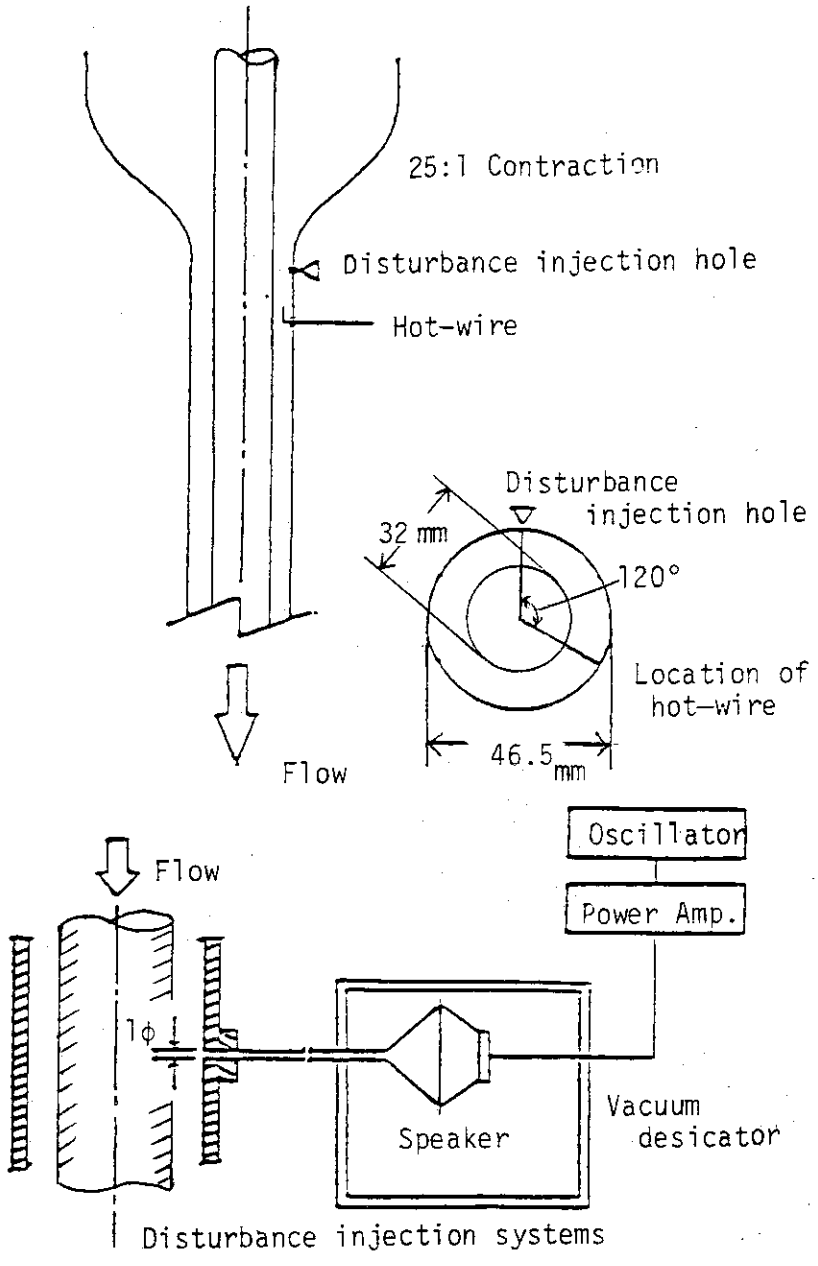

Fig. 3.13 Schematic diagram of experimental apparatus

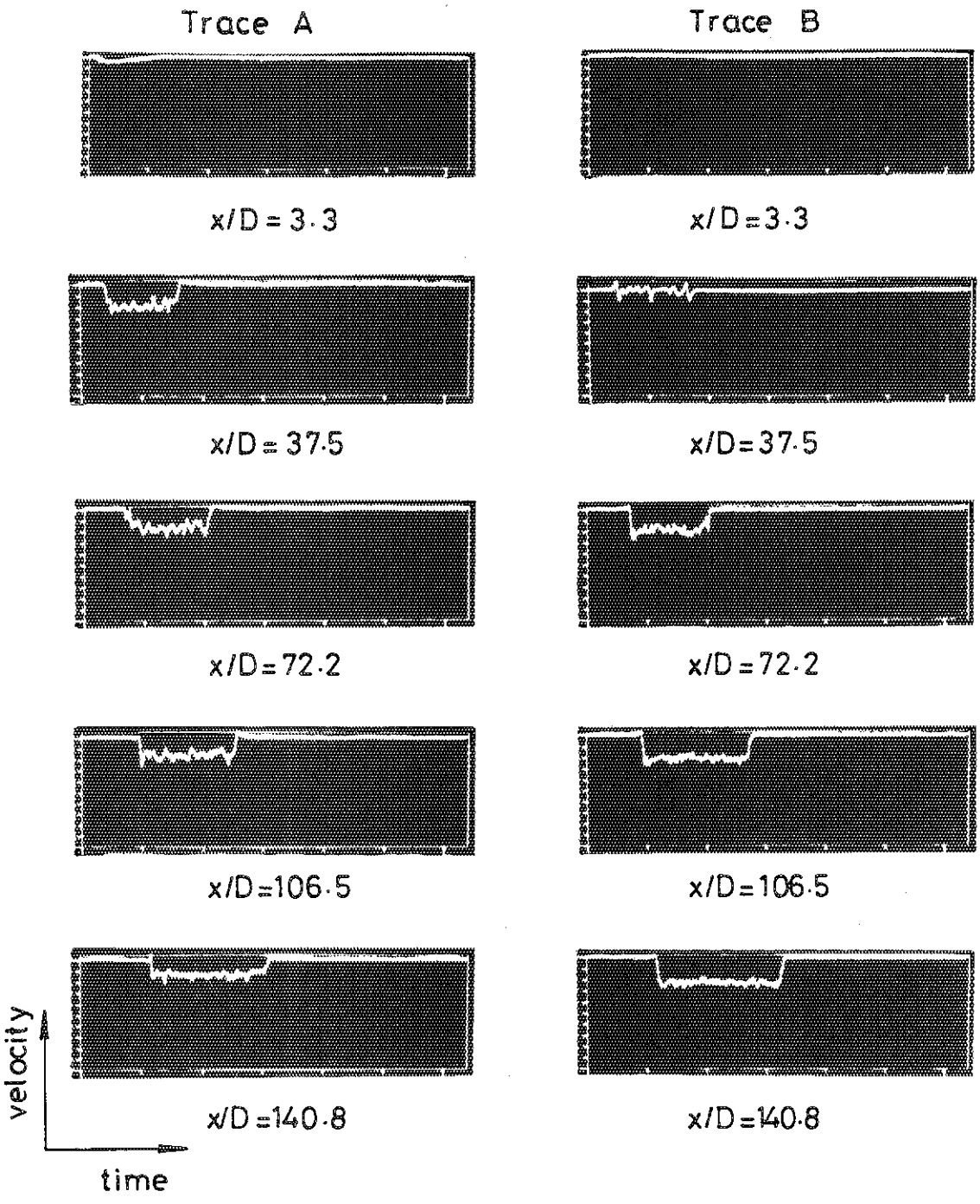

Fig. 3.14 Development of artificially excited turbulent slugs at Re=9090

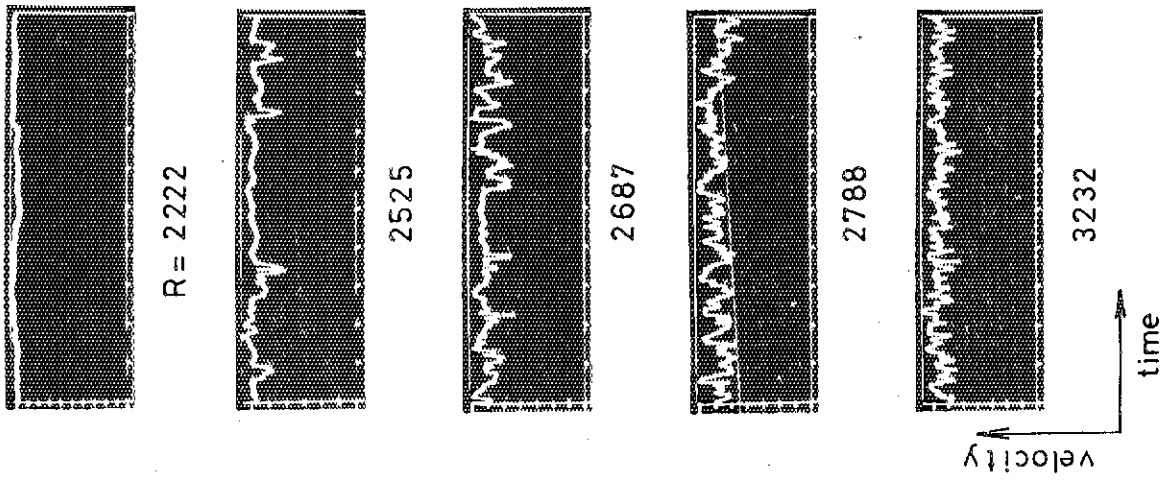

Fig. 3.16 Laminar-to-turbulent transition with high initial disturbance at x/D=140.8

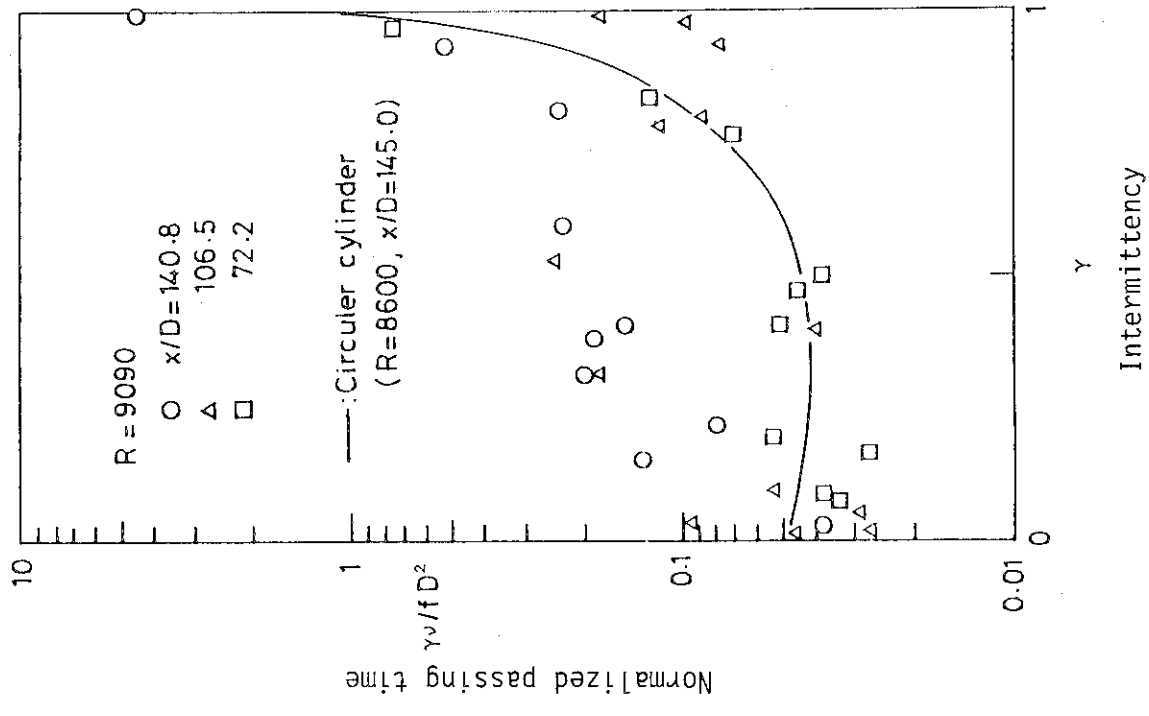

Fig. 3.15 Normalized passing time of turbulent slugs at x/D=72.2, 106.5 and 140.8

3.4 Combined Forced-free Laminar Heat Transfer to a Strongly Heated Gas in a Vertical Annulus

K. Hashimoto*, N. Akino and H. Kawamura

In the VHTR, a reactor core is designed so as to achieve a high outlet temperature. It is, therefore, necessary to investigate an effect of large temperature difference between wall and fluid on heat transfer and hydrodynamics in an annular channel.

Under abnormal conditions such as a loss of forced circulation, the flow is probably free convection or combined forced-free convection. Occurrence of flow reversal, in the combined convection, makes core temperature extremely high. In view of the VHTR core safety, it is practically important to investigate the laminar heat transfer of combined forced-free convection in a vertical annulus.

Many investigators have studied this problem theoretically and experimentally with respect to various channels under several conditions.[1,2,3] However, to our knowledge, no data are available on the laminar heat transfer of combined forced-free convection in developing fluid with temperature dependence of thermophysical properties. In the present study, the combined flow (both upward and downward flows) in a thermal and hydrodynamical entry region is considered. Thermal condition of the inner wall is isothermal and constant heat flux, and that of the outer wall is adiabatic.

Basic equations

Basic equations are described on the basis of the standard boundary layer approximation. Fluid properties are to be varied as a function of temperature. In this study, all calculations are made for He gas in an annulus with a radius ratio of 0.9. The conservation equations of mass, momentum and energy in a region of a vertical annulus become

---

* Kawasaki Heavy Industries, Ltd.

$$\frac{1}{r}\frac{\partial}{\partial r}(\rho r v) + \frac{\partial}{\partial z}(\rho u) = 0 \tag{3.1}$$

$$\rho u \frac{\partial u}{\partial z} + \rho v \frac{\partial u}{\partial r} = -\frac{\partial P}{\partial z} + \frac{1}{r}\frac{\partial}{\partial r}(\mu r \frac{\partial u}{\partial r}) \pm \rho g \tag{3.2}$$

$$\frac{\partial P}{\partial r} = 0 \tag{3.3}$$

$$c_p \rho u \frac{\partial t}{\partial z} + c_p \rho v \frac{\partial t}{\partial r} = \frac{1}{r}\frac{\partial}{\partial r}(\lambda r \frac{\partial t}{\partial r}) + \mu(\frac{\partial u}{\partial r})^2 . \tag{3.4}$$

Plus and minus signs in the buoyancy term of momentum equation refer to downward and upward respectively. These equations were solved on the condition that velocity and temperature profiles at the inlet are uniform.

Results

The value of $(Gr/Re)_i$ is chosen as a primary parameter for the effect of free convection, and the effect of thermophysical properties is expressed with an additional parameter t_e/t_i (isothermal wall condition) or $qDe/\lambda_i t_i$ (constant heat flux condition). Grashof number Gr is defined either as $De^3 g\Delta\rho/\rho\nu^2$ (isothermal wall condition) or as $De^4 gq\beta/\nu^2\lambda$ (constant heat flux condition).

It is seen from Figs. 3.17 and 3.18 that flow reversal disappears with decrease in a primary parameter $(Gr/Re)_i$ or with increases in t_w/t_i and $qDe/\lambda_i t_i$. Furthermore, occurrence of flow reversal is more possible in the case of downward flow than upward flow. With increase in a primary parameter $(Gr/Re)_i$, Nusselt number decreases for downward flow (Fig. 3.19), and increases for upward flow. Accordingly deceleration or acceleration at heated boundary occurs. The effect of thermophysical property variation is small. Figure 3.20 shows that a product of friction factor and Reynolds number slightly increases compared with an isothermal case.

Nomenclature

t	:	Temperature
P	:	Pressure
r	:	Radial coordinate
z	:	Axial coordinate
Z	:	Dimensionless axial coordinate
De	:	Hydraulic diameter of annulus
q	:	Heat flux
g	:	Gravitational acceleration
Nu	:	Nusselt number
Re	:	Reynolds number
f	:	Friction factor
ρ	:	Density
μ	:	Viscosity
ν	:	Kinematic viscosity
λ	:	Thermal conductance
c_p	:	Heat capacity
u	:	Axial velocity component
v	:	Radial velocity component

Subscripts

w	:	Wall
i	:	Inlet

References

1) Lawrence, W.T. & Chato, J.C. : J. of Heat Transfer, ASME, 88, 214 (1966).
2) Zeldin, B. & Schmidt, F.W. : J. of Heat Transfer, ASME, 94, 211 (1972).
3) El-Shaarawi, M.A.I. & Sarhan, A. : J. of Heat Transfer, ASME, 102, 617 (1980).

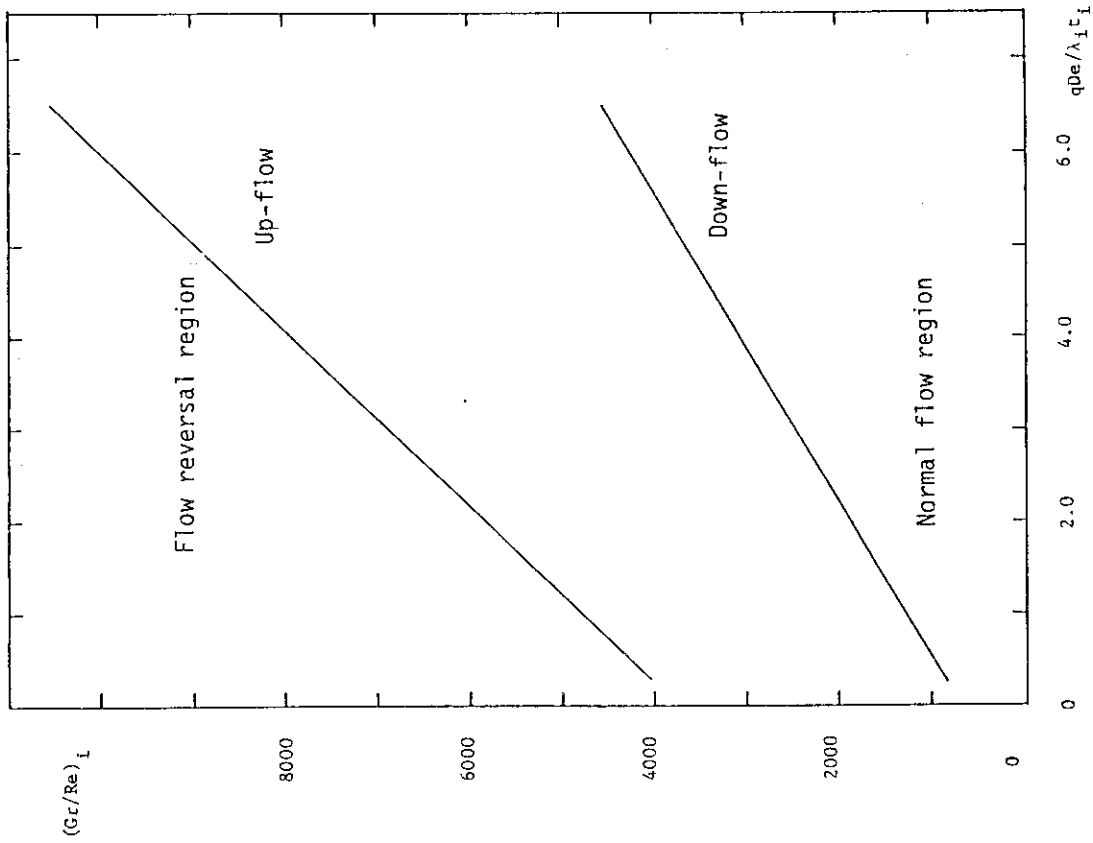

Fig. 3.18 Critical condition line for flow reversal (Constant heat flux condition)

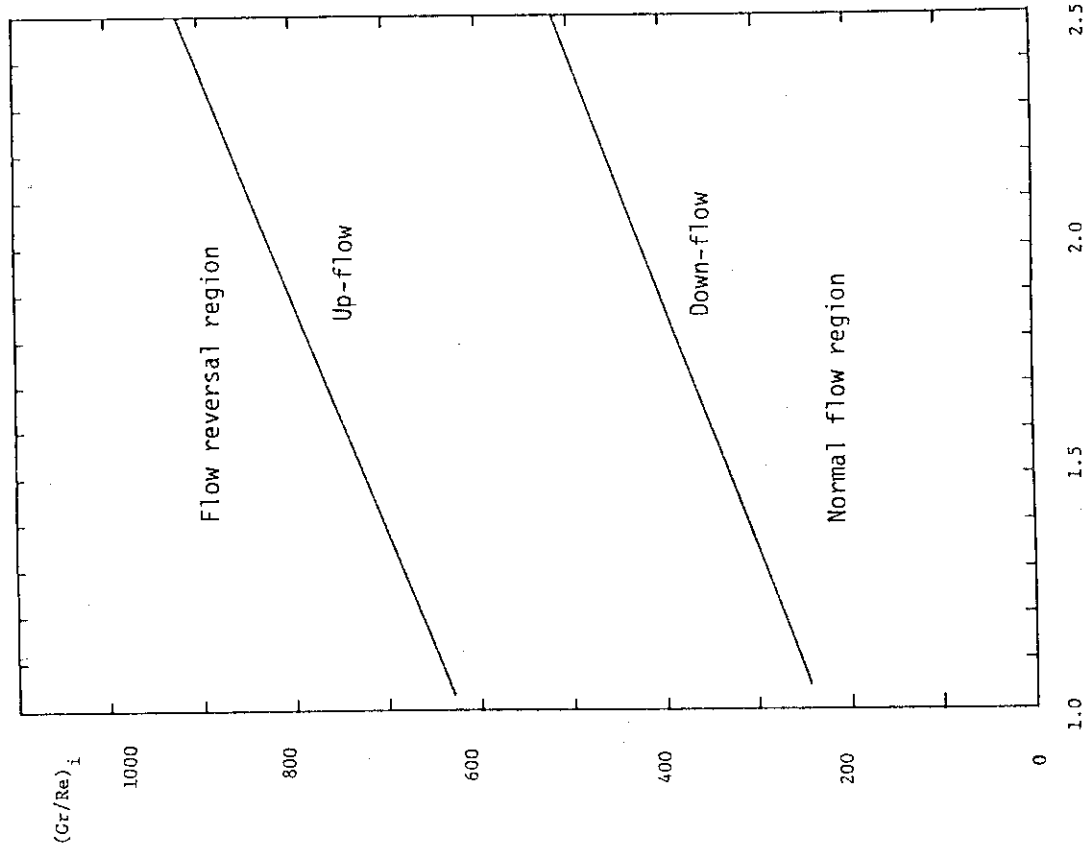

Fig. 3.17 Critical condition line for flow reversal (Isothermal wall condition)

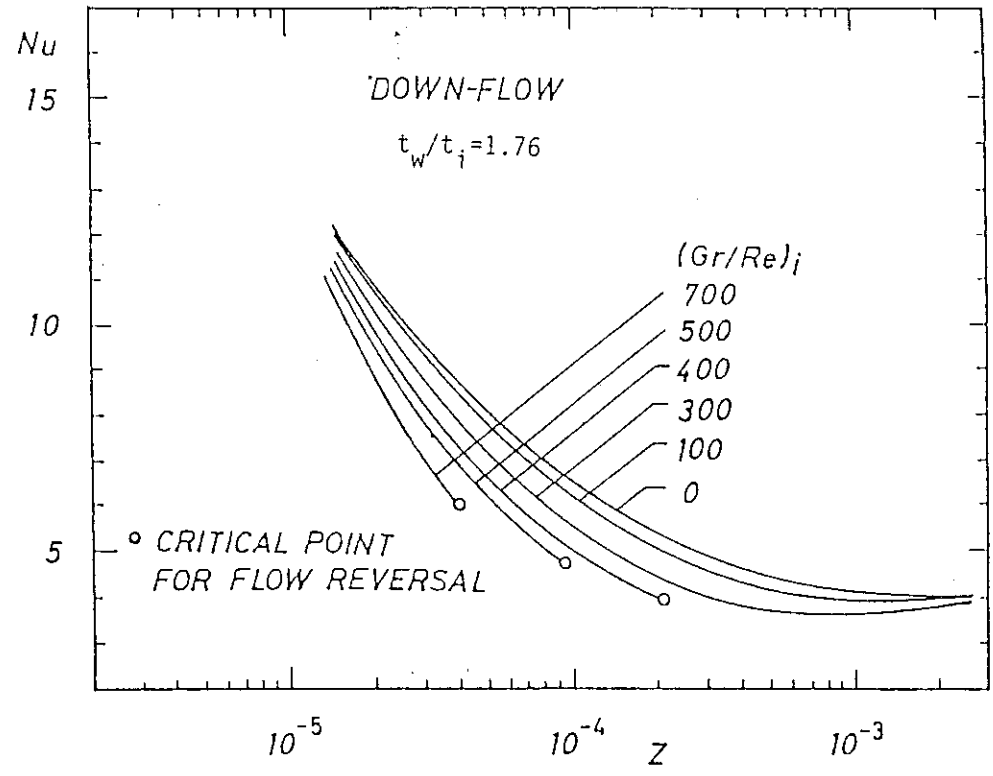

Fig. 3.19 Dependence of $(Gr/Re)_i$ on Nusselt number (t_w/t_i=1.76)

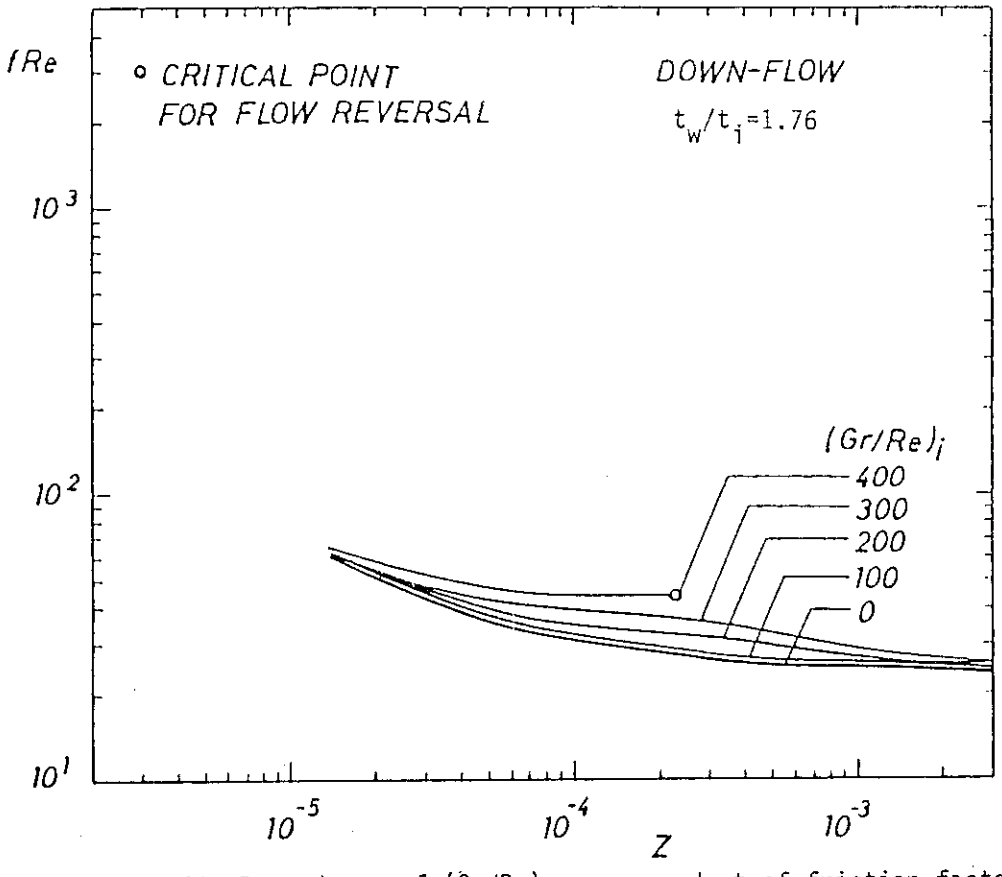

Fig. 3.20 Dependence of $(Gr/Re)_i$ on a product of friction factor and Reynolds number (t_w/t_i=1.76)

3.5 Experiment on Reversed Flow in VHTR Core

Y. Shiina and K. Fujimura

In the VHTR core, the coolant flows downward under a normal operating condition. In the case of an accident such as a loss of forced convection due to a failure of circulators, there might be some possibilities that high-temperature He gas flows reversely upward owing to a buoyancy force. In such a case, temperature distribution in the core might vary considerably. Hence, flow reversal of coolant becomes very important from the viewpoint of the VHTR safety. A reversed flow experiment has been conducted for this purpose. A multi-channel flow regime in the VHTR core was simulated with two circular channels which are 6 m in length, as shown in Fig. 3.21(a). One is heated by a sheathed heater and the other is cooled by water. Atmospheric air was used as fluid. As air density is larger than He gas density, it is easy to simulate the operating conditions of the VHTR.

Steady state heat and flow conditions were obtained by circulating air from top to bottom of the channels. Then the pump was off and time-dependent temperature distribution and flow rate in the two channels were measured. One example of the temperature profiles is shown in Fig. 3.21(b). The temperature profile, which decreases with increase in channel hight in a normal flow condition, becomes reversed in a reversed flow condition.

The driving force of coolant results only from a buoyancy effect due to density difference between the heated and cooled channels when a loss of forced convection occurred. Therefore reversed mass flow increases until buoyancy force and pressure drop are balanced. As pressure drop is proportional to flow rate in the case of small flow velocity, flow rate is proportional to buoyancy force.

Figure 3.22 shows a plot of Reynolds number $Re = (4/\pi)(m/\nu D)$ of reversed flow against Grashof number ($Gr=g\Delta\rho D^3/\rho\nu^2$), where m denotes reversed flow rate, ν kinematic viscosity of air, D channel diameter, g gravitational acceleration, ρ density of air, and $\Delta\rho$ density difference of airs which flow in heated and cooled channels. The solid line indicates a theoretical line, and agrees fairly well with the data. Therefore the method to calculate reversed flow rate is considered to be appropriate.

The further experiment will be carried out in the case of flow reversal with a weak forced convection and also in the case of a multi-channel natural convection.

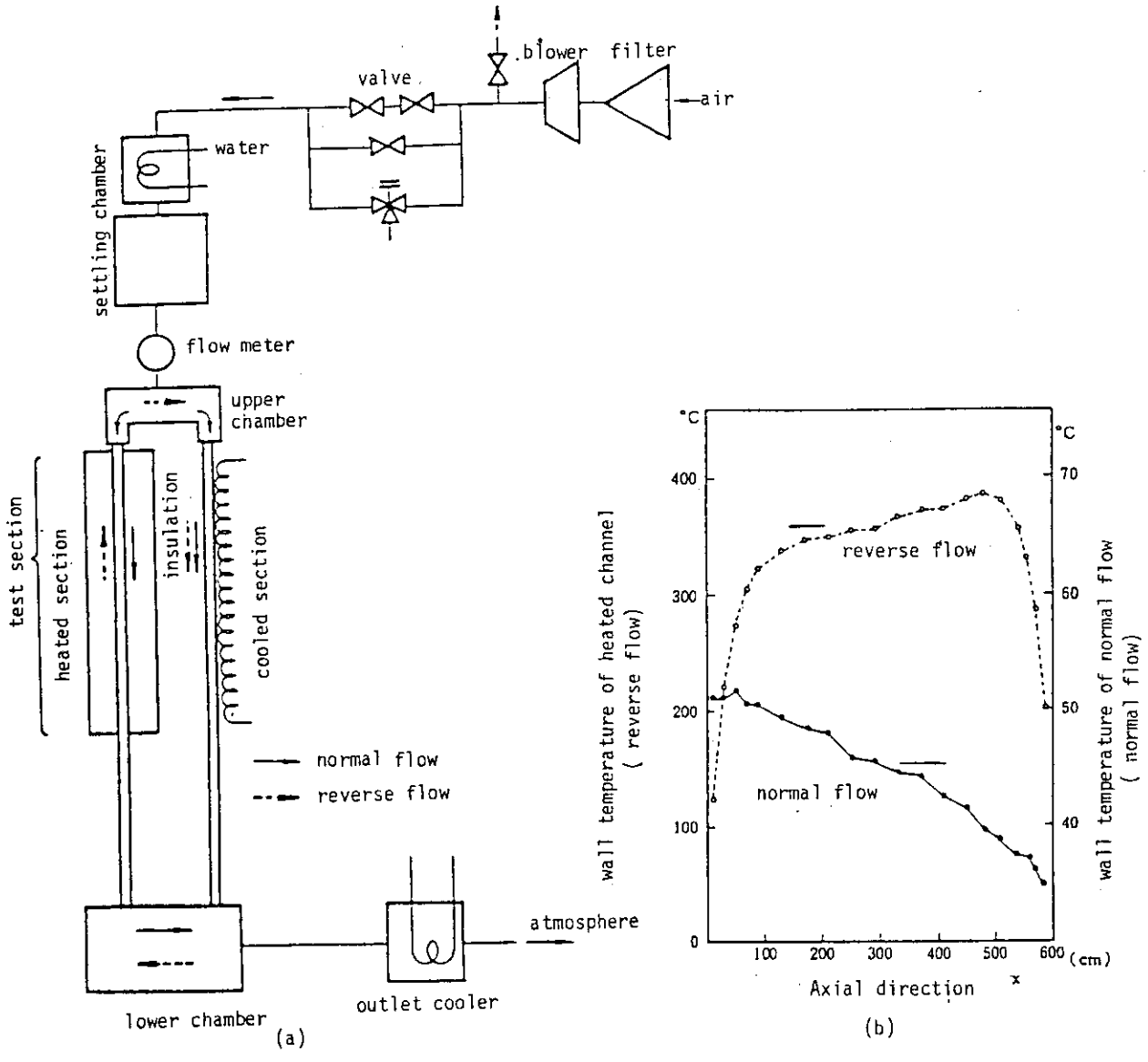

Fig. 3.21 Schematic diagram of reversed flow experiment and an example of temperature profile

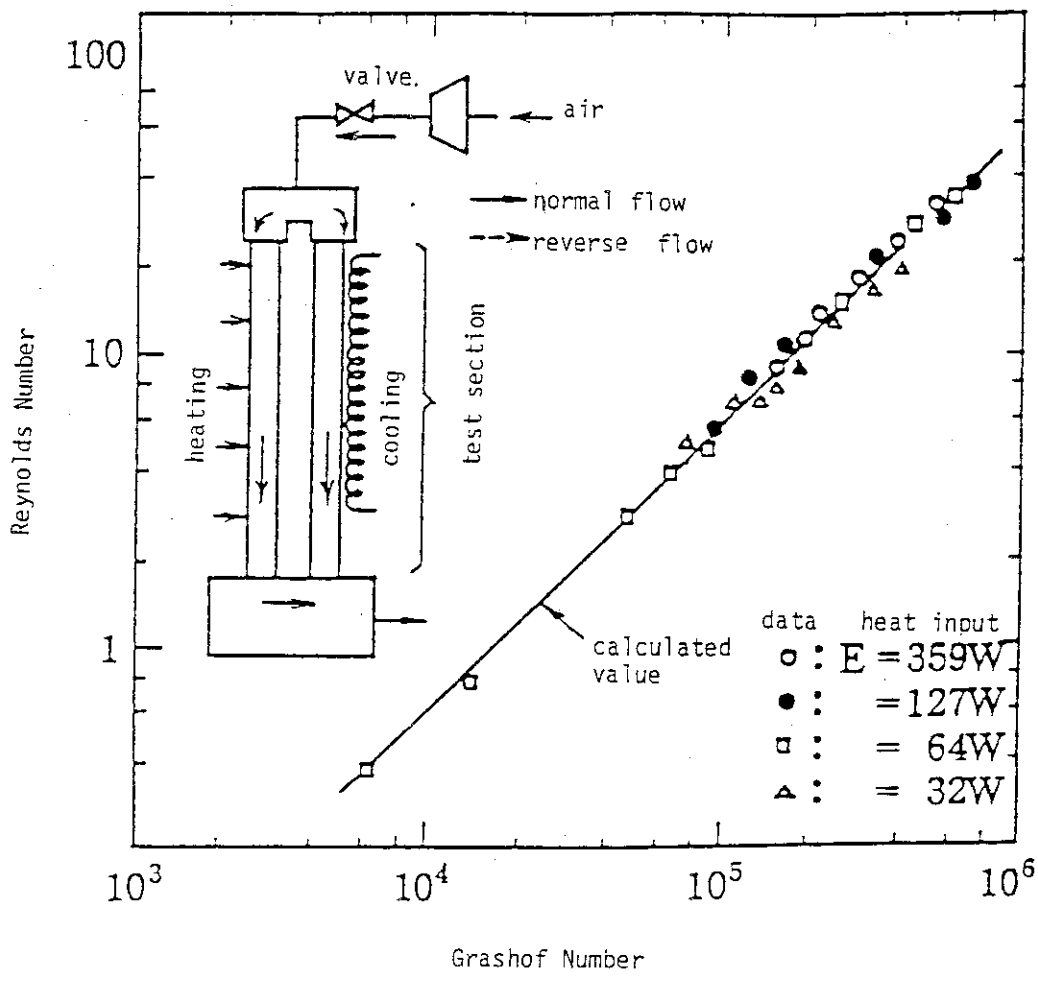

Fig. 3.22 Reynolds number as a function of Grashof number in the case of flow reversal

3.6 Natural Circulation in Parallel Vertical Channels with Different Heat Generations

T. Takeda, M. Seki and H. Kawamura

When forced circulation of coolant in the VHTR is lost, natural circulation takes place in the reactor core. In this case, the temperature of the channels in the center are higher than that in the core-periphery. The coexistence of these parallel vertical channels with different temperatures results in a very complicated natural circulation. Since only few studies were made on this problem, we have carried out an experiment on natural circulation in parallel vertical channels with different heat generations, and also developed a computer code to analyze the flow field.

Numerical analysis

Basic equations describing the natural circulation in parallel channels are momentum and energy equation: Equations (3.5) and (3.6). Rearrangement of the momentum equation yields Eq. (3.7).

$$\rho \frac{\partial u}{\partial t} = - \frac{\partial p}{\partial x} - \rho g - \left(\frac{\lambda}{D_H} + C_\lambda \right) \cdot \frac{1}{2} \rho |u| u \tag{3.5}$$

$$\rho c \frac{\partial T}{\partial t} + \rho c u \frac{\partial T}{\partial x} = \alpha \frac{L_h}{A_f} (T_w - T) \tag{3.6}$$

$$\frac{dm_k}{dt} = A_f (P_1 - P_2)/L_k - \bar{\rho} g A_f - \zeta_k |m_k| m_k \tag{3.7}$$

where $L_k = \int dx$, $\bar{\rho} = \int \rho dx / L_k$, $m_k = \rho A_f u$

$$\zeta_k = \left[\int \frac{\lambda}{2 D_H \rho A_f} dx + \sum_j \frac{C_{\lambda j}}{2 \rho A_f} \right] / L_k \ .$$

Experiment

An experimental apparatus is shown in Fig. 3.23. The test section has 5 vertical annular channels, each of which consists of a glass tube and a heater pin. The four channels are for pure natural circulation, and the other one is equipped with a circulation pump for weak forced circulation. The heater pin is 18 mm in diameter and 1810 mm in length. The effective heating length is 1000 mm and the maximum power is 2 kW. The pyrex glass tube is 27.2 mm in inner diameter and 1300 mm in length, with a branch tube of 0.5 mm in inner diameter to introduce dye for flow visulization.

The present experiment was made for pure natural circulation by using four channels. The power inputs to the channels are shown in Fig. 3.24 as a function of time. The power to the channel 1 (CH1) was kept Q_1 that was lower than boiling initiation. The power to CH2 was Q_2 ($0<Q_2<Q_1$), and zero power to CH4. Then the power to CH3 was increased stepwise from 0 to Q_3 or decreased stepwise from Q_3 to 0 with a small increment or decrement. After a steady state was established, data were taken.

Results and discussion

Experimental and numerical results are shown in Fig. 3.25. The mass flow rate in CH2 and CH3 normalized by the one in CH1; namely, m_2/m_1 and m_3/m_1 are shown as a function of the ratio of the power to CH1 and CH3, Q_3/Q_1. The solid lines indicate numerical results. Figures 3.25(a) and (b) are for $Q_2/Q_1=0$, Fig. 3.25(a) for increasing Q_3, and Fig. 3.25(b) for decreasing Q_3. At the point A in the figures, the flows in CH1 are upward, while the flows in CH2, CH3 and CH4 are all downward at the same mass flow rate. With a slight increase in Q_3 the state moves to the point B in the figures, where the flow directions are the same as the ones at the point A, but m_3 becomes smaller than m_2. With much increase in Q_3 at the point B, the flow direction of CH3 suddenly switches from down to up, and the state shifts to the point C in the figures. With further increase Q_3, the state moves to the point D in the figures.

When Q_3 is decreased from the point D in Fig. 3.25(b), the value of m_3/m_1 traces a curve obtained by increasing Q_3 until it reaches the

point C. Numerical results predict that further decrease in Q_3 makes the value of m_3/m_1 go to the point E, not return to the point B. The point E corresponds to the state where the flow in CH3 stops and the circulation takes place in the other channels. However, the state at the point E is too unstable to be realized in the experiment. The value of m_3/m_1 becomes negative before it reaches the point E, and hence it moves to the stable point A.

Figures 3.25(c) and (d) are for Q_2/Q_1=0.10, and Figs. 3.25(e) and (f) for Q_2/Q_1=0.15.

The flow differs according to the increase or decrease in Q_3. This means that both magnitude and changing history of Q_3 affect the circulating flow.

The numerical results agree well with the experimental results. In the case of the increase in Q_3, numerical results predict well the state where m_3/m_1 changes from negative to positive. At large values of Q_3, however, the experimental data of m_3/m_1 are higher than numerical results; instead, those of m_3/m_1 are lower, as shown in Figs. 3.25(c) and (e). This is partly due to neglecting of pressure losses in the upper and lower plenums in numerical calculations.

In the case of the decrease in Q_3, since the region near Q_3=0 is unstable, a difference between numerical and experimental results is produced, which is markable in Fig. 3.25(f). The further study both experimentally and numerically is now under way.

Nomenclature

A_f	:	Flow area
P_1	:	Lower plenum pressure
P_2	:	Upper plenum pressure
D_H	:	Hydraulic diameter
λ	:	Blasius' friction coefficient
C_λ	:	Accommodation coefficient for pressure drop at inlet and outlet

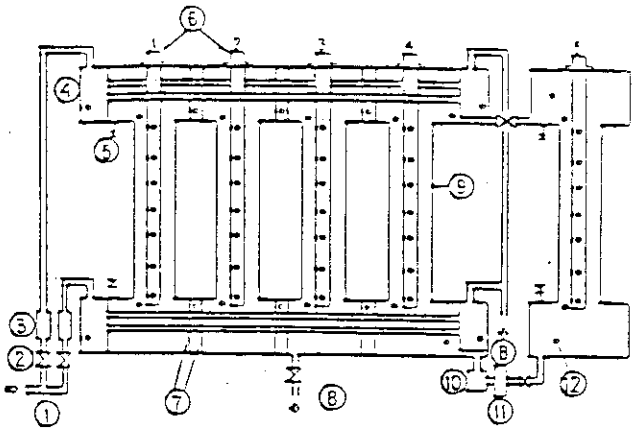

1	Water supply	7	Buffle plate
2	Flow control valve	8	Drain
3	Roter meter	9	Glass tube
4	Cooling water	10	Flow meter
5	Pressure tap	11	Circulation pump
6	Heater pin	12	Thermocouple

Fig. 3.23 Experimental apparatus

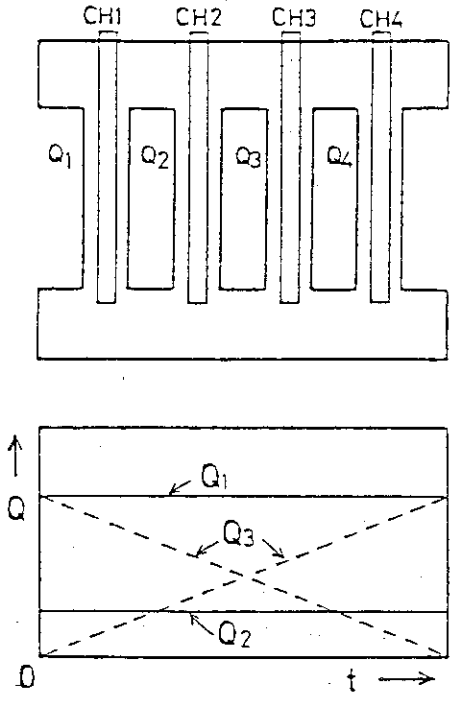

Fig. 3.24 Power inputs to channels as a function of time

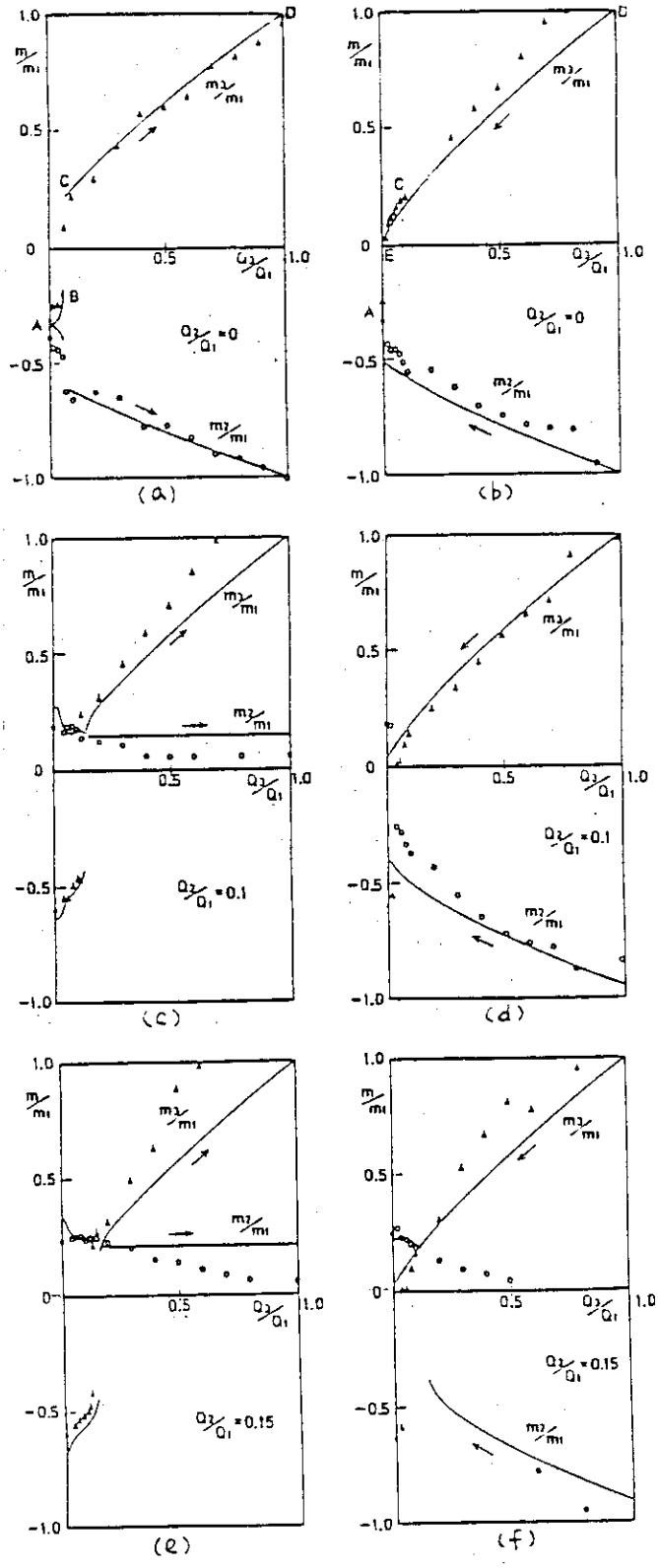

Fig. 3.25 Experimental and numerical results

3.7 Preliminary Thermal Cycling Tests of Tungsten-Copper Duplex Structures for Use as a Divertor Plate

M. Seki, M. Ogawa and A. Minato*

A fusion experimental reactor (FER) is now being designed in JAERI as a next generation machine. FER is equipped with a divertor as an impurity control system. A collector plate of the divertor is inherently exposed to very high thermal and nuclear loadings. Hence a duplex structure, which consists of an efficient heat sink and a protection armor against sputtering erosion, has been proposed in recent fusion reactor designs such as an international tokamak reactor (INTOR)[1]. FER employs a copper heat sink with a tungsten armor (W-Cu duplex) for the collector plate.

Two methods for bonding the tungsten tile to the copper heat sink have been discussed in INTOR workshop, namely brazing and mechanical contact. Basically a brazed structure gives rise to a large thermal contact conductance between the armor and the heat sink; a mechanically contacted structure, however, a small conductance. As the armor in mechanical contact is cooled only by radiation, it is heated up to a very high-temperature at which the tungsten will recrystallize. Since recrystallized tungsten is very brittle at low temperatures, it is preferable to employ a bonding method to produce the larger thermal conductance. In this case, however, large thermal stresses will be generated near the joint owing to the difference in thermal expansion coefficients, and cyclic plasma burning will result in thermal cycling of the joint of the tightly fixed duplex structure. Since only limited data are available on the thermal fatigue characteristics of W-Cu duplex, we have conducted an experiment to study the behavior of W-Cu joint under thermal cycling.

Experiment and results

An experimental apparatus is given in Fig. 3.26. Two test pieces of W-Cu duplex brazed with silver were prepared. A test piece was placed

---

* Department of Large Tokamak Development

in a plasma flow conduit pipe of 90 mm in diameter. In order to simulate the high heat flux in the collector plate, a high-temperature argon plasma flow was used to apply heat flux on the tungsten surface. The back surface of the copper was cooled by water. A structure of the test piece is shown in Fig. 3.27. A tungsten disk, 50 mm in diameter and 20 mm in thickness was brazed to a copper disk with the same diameter as was machined to accommodate cooling and supporting structures. Three thermocouples were mounted in the copper disk to measure temperatures in the vicinity of the joint and the cooled surface. The incident heat flux to the test piece was estimated by temperature drop in the copper disk (temperature difference between TC-2 and TC-3). Thermal stresses were estimated by using a finite element computer code. The brazing of tungsten and copper was considered to be ideal, and the thermal resistance at the interface and the thickness of the brazing zone were assumed to be zero.

At first, temperature distribution in the test piece was calculated on the assumption that the heat flux predicted by temperature drop in the copper disk was given to the tungsten surface and the temperature of the cooled wall was kept constant. Then, thermal stresses were computed for the temperature distribution. Hoop stresses along the center line are plotted against the vertical positions in Fig. 3.28. The stresses at the joint are estimated to be about 320 MPa in tungsten and about 220 MPa in copper.

200 times thermal cycling were appled for the test piece No.1, and 1100 times for No.2. No breaking-away and no observable cracks were found in both test pieces. The experiment is still in progress.

When we started the experiment, it was a serious concern that the brazed structure of tungsten and copper might be damaged in a small number of thermal cycling. The present result, however, proves that this structure can withstand for 1100 times thermal cycling.

Reference

1) IAEA : INTOR, Phase One, Report of IAEA Tokamak Reactor Workshop, IAEA (1982).

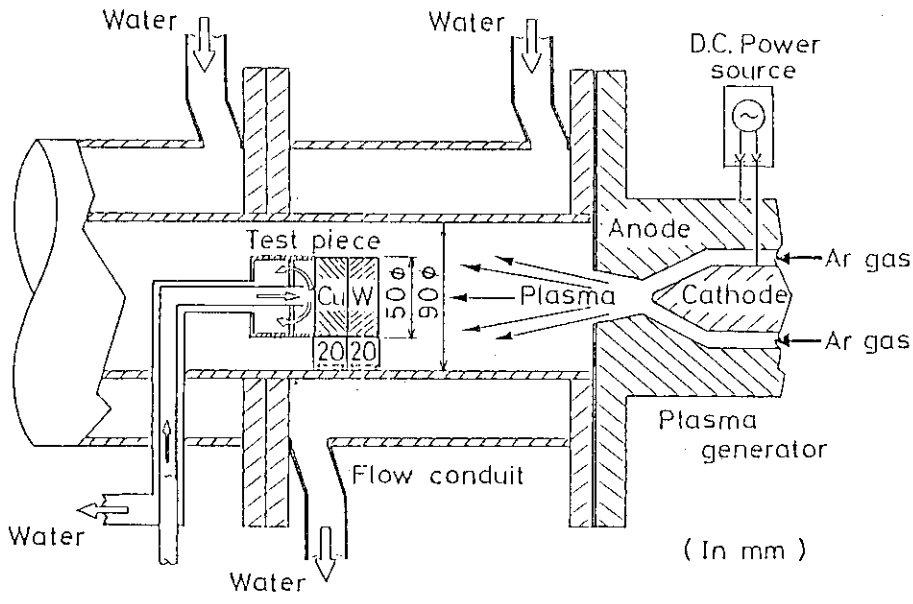

Fig. 3.26 Experimental apparatus

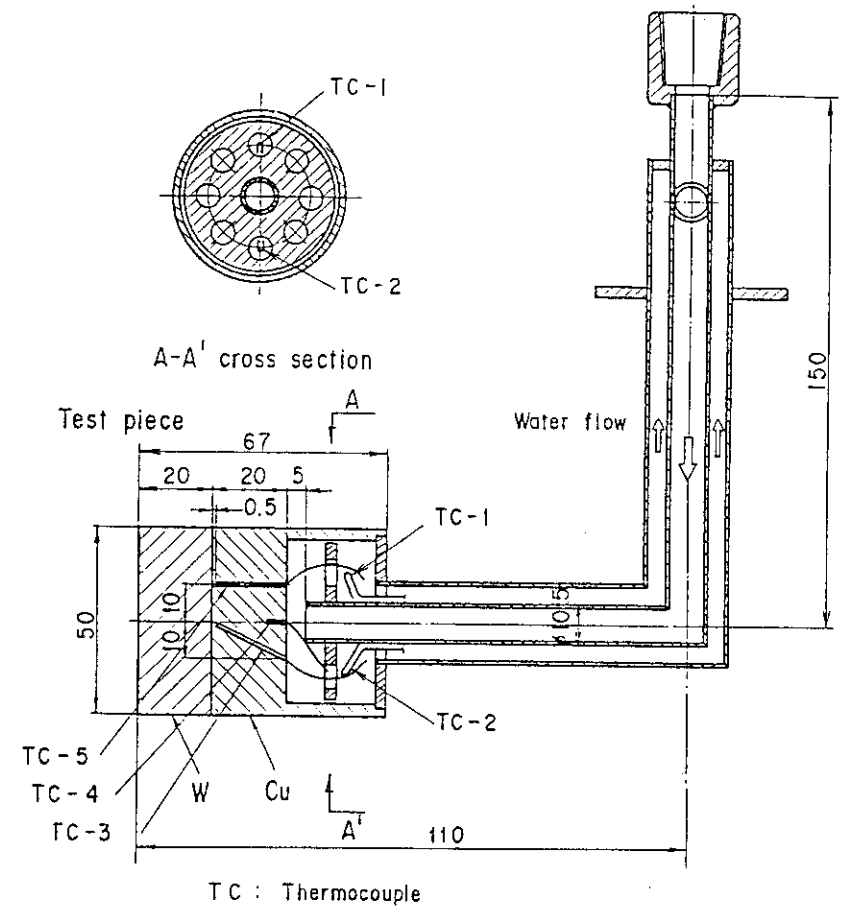

Fig. 3.27 Test piece

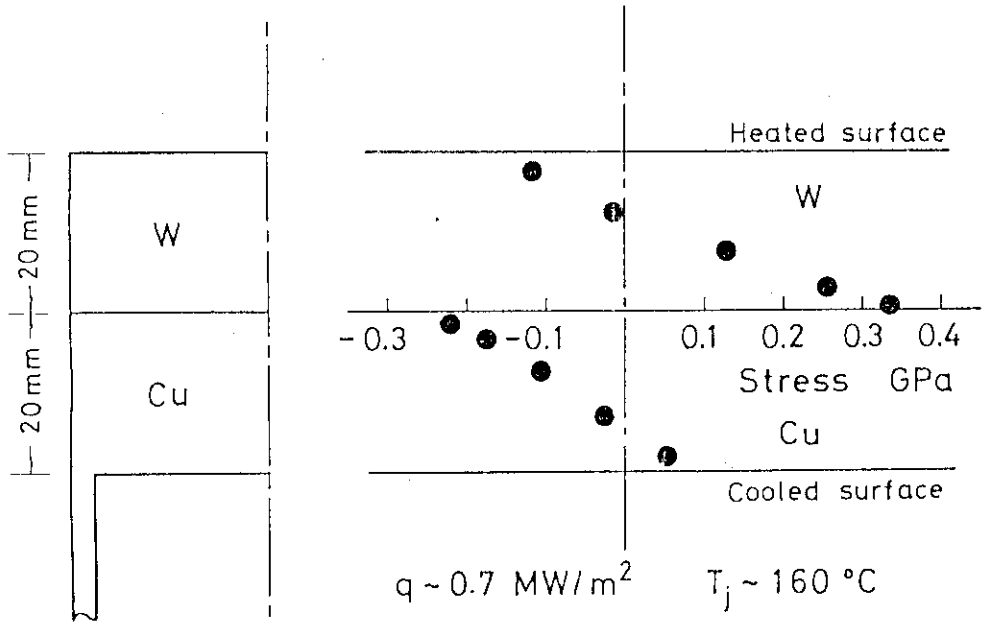

Fig. 3.28 Hoop stresses along the center-line of the test piece

4. RESEARCH ON STRUCTURAL MATERIALS

4.1 Screening Test of Thermal Barrier Materials

M. Eto, K. Fujisaki, S. Yoda, S. Ishiyama and T. Oku

Screening test of thermal barrier materials for the VHTR started in 1982 and was completed this fiscal year. Six kinds of carbon materials, three of which were manufactured abroad and the other three manufactured in Japan, were extensively examined. Tests have been also carried out on such reference materials as silicon nitride and pyrolytic graphite.

Experiments

The test items were: Young's modulus, bending strength, compressive strength, fracture toughness and Shore hardness. Tensile tests were done for only several materials selected. Physical and chemical properties were measured in Graphite Research Laboratory in collaboration with Materials Strength Laboratory.

Results and discussion

Table 4.1 summarizes the data obtained for the carbon materials which were manufacutred abroad, pyrolytic graphite and silicon nitride. In comparison of ASR-ORB with ASR-1RB it is apparent that impregnation increases the Young's modulus and strength pronouncedly.

The data obtained for domestic carbon materials are summarized in Table 4.2 and the strength of LCM-1 is found to be the highest. The strengths of the other two domestic materials as well as PG41 are fairly low.

Figure 4.1 shows compressive stress-strain curves of ASR-1RB carbon. The data indicate that the fracture stress is higher and fracture

strain is lower, as compared with the corresponding graphite, ASR-1RG.

In the future high-temperature data on the strength and Young's modulus will be obtained for the selected materials. Detailed measurements such as the variation of strength within a large block will also be made.

Table 4.1 Mechanical properties of several candidate graphite for thermal barrier of the VHTR

Test items	Specimen size (mm)	Specimen direction (*)	ASR－0RB (SIGRI)	ASR－1RB (SIGRI)	PG－41 (UCC)	Pyrolytic graphite	Silicon nitride
Bulk density (g/cm³)	6φ×50 or 9φ×80	AG	1.691±0.008 (20)	1.734±0.011 (20)	1.653±0.011 (20)	2.229	outer 1.966±0.016 (9) center 1.979±0.010 (10)
		WG	1.678±0.012 (20)	1.740±0.015 (20)	1.654±0.010 (20)		
Young's modulus (GPa)	6φ×50 or 9φ×80	AG	7.98±0.19 (20)	14.2±0.2 (20)	4.15±0.12 (20)	c : 28.95 a_1 : 77.59 a_2 : 69.25	outer 57.5±2.5 (9) center 58.4±1.8 (10)
		WG	8.44±0.19 (20)	15.6±0.4 (20)	4.77±0.17 (20)		
Tensile strength (MPa)	18.1φ×100 gage length (5φ×40)	AG	planned	unplanned	unplanned	unplanned	outer 12.6±2.9 (9) center 13.1±3.4 (5)
		WG					
Compressive strength (MPa)	6φ×12 or 9φ×22.5	AG	75.2±2.9 (20)	92.7±6.2 (10)	26.5±0.9 (20)	C : 271±33 (10)	outer 104±15 (10) center 86.2±22.1 (10)
		WG	71.9±3.2 (20)	93.8±5.4 (10)	24.3±0.8 (20)	a : 111±6 (10)	
Bending strength (MPa)	6φ×50 or 9φ×80	AG	16.6±2.7 (20)	21.8±1.5 (20)	9.06±0.68 (20)	C : 4.41±1.27 (10) a_1 : 112±11 (6) a_2 : 79.2±13.1 (5)	outer 29.7±5.4 (9) center 30.3±4.3 (10)
		WG	18.2±1.1 (20)	23.2±1.7 (20)	9.12±0.51 (20)		
Fracture toughness (MPa・m$^{1/2}$)	10×10×55	AG	0.74±0.01 (5)	0.92±0.03 (4)	0.40±0.01 (5)	unplanned	unplanned
		WG	0.76±0.02 (5)	1.12±0.03 (5)	0.44±0.00 (5)		
Shore hardness	12×12×25	AG	56.1±7.7 (50 points)	71.6±14.8 (90 points)	25.2±3.5 (60 points)	unplanned	unplanned
		WG	55.4±9.2 (50 points)	65.4±14.8 (30 points)	23.7±2.7 (60 points)		

( ): Number of specimens tested

AG or WG : parallell or perpendicular to the longitudinal axis of the block

Table 4.2 Mechnical properties of three domestic carbon materials

Test items	Specimen size (mm)	Specimen direction	C 140 X	EG - 100 B	LCM - 1	Number of specimens
Bulk density (g/cm^3)	9φx80	AG	1.572 ± 0.006	1.647 ± 0.012	1.562 ± 0.003	20
		WG	1.569 ± 0.006	1.645 ± 0.007	1.569 ± 0.009	20
Young's modulus (GPa)	9φx80	AG	5.91 ± 0.22	7.81 ± 0.44	8.31 ± 1.16	20
		WG	7.66 ± 0.55	7.63 ± 0.37	9.53 ± 0.46	20
Bending strength (MPa)	9φx80	AG	6.47 ± 0.56	6.93 ± 1.51	19.85 ± 1.30	20
		WG	6.76 ± 0.96	4.97 ± 0.86	25.10 ± 1.97	20
Compressive strength (MPa)	9φx22.5	AG	28.7 ± 1.3	29.5 ± 3.5	81.9 ± 3.7	20
		WG	23.4 ± 2.1	19.1 ± 1.7	90.1 ± 5.1	20
Fracture toughness ($MPa \cdot m^{1/2}$)	10x10x55	AG	0.276 ± 0.031	0.413 ± 0.114	0.581 ± 0.006	5
		WG	0.397 ± 0.050	0.378 ± 0.033	0.645 ± 0.028	5
Shore hardness	10x15x25	AG	35.9 ± 11.6	39.9 ± 10.5	52.4 ± 2.4	60 (points)
		WG	44.9 ± 10.7	38.6 ± 11.1	55.3 ± 1.6	60

AG, WG : parallell or perpendicular to the longitudinal axis of the block

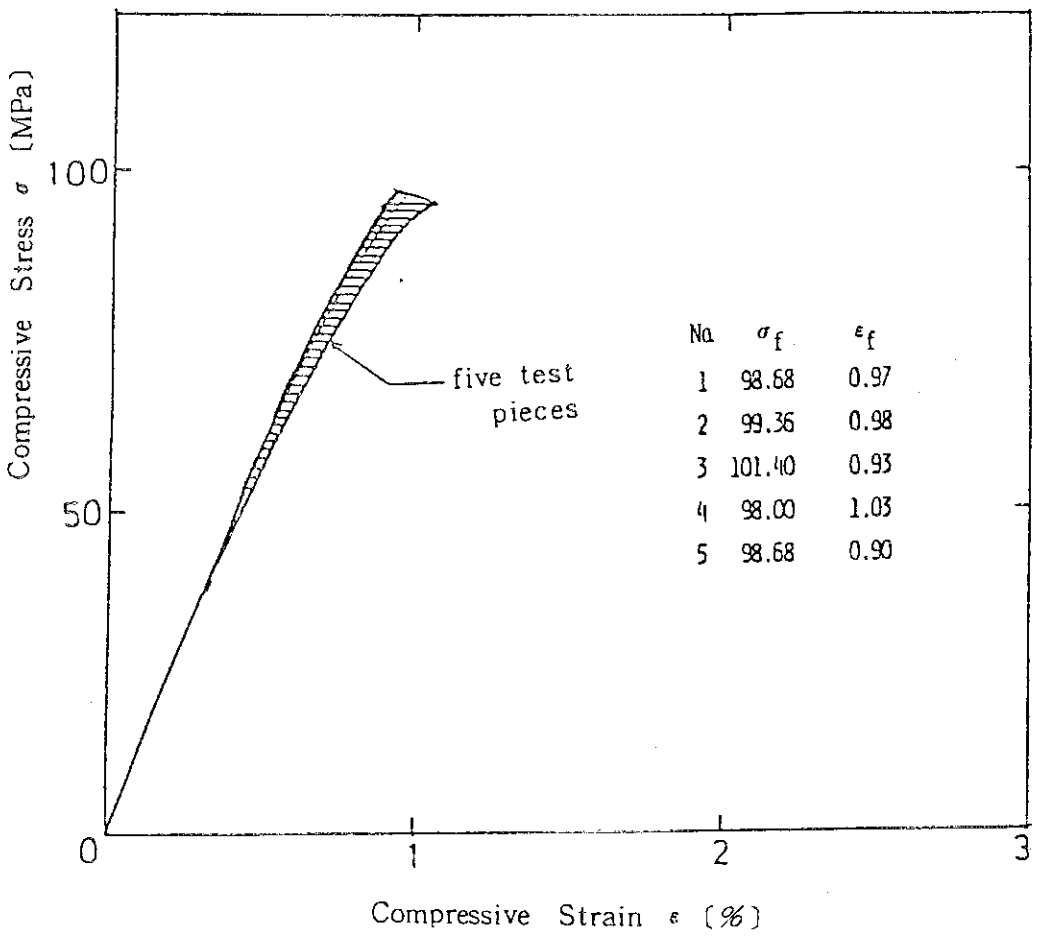

Fig. 4.1 Compressive stress-strain curves of ASR-1RB carbon

4.2 Fracture Toughness Test of Nuclear Graphites

S. Ishiyama, T. Sogabe, T. Oku and M. Eto

Under the conditions of reactor start-up, operation and shutdown, graphite components in the VHTR are subjected to thermal stress, irradiation induced stress and vibration caused by pressure fluctuation of helium coolant and earthquakes. Under these stresses, graphite which has micro cracks or flaws is possibly damaged or fractured owing to crack extention. From the standpoint of the VHTR safety, it is very important to estimate the resistibility to crack onset (fracture toughness) and extension (tearing modulus) of brittle material as graphite. However, fracture toughness test is accompanied with such difficult problems as the definition of crack front and a large scatter of data. A few results on fracture toughness[1,2,3] have been reported so far. The main purpose of this study is to examine the meaning of fracture toughness values obtained here and of tearing modulus defined as resistibility to crack extension. Elastic plastic fracture toughness (J_{IC}) tests were done according to ASTM-E813 recommended for metals.

Expeimental procedure

1) Material and specimen

Materials tested are purified fine-grained isostatically-pressed graphite IG-110 (Toyo Tanso Co., Ltd.) and anisotropic molded graphite PGX (UCC). These brands have the mechanical properties shown in Table 4.3. The size of IG-110 and PGX blocks were 230 x 540 x 850mm and 900ϕ x 210mm half circle respectively. Specimens for IG-110 graphite were machined in such a way as the direction of crack extension was perpendicular to the longitudinal axis of the blocks, as shown in Fig. 4.2. Specimens for PGX graphite were cutout in such a way as the direction of crack extension was perpendicular to the molding axis (//) or parallel to the molding axis ($\perp$). Five compact tension (CT) specimens recommended by ASTM-E399 were prepared for each graphite. Dimensions of the specimen are shown in Fig. 4.3.

2) Apparatus

CT specimens were fractured under a stroke-controlled condition using a one-ton servo-pulser testing machine at a cross-head speed of 0.01 mm/min. Load-displacement curve was recorded with loadline displacement (V_{LL}) measured by a COD (Crack opening displacement) gage (travel range:±2mm) clipped on knife edges placed on the loadline of CT specimen. During unloading, crack extension Δa was measured by a comparator (x50 mag.). J-integral values on the basis of the procedure detailed in ASTM-E813 were calculated from the area enclosed by a load-loadline displacement curve.

Result

In Figs. 4.4, 4.5 and 4.6, load-loadline displacement curves ($P\text{-}V_{LL}$) and change of crack extension of IG-110, PGX(//) and (⊥) are shown. Especially, in the case of IG-110, unstable fracture occurred after a peak load P_{max}. A J-Δa curve obtained from these data of all brands are shown in Figs. 4.7, 4.8 and 4.9. Where, the range of crack extension Δa was taken within 5mm, because the critical crack extension a_{cr} at which an unstable fracture initiates is known to be within about 5mm for all brands of graphites. J-Δa curves are almost linear shown as a solid line in the figures. These results indicate that the stable crack extension of graphites can be characterized by a slope dJ/da of the linear part. Definition of crack extension point (J_i) as the intercept of linear part is also possible. However, at the value J_{in} a little less than J_i, 0.01mm crack initiation from the tip of a notch is already observed by optical observations. Therefore it is believed that very slow crack extensions occur continously between the J-values J_i and J_{in}. These J-values of crack initiation J_{in} and intercept J_i and the slope dJ/da are tabulated in Table 4.4 Though PGX graphite, whose J_{in} and J_i are low, seems to have more resistibility against crack extension than IG-110, it is considered to be attributed to the difference of permanent deformation zone at the crack tip, including micro cracking region.

References

1) Marshall P. & Priddle E. K.: Carbon 11, 541(1973).
2) Ho F. H. et al.: GA-A16310.
3) Sato S. et al.: Carbon, 16, 95(1978).

Table 4.3 Mechanical properties of tested graphite

Item / Test specimen	Bulk density (d) [g/cm³]	Tensile strength (T_s) [MPa]	Compressive strength (C_s) [MPa]	Bending strength (B_s) [MPa]	Young's modulus (E) [MPa]
IG-110	1.77	24.4	71.2	33.6	8500
PGX(//)	1.73	7.8	33.6	14.9	6600
PGX(⊥)	1.73	7.3	30.4	15.6	8240

Table 4.4 Crack onset J-value and tearing modulus of IG-110 and PGX

Graphite grade	Specimen No.	Young's modulus [Gpa]	J_{in} [MPa·m]	J_i [MPa·m]	dJ/da [Mpa]
IG-110	2	8.50	0.979	0.887	0.0173
	3		0.907	0.871	0.0143
	5		0.775	0.790	0.0176
PGX(//)	2	6.60	0.377	0.522	0.0249
	3		0.304	0.391	0.0221
	4		0.374	0.360	0.0267
PGX(⊥)	3	8.24	0.714	0.776	0.0214
	4		0.539	0.489	0.0286
	5		0.923	0.815	0.0243

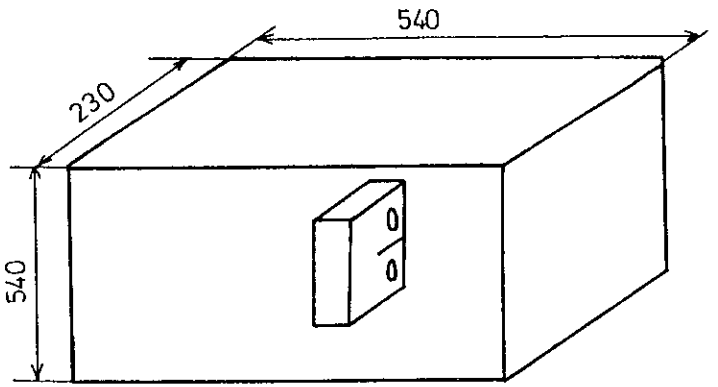

Sampling direction for IG-110

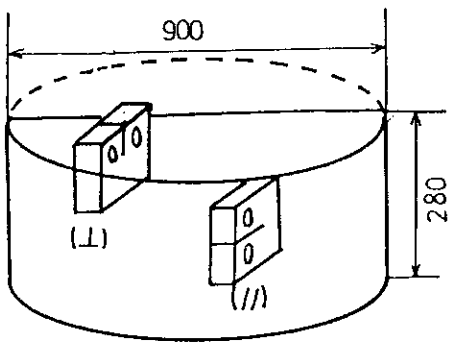

Sampling direction for PGX

Fig. 4.2 Sampling direction for IG-110 and PGX graphites

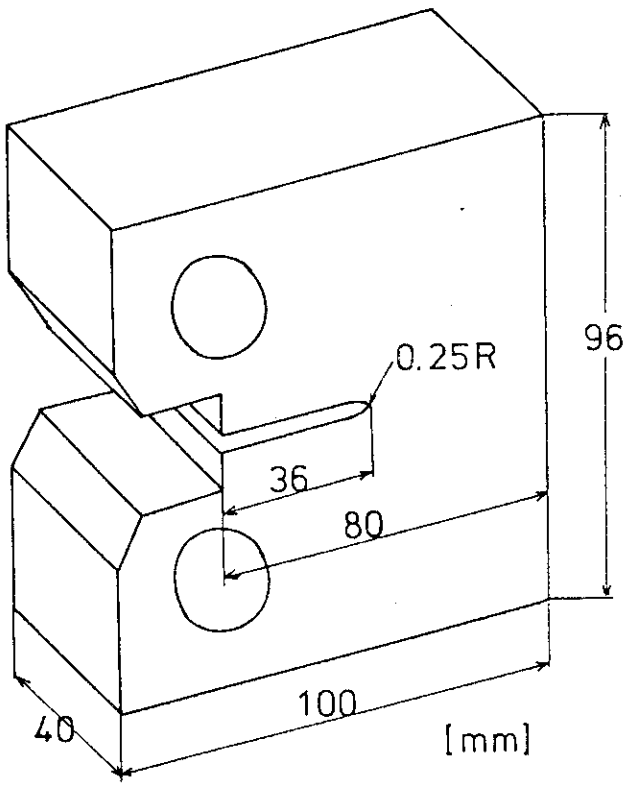

IG-110
PGX(//)
PGX(⊥)
5 pieces
for each

Compact Tension (CT) specimen

Fig. 4.3 Dimension of CT specimen

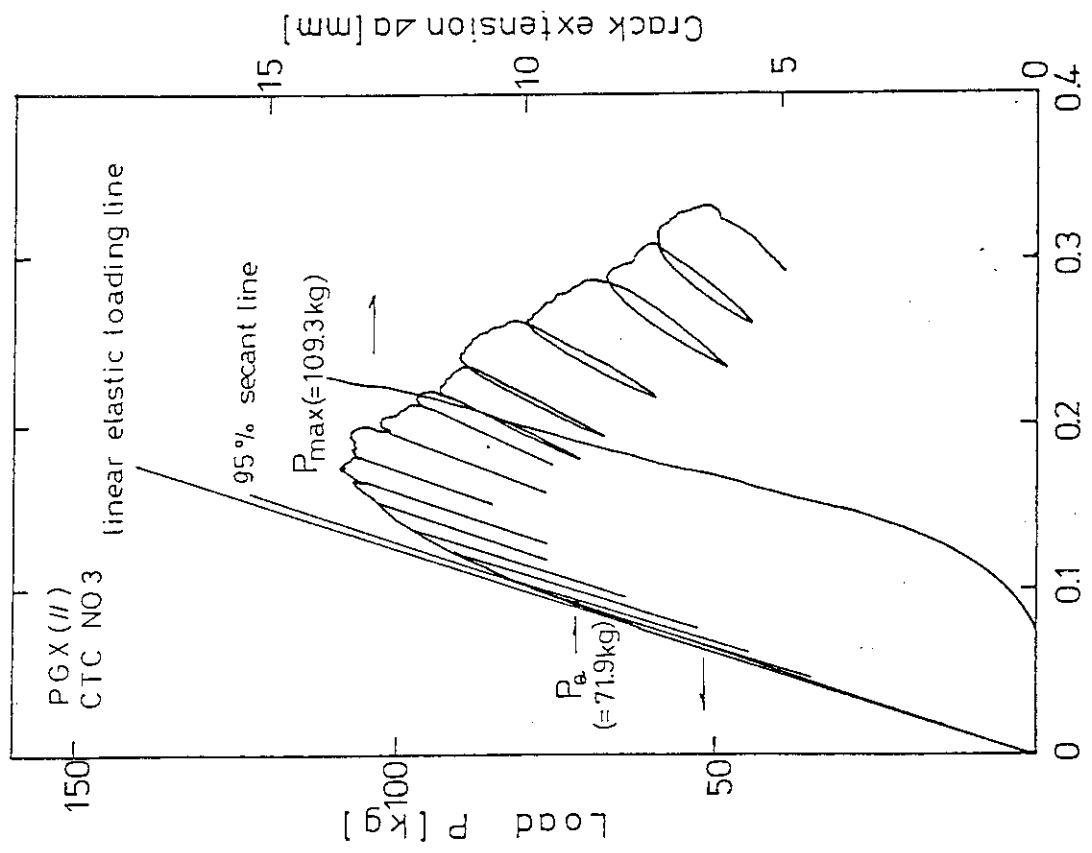

Fig. 4.5 P-V_{LL} curve of PGX(//) graphite

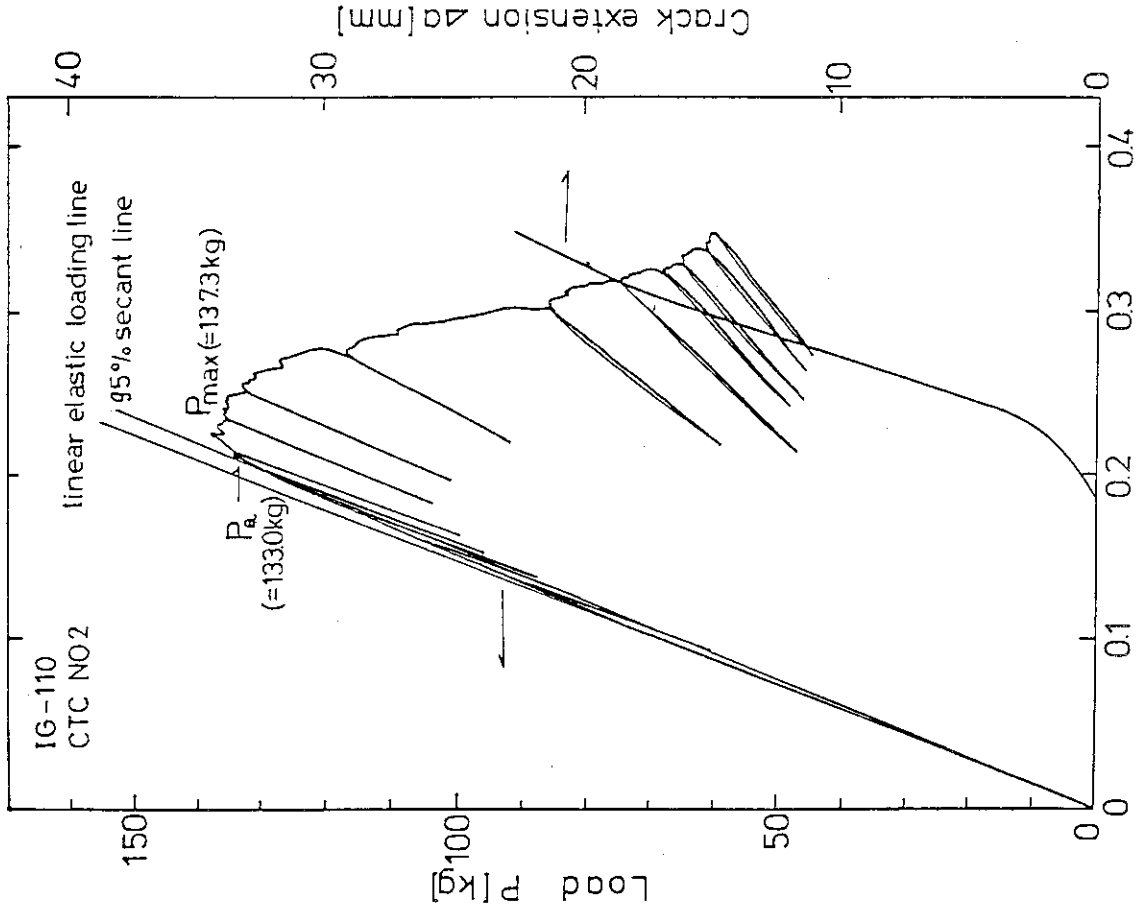

Fig. 4.4 P-V_{LL} curve of IG-110 graphite

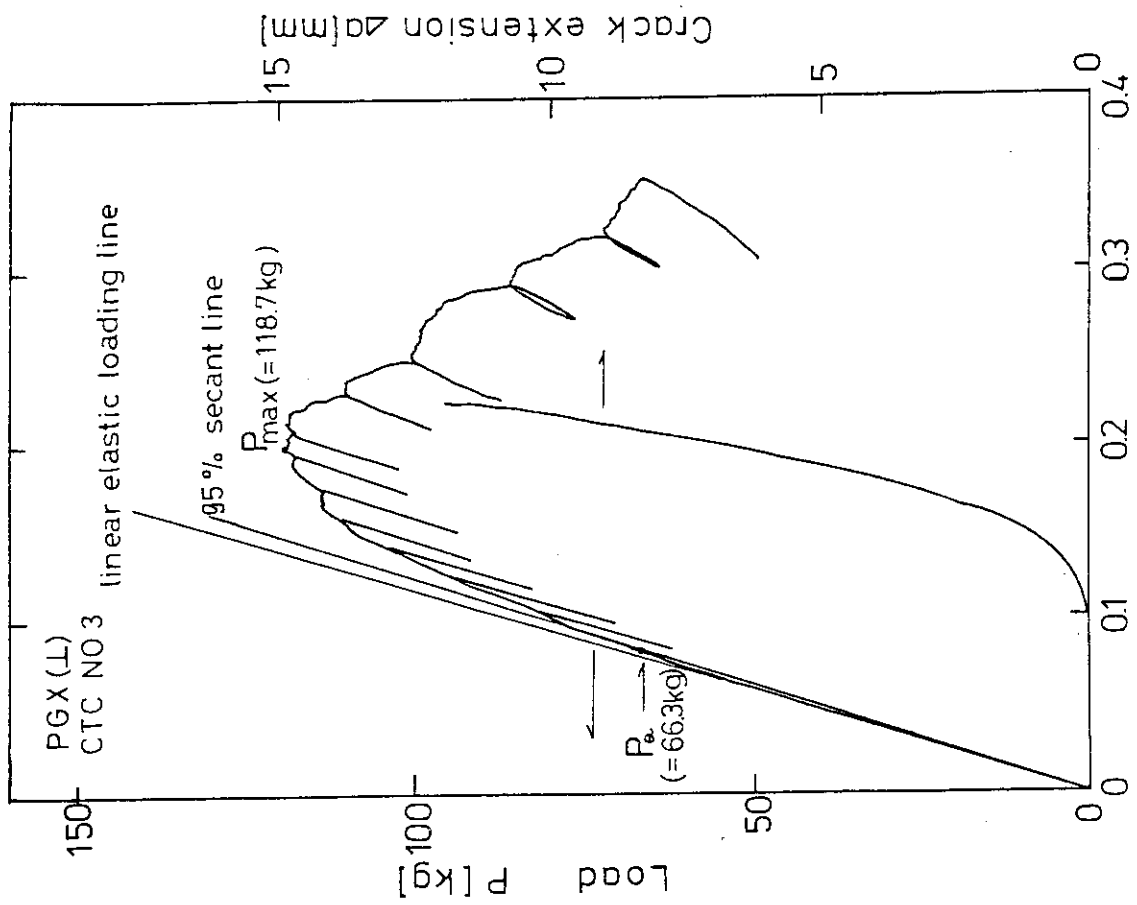

Fig. 4.6 P-V_{LL} curve of PGX(⊥) graphite

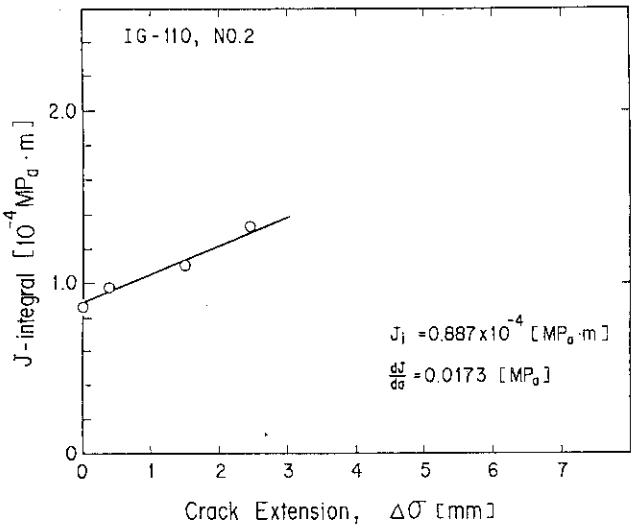

Fig. 4.7 J-Δσ curve of IG-110 graphite

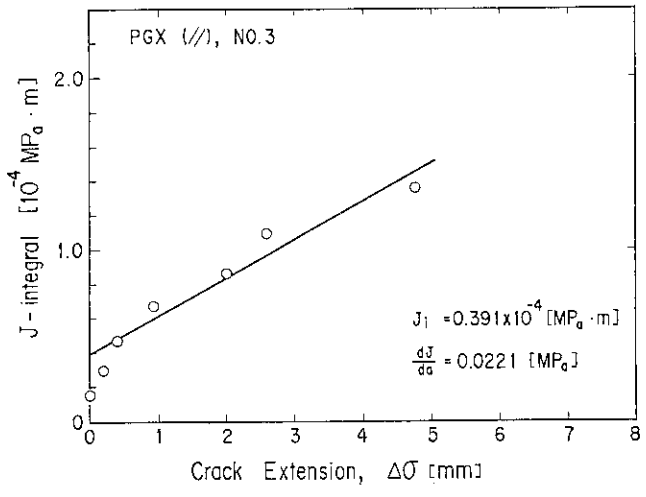

Fig. 4.8 J-Δσ curve of PGX(//) graphite

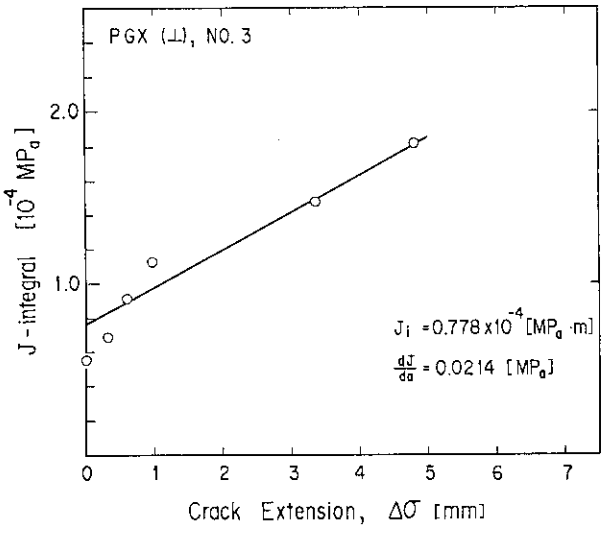

Fig. 4.9 J-Δσ curve of PGX(⊥) graphite

4.3 Effects of Oxidation on Compressive Deformation Behavior of Nuclear-Grade Isotropic Graphite

S. Yoda, K. Tanaka, M. Eto and T. Oku

Degradation of mechanical properties of nuclear graphite caused by thermal oxidation is one of the most serious problems for safety analysis and design of the HTGR. Extensive efforts have been made to investigate the effects of oxidation on the strength and Young's modulus[1-4]. However, further studies are still required to establish a thorough understanding of the subject.

In the present work, we examine first the deformation behavior of an isotropic graphite uniformly oxidized. This kind of graphite is a candidate material for the VHTR. The analysis for uniform oxidation has been extended to be applied to those with oxidation gradient (non-uniform oxidation).

Experiments

Oxidation was carried out in stagnant air using an electric furnace for two kinds of specimens with dimensions of 12 mm square by 25 mm long and 24 mm in diameter by 48 mm long respectively. Rectangular specimens were uniformly oxidized at 773 K, while cylindrical specimens non-uniformly at 973 K. Burn-off and density change were calculated from the weight loss and dimensions measured after the oxidation. Uniform oxidation did not usually result in significant dimensional changes.

Results and discussion

Table 4.5 summarizes stress-strain data for oxidized and unoxidized specimens with various values of σ/σ_0, where σ_0 and σ represent stresses of pre- and post-oxidized specimens respectively. It is interesting to note that σ/σ_0 is almost constant irrespectively of strain. The relationship between the ratio σ/σ_0 and burn-off level σ/σ_0 is shown on a logarithmic scale in Fig. 4.10. Using the least squares method for more than 80 data points, an empirical formula was obtained.

$$\frac{\sigma(\varepsilon)}{\sigma_0(\varepsilon)} = \left(\frac{\rho}{\rho_0}\right)^{4.56}, \tag{4.1}$$

where $\sigma(\varepsilon)$ denotes a stress at a given strain for the specimen uniformly oxidized to a density level of ρ. This equation means that stress-strain relationship for the oxidized specimen can be predicted on the basis of the data for unoxidized one and density change ρ/ρ_0 by oxidation.

Next, the analysis is proceeded to evaluate a compressive stress-strain relationship of a cylindrical specimen. If a hollow tube with inner and outer radii r and r+dr has density ρ and stress σ, a total applied load P is expressed by

$$P = \int 2\pi\sigma r dr. \tag{4.2}$$

As r is a function of ρ, namely

$$r = f(\rho), \tag{4.3}$$

from Eqs. (4.2) and (4.3), p can be rewritten as

$$P = \int_{\rho_c}^{\rho_s} 2\pi\sigma f(\rho) f'(\rho) d\rho, \tag{4.4}$$

where ρ_s and ρ_c are densities at the surface and the center of the specimen respectively. From Eq. (4.1), we get

$$\sigma(\varepsilon) = A\sigma_0(\varepsilon)\rho^{4.56}, \tag{4.5}$$

where A is expressed as $A = \rho_0^{-4.56}$. Substituting Eq. (4.5) into Eq. (4.4), we get

$$P = \sigma_0(\varepsilon) 2\pi A \int_{\rho_c}^{\rho_s} \rho^{4.56} f(\rho) f'(\rho) d\rho. \tag{4.6}$$

It is worthwhile to note that Eq. (4.6) can easily be integrated, as two variables, ε and ρ, are separated. Thus a stress-strain relationship with oxidation gradient whose profile is shown in Fig. 4.11 can be given by

$$\sigma(\varepsilon) = \frac{2A\sigma_0(\varepsilon)}{r_s^2} \int_{\rho_c}^{\rho_s} \rho^{4.56} f(\rho) f'(\rho) d\rho, \tag{4.7}$$

where r_s is the outer radius of the speciemn. This equation indicates that the compressive stresses of the specimens with oxidation gradient can be calculated from the stresses of the unoxidized specimen multiplied by a constant. This method of prediction is clearly verified in Table 4.6, where the stresses at a given strain for specimens A and B whose stress-strain curves are shown in Fig. 4.12 and σ/σ_0 are indicated. Burn-off of specimens A and B measured from weight loss are 4.75% and 11.75% respectively. It is seen from this table that σ/σ_0 is almost constant irrespectively of strain. These experimental results are in good agreement with the analysis. It is, therefore, concluded that Eq. (4.7) can be applied to the calculation of stress-strain relationship for the specimens with oxidation gradient. The density profile for specimen A shown in Fig. 4.13 is approximated as follows:

$$\begin{aligned} r &= 12.44 - 0.53\rho && \rho_s = 1.12 \leqq \rho \leqq 1.50 \\ r &= 169.98 + 233.05\rho - 74.77\rho^2 && 1.50 \leqq \rho \leqq 1.75 \\ r &= 1496 - 850\rho && 1.75 \leqq \rho \leqq 1.76 = \rho_c \end{aligned} \qquad (4.8)$$

where r and ρ are expressed in units of mm and g/cm^3 respectively. Substituting Eq. (4.8) into Eq. (4.7) with the aid of Eq. (4.1), we obtain

$$\sigma(\varepsilon)/\sigma_0(\varepsilon) = 0.82. \qquad (4.9)$$

This value agrees well with the measured ratio of flow stress σ/σ_0 for specimen A shown in Table 4.6. Also, the oxidation profile for the specimen B was expressed as similar polynominal equations and a similar calculation was carried out for the specimen B. We obtain $\sigma(\varepsilon)/\sigma_0(\varepsilon) = 0.65$, which also agrees well with experimental result shown in Table 4.6. The calculated stress-strain relationship is given in Fig. 4.12 by broken lines, showing an excellent agreement with the measurement.

Summary

The compressive deformation behavior of nuclear-grade uniformly oxidized isotropic graphite IG-11 was studied in detail, and a semiempirical analysis has further been proceeded for the specimen with oxidation gradient.

The ratio of flow stress σ/σ_0 at the same total strain is almost constant irrespectively of strain, and decreases with increase in burn-off. The stress-strain relationship for graphite with oxidation gradient can be reproduced analytically fairly well using the relationship for uniformly oxidized one.

In addition, the compressive fracture strength of the uniformly oxidized graphite is correlated to the apparent density.

Plastic strain caused by applied compressive stress is expressed as a function of burn-off.

The ratio of Young's modulus of the uniformly oxidized graphite is expressed as a function of burn-off, which also reproduces well the nature of the graphite with oxidation gradient.

References

1) Eto M. and Growcock F. B. : BNL-NOREG-51439 (1981).
2) Walker P. L., Rusinko Jr. F. and Austin L. G. : Adv. Catalysis 11, 133 (1959).
3) Sugihara T and Eto M. : Inter. Symposium on Carbon, p. 244, (Toyohashi, Japan), (1982).
4) Eto M. and Sugihara T. : ibid., p. 240 (1982).

Table 4.5 Flow stress of unoxidized specimen under compressive stress and flow stress ratios of specimens oxidized to various burn-off levels to that of the unoxididez specimen at any strains, each ratio being almost constant irrespectively of strain

Total Strain	VIRGIN ρ_o=1.76	0.9% B. O.		3.8% B. O.		6.0% B. O.		9.6% B. O.		16.0% B. O.	
(%)	Stress(MPa) σ_o	Stress	σ/σ_o	Stress	σ/σ_o	Stress	σ/σ_o	Stress	σ/σ_o	Stress	σ/σ_o
0.25	16.67	14.09	0.88	12.28	0.74	11.83	0.71	10.83	0.65	8.90	0.53
0.50	29.38	26.11	0.89	22.20	0.76	21.02	0.71	18.75	0.64	15.53	0.53
0.75	39.45	33.89	0.86	30.18	0.76	28.26	0.71	25.07	0.64	20.39	0.52
1.00	47.58	40.83	0.86	36.53	0.77	34.07	0.71	29.86	0.63	24.43	0.51
1.25	53.99	46.44	0.86	41.64	0.77	38.56	0.71	33.73	0.63	27.63	0.51
1.50	59.27	51.04	0.86	45.84	0.77	42.23	0.71	37.00	0.63	30.12	0.51
1.75	63.44	54.81	0.86	49.32	0.78	45.19	0.71	39.85	0.63	32.08	0.51
2.00	66.90	58.08	0.87	52.18	0.78	47.74	0.71	42.40	0.64	33.74	0.50
2.25	69.95	60.73	0.87	54.64	0.78	49.88	0.71	44.40	0.64	35.29	0.51
2.50	72.59	63.28	0.87	56.79	0.78	51.72	0.71	46.47	0.64		
2.75	74.83	65.32	0.87	58.73	0.79	53.46	0.71	48.21	0.64		
3.00	76.86	67.16	0.87	60.34	0.78	54.68	0.71	49.53	0.64		
3.25	76.96	68.90	0.90	61.90	0.80	56.01	0.73				
3.50	80.32	70.43	0.88	63.34	0.79	56.59	0.71				
		Average	0.87		0.78		0.71		0.64		0.51

Table 4.6 Flow stress of unoxidized specimen under compressive stress and flow stress ratios of specimens with oxidation gradients to that of the unoxidized specimen at any strains, indicating each ratio is almost constant irrespectively of strain

Total Strain	VIRGIN	Specimen A		Specimen B	
(%)	stress (MPa) σ_o	stress (MPa) σ	σ/σ_o	stress (MPa) σ	σ/σ_o
0.25	16.67	13.64	0.82	10.09	0.61
0.50	29.38	25.18	0.86	18.38	0.63
0.75	39.45	33.87	0.86	24.66	0.63
1.00	47.58	40.13	0.84	29.59	0.62
1.25	53.99	45.30	0.84	33.63	0.62
1.50	59.27	49.26	0.83	36.65	0.62
1.75	63.44	52.56	0.83	39.46	0.62
2.00	66.90	55.31	0.83	41.47	0.62
2.25	69.95			43.38	0.62
2.50	72.59			45.40	0.63
2.75	74.83			46.63	0.62
3.00	76.86			47.75	0.62
		Average	0.84		0.62

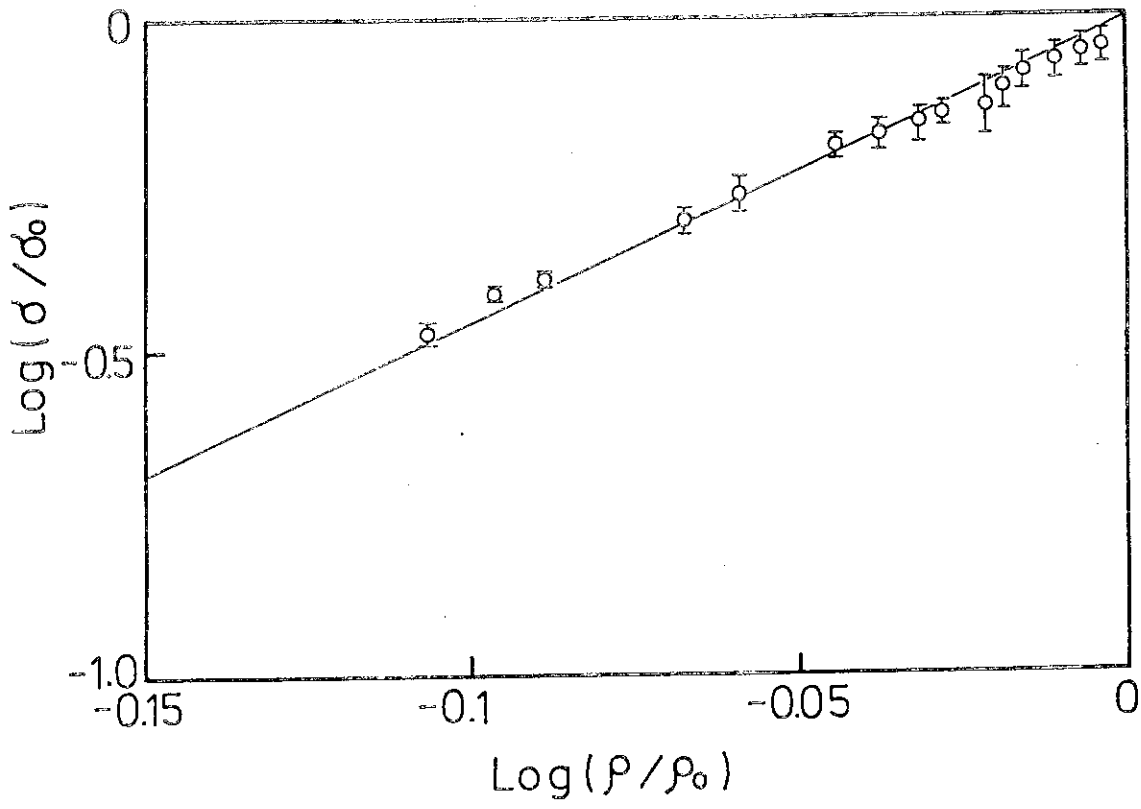

Fig. 4.10 Relationship between flow stress and density for uniformly oxidized specimens

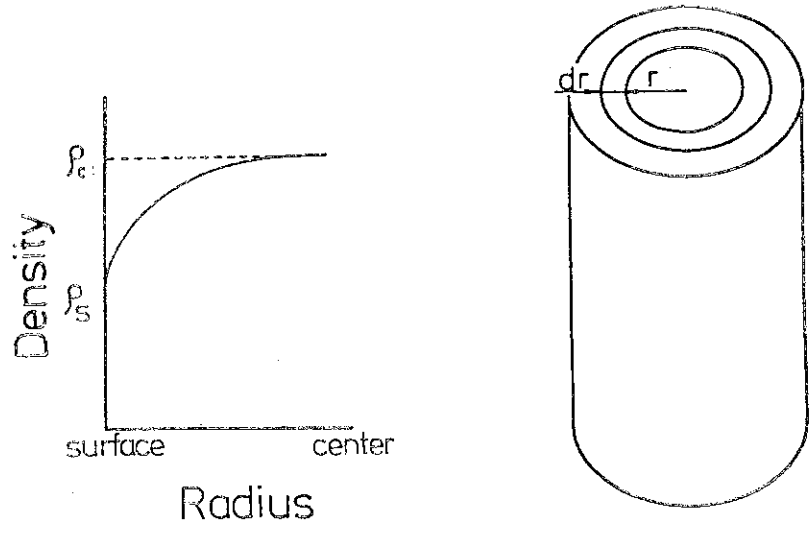

Fig. 4.11 Schematic representation of cylindrical specimen with oxidation gradient in the radial direction

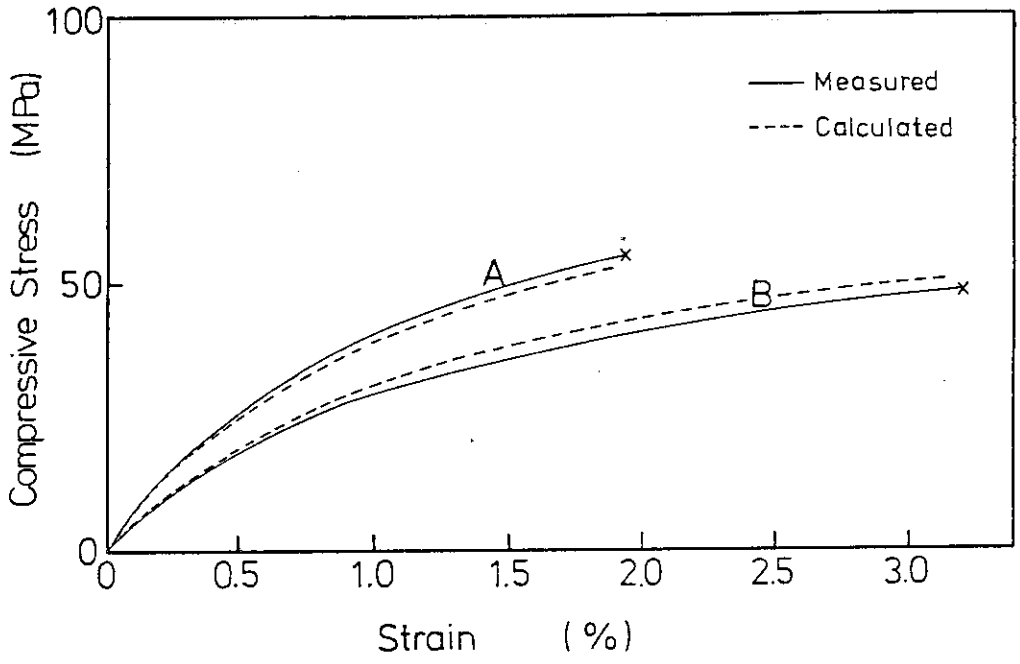

Fig. 4.12 Compressive stress-strain curves for specimens with oxidation gradients as shown in Fig. 4.11.

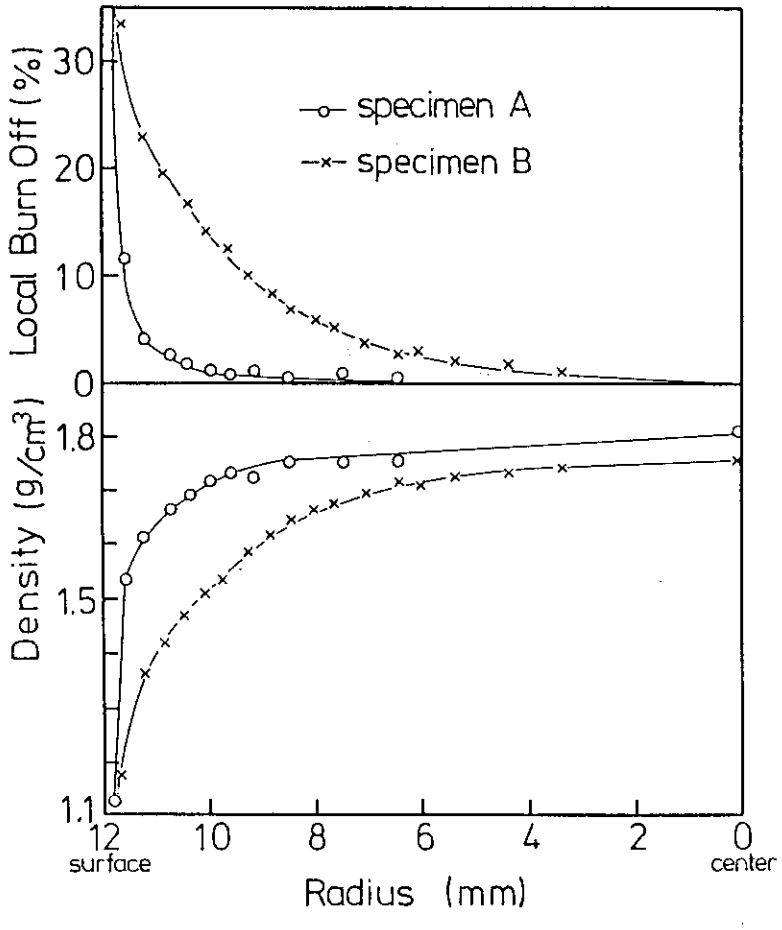

Fig. 4.13 Local burn-off profile of specimens A and B with 4.75 and 11.75 % weight loss respectively

4.4 Ring Compressive Fatigue Test of Graphite

S. Ishiyama, T. Oku, K. Fujisaki and M. Eto

Fatigue strength of graphites is one of the indispendable subjects for the design requirements of the VHTR core structure. Pre- and post-irradiated static and fatigue strength tests of nuclear-grade graphite were performed for three sizes of ring compressive specimens. The principal purpose of this study is to provide the effect of neutron irradiation on cyclic fatigue life of an isotropic nuclear-grade graphite, taking advantage of the fact that many ring type specimens are able to be accommodated into an irradiation capsule.

Experimental procedure

(1) Material and specimen

Three sizes of ring type specimens (small, medium and large types: inner and outer diameters, and width are 8.5 x 5.2 x 5, 14.5 x 8.8 x 5, 24.8 x 14.8 x 10 mm respectively) were mechined from a purfied fine-grained isostatically-pressed IG-110 cylindrical graphite block (Toyo tanso Co. Ltd.). Specimens were sampled in such a way as the concentric axis was parallel to the longitudinal one. Bending and compression test specimens 5ϕ x 50, 5ϕ x 10mm were sampled from the same block.

(2) Apparatus

Specimens were fatigued using a 0.15 ton servo-hydraulic fatigue machine. Ring compressive static and fatigue strength tests (under $0.90L_{fu}$, $0.85L_{fu}$, $0.80L_{fu}$, $0.75L_{fu}$ stress levels) were performed at loading speeds of $60L_{fu}$(kg/min) and $\pm 60L_{fu}$ of saw-toothed wave respectively, where L_{fu}

is the mean of fracture loads for each type of ring specimen. The ratio of the minimum load to the maximum one was set to be 0.1. The outer diameter of each specimen was measured continuously using an extensometer (travel range: ±2mm) during the fatigue tests.

(3) Irradiation

Irradiations were carried out in an incore vertical hole of JRR-2. The capsules ICM-25H (three cycles, 796.5 hours) and ICM-34H (seven cycles, 1710.02 hours) were irradiated under the condition that irradiation temperatures were 575 ∿ 650°C, 530 ∿ 630°C respectively, and fluences were 1.92∿3.20 x 10^{20} n/cm^2 and 2.80∿4.92 x 10^{20} n/cm^2 respectively.

Results

(1) Static strength

Ring compressive strength was estimated using the formula derived from the curved beam theory:

$$\sigma_r = \frac{b-(1+2k)}{2\pi a l(b-a)k(k+1)} \cdot P \qquad (4.10)$$

where

P : peak load (kg)
a : inner radius of ring specimen
b : outer radius of ring specimen
l : width
k : shape factor $\left(= -1+\frac{b+a}{2(b-a)}\ln\frac{b}{a}\right)$

Figure 4.14 shows the strength distribution for pre- and post-irradiated ring specimens, which was fitted to the Weibull distribution function. Mean strength of each type of rings and Weibull modulus are shown in Table 4.7. Ring compressive strength increased as the ring size became smaller and also increased about 20 % by neutron irradiation.

(2) Fatigue strength

Pre- and post-irradiation fatigue data are summarized in Fig. 4.15. where the applied stress (σ_a) was normalized by the mean ring compressive strength (σ_{ru}) of each type of rings before irradiation. In the pre-irradiation fatigue test, there seems to be no difference in the scatter of life among three types of rings (△,□, o indicate small, medium and large types of ring specimens respectively). Applied stress and fatigue life were tried to be correlated to the following equation:

$$\mathrm{Log}_{10}(\sigma_a/\bar{\sigma}_{ru}) = A + B\ \mathrm{Log}_{10}N_f, \tag{4.11}$$

where

σ_a : applied stress
$\bar{\sigma}_{ru}$: mean pre-irradiated ring compressive strength
N_f : fatigue life
A,B : constant.

Two solid lines in Fig. 4.15 are the mean S-N curve for pre- and post-irradiated fatigue data. Constants A, B in Eq. (4.11) and relative fatigue strength ($\sigma_a/\bar{\sigma}_{ru}$) at 10^5 cycles are tabulated in Table 4.8.

Table 4.7 Ring compressive strength of pre- and post-irradiated IG-110 graphite

Item / Ring type	Pre-irradiation		Post-irradiation	
	Strength [MPa]	Weibull modulus	Strength [MPa]	Weibull modulus
L-type (24.8 - 14.8)φx 10mm	44.3±2.3	20.8	-	-
M-type (14.5 - 8.8)φx 5mm	48.1±2.4	21.5	56.0±1.9	33.3
S-type (8.5 - 5.2)φx 5mm	51.3±2.5	22.8	60.9±2.8	23.4

Table 4.8 Mean S-N curve of pre- and post-irradiated IG-110 and PGX graphite

	$\mathrm{Log}_{10}(\sigma_a/\bar{\sigma}_{ru}) = A + B\ \mathrm{Log}_{10}N_f$	
	Pre-irradiated	Post-irradiated
A	0.001	0.056
B	-0.026	-0.023
Stress ratio at 10^5 cycles	0.745	0.872

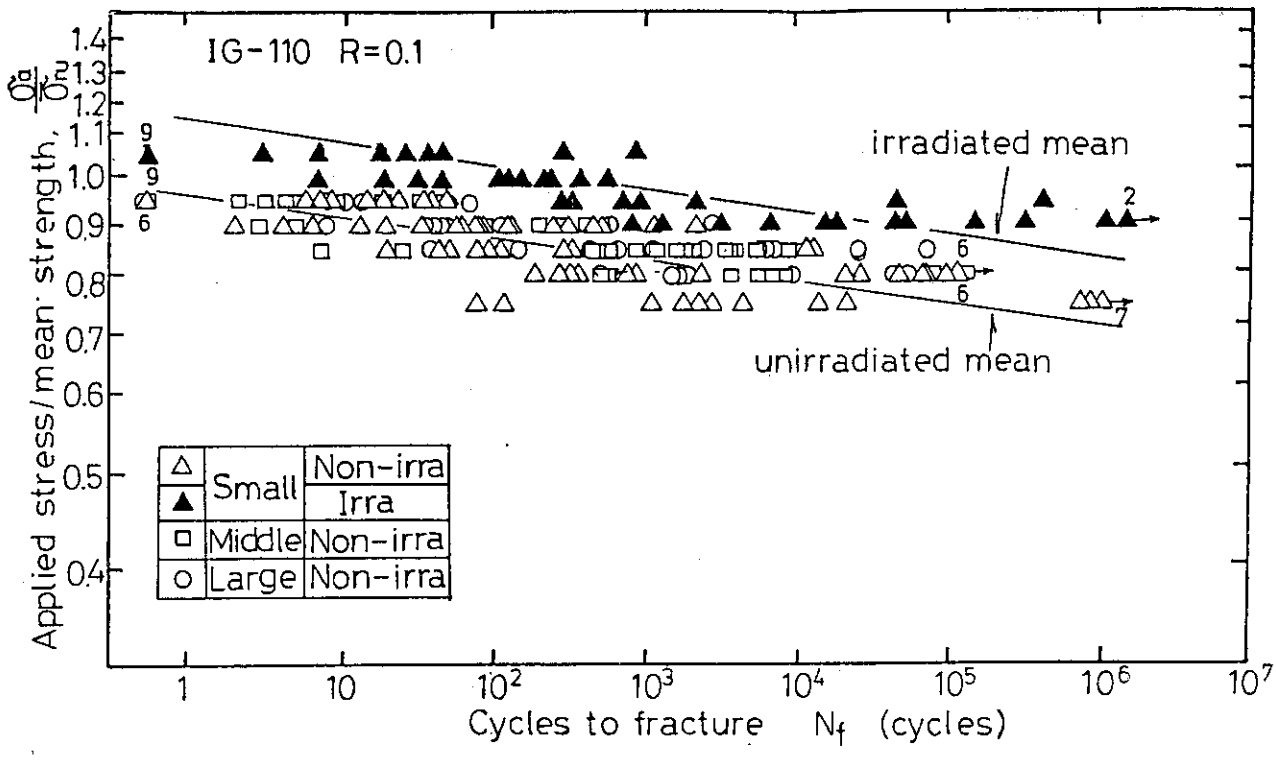

Fig. 4.14 Bending strength distribution of irradiated and non-irradiated specimens

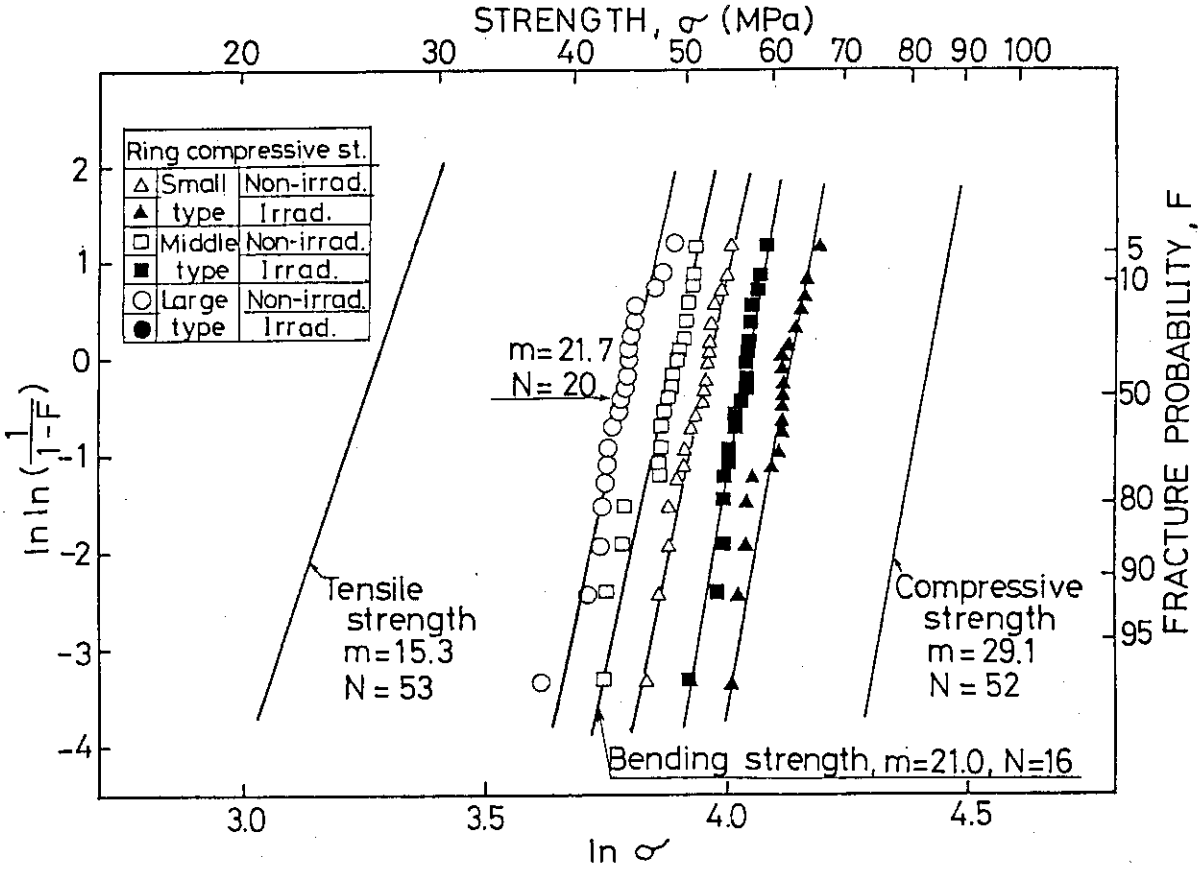

Fig. 4.15 Fatigue life curve of pre- and post-irradiated IG-110 graphite

4.5 Experiments on Neutron Irradiation Embrittlement in 2¼Cr-1Mo Steel

M. Suzuki, K. Fukaya, T. Kodaira and T. Oku

It was shown in the previous report [1] that neutron irradiation embrittlement in 2¼Cr-1Mo steel was small up to about 10^{19}n/cm^2 (E>1MeV) at 400°C. Further investigation concerning the effect of neutron irradiation on temper embrittlement of steel is required. Therefore we have studied how the neutron irradiation affects the embrittlement of the steel with isothermal aging at 475°C for 1000 hours.

Experimental procedure

Neutron irradiation was carried out using the Japan Material Testing Reactor (JMTR) at about 400°C, neutron fluence of up to about 1 x 10^{18} n/cm^2 (E>1 MeV). Two different sets of specimens were made from the 160 mm thick normalized and tempered 2¼Cr-1Mo steel: one was as-received and the other was pre-irradiation aged material at 475°C for 1000 hours.

Results and discussion

Figure 4.16 represents Charpy impact properties before and after neutron irradiation, including those of thermal controlled specimens, which had the same thermal history as the irradiated ones. In the non-aged specimens before irradiation, these properties were not affected much by neutron irradiation except for the decrease in upper shelf energy. On the other hand, in the pre-irradiation thermally aged specimen, a marked increase in the ductile to brittle transition temperature (DBTT) was observed, and the decrease in upper shelf energy was almost the same as the non-aged one. According to the fractographic observation by a scanning electron microscope, it can be concluded that the embrittlement due to thermal aging is attributed to the weakening of grain boundary. When the strength of grain boundary decreases on account of impurity segregation, the embrittlement becomes more pronounced owing to neutron irradiation.

Reducing the impurity elements such as phosphorus (P) which cause the intergranular brittleness is, therefore, considered to be important it suppresses the embrittlement of this material in a practical use.

Future plan

For the evaluation of structural integrity of the pressure vessel, fracture toughness data of irradiated 2¼Cr-1Mo steels will be required as well as the DBTT data.

Reference

1) JAERI, Div. of High Temperature Engineering: Annual Report of the Division of High Temperature Engineering, (Oct. 1983), JAERI-M 82-322 (1983).

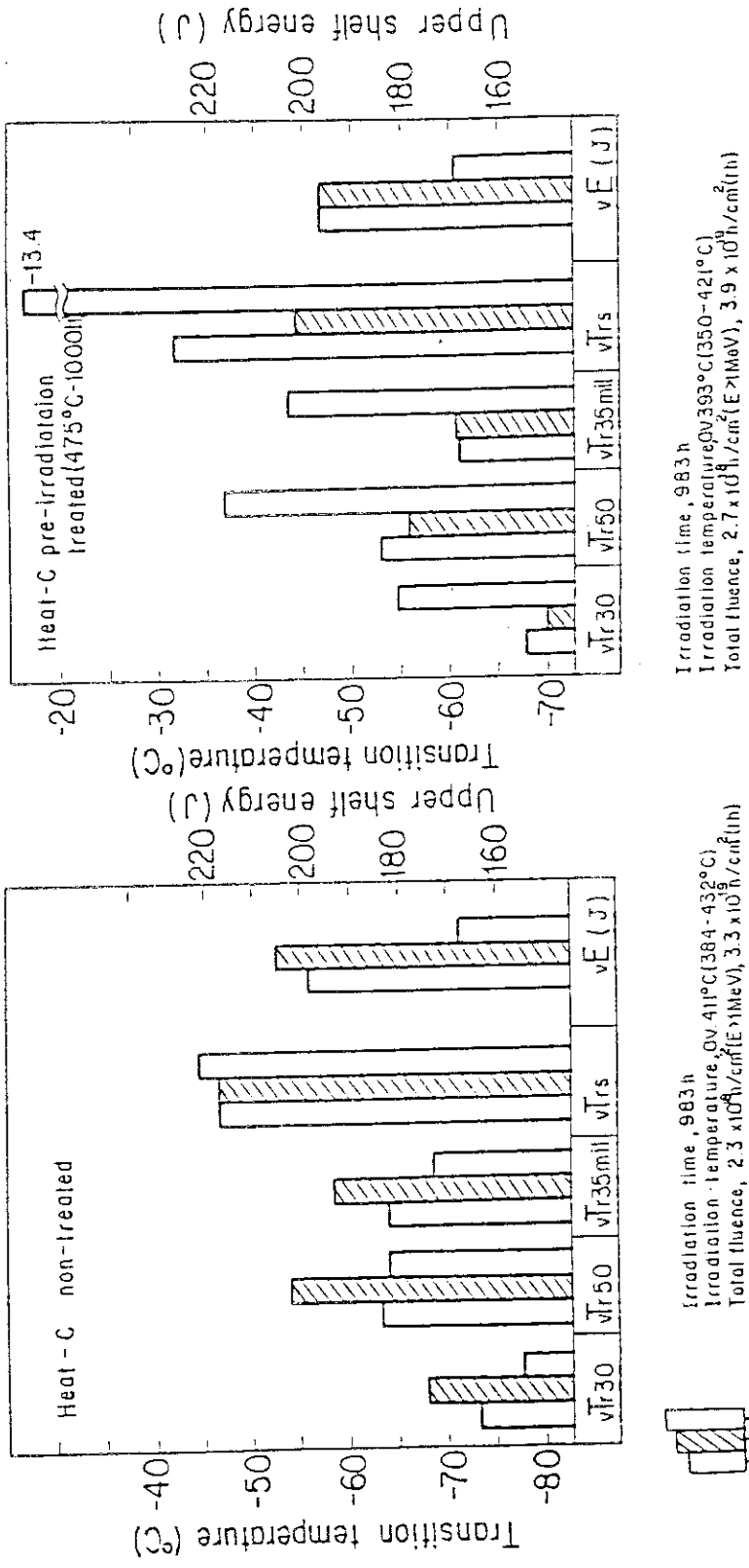

Fig. 4.16 Charpy impact properties before and after neutron irradiation

4.6 Toughness Degradation Caused by Isothermal Aging

T. Kodaira, K. Fukaya, M. Suzuki and T. Oku

A 2¼Cr-1Mo steel is planned to be used for reactor pressure vessel and other structural components of the VHTR. Since the operating temperature of those components including the reactor pressure vessel is designed at about 400°C, temper embrittlement of the 2¼Cr-1Mo steel is considered to be the most important subject for the integrity of the components. This embrittlement occurs owing to the weakening of prior-austenitized grain boundary[1], which promoted by intergranular segregation of impurity elements contained in the steel such as phosphorus (P), tin (Sn) and so on[2].

In the present study, the degree of embrittlement caused by isothermal aging is examined up to 30000 hours with a temperature range from 400°C to 500°C using the commercial grade 2¼Cr-1Mo steel, heat-treated in the normalized and tempered conditions.

Experimental procedure

The materials used in the present experiment are 2¼Cr-1Mo steel plates with a thickness of 160 mm designated as A387 Gr.22 Cl.2 according to the ASTM specification. The testing blocks with a dimension of 250 mm (in the rolling direction) by 60 mm by 15 mm (in the thickness direction) were taken from the quarter thickness portion of materials. These blocks were heated in air in a temperature region from 400°C to 500°C for time up to 30000 hours. After heating, Charpy and tensile test specimens were mechined. Tensile tests were conducted on the specimen with a gage length of 22 mm long and a diameter of 4 mm using an Instron type tensile testing machine at room temperature in a nominal strain rate of 3.2×10^{-4}/sec. Charpy impact tests were carried out with the standard Charpy specimen using a 300 J Charpy impact testing machine.

Results and discussion

Isothermal aging has the most pronounced effect on the Charpy impact properties. Typical example of the shift of absorbed energy transition curve caused by isothermal aging at 450°C is shown in Fig. 4.17. It is well known that the ductile to brittle transition temperature (DBTT) increases with aging time, and a shift of 42°C is observed after 30000 hours' heating. On the other hand, tensile properties such as 0.2% proof stress showed little change as shown in Fig. 4.18.

Figure 4.19 represents the increment of DBTT as a function of aging time and temperature, and indicates that the higher the aging temperature becomes, the more the DBTT shifts.

Change in the fracture mode with progress of the embrittlement was observed by a scanning electron microscope (SEM)[3]. When the fracture of non-embrittled materials occur brittly at temperatures below DBTT, the entire surface reveals transgranular type cleavage fracture. On the other hand, intergranular type fracture appears in embrittle materials. An Auger electron spectroscopic analysis indicates that phoshorus dominantly segregates at the grain boundary[3].

Future plan

The examination of embrittlement due to isothermal aging is to be conducted for the joint welded by a gas-metal-arc method on the included angle.

References

1) Erwin, W. G. and Kerr, J. G. : WRC Bulletin, 275,(1982).
2) Bruscate, R. : Weld. J., 49, 4, p.148-156 (1970).
3) Suzuki, M. et al. : "Study on Toughness Degradation Caused by Temper Embrittlement and Neutron Irradiation in 2¼Cr-1Mo Steel for Pressure Vessel of VHTR", proceeding of 5th Int. Conf. on Pressure Vessel Tech., San Francisco (1984).

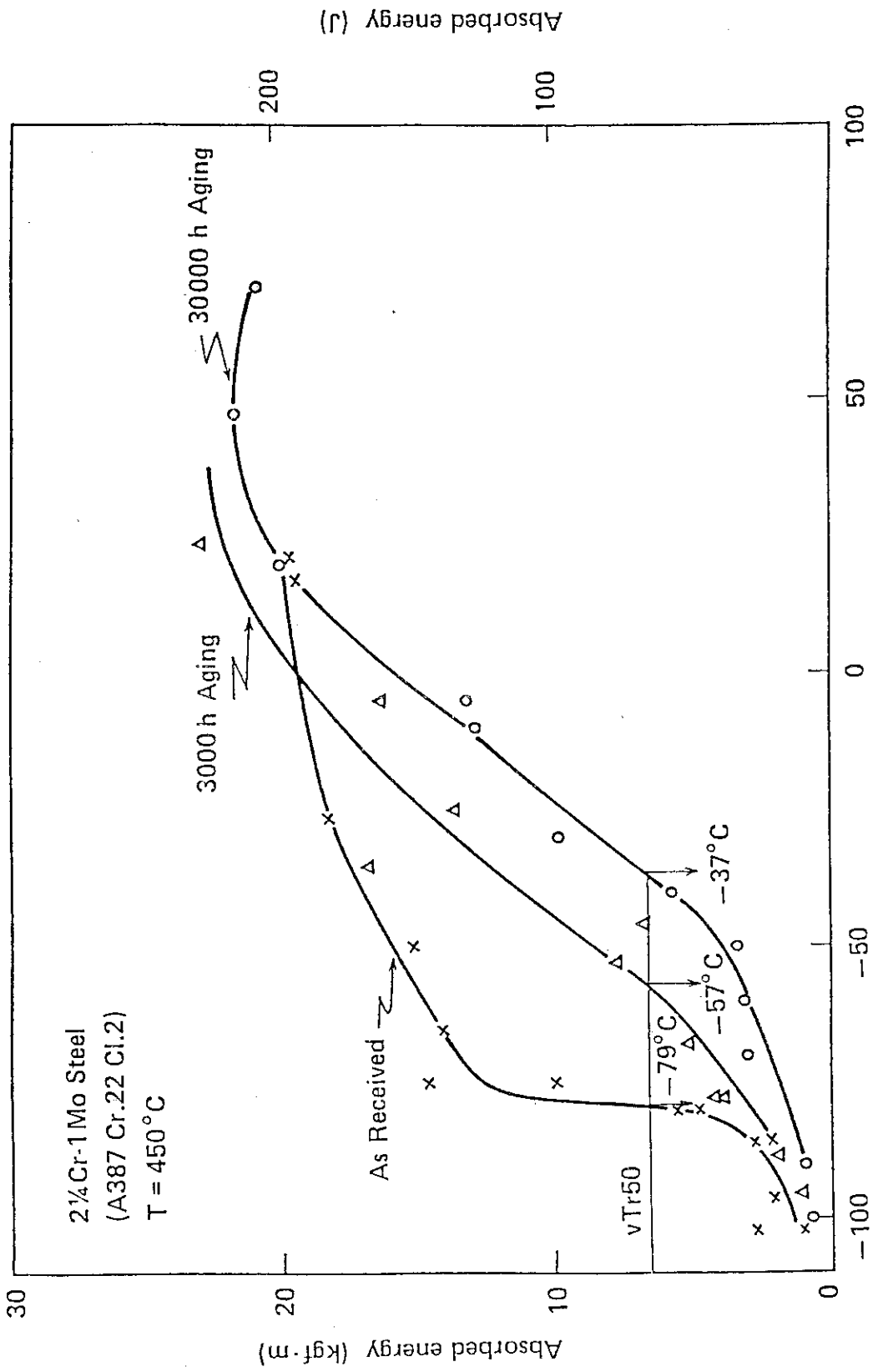

Fig. 4.17 Effect of thermal aging on notch ductility of A387 Gr.22 Cl.2 base metal

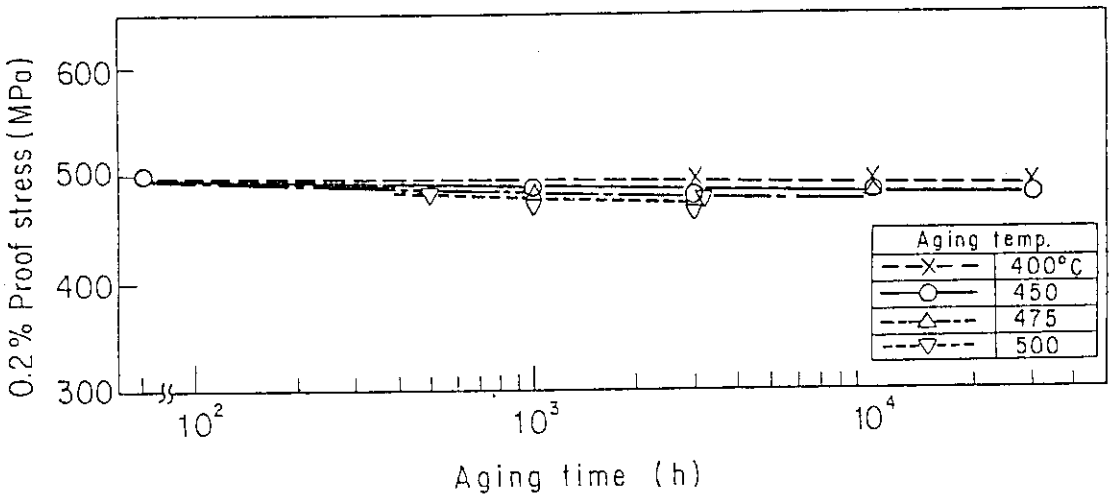

Fig. 4.18 0.2 % proof stress as a function of aging time

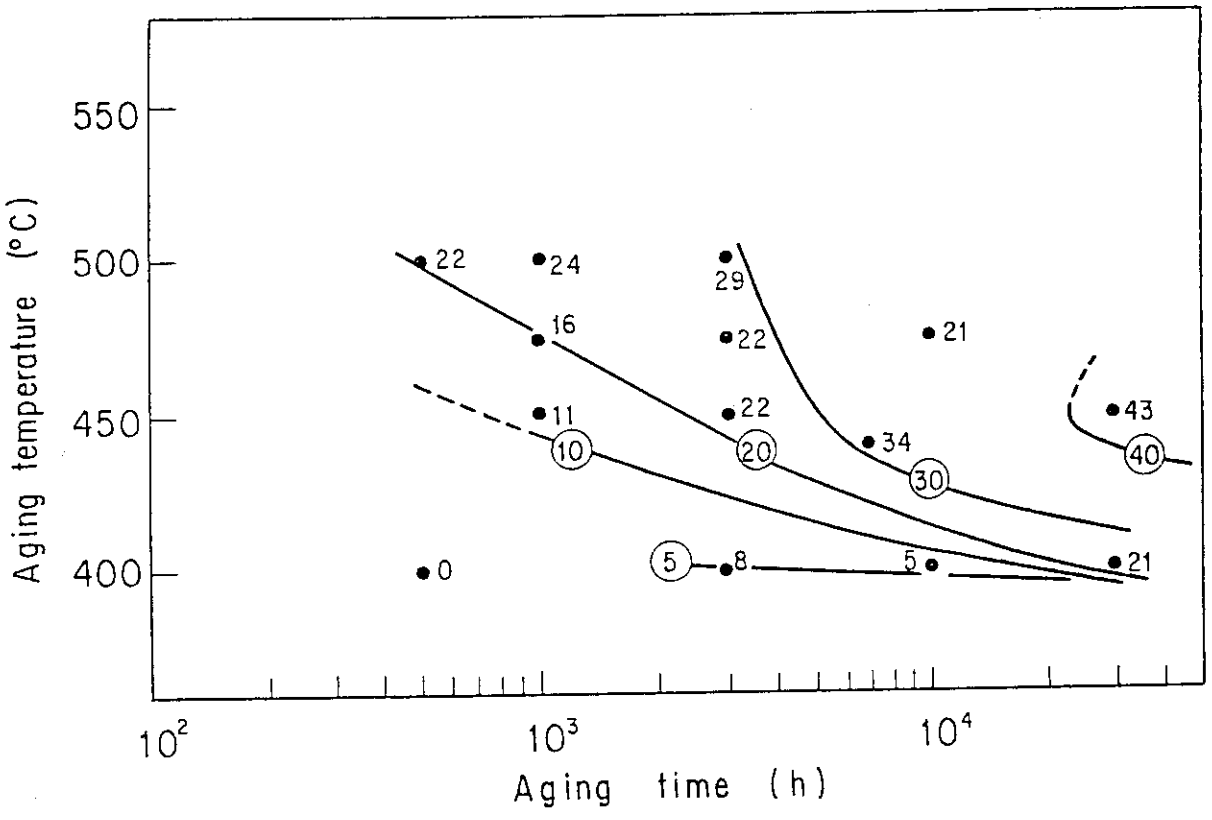

Fig. 4.19 Experimental aging time and temperature curves of constant increase in transition temperature

4.7 Embrittlement Caused by Stress Aging Treatment

M. Suzuki, K. Fukaya, T. Oku and T. Kodaira

The temper embrittlement of 2¼Cr-1Mo steels has been examined, because the embrittlement of this kind of steel occurs in the VHTR pressure vessel by a long-term operation. Our concern has been focussed on the effect of applied stress on temper embrittlement. The purpose of the present experiment is to clarify the effect of the loading direction on the temper embrittlement of 2¼Cr-1Mo steel subjected to sustained loading.

Experimental procedure

A test specimen was a normalized and tempered 2¼Cr-1Mo steel designated as A387 Gr.22 Cl.2 according to the ASTM specification. The testing block for the stress aging treatment has a cross section of 12 x 60 mm^2 and a gauge length of 480 mm, so that forty Charpy specimens can be machined in such a way as the long axis of the specimen is parallel or perpendicular to the loading direction. The extracting direction of the specimen, the rolling direction and the loading direction are shown in Fig. 4.20. Aging temperature, stress level and the maximum time for stress aging were 450°C, 210 MPa and 3000 hours respectively. Detailed experimental conditions are shown in Table 4.9.

Results and discussion

In Fig. 4.21 is shown the change in transition temperature determined by 50 ft·lb (68J) absorbed energy level as a function of aging time. It indicates that the degree of embrittlement depends on the direction where the specimen was cut out. R-specimen showed much more increase in transition temperature than W-specimen. Clearly, there was an effect of applied stress on the embrittlement in R-specimen, which was machined parallel to the loading direction. The embrittlement was enhanced by the applied stress more than the stress-free isothermally aged materials

for 600 and 3000 hours, and the increment of the transition temperature for 3000 hours' aging exceeded one of the step-cooled material.

With the aid of a scanning electron microscope and an Auger electron microscopic analyser, the embrittlement was attributed to the further weakening of grain boundaries by stress application, where phosphorus (P) was segregated substantially to cause temper embrittlement.

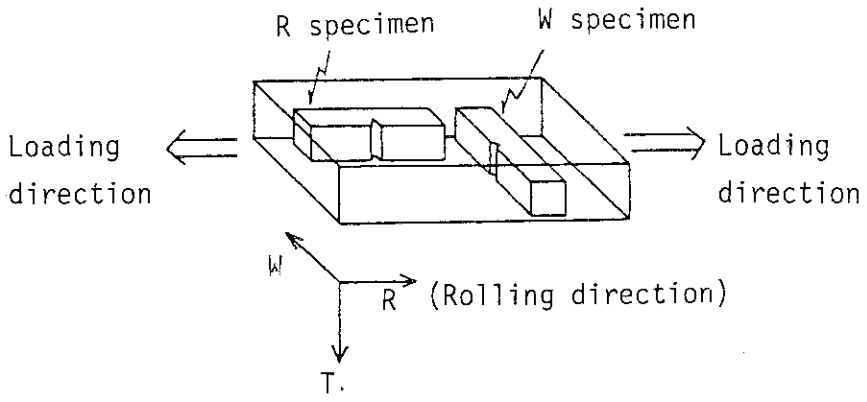

Fig. 4.20 Relation among specimen cut-off direction, rolling direction in steel making process and loading direction

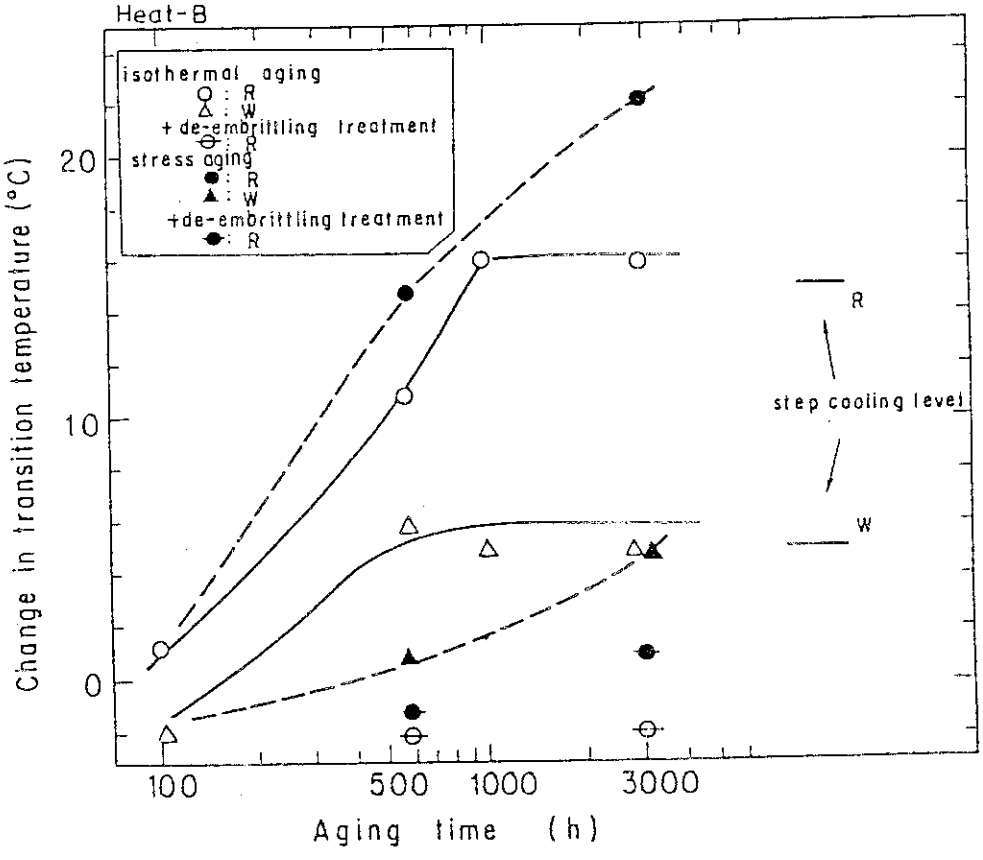

Fig. 4.21 Change in trasition temperature as a function of aging time for stress-aged and isothermally aged materials

Table 4.9 Condition for embrittling treatment

Specimen symbol	Embrittling treatment	Treatment condition
A0	As received	
A1	Isothermal ageing	450 °C, 100 h
A2	Isothermal ageing	450 °C, 600 h
A3	Isothermal ageing	450 °C, 1 000 h
A4	Isothermal ageing	450 °C, 3 000 h
C1	Stress ageing	450 °C, 210 MPa, 600 h (0.13 %)
C2	Stress ageing	450 °C, 210 MPa, 3 000 h (0.38 %)
S1	Step cooling	G.E. type step cooling

Parenthesized values indicate creep strains.

4.8 Fracture Toughness Test

T. Kodaira, M. Matsumoto, K. Fukaya and T. Oku

Since any kinds of 2¼Cr-1Mo steel have never been used for a pressure vessel of nuclear reactor, collecting fracture toughness data of irradiated and unirradiated steels is very urgent to evaluate structural integrity of the VHTR pressure vessel. In accordance with the need mentioned above, fracture toughness tests have been carried out with small specimens based on J-integral. The dynamic fracture toughness data are presented in this section.

Experimental procedure

Three kinds of thick pressure vessel steels were used in this experiment. These are A387 Gr.22 Cl.1, Cl.2 and A542 Cl.1, and small three point bend specimens with the same dimension of a Charpy specimen (10 x 10 x 55 mm) are cut perpendicular to the rolling direction out of the quarter thickness.

Dynamic fracture toughness tests were conducted at several temperature between -60°C and 120°C using an instrumented Charpy testing machine with a capacity of 300 J. The onset of crack was initiated at the point of the maximum load, and dynamic fracture toughness values (K_{Id}) were calculated by the following equation[1]. As for the linear elastic fracture tonghness values, K_{Id} are given by

$$K_{ID} = \frac{P_{max} \cdot S}{B \cdot W^{3/2}} \cdot f(a/w) \ , \qquad (4.12)$$

where P_{max}: maximum load, S: span, B: thickness, W: width, a: crack length and f(a/s): configuration factor.

In the case of elastic and plastic fracture, J_{Id} value is calculated by Eq. (4.13), and it converts into K_{Id} using Eq. (4.14).

$$J_{Id} = 2A/B(w - a) \qquad (4.13)$$

$$K_{Id} = \sqrt{J_{Id} \cdot E/(1 - \nu^2)} \quad , \qquad (4.14)$$

where, A: potential energy up to the maximum load, E: Young's Modulus and ν: Poisson's ratio.

Experimental results

Figure 4.22 shows the results of dynamic fracture toughness test of three steels. In the upper shelf region, the fracture toughness are nearly the same among three steels. On the other hand, A387 Gr.22 Cl.1 steel has the lowest toughness and A387 Gr.22 Cl.2 steel is the most excellent in transition region.

Figure 4.23 shows the results of static and dynamic fracture toughness (K_{Ic} and K_{Id}) tests of three steels, comparing these data with the reference fracture toughness K_{IR}. It is noticed that almost all K_{Ic} and K_{Id} values of three steels have the higher toughness than K_{IR}, except for K_{Id} data of A387 Gr.22 Cl.1 steel. It can be also pointed out that A387 Gr.22 Cl.2 steel is better for the prevention of unstable fracture.

Future plan

The following experiments will be done to obtain the basic data for the evaluation of structural integrity of the VHTR pressure vessel.

1) K_{Ic} and K_{Id} fracture toughness data of welded joints,
2) Nil ductility transition temperature (NDT) data, and
3) Cyclic crack growth rate data of base metal and welded joints.

Reference

1) Server, W.L. : J. of Testing and Evaluation, 6, 1, p.29-34, (1978).

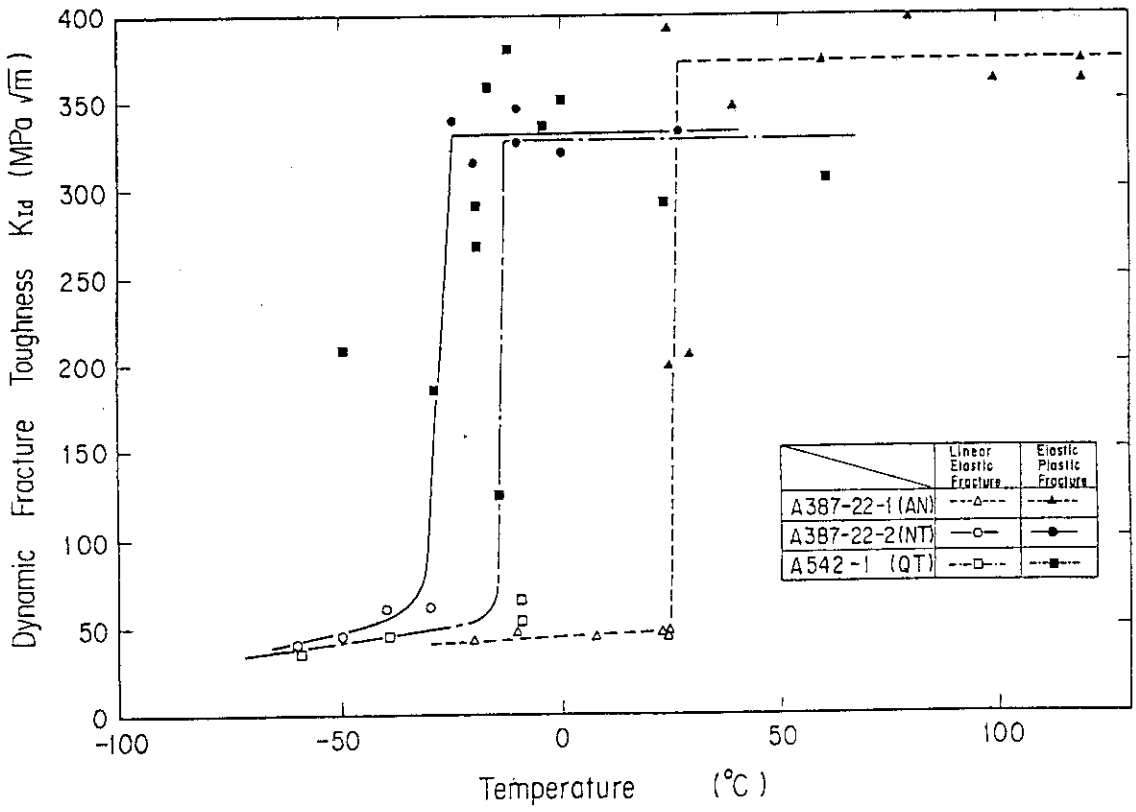

Fig. 4.22 Dynamic fracture toughness K_{Id} of three 2¼Cr-1Mo steels

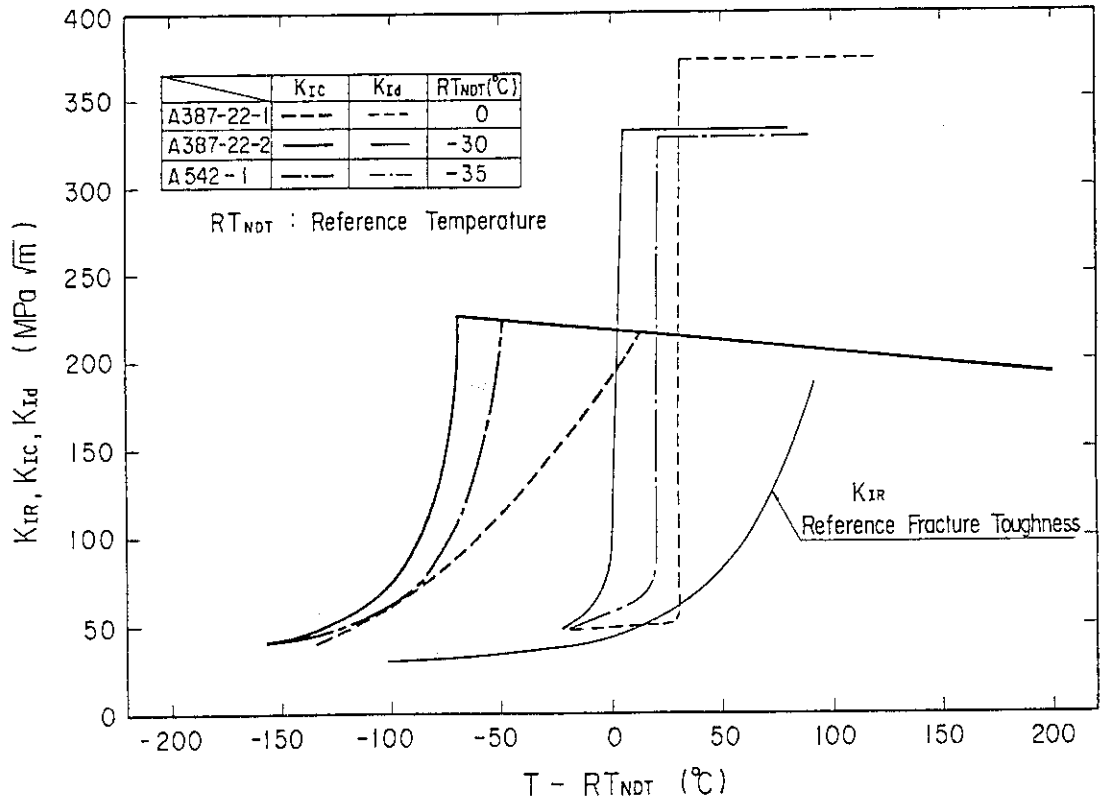

Fig. 4.23 K_{IR}, K_{IC} and K_{Id} fracture toughness of three 2¼Cr-1Mo steels